Inclusion behavior in an Aluminum bath stirred by induction

Akshay Bansal

Akshay Bansal. Inclusion behavior in an Aluminum bath stirred by induction. Engineering Sciences [physics]. Université de Lorraine, 2016. English. NNT : 2016LORR0090 . tel-01752360

Thèse

Pour l'obtention du titre de :

Docteur de l'Université de Lorraine

Ecole doctorale : Energie, Mécanique et Matériaux

Présentée par :

Akshay Bansal

Comportement inclusionnaire dans un bain d'aluminium brassé par induction

Inclusion behavior in an Aluminum bath stirred by induction

Thèse soutenue publiquement le 13 Juillet 2016 à Nancy devant le jury composé de :

Mr. Hervé Duval	Ecole Centrale de Paris	Rapporteur
Mr. Christian Karcher	Technische Universität Ilmenau	Rapporteur
Mr. Yves Delannoy	Université Grenoble Alpes – SIMAP	Examinateur
Mr. Emmanuel Waz	Constellium Technology Center	Examinateur
Mr. Jean-Pierre Bellot	Université de Lorraine – Institut Jean Lamour	Examinateur
Mr. Pierre Chapelle	Université de Lorraine – Institut Jean Lamour	Examinateur

Département SI2M – Equipe Procédés d'élaboration
Institut Jean Lamour – *UMR 7198 – CNRS,* Parc de Saurupt – CS 50840 – 54011 Nancy Cedex

Université de Lorraine
Pole M4 : matière, matériaux, métallurgie, mécanique

Acknowledgement

First of all, I would like to acknowledge Institut Jean Lamour where I conducted my doctoral research. IJL's researchers, engineers and administrative staff played a vital role throughout my PhD, in providing a conducive research environment. I was welcomed into team 301 *Procédés d'élaboration* where I had an excellent opportunity to learn and share both scientific and day to day know-how with each member.

My PhD advisors Jean-Pierre Bellot and Pierre Chapelle have been instrumental in my evolution as a researcher. They have not only carefully guided me, but they also infused in me invaluable scientific rigor and discipline. These attributes will be the pillars of all my future endeavors as a research engineer. I sincerely thank them for their understanding and encouragement during the challenging moments of my research work.

I had the pleasure of working in direct collaboration with scientists from Constellium Technology Center – Pierre Le Brun and Emmanuel Waz. I would like to express my gratitude for their continuous and constructive support and the enriching experience as a part of ANR project Principia.

I thank Christian Karcher and Hervé Duval who agreed to review my dissertation and provide me with their positive critique. Furthermore, I would also like to thank Yves Delannoy and Emmanuel Waz for examining my work as part of the thesis oral examination committee.

No research work is complete without discussions, coffee breaks and brainstorming sessions with colleagues. I was fortunate to share my doctoral journey with several wonderful people at work: Nicole, Laurent, Jessica, Nico, Jonathan, Vincent, Mathilde, Caroline, Youssef, Suresh, Jacob, Julien and several others.

I shared my daily life as a PhD student outside IJL with my dear friends: Kanika, Saikat da and Mike-ji, who became my family away from home.

I have no words to express my love and gratitude for my mother, father, grandmother, grandfather and brothers who selflessly supported my quest and who were always present, a source of constant strength and joy.

To my family,

Table of Contents

List of Figures

List of Tables

Nomenclature

	Constants and Mathematical Symbols	
μ_0	Permeability of free space constant	4π x 10^{-7} $\mathrm{H.m^{-1}}$
g	Acceleration due to gravity constant	$9.81\ \mathrm{m.s^{-2}}$
ε_0	Permittivity in vacuum (electric constant) = $1/\mu_0 c^2$	8.85 x 10^{-12} $\mathrm{F.m^{-1}}$
π	Pi	-
	Greek symbols	
α	Indicator function distinguishing mixture phases	-
α_l	Liquid metal volume fraction	-
α_p	Particle volume fraction	-
α^{frag}	Fragmentation efficiency	$\mathrm{m^3}$
β_{ij}^{agg}	Aggregation kernel between two particles of sizes $d_{p,i}$ and $d_{p,j}$	$\mathrm{m^3.s^{-1}}$
β_i^{frag}	Fragmentation kernel for a particle of size *i*	$\mathrm{m^3.s^{-1}}$
β_{ij}^{lam}	Laminar aggregation kernel	$\mathrm{m^3.s^{-1}}$
β_{ij}^{sed}	Differential sedimentation collision kernel	$\mathrm{m^3.s^{-1}}$
β_{ij}^{t}	Turbulent collision kernel	$\mathrm{m^3.s^{-1}}$
γ_f	Liquid metal surface tension coefficient	$\mathrm{N.m^{-1}}$
$\dot{\gamma}$	Shear rate	$\mathrm{s^{-1}}$
δ_{EM}	Electromagnetic skin depth	m
$\Delta\varphi(x,y)$	Luminous intensity phase shift	rad
$\Delta z(x,y)$	Vertical displacement of a pixel	m
ε	Turbulence dissipation rate	$\mathrm{m^2.s^{-3}}$
η_k	Kolmogorov length scale	m
$\lambda_i^{\pm}(x)$	Distribution function used in Cell Average technique	-
μ_{eff}	Effective dynamic viscosity	$\mathrm{kg.m^{-1}.s^{-1}}$
μ_f	Dynamic viscosity	$\mathrm{kg.m^{-1}.s^{-1}}$
μ_{yoke}	Magnetic permeability of yokes	$\mathrm{H.m^{-1}}$
ν_f	Kinematic viscosity of the flow	$\mathrm{m^2.s^{-1}}$
ξ_i	Internal property of an inclusion with an index i	-
$\dot{\xi}(\xi,x,t)$	Evolution rate of the internal coordinates	-
ρ or ρ_f	Liquid metal density	$\mathrm{kg.m^{-3}}$
ρ_p	Particle density	$\mathrm{kg.m^{-3}}$
ρ_q	Charge density	$\mathrm{C.m^{-3}}$
$\sigma_{el,f}$	Electrical conductivity of the flow	$\mathrm{\Omega^{-1}.m^{-1}}$
$\sigma_{el,p}$	Particle electrical conductivity	$\mathrm{\Omega^{-1}.m^{-1}}$
τ_{em}	Characteristic removal time due to EM migration	s
τ_{agg}	Characteristic removal time due to aggregation	s
τ_{sed}	Characteristic removal time due to sedimentation	s
τ_p	Particle response time	s
τ_η	Kolmogorov time scale	s
$\boldsymbol{\tau}_{oxide}$	Tangential shear stress due to the oxide layer	$\mathrm{N.m^{-2}}$
τ_{wall}	Wall shear stress	$\mathrm{N.m^{-2}}$
φ_i	Number density for a class *i*	# of inclusions . $\mathrm{kg^{-1}}$ of melt
$\Phi_{sed,i}$	Total flux due to sedimentation for class *i* across crucible bottom	kg of inclusions . $\mathrm{s^{-1}}$
$\Phi_{em,i}$	Total flux due to EM migration for class *i* cross all boundaries	kg of inclusions . $\mathrm{s^{-1}}$
χ_{Joule}	Joule heating	$\mathrm{W.m^{-3}}$
$\dot{\chi}(\xi,x,t)$	Evolution rate of the external coordinates	-

$\Psi_{em,i}$	Removal frequency for the EM migration effect (all interfaces) for a class i	# of inclusions . s^{-1}
$\Psi_{agg,i}$	Removal frequency for the aggregation phenomenon averaged over the entire bath for a class i	# of inclusions . s^{-1}
$\Psi_{sed,i}$	Removal frequency for the sedimentation effect at the crucible bottom wall for a class i	# of inclusions . s^{-1}
ω	Specific dissipation rate of k	s^{-1}
Ω_{ξ}	Internal coordinate domain	-
Ω_{x}	External coordinate domain with a physical space of x_i	-
	Latin alphabets	
$\boldsymbol{A}$	Magnetic vector potential	$\mathrm{T.m}$
A_{θ}	Azimuthal component of the magnetic vector potential	$\mathrm{T.m}$
A_{int}	Interfacial area density	m^{-1}
$\boldsymbol{B}$	Magnetic induction	T
B_0	Magnetic induction amplitude	T
$B(z)$	Magnetic induction z component	T
B_i	Net flux of particle birth in class *i*	# of inclusions . m^{-3} of melt . s^{-1}
B_i^a	Total birth due to aggregation in class *i*	# of inclusions . m^{-3} of melt . s^{-1}
B_i^{agg}	Birth contribution due to aggregation assigned to the nearby pivots	# of inclusions . m^{-3} of melt . s^{-1}
B_i^f	Total birth due to fragmentation in class *i*	# of inclusions . m^{-3} of melt . s^{-1}
B_i^{frag}	Birth contribution due to fragmentation assigned to the nearby pivots	# of inclusions . m^{-3} of melt . s^{-1}
C_D	Drag force coefficient	-
C_f	Friction force coefficient	$\mathrm{kg.m^{-2}.s^{-1}}$
d_p	Particle diameter (with indices i,j,k for different classes)	m
$d_{p,0}$	Diameter of a primary particle constituting an aggregate	m
$d_{p,c}$	Threshold diameter for fragmentation	m
$d_{p,ij}$	Collision diameter between two particles of sizes $d_{p,i}$ and $d_{p,j}$	m
$\bar{d}$	Average diameter	m
$\overline{d_{32}}$	Average Sauter diameter	m
dS	Surface of a cell face	m^2
D_i	Net flux of particle death in class *i*	# of inclusions . m^{-3} of melt . s^{-1}
D_i^a	Total death due to aggregation in class *i*	# of inclusions . m^{-3} of melt . s^{-1}
D_i^f	Total death due to fragmentation in class *i*	# of inclusions . m^{-3} of melt . s^{-1}
$\boldsymbol{E}$	Electric field	$\mathrm{V.m^{-1}}$
$\boldsymbol{E_s}$	Electrostatic field	$\mathrm{V.m^{-1}}$
$\boldsymbol{E_I}$	Induced electric field	$\mathrm{V.m^{-1}}$
f	Inductor coil current frequency	Hz
$\boldsymbol{f}_{oxide}$	Friction force due to oxide layer	$\mathrm{N.m^{-3}}$
$\boldsymbol{F_{Lorentz}}$	Lorentz force due to magnetic induction	N or $\mathrm{N.m^{-3}}$ (volumetric force)
$\boldsymbol{F_p^B}$	Buoyancy force felt by a particle	N
$\boldsymbol{F_p^{em}}$	Force acting on a particle due to surrounding EM effect	N
$\boldsymbol{F_p^D}$	Drag force felt by a particle	N
h_m	Dome height	m
H_i	Net new population of particles	# of inclusions . m^{-3} of melt . s^{-1}
H_i^{agg}	Net new population of particles due to aggregation in class *i*	# of inclusions . m^{-3} of melt . s^{-1}
H_i^{frag}	Net new population of particles due to fragmentation in class *i*	# of inclusions . m^{-3} of melt . s^{-1}
$H(x)$	Heaviside step function	-
I_{turb}	Turbulence intensity	-
I_{xy}	Luminous intensity of a pixel positioned at $(\mathrm{x,y})$	lm
$\boldsymbol{j}$	Induced current density	$\mathrm{A.m^{-2}}$
j_e	External or coil current density	$\mathrm{A.m^{-2}}$
k	Turbulence kinetic energy	$\mathrm{m^2.s^{-2}}$
l^*	Characteristic length scale at the wall	m

L	Characteristic length of a geometry	m
$\boldsymbol{n}$	Normal vector to a surface	-
$n(\xi,x,t)$	Number density with ξ properties, located at x and at instant t	-
$n(v_p)$	Number density with only particle volume as the internal coordinate	# of inclusions . m^{-3} of melt . m^{-3} of inclusions
N_i	Number density for a class *i*	# of inclusions . m^{-3} of melt
$N_{i,bath}$	Number density averaged over the bath for a class i	# of inclusions . m^{-3} of melt
NI	Number of coil turns (N) multiplied by current in each turn (I)	A. tr
P_{gen}	Generator power	W
q	Electric charge	C
$r_{furnace}$	Furnace radius	m
R_ω	Shield parameter	-
Re_m	Magnetic Reynolds number	-
Re_p	Reynolds number for a particle	-
St_p	Stokes number for a particle	-
$\boldsymbol{t}$	Tangential vector to a surface	-
T_m	Melting temperature of a metal	K
$\boldsymbol{u}$	Velocity	$\mathrm{m.\,s^{-1}}$
u^*	Wall friction velocity	$\mathrm{m.\,s^{-1}}$
$\boldsymbol{u_{em,i}}$	EM migration velocity of particle in class *i*	$\mathrm{m.\,s^{-1}}$
$\boldsymbol{u_f}$	Velocity vector of the flow	$\mathrm{m.\,s^{-1}}$
$\overline{\boldsymbol{u_f}}$	Mean velocity vector of the flow	$\mathrm{m.\,s^{-1}}$
u_f'	Fluctuating velocity	$\mathrm{m.\,s^{-1}}$
u_i	Velocity component along i direction	$\mathrm{m.\,s^{-1}}$
$\boldsymbol{u_p}$	Particle velocity	$\mathrm{m.\,s^{-1}}$
$\overline{\boldsymbol{u}}_{\boldsymbol{p}}$	Mean particle velocity	$\mathrm{m.\,s^{-1}}$
$u_p{}'$	Fluctuating particle velocity	$\mathrm{m.\,s^{-1}}$
u_η	Kolmogorov's free surface velocity	$\mathrm{m.\,s^{-1}}$
$u_\perp$	RMS of the fluctuations of the normal velocity to the wall	$\mathrm{m.\,s^{-1}}$
$\boldsymbol{u_{sed,i}}$	Sedimentation velocity of particle in class *i*	$\mathrm{m.\,s^{-1}}$
v_d	Turbulent deposit velocity of particles	$\mathrm{m.\,s^{-1}}$
v_p	Particle volume	$\mathrm{m^3}$
V	Scalar electric potential	V
V_{bath}	Bath volume	$\mathrm{m^3}$
V_{cell}	Cell volume	$\mathrm{m^3}$
v_i, v_{i+1}	Volume intervals of a class *i*	$\mathrm{m^3}$
$\bar{v}_i$	Average volume of all newborn particles due to aggregation in class *i*	$\mathrm{m^3}$ of inclusions
$\bar{v}_i^{frag}$	Average volume of all newborn particles due to fragmentation in class *i*	$\mathrm{m^3}$ of inclusions
$V_{ij}{}^t$	Total turbulent collision rate between two particles i and *j*	$\mathrm{m.\,s^{-1}}$
V_i^{agg}	Total aggregate volume feeding class *i* due to aggregation	$\mathrm{m^3}$ of inclusions . m^{-3} of melt . s^{-1}
V_i^{frag}	Total aggregate volume feeding class *i* due to fragmentation	$\mathrm{m^3}$ of inclusions . m^{-3} of melt . s^{-1}
$\boldsymbol{V}_{m,int}$	Near interface melt velocity	$\mathrm{m.\,s^{-1}}$
$\boldsymbol{V}_{oxide}$	Oxide layer velocity	$\mathrm{m.\,s^{-1}}$
x_i	Fixed pivot defining a class *i*	$\mathrm{m^3}$
y^+	Dimensionless wall distance	m

Abbreviations

CFD	Computational Fluid Dynamics	PBE	Population Balance Equation
DCM	Drift Concentration Method	PBM	Populatin Balance Methodd
IMF	Induction Melting Furnace	VOF	Volume Of Fluid
MHD	Magneto Hydro Dynamics		

Introduction

This doctoral research is anchored in the National Research Agency of France (ANR France) sponsored project PRINCIPIA (PRocédés INdustriels de Coulée Innovants Pour l'Industrie Aéronautique), with the aim of improving development and processing of high performance aerospace aluminum alloys.

In the current dissertation, we present various experimental and numerical tools developed in order to analyze the behavior of small particles, otherwise called inclusions, in a molten aluminum bath stirred in an induction furnace.

In this part, a brief introduction to the context of this project is followed by some details concerning the aluminum alloy processing, providing the necessary background for our research work. We then discuss the thesis objectives followed by the dissertation outline.

i. Porosities and inclusions in aerospace alloys

The aeronautical industry uses different aluminum alloys for various structural elements of an airplane such as the fuselage, the internal body and the wings, thus making it an important market (worldwide ~ 200 000 tons per year) for the high performance aluminum alloys. However, the recent advent of the composites and related materials has mounted a stiff challenge to the aluminum industry, primarily in reducing the total weight of the structure.

As a general rule, the continuous quest for superior alloy quality and performance is the driving force behind innovation in the aerospace aluminum industry. The focus turns towards ensuring an improved property to weight ratio as well as better recyclability of the alloys. This need has given rise to a number of aerospace aluminum alloys, with the latest focus on the Al-Li alloy family, which has been instrumental in attaining these goals. Notwithstanding, the processing of Al-Li alloys comes with its set of issues. Aluminum and Lithium oxidize easily and may lead to the presence of oxide type inclusions in the bath. Moreover, Lithium increases the solubility of Hydrogen in the bath. The performance of those alloys is also dependent on the number as well as the size of porosities (Figure 1), which adversely affect the properties of the final product. These porosities mainly germinate during the solidification phase of the alloy processing, whereby the inclusions (Figure 2) may become the hosting sites for the dissolved hydrogen. Besides being involved in the formation of porosities, the presence of inclusion populations also affects the physico-chemical properties of the alloy, where an increase in the number density of inclusions may lead to a reduced fatigue resistance, thermo-electrical conductivity as well as ductility [1]. The inclusion type, size, morphology and concentration directly depend on the type of alloy, the process operating parameters and the geometry of the installation.

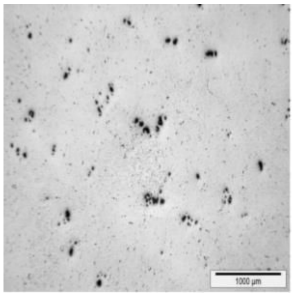

Figure 1: Porosities in an aluminum alloy rolled sheet

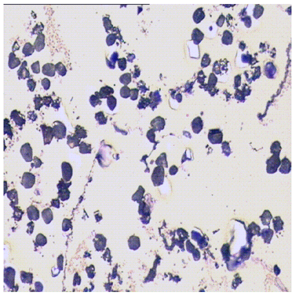

Figure 2: An example of inclusions of type $MgAl_2O_4$ with average particle size of 50 µm

© Constellium Technology Center

In order to tackle the porosity issue, aerospace alloys such Al-Zn (7xxx) and Al-Cu-Li (2xxx) require an improvement of the existing processes as well as development of new innovative processes in the casthouse.

ii. An overview of aluminum processing

As seen in Figure 3, aluminum alloy processing in the casthouse consists of several elements, each with specific tasks. The cycle starts with obtaining liquid metal either through smelting in an electrolytic cell or through recycling in a melting furnace. The melting furnace primarily uses two kinds of technologies – Induction Melting Furnace (IMF) or a gas (or oil) fired furnace, with a maximum capacity reaching several tens of tons of metal. Addition of alloying elements takes place at this stage. Due to the presence of water vapor in the gas fired furnace, the oxidation of the liquid metal leads to a severe mass loss whereas an IMF does not suffer with such limitations. The largest melting furnaces available on the market are gas fired furnaces and channel induction furnaces [2].

The liquid metal is then transferred to a holding furnace for further elaboration and attaining necessary physical parameters (primarily the temperature and the composition) before moving on to the purification part of the cycle. This stage is of particular interest as it also acts as a settling mode where capture of some inclusions may be performed. Almost all the holding furnaces are gas fired, but in some circumstances, the relatively less known induction technology is used. The purification step usually consists of a degasser and a filter. The degasser is based on the principle of flotation using the rotor technology for stirring and gas injection. The degasser helps eliminate the dissolved hydrogen and capture some of the suspended inclusions remaining in the metal [3]. The filtration process uses different types of filters to capture the inclusions present in the metal [4]. This is followed by the terminal step of casting, where the liquid metal is cast into ingots using semi-continuous casting or into rolled sheets using continuous casting. In the present research, we focus on the induction melting and stirring process during the holding step.

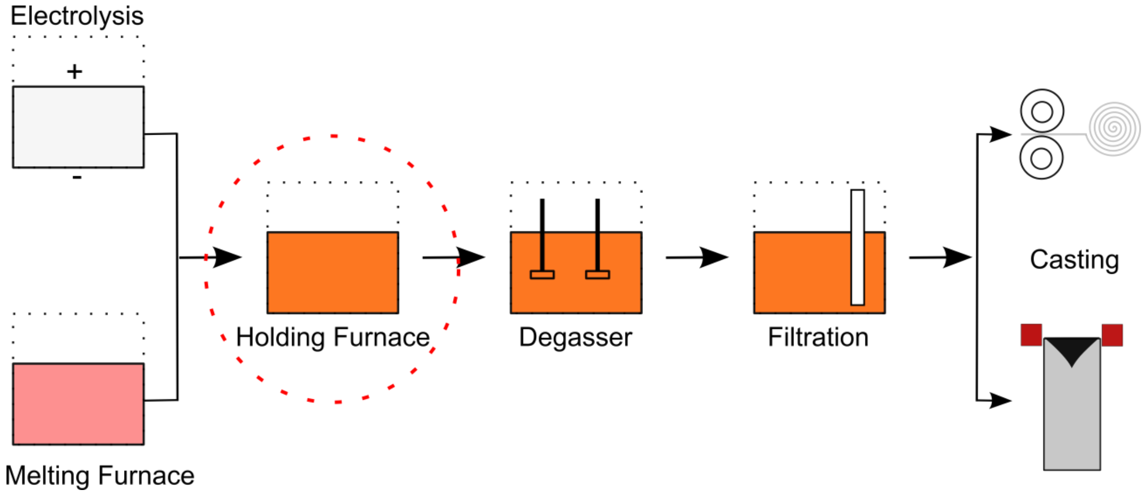

Figure 3: A layout of aluminum alloy processing in a casthouse

© Constellium Technology Center

iii. Dissertation objectives

As previously discussed, the induction melting furnace is an important casthouse installation which allows melting and processing of alloys. Since porosities in aluminum alloy products lead to a severe loss in the overall performance, it is a must to control any porosity generation. While processing the alloys, different varieties of inclusions are generated due to the phenomena involved, which may become a germination site of these porosities. This leads to the major objective of the dissertation, which is to study and provide efficient measures to control the inclusion population in an induction melting furnace.

The phenomena to be considered may be conveniently separated into two interlinked themes – (i) Magnetohydrodynamics (MHD) stirring of the molten aluminum bath, and (ii) Inclusion population behavior in the bath, both of which require a proper scientific description. In order to predict the inclusion dynamics and capture in induction melting and stirring furnaces, the above phenomena must be numerically modeled. Furthermore, the performance of the developed numerical tools must be verified by comparing the model calculated results with experimental measurements at both laboratory and industrial scale.

The objectives of the thesis are summarized as follows:

- Describing the phenomena and developing a numerical tool capable of:
    - Predicting magnetohydrodynamics in an IMF
    - Predicting inclusion behavior in an IMF
    - Assessing the inclusion capture at various interfaces (crucible walls and free surface)
- Validating the model using experiments

iv. Dissertation outline

After a brief introduction of the project, its context and the dissertation objectives, we move on to the main body of this document, which is organized into three parts – *Part A, Part B* and *Part C*. The first two put an emphasis on the theoretical concepts and the numerical tools developed over the course of the project, while the third part describes the application of these tools. Each part is further distributed into chapters, sections and sub sections. A detailed literature survey concerning each task is presented when required.

Part A describes the underlying concepts of the magnetohydrodynamic phenomena in an IMF. The corresponding experimental tools and the numerical model are presented.

Part B focuses on the phenomena influencing the inclusion behavior in an IMF and presents the numerical model developed to describe those phenomena.

Part C presents the application of the tools introduced in Parts A & B. We first focus on the application of the tools on a laboratory scale IMF (IJL Nancy) and analyze the obtained results. Further, we examine and discuss the numerical results of the simulations of an industrial scale IMF at a Constellium facility.

Finally, an overall conclusion of this research work along with the prospective future work is presented followed by several annexes providing other information pertaining to each part.

Part A: Magnetohydrodynamics

In this part, we introduce the MHD phenomena followed by a brief literature survey on induction melting furnace, from both experimental and numerical point of view. Later we describe the experimental tools used in our project, primarily to study the bath free surface deformation. We conclude this part of the dissertation with a chapter on numerical modeling of an induction melting furnace which encompasses the electromagnetic model as well as the hydrodynamic model.

1. Fundamentals of Magnetohydrodynamics

After a brief introduction to MagnetoHydroDynamics (MHD) and Electromagnetic Processing of Materials (EPM) in section A.1.1, we focus on EPM in an IMF in section A.1.2. In this section, the general working of an IMF is enunciated, followed by a theoretical background on electromagnetic fields and hydrodynamics. Later, in section A.1.3, we provide a literature survey on experimental and numerical studies performed in relation to IMFs. We also take up a literature survey on the influence of an oxide layer covering the liquid metal free surface.

1.1 Introduction

The interdisciplinary field of Magneto Hydro Dynamics (MHD) is a relatively new domain. Only in the mid 20th century did the scientists and engineers show any real interest in MHD.

> *"MHD can be described as the study of mutual interaction of fluid flow and magnetic fields."*
> Davidson [5]

Examples of fluids which are electrically conducting can be liquid metals, plasmas, electrolytes etc. Handbooks on MHD such as Davidson [5] and Tillack and Morley [6] provide an excellent stepping stone into the realm of MHD. The principles of MHD are applied at numerous scales, from the interstellar space to a laboratory scale EM levitation furnace. Some examples of application of MHD are as follows:

- Terrestrial magnetic field maintained by the fluid motion in the earth's core
- Solar magnetic fields which generate solar flares
- Magnetic confinement of high temperature plasmas to sustain fusion reactors
- MHD pumps & seawater propulsion using MHD
- Control of turbulent boundary layers to reduce drag
- Heat & mass transfer in liquid metal processing

It can be clearly seen that MHD has been applied across the board, but in the context of the present project, the author shall lay stress on Electromagnetic Processing of Materials – EPM and more particularly on induction melting and stirring.

The 1982 IUTAM symposium [7] held at Cambridge University, UK, led to a significant change in the way MHD was applied to EPM. Ever since considerable advances have been made in this field and several conferences and research projects have been dedicated solely to EPM. Asai [8], Moffatt [9], Bojarevics and Pericleous [10] and Mühlbauer [11] review several EPM and induction furnace related topics.

Simultaneously, an increase in the demand of very high quality materials was seen coming from the aerospace industry and other high precision industries. This augured well with the developing EPM field which enabled a better control of processing and casting of liquid metals, thereby ensuring higher alloy quality and efficiency of the processes. Heating, pumping, stirring, holding, repelling and levitating of liquid metals are just some of the examples of such processes. Figure 4 represents an impressive spread of EPM's applications as well related physical phenomena.

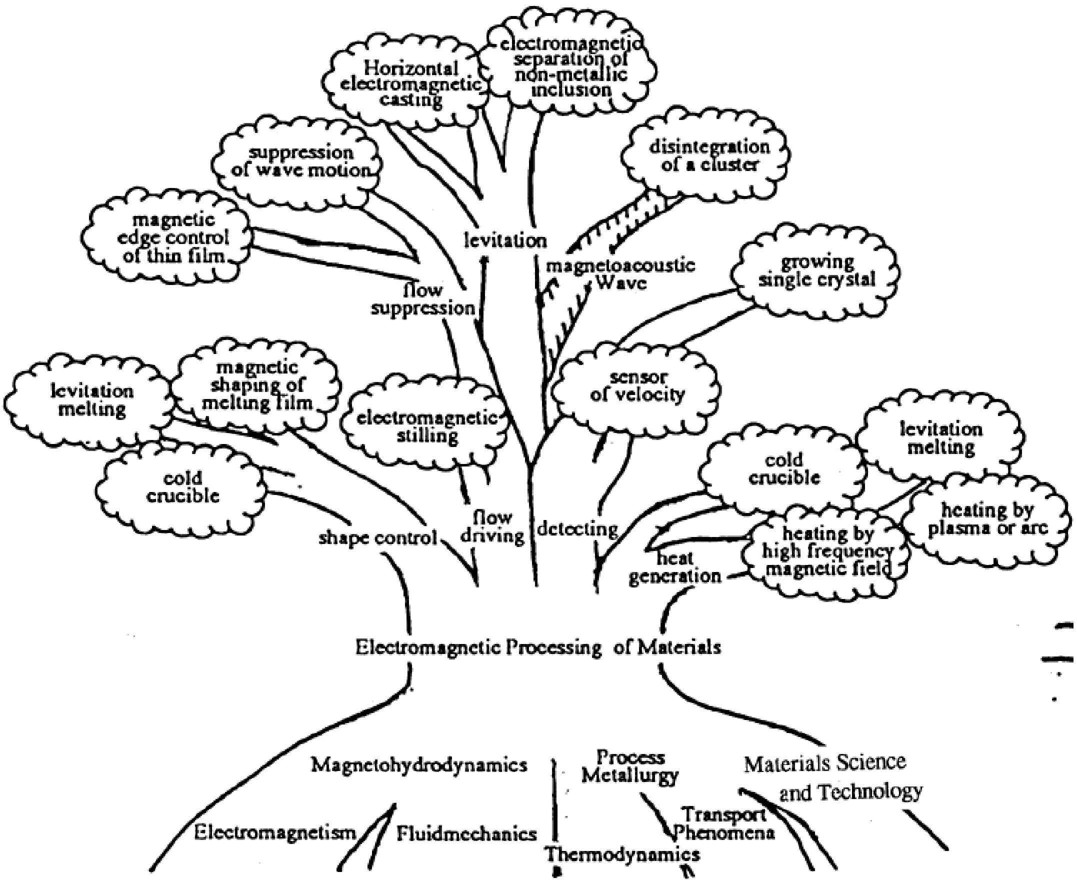

Figure 4: EPM and its varied applications [8]

1.2 EPM in an induction melting furnace

During liquid metal processing, an IMF may be used during the adding, mixing and melting of matter as well as for holding the mixture at its liquid state. The process, frequently used at the industrial scale, allows treatment of materials in a non-intrusive manner, without any use of mechanical stirrers or melters. While the overall quality and efficiency are improved, the liquid metal processing in an IMF has its own set of problems. Entrapment of inclusions, varying response of alloying elements to operating parameters and wearing down of the crucible walls due to turbulent stirring, are some of the issues encountered in an IMF.

1.2.1 General working of an induction melting furnace

In the late 19th century, Ferranti first designed an induction furnace to heat and melt steel [11]. Early 20th century saw several applications and designs of induction melting. In the 1950's, modern industrial scale furnaces like Otto Junker's design [12], seen in Figure 5, were capable of melting, stirring and holding several tons of metal. Notwithstanding, it was only in the 1970's that researchers started detailed experiments and numerical studies on phenomena encountered in an IMF and related processes.

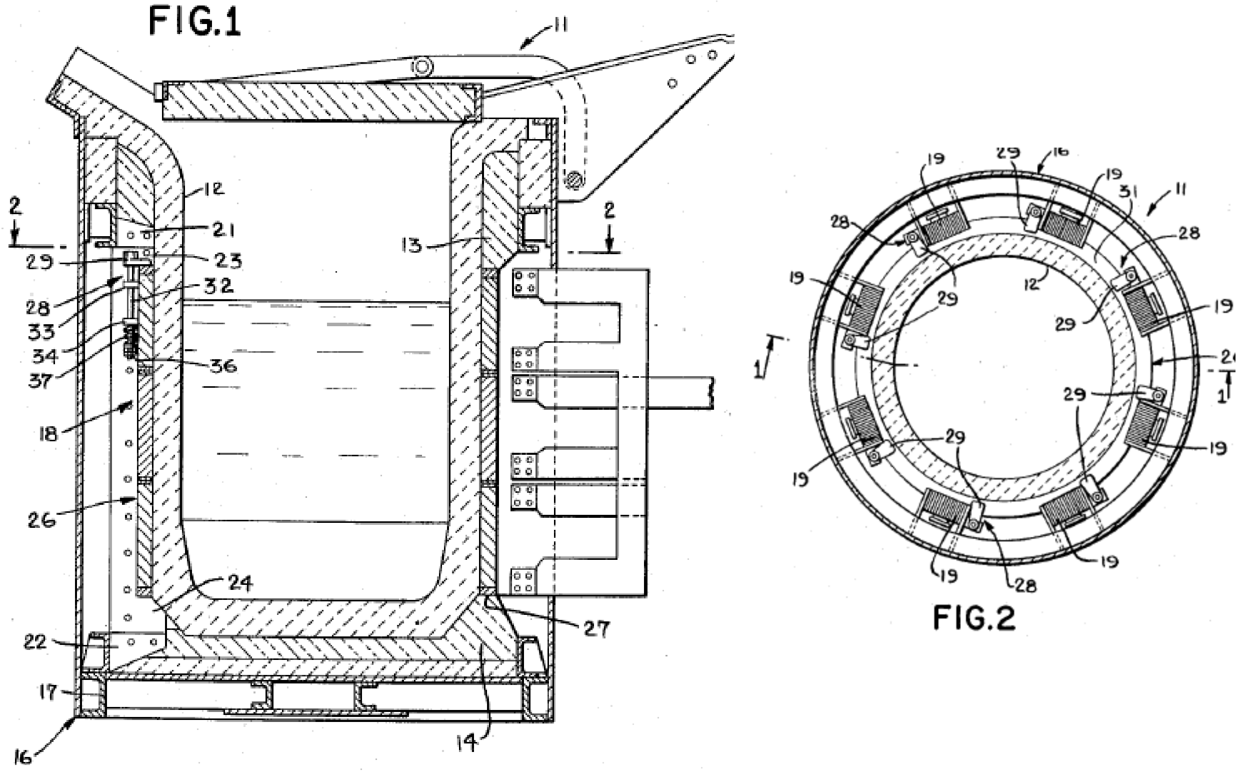

FIG.1

FIG.2

Figure 5: Otto Junker's design of an industrial scale IMF – section and top views [12]

In an IMF (Figure 5), a refractory vessel (n° 12) filled with a charge of metal is surrounded by an induction coil in the form of a solenoid (n° 26). The time-varying magnetic field produced by the induction coil acts on the metal thereby leading to induced currents and hence volumetric Lorentz forces inside the conducting metal. The induced currents have both thermal and mechanical effects [5]. The thermal effects, which originate from Joule heating, lead to energy dissipation as heat into the metal which may allow melting of the metal. The amount of heat produced by Joule heating can be expressed as: $\chi_{Joule} = j^2/\sigma_{el,f}$, where j and $\sigma_{el,f}$ represent respectively, the induced current density in the metal and the electrical conductivity of the metal. Mechanical forces result in the electromagnetic stirring of the metal, governed by the Lorentz forces. Often the stirring mechanism is very turbulent, leading to temperature homogenization of the liquid metal bath.

Induction processes are heavily influenced by the electromagnetic skin effect [5]. The skin effect concentrates the induced current and therefore the electromagnetic forces in a layer adjacent to the surface of the conductor, with a maximum induced current density at the surface and a gradual decrease towards the interior of the conductor. Figure 6 shows this effect near the conductor surface.

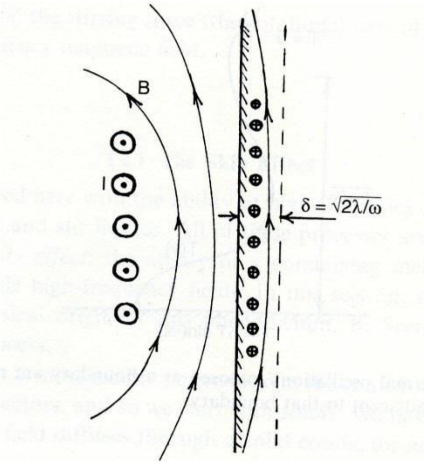

Figure 6: Skin effect in electromagnetic induction [5]

The skin depth δ_{EM} (Eq. 1) is the order of magnitude of the penetration depth of the electromagnetic field into the conductor. f and μ_0 represent respectively the inductor current frequency and the magnetic permeability in free space.

$$\delta_{EM} = \frac{1}{\sqrt{\pi \mu_0 \sigma_{el,f} f}} \quad (1)$$

Figure 7 presents the evolution of skin depth as a function of current frequency for some materials: Mercury, Gallium, Aluminum and Iron. Table 1 reports their respective electrical conductivity $\sigma_{el,f}$ and density ρ_f.

Table 1: Material properties of Hg, Ga, Al, Fe

	Electrical conductivity $\sigma_{el,f}$ (Ω^{-1}.m^{-1})	Density ρ_f (kg.m^{-3})
Mercury	$1.1\text{x}10^6$	13600
Gallium	$3.8\text{x}10^6$	6095
Aluminum	$4.1\text{x}10^6$	2385
Iron	$9.0\text{x}10^5$	7870

Across all the studied materials, these curves illustrate a general trend of the skin depth decreasing with an increasing frequency. The effect of the electrical conductivity is quite remarkable as we see that the skin depth for Iron is almost double the skin depth noted for Aluminum for the entire frequency range (from 50 Hz to 5 kHz).

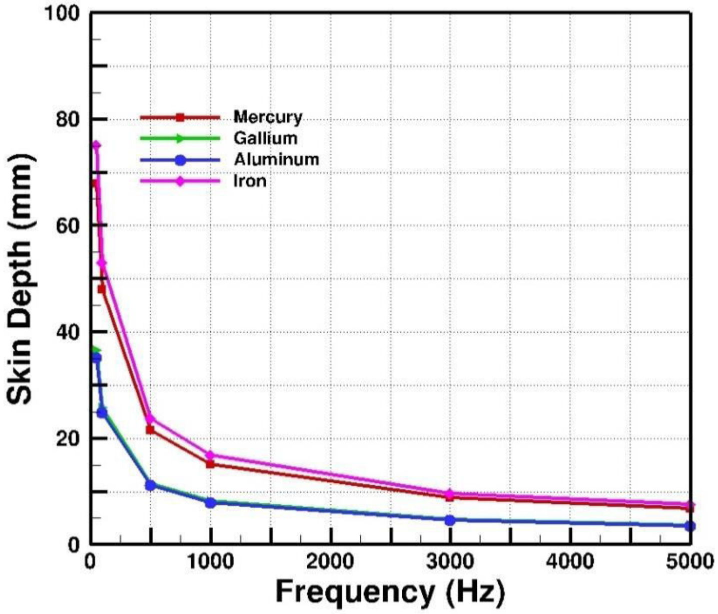

Figure 7: Skin depth as a function of current frequency for Hg, Ga, Al, Fe

In some specialized literature [13] [14], the dimensionless shield parameter R_ω is frequently utilized. As expressed in Eq. 2, this parameter is the square of the ratio of a characteristic dimension of the geometry L and the skin depth δ_{EM}. The driving Lorentz forces are mainly confined within the skin depth for $R_\omega \gg 1 (\delta_{EM} \ll L)$, while a more uniform distribution of the driving forces in the bath is expected when $R_\omega \sim 1 (\delta_{EM} \sim L)$.

$$R_\omega = 2\left(\frac{L}{\delta_{EM}}\right)^2 = \mu_0 \sigma_{el,f} \omega L^2 \tag{2}$$

In Eq. 3, the Hartmann number Ha compares the electromagnetic forces to the viscous forces. The number is strongly dependent on the magnetic induction value, which varies as a function of the electromagnetic penetration within the bath. B_0, L and μ_f respectively represent the maximum amplitude of the magnetic induction, the characteristic length and dynamic viscosity of the fluid. Meanwhile, the Stuart number (or the interaction parameter) in Eq. 4 confronts the electromagnetic forces with the inertial forces and is expressed as a ratio of the Hartmann number and the Reynolds number.

$$Ha = B_0 L \sqrt{\frac{\sigma_{el,f}}{\mu_f}} \tag{3}$$

$$N = \frac{Ha^2}{Re} = \frac{B_0^2 L \sigma_{el,f}}{\rho_f u} \tag{4}$$

IMFs often exhibit liquid metal free surface as a dome (or a meniscus). This dome shape is achieved as a result of an equilibrium between the electromagnetic force, the hydrodynamic pressure, the gravitational force and the surface tension force. The dome height h_m under a magneto-static hypothesis, where the magnetic pressure is in equilibrium with the gravitational forces, is defined in Eq. 5 [15].

$$h_m = \frac{B_0^2}{2\mu_0 \rho_f g} \tag{5}$$

Figure 8 presents the evolution of the dome height as a function of the magnetic induction B_0 for the above mentioned materials. The general trend of the dome height increasing with the magnetic induction follows from Eq. 5. Aluminum, being the least dense among these materials, attains the largest dome height, while Mercury, almost 5 times denser, attains the lowest dome height. The dome height reduces the total contact surface between the liquid metal and the crucible, and could lead to higher energy efficiency as well as a lower maintenance of the crucible walls.

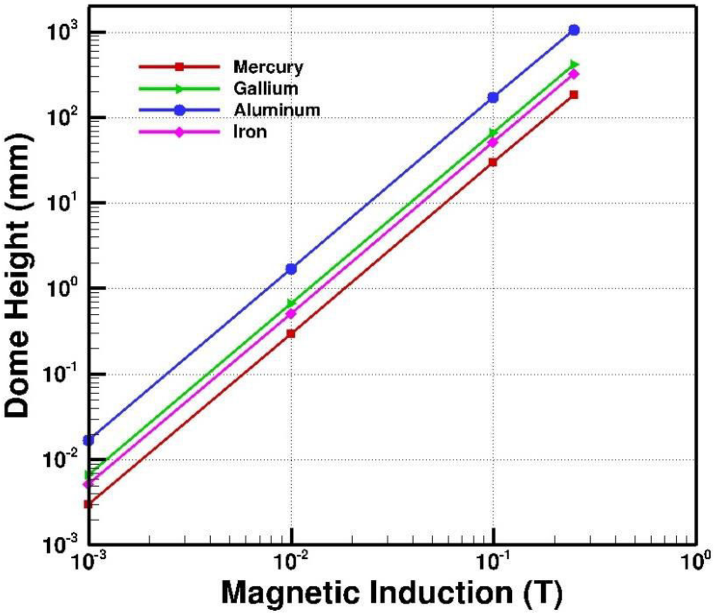

Figure 8: Dome height as a function of magnetic induction for Hg, Ga, Al, Fe

The liquid metal free surface found within the crucible may not be axisymmetric [16] as its nature primarily depends on the induction coil configuration, the crucible geometry, the screening elements as well as the operating parameters.

1.2.2 Theoretical background

1.2.2.1 Electromagnetic Phenomena

A particle moving with a velocity $\boldsymbol{u}$ and carrying a charge q in the presence of an electric field $\mathbf{E}$ and a magnetic induction $\boldsymbol{B}$ is subjected to a force expressed as: $\boldsymbol{f_q} = q(\boldsymbol{E} + \boldsymbol{u} \times \boldsymbol{B})$. The first and the second terms on the right hand side of the equation respectively signify the electrostatic force and the Lorentz force. Furthermore, the total electric field is the sum of the electrostatic and induced electric fields: $\mathbf{E} = \mathbf{E}_{\boldsymbol{S}} + \mathbf{E}_{\boldsymbol{I}}$. The divergence and the curl of each component along with those of the total electric field are presented in Figure 9 [17].

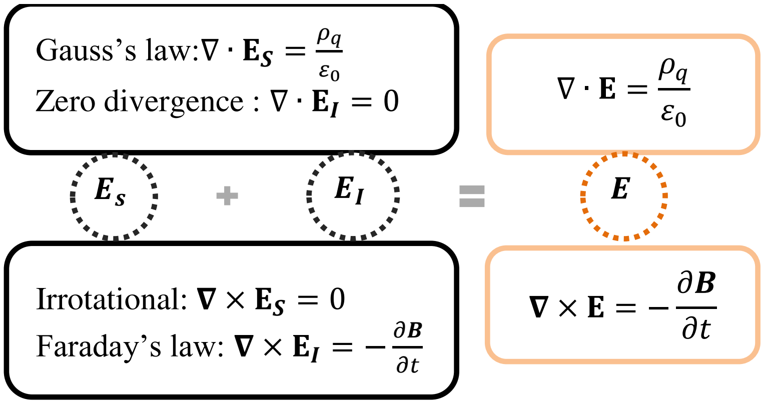

Figure 9: Governing equations of the static and induced electric fields

According to Ohm's law, as stated in Eq. 6, the current density $\boldsymbol{j}$ is a function of the electric field $\boldsymbol{E}$, the velocity $\boldsymbol{u}$ and the magnetic induction $\boldsymbol{B}$.

$$\boldsymbol{j} = \sigma_{el,f}(\boldsymbol{E} + \boldsymbol{u} \times \boldsymbol{B}) \tag{6}$$

$$\boldsymbol{\nabla} \times \mathbf{B} = \mu_0 \boldsymbol{j} \tag{7}$$

Substititution of Ampere's law (Eq. 7) in Eq. 4, followed by the curl, provides us with Eq. 8.

$$\boldsymbol{\nabla} \times (\boldsymbol{\nabla} \times \mathbf{B}) = \mu_0 \sigma_{el,f}(\boldsymbol{\nabla} \times \boldsymbol{E} + \boldsymbol{\nabla} \times (\boldsymbol{u} \times \boldsymbol{B})) \tag{8}$$

Using the vector calculus identity: $\boldsymbol{\nabla} \times (\boldsymbol{\nabla} \times \mathbf{B}) = \nabla(\nabla \cdot \boldsymbol{B}) - \nabla^2 \boldsymbol{B}$ and susbtituting $(\boldsymbol{\nabla} \times \boldsymbol{E})$, thanks to Faraday's law (Eq. 9), we obtain Eq. 10. Furthermore, due to the solenoidal nature of the magnetic induction, its divergence is null: $\nabla \cdot \boldsymbol{B} = 0$, which when substituted in Eq. 10, provides us with the induction equation Eq. 11.

$$\boldsymbol{\nabla} \times \boldsymbol{E} = -\frac{\partial \boldsymbol{B}}{\partial t} \tag{9}$$

$$\nabla(\nabla \cdot \boldsymbol{B}) - \nabla^2 \boldsymbol{B} = \mu_0 \sigma_{el,f}(-\frac{\partial \boldsymbol{B}}{\partial t} + \boldsymbol{\nabla} \times (\boldsymbol{u} \times \boldsymbol{B})) \tag{10}$$

$$\frac{\partial \boldsymbol{B}}{\partial t} = \boldsymbol{\nabla} \times (\boldsymbol{u} \times \boldsymbol{B}) + \frac{1}{\mu_0 \sigma_{el,f}} \nabla^2 \boldsymbol{B} \tag{11}$$

The first term on the right hand side of the induction equation represents the electromotive force generated due to the conducting fluid's effect on the magnetic induction. In most of the industrial processes, these forces are deemed negligible as the fluid velocity has very little influence on the magnetic induction, thereby reducing the induction equation to the form of a diffusion equation. Magnetic Reynolds number (Re_m) defined in Eq. 12 is introduced to distinguish such cases ($Re_m \ll 1$). Classically, for laboratory scale furnaces with a characteristic length scale of 0.1 m and considering a metal bath with an electrical conductivity of 10^6 Ω^{-1}.m^{-1} and a characteristic velocity of $0.5\ \mathrm{m.s^{-1}}$, $Re_m$is indeed found to be much smaller than unity ($Re_m \approx 0.06$).

$$Re_m = \mu_0 \sigma_{el,f} u L \tag{12}$$

Another form of the induction equation can also be obtained by replacing the magnetic induction by the vector potential **A**.

$$\boldsymbol{\nabla} \times \mathbf{A} = \mathbf{B} \tag{13}$$

Table 2 summarises the important laws in the domain of electomagnetics and their corresponding mathematical expressions [5] [17].

Table 2: Governing equations of Electrodynamics

Ampere's law	$\boldsymbol{\nabla} \times \mathbf{B} = \mu_0 \boldsymbol{j}$
Faraday's law	$\boldsymbol{\nabla} \times \mathbf{E} = -\frac{\partial \boldsymbol{B}}{\partial t}$
Solenoidal nature of magnetic induction	$\nabla \cdot \boldsymbol{B} = 0$
Ohm's law	$\boldsymbol{j} = \sigma_{el,f}(\boldsymbol{E} + \boldsymbol{u} \times \boldsymbol{B})$
Conservation of charge	$\nabla \cdot \boldsymbol{j} = 0$
Induction equation	$\frac{\partial \boldsymbol{B}}{\partial t} = \boldsymbol{\nabla} \times (\boldsymbol{u} \times \boldsymbol{B}) + \frac{1}{\mu_0 \sigma_{el,f}} \nabla^2 \boldsymbol{B}$

The Lorentz force due to the magnetic induction follows from Eq. 14 which will act as a source term in the hydrodynamics governing equations. The Lorentz force creates a magnetic pressure as well as acts as a driving force in the conducting fluid.

$$\boldsymbol{F_{Lorentz}} = \boldsymbol{j} \times \boldsymbol{B} \tag{14}$$

1.2.2.2 Hydrodynamics

Navier-Stokes equations are the cornerstone of any fluid dynamics topic. These equations arise from Newton's second law applied to fluid motion [18] in the specific situation where the fluid is assumed to be newtonian and incompressible. Once the velocity field is resolved, other quantities of interest such as flow and shear rates may be calculated. The non-linearity and the coupling between the continuity and the momentum equations make the set of NS equations quite attractive for various numerical methods:

Continuity
$$\frac{\partial \rho}{\partial t} + \nabla \cdot (\rho \boldsymbol{u_f}) = 0 \tag{15}$$

Momentum conservation
$$\frac{\partial (\rho \boldsymbol{u})}{\partial t} + \boldsymbol{u} \cdot \nabla(\rho \boldsymbol{u}) = -\nabla p + \nabla \cdot (\mu_{eff} \nabla \boldsymbol{u}) + \boldsymbol{F} \tag{16}$$

$\mathbf{u_f}$, ρ, μ_{eff},p, **F** respectively being the velocity vector, the density, the effective dynamic viscosity, the pressure and the external forces. The first and second terms on the left hand side of the momentum conservation equation respectively correspond to the unsteady term and the convective transport term. The first, the second and the third terms on the right hand side of the equation describe the pressure gradient, the viscous forces and the external body forces respectively. Table 2 along with the NS equations (Eq. 15 and 16) provide the governing equations for describing the stirring phenomena in the induction furnace. It must be noted that the Lorentz forces acting on the metal are taken into account by means of the external body force term in the momentum conservation equation (Eq. 16).

Turbulence can be defined as a flow regime where the internal mechanisms of the energy transfer maintain various structures at different spatial scales [5]. Although at the onset, it seems that the turbulent flow is fully random, instead it is an overlapping of patterns. These patterns which are organized in an energy spectrum are marked by an energy transition or cascading from the larger scales (integral scales) to the smaller or Kolmogorov scale. The Reynolds number is the ratio of the inertial and the viscous forces and indicates the different turbulence regimes in a flow. Some elements of the turbulence modeling are later discussed in section A.3.

$$Re = \frac{uL}{\nu_f} \tag{17}$$

Any flow consisting of two or more distinct phases, flowing simultaneously in mixture with some level of phase separation at a scale well above the molecular level, can be termed as a multiphase flow [19]. In our project, the hydrodynamics inside the crucible is a two phase flow comprising the separate phases of liquid metal and air. The interface between the two phases is termed as a free surface, provided that the gas phase (air) exerts negligible tangential shear stress upon the interface.

1.3 Literature survey

1.3.1 Experimental investigation in an IMF

Several authors have performed experimental analyses in the IMF or similar installations (EM casting, channel induction furnaces etc.). These studies have primarily focused on studying the fluid flow or the free surface and provide valuable insight into the induction stirring process as well as the orders of magnitude of velocities and free surface deformations for various furnace configurations.

1.3.1.1 Velocimetry

The velocimetry can be further categorized into bath surface velocity measurements and bulk flow measurements. Certain techniques also allow measurement of the velocity fluctuations and thus give a clearer idea about bath turbulence.

The measurement of bath surface velocity was performed by Tarapore et al. [20] [21], who used a simple optical system to capture images of an immersed moving glass bead, lit under stroboscopic lighting. This was performed for mercury and steel baths in a laboratory scale and an industrial scale IMF respectively, and the results were found to be reasonably reproducible. Taberlet and Fautrelle [22] and El-Kaddah et al. [23] on the other hand used an intrusive hot wire anemometry technique inside a mercury bath in an IMF to measure the melt velocity, its fluctuations and thus the turbulent spectra. Their analysis showed that the average velocity as well as the turbulence increased with an increase in the coil current intensity. However, it was also shown that the velocity, the fluctuations and the flow structures varied as a function of the current frequency and were thus controlled by the electromagnetic skin depth. Vives and Ricou [24] [25] used an electrical probe to measure the instantaneous velocity for a higher temperature (~700 °C) aluminum bath during continuous casting using electromagnetic forces or while stirring in an IMF. The established experimental protocol was put to good use to ascertain melt velocity and its variance as a function of operating or design parameters of the installation.

More recently, Umbrashko et al. [26] and Bojarevics et al. [27] both measured the melt velocity using an electric potential probe, for a Wood's metal and a gallium bath respectively. Cramer et al. [28] provide an example of application of the Ultrasound Doppler Velocimetry (UDV), which was recently used to spatially map the liquid metal flow with quite a high resolution ($0.1\ \mathrm{mm.s^{-1}}$). The state of the art non-contact technique of Lorentz Force Velocimetry (LFV) developed at TU Ilmenau [29] provides a novel way of measuring the melt velocity in liquid metal flow. The technique has been satisfactorily compared with numerical modeling [30] and ongoing research shows numerous applications [31], even at the industrial scale. Argyropoulos [32] also reviews several techniques used to measure velocity in such liquid metals, with some applicable to an IMF.

1.3.1.2 The free surface

The free surface measurements can also be distinguished into two categories: the free surface deformation or meniscus shape measurements and the free surface oscillation or its instability measurements. In 2007, Fautrelle et al. [16] reviewed most of the free surface related issues in EPM and IMFs.

The free surface deformation or its shape was measured by Li et al. [33], Etay et al. [34] and Perrier et al. [35], who studied Wood's metal (T_m = 70 °C), mercury (T_m = -39 °C) and gallium (T_m = 30 °C) baths respectively, using a contact probe. While Li et al. worked with an electromagnetic casting installation, Etay et al. and Perrier et al. primarily worked with induction furnaces. Based on the coupling of the electrical resistance with the vertical displacement, their probe (Figure 10) measured with a precision of ±0.5 mm and was adapted to a bath temperature range of 20 °C to 70 °C. Kageyama and Evans [36] also talk about free surface deformation measurements performed by Fukumoto (reference not found) for a tin bath, presumably by using a contact probe. More recently, Kirpo [37] also used a contact probe to measure the free surface deformation of a Wood's metal bath in an IMF.

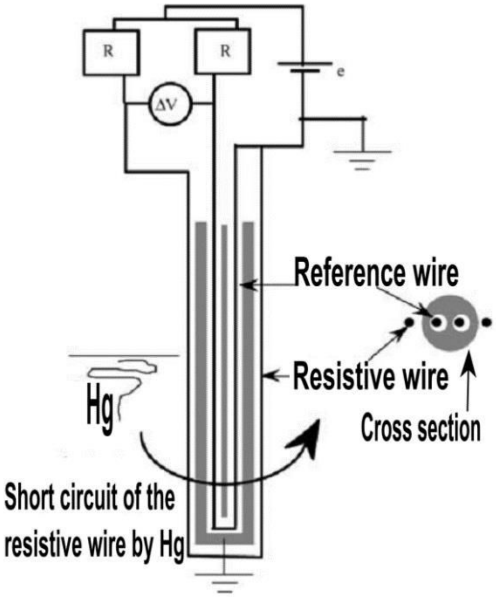

Figure 10: Electric contact probe [34]

Debray and Fautrelle [38] measured the free surface deformation instabilities of a mercury bath in an induction coil with very low current frequency (2-10 Hz), using a carbon fiber electrical resistive probe. The bath free surface oscillations and instabilities as a function of magnetic induction and current frequency were also experimentally studied by Etay and Fautrelle [15] and Perrier et al. [35]. It was observed [15] that for very low frequencies (1-20 Hz), the magnetic field agitates the free surface vigorously, while for higher frequencies, the surface waves perpendicular to the magnetic field become calmer. An interesting example of unsymmetrical liquid metal free surfaces was also observed by Fautrelle et al. [39], where the main impacting factors were the coil geometry as well as the magnetic induction by the inductor coils. The dynamics of a galinstan (gallium alloy) free surface was also investigated by Mohring et al. [40], subjected to high frequency (20-50 kHz) magnetic field. It was found that with increasing inductor current, the free surface transitioned from an oscillating capillary surface wave to a static surface deformation wave until an electromagnetic pinch effect appears at a critical current value, while confirming the surface wavelength's correlation with the current frequency.

1.3.2 Numerical modeling of an IMF

Numerical modeling is an efficient tool which helps analyze and predict the coupled phenomena involved in induction processes. Bojarevics and Pericleous [10] reviewed in 2007 some modeling techniques for the induction melting and stirring processes. Along with velocity measurements, Tarapore et al. [20] [21] provided in the mid 70's, a predictive in-house numerical tool (based on the finite difference method) for fluid flow in an IMF as a function of the operating and design parameters and found the two set of experimental and numerical results, comparable. Nevertheless, with several assumptions such as no calculation of the free surface curvature and a steady state calculation, the numerical model was still at a nascent stage. More recently, similar comparisons between numerical modeling results and velocity measurements were performed by El-Kaddah et al. [23], Li et al. [33], Kageyama and Evans [36] [41] and Umbrashko et al. [26]. Of course, with time, the various links between each phenomenon reached better understanding, resulting in an increased complexity and performance of the numerical model. Some of the improvements include the modeling of the turbulence, the description of the transient free surface deformation and finally the coupling between electromagnetic and hydrodynamic phenomena.

The stirring of the liquid metal in an induction furnace, which is often turbulent in nature, was modeled with a RANS (Reynolds Average NS equations) approach by El Kaddah et al. [23] who applied the k-ε model. Baake et al. [42] and Courtessole and Etay [43] used the k-ε RNG model, in order to improve upon k- ε model accuracy in rotating cavities. On the other hand, Umbrashko et al. [26] performed Large Eddy Simulations (LES) to simulate the large turbulent scales and advised its use to correctly estimate the heat and mass transfer between various recirculation zones inside a metal bath. More recently, Spitans et al. [44] and Scepanskis et al. [45] used the k-ω SST turbulence model to simulate a laboratory scale as well as an industrial scale furnace.

A key aspect of the induction process simulation is the numerical prediction of the liquid metal free surface deformation. It was discussed by Nakata and Etay [13], Fugate and Hoburg [46], as well as by Zhu et al. [47], who used the magneto-hydrostatic approximation, where only the gravitational force, the electromagnetic force and the surface tension force are assumed to be in equilibrium at the free surface. Pesteanu and Baake [48] on the other hand considered the hydrodynamic pressure contribution while treating the free surface deformation and used a variant of the Volume Of Fluid (VOF) method to predict the deformation. It must be noted that a weak coupling between the electromagnetic and the hydrodynamics was considered in the numerical models described by the above authors, whereby the Lorentz forces generated by the inductor in the metal bath were calculated separately and subsequently transferred to the fluid flow simulation. Delannoy and Garnier [49] proposed a stronger coupling in which the Lorentz forces were calculated at the same time as the hydrodynamics. Likewise, Courtessole and Etay [43] applied this strong coupling strategy to model the interactions between two non-miscible liquid zones in an induction furnace. The modeling approach in the present work is similar to the above, where the Lorentz forces are calculated while taking into account an updated free surface deformation at each time step.

1.3.3 Oxide layer covering the free surface

A very small oxygen partial pressure (~ 10^{-50} atm) [50] is sufficient to oxidize partially if not completely an aluminum bath surface. Since the induction melting often takes place under atmospheric conditions, the surface is instantaneously covered by an oxide layer. The layer may have different impacts on the hydrodynamics of the bath, namely it may modify the physical properties (surface tension) or affect the bath hydrodynamics (bulk or even the free surface).

The main question studied in the literature is the influence of the oxide layer on the surface tension of the metal. Several techniques (reviewed by Egry et al. [51]), such as the sessile drop method (Eustathopoulos et al. [52], Bainbridge and Taylor [53]) or the maximum bubble pressure method (Goumiri et al. [54], Garcia-Cordovilla et al. [55]), were used to measure the surface tension of a liquid aluminum bath sample. It was found that the surface tension for 99.99 % pure aluminum decreases from 1.1 N/m to 0.86 N/m [55] as the surface oxidation increases. This would be due to the continuous formation of oxide islands up until the saturation of the liquid surface (homogenous layer).

Goumiri and Joud [56] also studied the aluminum oxide layer, its formation and dependence on temperature while using the Auger electron spectroscopy. Furthermore, Frisvold [57] provided an extensive theoretical analysis of the surface tension constant using Gibbs free energy formulation, for various binary aluminum alloys. Schoutens [58] built a similar theoretical model, but focused on the theoretical calculation of the surface tension with and without the oxide layer and found it to be similar to the above results [55]. Kahl and Fromm [59] and more recently Syvertsen [60] [61] performed measurements of the oxide layer strength using a rotating disc method. It was proposed that the oxide layer strength is a sum of the interfacial tension between the melt and the oxide, the tensile strength of the oxide layer and the surface tension of the oxide (with air).

1.3.4 Conclusions of literature survey

The measurement of liquid metal velocities is an important tool for understanding and controlling IMF phenomena as well as for validating numerical modeling results. However, in the present project we directed our focus on the experimental study of the bath free surface deformation, as it is much faster, accessible and easier to put in place. It is noteworthy that all the free surface measurements were limited to low liquid metal bath temperature, carried out solely by the intrusive contact probe technique. With temperatures rising to 700 °C (such as in the case of an aluminum bath), the contact probe technique is difficult to adapt. Furthermore, these experiments provide non instantaneous discrete measurements (up to 20 points) of the free surface which are inadequate for a complete free surface description. Thus a more comprehensive technique is required to measure the entire free surface deformation and its fluctuations, at high temperatures.

Up until recently, most of the numerical models made strong assumptions when addressing the bath free surface modeling by employing a magneto-hydrostatic formulation when treating the free surface. However, a much larger use of a two-way free surface – hydrodynamics coupling can be noticed in recent works. This fully coupled strategy is employed in our study.

Much of the literature concerning oxide layers of liquid aluminum has dealt with the experimental or the theoretical analysis of its effect on the surface tension of the metal. Some research was also focused on the oxide layer strength. However, the impact of the oxide layer on the deformation of the free surface and on the hydrodynamics of the metal bath is a subject which has received little attention in the literature.

2. Experimental analysis of a lab scale IMF

In this section, we begin by introducing IJL's laboratory scale induction melting furnace along with its schematics and geometrical dimensions. The investigated alloys and some of their physical properties are then presented. We then move on to the operating parameters of the installation and highlight the techniques used to measure them. Finally, we present the two techniques used for the free surface deformation measurement.

2.1 Introduction to IJL's IMF

A laboratory scale IMF with a nominal power of 50 kW, capable of melting up to 4 kg of aluminum, is currently installed at the Institut Jean Lamour. Figure 11 presents the exterior vessel of the furnace with its lid (open position in the figure). The inner chamber can be placed under a vacuum, but in our case, the aluminum processing was carried out under atmospheric conditions. The IMF installation has an alternating current generator, characterized by an AC frequency f and a generator power P_{gen}. Figure 12 presents a view of the inductor and the crucible settled inside the vessel. The crucible is the control volume where the metal is melted and stirred thanks to the electromagnetic phenomena. A water cooling circuit controls any possible overheating in the vessel walls, the inductor coils as well as in the generator.

Figure 11: IJL's IMF installation

Figure 12: Zoom of the inductor and the crucible inside the vessel (top view)

2.1.1 IJL IMF schematics

Figure 13 presents the IMF schematics, in which the inductor consists of an eight turn coil. The interior diameters of the alumina crucible and the inductor are 106 mm and 200 mm respectively, while their corresponding heights are 200 mm and 250 mm. The crucible rim is offset by 5 mm with respect to the inductor top. There are no elements around the crucible which can act as shields.

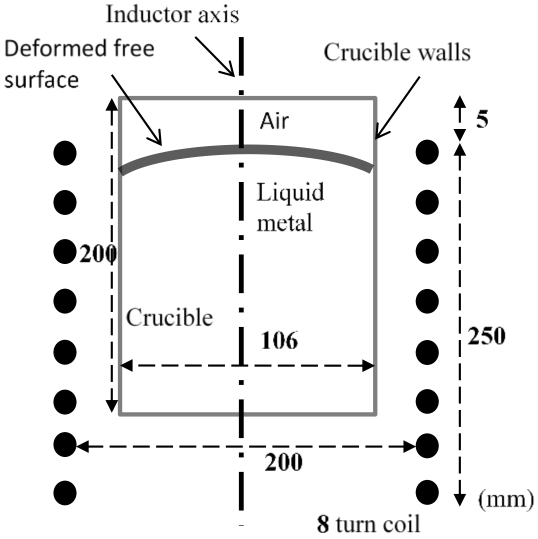

Figure 13: IJL's IMF schematics

The geometrical dimensions of the inductor and crucible are summarized in Table 3. The space between the inductor and the crucible is filled up with ramming material, which is made up of alumina or mullite and silicon compounds. It acts as a safety feature in case of any rupture of the alumina crucible as well as insulates the region between the crucible and the inductor.

Table 3: Details of IJL inductor and crucible

	Inductor	Crucible
N° of coil turns	8	-
Exterior diameter (mm)	216	121
Interior diameter (mm)	200	106
Exterior height (mm)	250	225
Interior height (mm)	-	200
Material	Copper alloy	Alumina

2.1.2 Investigated aluminum alloys

During the experimental analysis of IJL's IMF, we primarily used aluminum alloy Al-1050 which is composed of at least 99.5 % of aluminum. Table 4 summarizes some thermo-physical properties of the alloy Al-1050 along with the temperature dependence laws valid for a temperature ranging from 660 °C to 1200 °C.

Table 4: Al-1050 properties at T_m with temperature dependence laws *[62] [63]*

	Value at T_m (660 °C)	Temperature dependence law
Density (kg.m^{-3})	2390	$\rho_f(T) = \rho_f(T_m) - 0.15(T - T_m)$
Dynamic viscosity (mPa.s)	1.28	-
Surface tension (N.m^{-1})	0.868	$\gamma_f(T) = \gamma_f(T_m) - 0.25\text{x}10^{-3}(T - T_m)$
Electrical conductivity (Ω^{-1}.m^{-1})	4.04.10^6	$\sigma_{el,f}(T) = 5.91\text{x}10^6 - 2.03\text{x}10^3\text{T}$

Some experiments were also performed with the alloys Al-5182 (Al-Mg) and Al-7050 (Al-Zn). The thermo-physical properties of these alloys are quite similar with respect to Al-1050 and are available in Annex 1. Nevertheless, as it will be discussed in Part C, in its liquid form, alloy Al-5182 with a strong magnesium content can be very reactive with air at the free surface and would thus oxidize much more than Al-1050.

2.1.3 Operating parameters

- The liquid metal filling inside the crucible

The relative positioning of the free surface at rest with respect to the inductor is an important parameter and plays a crucial role in the free surface deformation. The crucible can hold a maximum of 4 kg of Al-1050.

- The electrical parameters of the setup

The generator power and the frequency of the alternating current are the primary electrical parameters of the setup (as indicated on the generator display board). The power was varied from 0 kW to a maximum of 20 kW and the frequency from 3.4 kHz to 3.8 kHz. For the remainder of the experiments, the frequency was fixed at 3.5 kHz. Other important electrical conditions of particular interest in our study were the current intensity circulating inside the inductor coil and the magnetic induction generated by the coil current in the internal volume of the crucible.

2.1.4 Measurement of operating parameters

Measurements of the coil current intensity (which is also an input parameter of the numerical model that will be presented later in this chapter) and of the generated magnetic induction were performed. These measurements, on one hand, allowed us to better characterize the experimental setup and on the other hand, provided data to perform an intermediate validation of the numerical model.

2.1.4.1 Measuring the current intensity

Current intensity was measured using a variant of the current transformer technique [64]. In accordance with Ampere's law, any conductor carrying a given current intensity will generate a proportional magnetic induction. Thanks to a current transformer, this magnetic induction may be converted to a secondary current which acts as an output. Due to its simple yet efficient use, we have selected a variant of the current transformer technique – Rogowski's coil for the rest of our study (Figure 14).

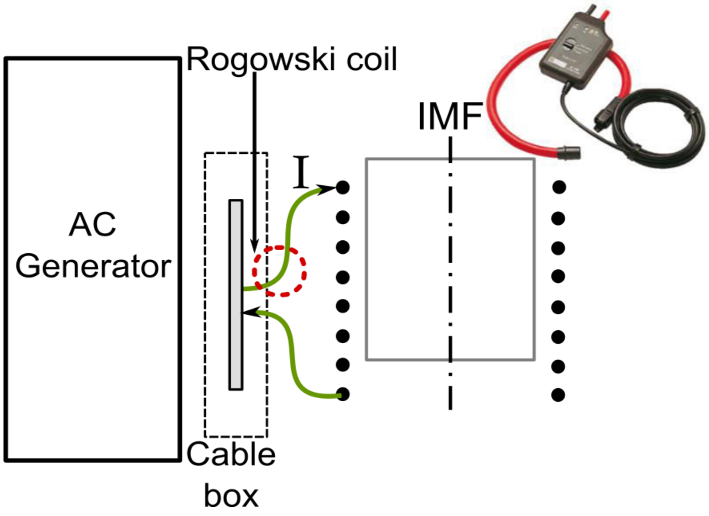

Figure 14: Rogowski coil and its position

A Chauvin Arnoux Rogowski's coil– AMPFLEX A100 300-3000/3, was placed at the entry point of the inductor, where the RMS of current intensity was measured every 0.5 second. The measurement range of the coil is 0.5 A to 3000 A AC, with a precision of 1%. The coil works within a frequency bandwidth of 10 Hz to 20 kHz. The current intensity was measured simultaneously while measuring the magnetic induction and also during the free surface deformation experiments.

2.1.4.2 Measuring the magnetic induction

A Hall's effect Gaussmeter was used to measure the magnetic induction [65]. Hall's effect was discovered by Edwin H. Hall in late 19th century and is derived from the Lorentz force relationship, which established that the force experienced by a moving charge subjected to a magnetic induction is described as $\boldsymbol{F} = q(\boldsymbol{E} + \boldsymbol{u} \times \boldsymbol{B})$. A Hall's effect Gaussmeter is a device consisting of a flat thin rectangular conductor or semi-conductor with two pairs of electrodes perpendicular to each other. When an electric field E_x is applied along the x axis, and a magnetic induction B_z perpendicular to the electric field, the free charge flowing along the x axis will be deflected towards the y axis, which will ultimately lead to a generation of an electric field in this direction: $E_y = v_x B_z$ (Figure 15), which further leads to an output electrical voltage duly measured by the Gaussmeter. A F.W. Bell-5180 Gaussmeter with an axial probe SAD18-1904 (Figure 16) was used to measure the magnetic induction along the axis of the inductor. This Gaussmeter functions in a large range, from 0.01 mT to 3 T with a precision of 100 nT and for a working bandwidth of up to 25 kHz. The probe position inside the crucible is illustrated in Figure 17.

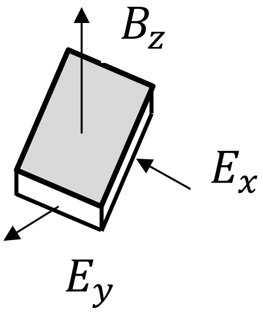

Figure 15: Hall's effect

Figure 16: Gaussmeter with axial probe

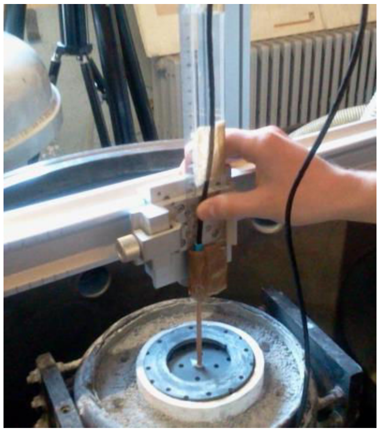

Figure 17: Probe position inside the crucible

2.2 Experimental techniques for measurement of free surface deformation

The free surface deformation measuring techniques must work under the following constraints which were observed during the preliminary experiments.

- A mirror like reflective surface

The liquid metal bath free surface which attains the shape of a dome is spontaneously covered by an oxide layer. The oxide layer for Al-1050 for example was observed to have a mirror like reflective surface, meaning that at least in the range of visible wavelengths the optical reflection coefficient must be close to 1 whereas the emissivity must be close to zero.

- High temperature range

The bath temperature may reach a range of 700 °C to 1000 °C. Such high temperatures automatically lead to a thermal radiation in the vicinity of the free surface and the crucible rim, thereby imposing an important constraint on the choice of the technique.

A brief survey on techniques capable of measuring free surface deformation was performed. Table 5 presents these techniques, which can be broadly classified as contact or contactless techniques. Obviously each technique has its strengths as well as limitations, subject to the mode of application (see Annex 2).

Table 5: Experimental techniques for measuring free surface deformation

Contact techniques	Contactless techniques
▪ Electrical probe ▪ Thermocouple probe	▪ Laser telemetry ▪ Interferometry ▪ Laser triangulation ▪ Structured light ▪ Photogrammetry & Stereoscopy

The electric probe contact technique [34] [35], as discussed earlier in section A.1.3.1.2, was used for very low bath temperatures, rendering it unsuitable for the current project. A common feature for contactless techniques is their application to fragile or deformable objects, for real time measurements or when working in hostile environments. Also, with increased efficiency of image processing algorithms, certain image based contactless techniques could help reconstruct a viable 3D image of the free surface deformation. In the following sections, we briefly discuss two contactless optical techniques – laser telemetry and structured light, which were found to satisfy the requisites of the project.

2.2.1 Laser telemetry

Laser telemetry is a contactless technique based on the measurement of the time interval Δt lapsed for the light to complete a journey between the sensor and the object under study (based on the principle of time of flight) [66]. Figure 18 clearly illustrates the working principle of the laser telemetry. A combination of telemeters can scan surface deformation. Also the coaxial transmitter-receiver system provides a maneuverability advantage over other optical techniques. Limitations of this technique include the fact that the temperature at the sensor should remain between 0 °C and 50 °C.

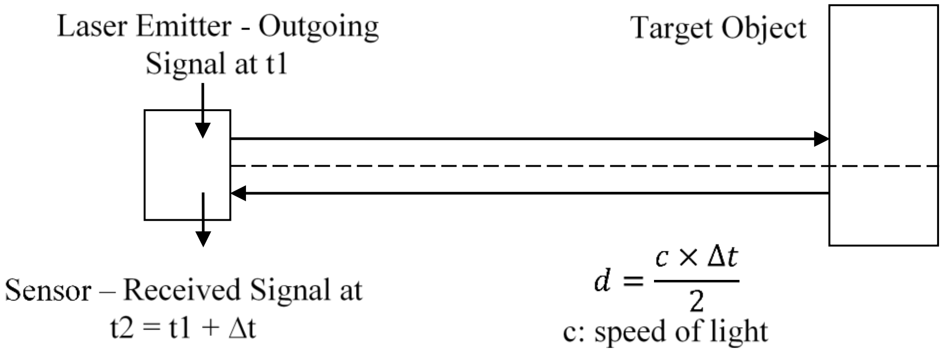

Figure 18: Laser telemetry principle

Additionally, laser orientation should be perpendicular to the object's surface in order to have a reliable measurement which usually has a precision of ±1 mm. Laser telemetry finds applications in various domains like construction, mechanical engineering etc. Some examples of surface profiling using laser telemetry were found in the literature, such as Maatta and Kostamovaara [67], who used it to profile the thickness of hot (~1000 °C) refractory linings.

2.2.2 Structured Light

A structured light, as seen in Figure 19, is a band of patterns comprising of an alternating color or texture stripes, which is projected onto the surface under study. Any deformation on the surface will consequently deform the projected fringe pattern which is then captured as an image by a video camera. Geng [68] can be consulted for a review on the structured light technique. This technique has found widespread applications such as in medical imaging, vehicle frame modeling, profiling and architecture, but no application in the liquid metal domain was found in the literature.

Each pixel of coordinates (x,y) on the structured light pattern (see Figure 19) has a luminous intensity associated to it I_{xy}. The key aspect of recreating the complete surface shape lies in differentiating each pixel coordinate (x,y) and its corresponding luminous intensity I_{xy}. The 3D profile of the surface may then be determined by processing the captured image using the principle of triangulation.

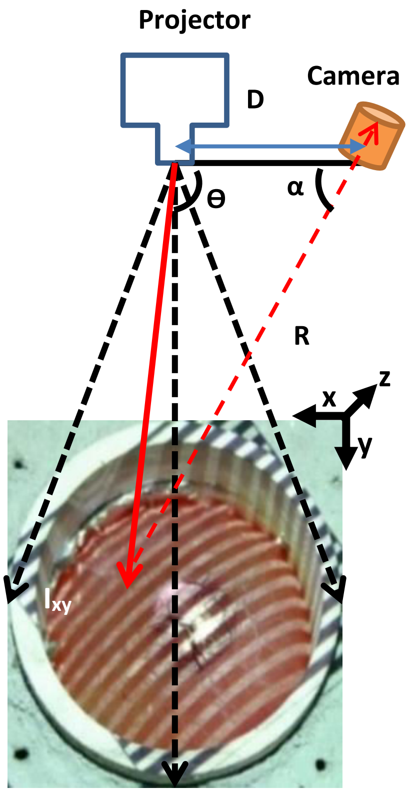

Figure 19: Structured light pattern projection along with triangulation principle

The principle of triangulation has been used for a few centuries while calculating the distances of a point by measuring the angles it makes with the reference points. For any point on the surface, the relative distance (point – sensor) is calculated using the principle [69], thanks to which a complete extraction of a three-dimensional surface shape is possible.

$$R = D\frac{\sin\theta}{\sin(\theta + \alpha)} \tag{18}$$

In Figure 19, triangulation is employed to find distance R using the geometric parameters of the system (distance projector-camera – D – calibrated and known), and the angles made by the projector and the camera with the point in question (Θ and α), in Eq. 18. Several techniques for identifying each pixel are available and can be categorized as sequential or single shot methods [60]. Among them, the sequential hybrid multiple shot and the single shot methods were used in our study and are presented below.

2.2.2.1 *Sequential hybrid method*

The sequential hybrid method involves projecting a sequence of carefully designed variable fringe patterns. This is a two-step method. The first step consists of considering a black and white binary pattern (Figure 20) with a given step size (p) as a base image. During the second step, several sinusoidal fringe patterns with an imposed phase shift are built from the base image and are projected onto the surface. The two steps are then repeated for the next pattern with a refined step size.

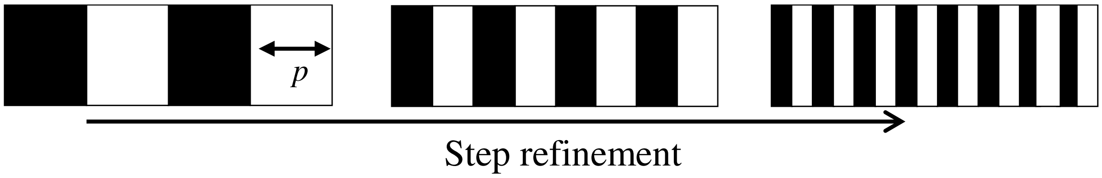

Figure 20: Step variation for sequential hybrid method

At a given pixel, the luminous intensities recorded for each imposed phase shift of the projected patterns allow the calculation of a phase shift $\Delta\varphi(x, y)$, associated to the deformation of the surface. Using the principle of triangulation (Figure 19), it is then possible to calculate the vertical displacement of that pixel $\Delta z(x, y)$.

$$\Delta z(x,y) = \frac{p}{\sin(\theta + \alpha)} * \frac{\Delta\varphi(x,y)}{2\pi} \tag{19}$$

In Eq. 19, θ and α are respectively the angle formed between the projector and a pixel on the surface (Point A – Projector – Camera) and the angle formed between the pixel and the camera (Point A – Camera – Projector).

This technique provides an accurate evaluation (±0.1 mm) of the deformation of the free surface but averages out any high frequency fluctuations while performing the step variation along with the phase shifting.

In our study, shadowed zones on the free surface resulting from the curvature of the surface were reduced by combining images from two video cameras instead of only one. The sequential hybrid method also allowed a temporal study of the free surface, albeit with a low frequency (0.03 Hz) of measurements due to the two-step method. The measurements were repeated for 180 seconds, where each measurement lasted 30 seconds, during which the sequential hybrid projections were performed during the first 4 seconds, followed up by 26 seconds of image processing.

2.2.2.2 Single shot method

This method is based on the projection of a single black and white stripe pattern. The projected pattern is distorted according to the observed surface geometry (Figure 21). The image of the deformed pattern captured by only one video camera is then processed by analyzing (using a Fast Fourier Transformation algorithm) the variation of the step size (d1, d2) along the pattern. Once the phase shift for each pixel is found, the principle of triangulation is used to calculate the vertical displacement of each pixel, from which the 3D profile of the surface may be reconstructed.

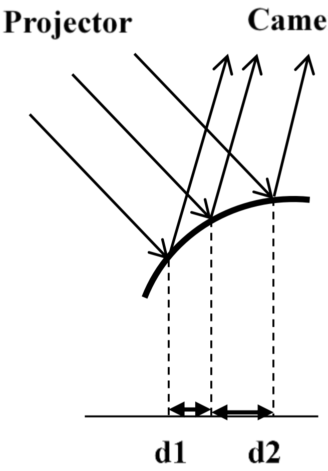

Figure 21: Single shot technique – deformed pattern captured by a camera

The main advantage of the single shot method over the sequential hybrid method is the possibility to study the temporal fluctuation of the surface at a higher frequency of 1 Hz. Though this makes it suitable for dynamic assessment of the surface, the measurement precision suffers and decreases to ±1 mm.

A company specialized in optical metrology *Holo3* [70] participated in the experimental campaign by supplying the optical system (Figure 22) along with its measurement and post processing software.

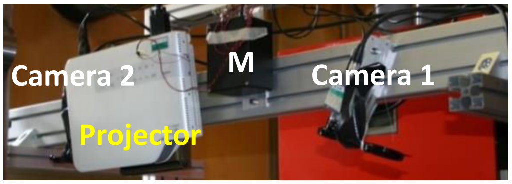

Figure 22: Optical System – Holo3

Some details of the optical system are as follows:

- High resolution projector (1280x800 pixels) with a maximum luminosity of 2500 lm
- Cameras (SONY-XCD-U 100) with a resolution of 1600x1200 pixels
- Modulator (M) which helped perform the intensity phase shift of the fringe as well as synchronized the images captured by the two cameras.

3. Numerical model of IMF

In this section, we first describe the electromagnetic model and then move on to the numerical model of the turbulent bath, the free surface model and the numerical treatment of the oxide layer which covers the free surface. Lastly we express the boundary conditions applied on each boundary of the computational domains, along with some generalities on the numerical model implementation.

The developed model uses ANSYS Fluent software 13.0 to calculate the hydrodynamics of the liquid metal bath while separate User Defined Functions (UDF) are hooked in to solve the induction equation and to simulate the effects of the oxide layer covering the free surface.

Figure 23 represents the two main elements of the setup considered in the numerical model, namely the crucible containing the metal bath and the inductor. The inductor which has a helicoidal coil design was simplified and modeled as an axisymmetric continuous sheet of current (considering that the inductor is formed of tightly wrapped coils). This assumption might suppress any asymmetries of the generated magnetic induction and thereby 3D features of the bath free surface deformation, but it eases up on the calculation load. However, the experimental results which will be presented in section C.1.1.2, show that for the conditions considered in our study the free surface is almost symmetric with respect to the inductor axis. This justifies the 2D axisymmetric approach retained here for the modeling of the induction furnace.

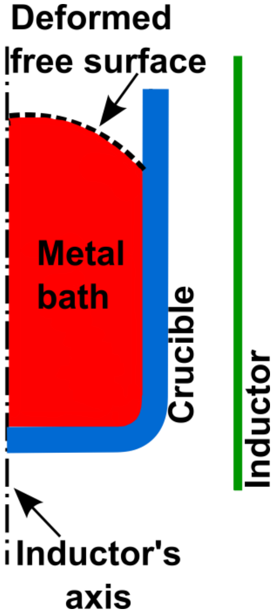

Figure 23: Modeling of the induction furnace

Since the physical properties of the liquid metal are temperature-dependent, the value of the temperature of the bath is an indirect input of the simulation. Also, it was considered that the temperature in the stirred metal bath was homogenous and thus the heat transfer equation was not solved.

However, for the sake of confirmation, let us posit that the bath temperature is not homogenous and a significant temperature difference exists (ΔT~10 °C) which may lead to convective forces. The buoyancy force due to natural thermal convection would be in the vicinity of 10 $N.m^{-3}$, which is negligible when compared to the Lorentz forces acting on the liquid metal (~ 10^6 $N.m^{-3}$).

Moreover, the buoyancy forces can also be contrasted against the viscous forces and represented by the Grashof number in Eq. 20. β and ΔT respectively represent the thermal expansion coefficient and the temperature difference. Furthermore, the ratio of the buoyancy and the inertial forces may also be computed in Eq. 21 with the help of the Reynolds number.

$$Gr = \frac{g\beta \Delta T L^3}{{\nu_f}^2} \tag{20}$$

$$\frac{Gr}{Re^2} = \frac{g\beta \Delta T L}{u^2} \tag{21}$$

Finally, the Marangoni number in Eq. 22 can also be used to show the importance of the thermo-capillary forces acting at the liquid surface. $\frac{d\gamma}{dT}$ and α respectively represent the rate of change of the surface tension constant with respect to temperature and the thermal diffusivity of the liquid metal. A comparison between the surface and the inertial forces is obtained in eq. 23. We will discuss the hydrodynamics results using these dimensionless numbers in Part C.

$$Ma = \frac{d\gamma}{dT} * \frac{L\Delta T}{\mu_f \alpha} \tag{22}$$

$$X^* = \frac{Ma}{Re^2 Pr} \tag{23}$$

In the following sections, we present each phenomenon considered in our numerical model:

- The electromagnetic induction
- The turbulent flow of the metal bath inside the crucible
- The deformation of the free surface of the metal bath
- The presence of an oxide layer covering the metal bath free surface

3.1 Electromagnetic model

As previously enunciated in section A.1.2.2, the induction equation which governs the electromagnetic phenomena involved in the furnace reads as:

$$\frac{\partial \boldsymbol{B}}{\partial t} = \frac{1}{\mu_0 \sigma_{el,f}} \nabla^2 \boldsymbol{B} \tag{24}$$

In the above equation, the effect of the liquid metal velocity on the magnetic induction lines is neglected, as justified in section A.1.2.2.1. A set of UDF – Induc 14.0.0, provided by SIMaP laboratory in Grenoble [49] [71] was used to solve the induction equation. This set of UDF solves the induction equation under the *quasi-steady* hypothesis of electromagnetism by using the vector potential–scalar electric potential ($\mathbf{A} - \mathrm{V}$) formulation. The quasi-steady approximation means that all electrostatic phenomena are neglected and the propagation of electromagnetic waves is supposed to be instantaneous. As already seen in section A.1.2.2, the rotational of the vector potential is linked to the magnetic induction vector ($\boldsymbol{\nabla} \times \mathbf{A} = \mathbf{B}$). The $\mathbf{A} - \mathrm{V}$ formulation implicitly contains the Coulomb gauge $\nabla \cdot \mathbf{A} = 0$, which is necessary to ensure the uniqueness of the solution. In our problem, the induction equation may be rewritten in terms of the vector potential.

$$\frac{\partial \boldsymbol{A}}{\partial t} = \frac{1}{\mu_0 \sigma_{el,f}} \nabla^2 \boldsymbol{A} + \frac{1}{\sigma_{el,f}} j_e \tag{25}$$

j_e represents the external current density circulating in the inductor coils. In a harmonic regime, the use of phasors allows us to write the vector potential in a complex exponential form with separate factors of space and time dependence.

$$\underline{\boldsymbol{A}} = \underline{\boldsymbol{A_0}} e^{i\omega \mathrm{t}} \tag{26}$$

$\boldsymbol{A_0}$ and ω are respectively the complex amplitude and the angular frequency. By substituting Eq. 26 in Eq. 25, we obtain the complex differential form of the induction equation for the magnetic vector potential **A**.

$$\Delta \underline{\boldsymbol{A}} - i\mu_0 \sigma_{el,f} \omega \underline{\boldsymbol{A}} + \mu_0 j_e = 0 \tag{27}$$

Due to the 2D axisymmetric approach, only the azimuthal component A_θ is solved since the other components (A_r, A_z) are null. The calculation of the equation in A_θ is then further separated into calculation of two equations corresponding to the real and the imaginary parts: $A_\theta = A_{\theta,real} + iA_{\theta,imag}$.

From the distribution of the magnetic vector potential, it is possible to explicitly calculate (Table 6) the distributions of the magnetic induction $\boldsymbol{B}$**,** the inducted current density $\boldsymbol{j}$ and the Lorentz force acting on the liquid metal bath $\boldsymbol{F}$.

Table 6: Variables calculated from the vector potential distribution

Magnetic induction	$\mathbf{B} = \boldsymbol{\nabla} \times \mathbf{A}$
Current density	$\mathbf{j} = (\boldsymbol{\nabla} \times \mathbf{B})/\mu_0$
Lorentz force	$\mathbf{F_{Lorentz}} = \mathbf{j} \times \mathbf{B}$

3.2 Hydrodynamics model

3.2.1 Liquid metal bath modeling

The momentum conservation equation and the continuity equation which are the basis for describing the hydrodynamics of the liquid metal bath subjected to the electromagnetic Lorentz forces have been taken up in section A.1.2.2.2.

3.2.1.1 Flow modeling

Each velocity component u_i may be decomposed into a sum of a time averaged value $\bar{u}_i$ and a random fluctuation $u_i{}'$, as expressed in Eq. 28. Similarly, other physical variables (p, f_i) can also be written as a sum of an average part and a fluctuating part. The root mean square (RMS) of the velocity fluctuations u_f' (assuming an isotropic fluctuating velocity) may then be expressed as a function of the turbulence kinetic energy k in Eq. 29.

$$u_i = \bar{u}_i + u_i{}' \tag{28}$$

$$RMS(u_f') = \sqrt{\frac{1}{3}\left(\overline{u_1'^2} + \overline{u_2'^2} + \overline{u_3'^2}\right)} = \sqrt{\frac{2}{3}k} \tag{29}$$

Furthermore, we can define the turbulence intensity I_{turb} as the ratio of the RMS of the velocity fluctuations to the mean velocity: $I_{turb} = RMS(u_f')/\ \overline{u_f}$. Typically for metallurgical processes, the turbulence intensity may range from 0.01 (very low intensity) to 0.4 (highly turbulent) [22].

Navier-Stokes Equations (Eq. 15 and Eq. 16) can be transformed using these time averaged quantities into the Reynolds Average Navier-Stokes equations (RANS) which form the base of our flow modeling strategy.

$$\frac{\partial \rho}{\partial t} + \frac{\partial(\rho \overline{u_i})}{\partial x_i} = 0 \tag{30}$$

$$\frac{\partial(\rho\overline{u_i})}{\partial t}+\overline{u_j}\frac{\partial(\rho\overline{u_i})}{\partial x_j}=-\frac{\partial\overline{p}}{\partial x_i}+\mu_f\frac{\partial^2\overline{u_i}}{\partial x_j\partial x_j}-\frac{\partial\rho\,\overline{u_i'\,u_j'}}{\partial x_j}+\overline{f_i} \tag{31}$$

Compared to Eq. 16, Eq. 31 contains an additional term $\rho\overline{u_i'\,u_j'}$, signifiying stress due to the fluctuation velocity field, otherwise termed as the Reynolds stress. This nonlinear term requires additional modeling (the Boussinesq assumption relating the turbulence stresses to the mean flow with the introduction of the turbulent viscosity μ_t to close the system of equations), which gives rise to different turbulence models such as $k-\varepsilon$ and $k-\omega$ models.

The turbulence kinetic energy k, as defined in Eq. 29, describes the mean kinetic energy (per unit mass) due to the fluctuating velocity.The rate at which this kinetic energy is dissipated due to the fluctuating viscous stress is called the turbulence dissipation rate ε. The specific dissipation rate of the turbulence kinetic energy is simply the turbulence dissipation rate per turbulence kinetic energy: $\omega=\varepsilon/k$. In the present work, we have selected the $k-\omega$ Shear Stress Transport (SST) turbulence model proposed by Menter [72], which is an improvement of the standard $k-\omega$ model. This model involves solution of two transport equations, one each for k and ω.

$$\frac{\partial(\rho k)}{\partial t}+\frac{\partial(\rho k u_i)}{\partial x_i}=\frac{\partial}{\partial x_j}\left(\Gamma_k\frac{\partial k}{\partial x_j}\right)+\widetilde{G_k}-Y_k \tag{32}$$

$$\frac{\partial(\rho\omega)}{\partial t}+\frac{\partial(\rho\omega u_i)}{\partial x_j}=\frac{\partial}{\partial x_j}\left(\Gamma_\omega\frac{\partial\omega}{\partial x_j}\right)+G_\omega-Y_\omega+D_\omega \tag{33}$$

Table 7 presents the terms, specific to this model, expressed in the above equations:

Table 7: Definition of some of the $\mathrm{k}-\omega$ turbulence model terms [73]

$\widetilde{G_k}$, G_ω	Generation of k due to mean velocity gradients and generation of ω	Y_k, Y_ω	Dissipation due to turbulence
Γ_k, Γ_ω	Effective diffusivity of k and ω	D_ω	Cross diffusion term

The SST formulation of the $k-\omega$ turbulence model brings together the best features of the common turbulence models: $k-\omega$ and $k-\varepsilon$. The low Reynolds turbulence in the inner region of the boundary layer is modeled by the $k-\omega$ model, while the SST model switches to $k-\varepsilon$ model in the higher Reynolds region of the flow. These features make SST model a lot more attractive in terms of accuracy and reliability when compared to the standard $k-\omega$ model. In free surface flows, high turbulence generation can be observed at the interface due to a high velocity gradient. This requires turbulence damping in the interfacial region in order to conserve accuracy for the model. For this purpose, a turbulence damping term is added as a source term $S_{damp,t}$ in the specific dissipation rate conservation equation following the methodology proposed in the ANSYS Fluent.

$$S_{damp,t} = A_{int} \Delta n \beta \rho_i \left(\frac{B 6 \mu_i}{\beta \rho_i \Delta n^2} \right)^2 \tag{34}$$

ρ_i, μ_i, A_{int} and Δn are respectively the density for phase i, its dynamic viscosity, the interfacial area density and the typical grid size across the interface. $\beta = 0.075$ is a constant, whereas the damping factor B was kept equal to 10 following the recommendations in Egorov's work [74].

3.2.1.2 Free surface modeling

A correct computation of the hydrodynamics of the metal bath requires an accurate representation of the shape of its free surface. The method selected in the present work for describing the evolution of the shape of the free surface is the Volume Of Fluid (VOF) method, first proposed by Hirt and Nichols [75], where a scalar indicator binary function α is used to distinguish between the metal and air regions. The volume fraction of metal within a control volume is used to define the indicator function (Figure 24).

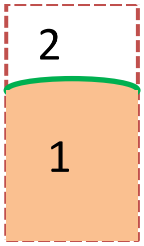

Control volume filled only by phase 1 (metal)	$\alpha = 1$
Control volume filled only by phase 2 (air)	$\alpha = 0$
Interface is present	$0 < \alpha < 1$

Figure 24: Indicator function in a control volume

The time evolution of the volume fraction inside a control volume is calculated by solving the transport equation Eq. 35.

$$\frac{\partial \alpha}{\partial t} + u_i \frac{\partial \alpha}{\partial x_i} = 0 \tag{35}$$

Once the volume fraction equation has been solved, the mixture properties φ_m (density, viscosity and electrical conductivity) in the computational cells containing the free surface are obtained using the following mixture law.

$$\varphi_m = (1 - \alpha)\varphi_2 + \alpha \varphi_1 \tag{36}$$

The VOF method is sensible to any interface topology variation and easily captures any coalescence, break-up or any other deformation. Moreover, it naturally ensures the conservation of the mass of the traced fluid. One of the critical issues with the VOF method is the discretization of the advection term in the abovementioned volume fraction transport equation. Lower order schemes like the first order upwind method are likely to smear the interface due to numerical diffusion and higher order schemes are unstable and mostly result in numerical oscillations. Therefore, it is necessary to employ specific advection schemes that can keep the interface sharp and calculate correct volume fractions. These schemes are described in Annex 3. The GeoReconstruct technique based on the PLIC method [73] was selected for the present study as this scheme provides the best compromise for calculation of a sharp interface while limiting computing resources.

3.2.2 Oxide layer friction force model

In section A.1.3.3, we discussed the presence of an oxide layer on the aluminum bath free surface. A mathematical description of its possible impacts on the bath hydrodynamics and on the bath free surface deformation is presented in this section.

We consider the oxide layer as an immobile and homogenous thin layer, which covers the entire free surface (refer Annex 7). This assumption may become questionable for certain grades of aluminum alloys, under certain processing operating parameters. This was indeed the case during some experiments held at the industrial scale, where it was observed that the surface oxide broke apart and renewed itself at regular time intervals. In our model, the oxide layer is treated as a pseudo-wall, which produces a friction force on the metal underneath the free surface, resulting in the development of a boundary layer near the oxide layer.

A force balance at the free surface in an infinitesimal control volume (Figure 25) gives the relationship in Eq. 37.

$$\bar{\bar{T}}_l.\boldsymbol{n} = \bar{\bar{T}}_g.\boldsymbol{n} + \gamma k\boldsymbol{n} - \boldsymbol{\nabla}_t\gamma \tag{37}$$

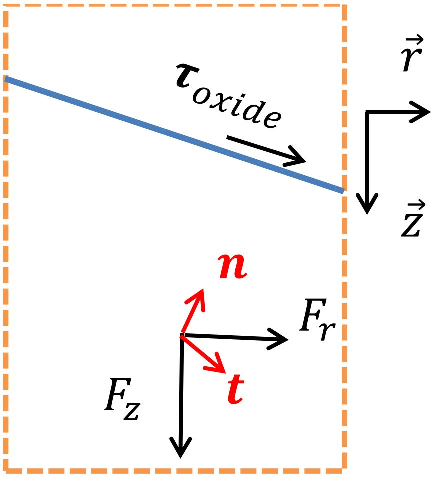

Figure 25: Representation of an oxide layer in an interfacial cell

$\overline{\overline{T_l}}$ represents the stress tensor applied by the liquid metal on the gas phase while $\overline{\overline{T_g}}$ represents the stress tensor applied by the gas on the liquid metal. $\gamma, k, \boldsymbol{n}$ represent respectively the surface tension coefficient, the curvature and the normal vector. Each stress tensor can be further written as a function of the pressure and a shear stress tensor: $\overline{\overline{T}} = -P\overline{\overline{I}} + \overline{\overline{\tau}}$. We consider that the surface tension is homogenous (i.e. no Marangoni effect), hence the gradient of the surface tension is neglected ($\vec{\nabla}_t \gamma = 0$). The projection of Eq. 37 along the normal direction to the interface gives us the following relationship:

$$-P_l + \tau_{nn,l} = -P_g + \tau_{nn,g} + \gamma \mathrm{k} \tag{38}$$

The normal stress term $\tau_{nn,l}$ relative to the liquid is classically neglected as it is deemed very small compared to the pressure forces. The normal stress term $\tau_{nn,g}$ relative to the gas is also neglected, which leads to the well-known Laplace's equation:

$$P_g = P_l + \gamma\, \mathrm{k} \tag{39}$$

As discussed in section A.1.3.3, the presence of the oxide layer reduces the surface tension of the metal from 1.1 N/m to 0.86 N/m. In our model, the effective surface tension force occurring at the free surface between the air and the oxide layer covering the liquid metal is taken into account by adding an equivalent volumetric source term in the Navier-Stokes equations. This is performed by using the Continuum Surface Force (CSF) model available in ANSYS Fluent.

The projection of Eq. 37 along the tangential direction to the interface is written in Eq. 40. In the case of a "true" free surface (without oxide layer), the tangential shear stress in the liquid at the interface ($\tau_{nt,l} = 0$) would be negligible and we would have applied a slip condition. However, in the present case, it is considered that the oxide layer is responsible for friction effects, thus exerting a tangential shear stress on the metal τ_{oxide}. The shear stress due to the oxide layer is therefore expressed in Eq. 41, where the oxide layer is considered as immobile ($\boldsymbol{V}_{oxide} = 0$).

$$\tau_{nt,l} = \tau_{oxide} \tag{40}$$

$$\tau_{oxide}\boldsymbol{t} = -C_f\left(\boldsymbol{V}_{m,int} \cdot \boldsymbol{t} - \boldsymbol{V}_{oxide}\right)\boldsymbol{t} = -C_f\left(\boldsymbol{V}_{m,int} \cdot \boldsymbol{t}\right)\boldsymbol{t} \tag{41}$$

The friction coefficient C_f is an adjustable coefficient which is discussed in the coming sections, while $\boldsymbol{V}_{m,int}$ is the melt velocity near the interface (which is assimilated to the mixture (metal + air) velocity in the interfacial cell). In our model, this shear stress is translated into a volumetric force source term as described in Eq. 42, which is added to the N-S equations. A_{int} represents the interfacial area density in the interfacial cell. Of course this force is only activated for the interface cells which satisfies the criterion: $0< \alpha_l < 1$.

$$\boldsymbol{f}_{oxide} = \tau_{oxide}\boldsymbol{t}\,A_{int} = -C_f A_{int}\left(\boldsymbol{V}_{m,int}\cdot\boldsymbol{t}\right)\boldsymbol{t} \tag{42}$$

Friction force projection

In this section, the friction force $\boldsymbol{f}_{oxide}$ defined above is projected on to (r, z) coordinate system, as represented in Figure 25. The tangential and the normal vectors at the interface and the mixture velocity vector at the interfacial cell center can be expressed as:

$$\begin{gathered}\boldsymbol{t} = t_z\boldsymbol{z} + t_r\boldsymbol{r}\ ;\ \boldsymbol{n} = n_z\boldsymbol{z} + n_r\boldsymbol{r}\\ \boldsymbol{V}_{m,int} = V_{m,int,z}\boldsymbol{z} + V_{m,int,r}\boldsymbol{r}\end{gathered} \tag{43}$$

In VOF, the interface normal vector may be expressed as a function of the gradient of the volume fraction as well as its modulus (Eq. 44), while the zero scalar product of orthogonal vectors ($\boldsymbol{n}$ and $\boldsymbol{t}$) gives Eq. 45.

$$\boldsymbol{n} = \frac{\boldsymbol{\nabla}\alpha}{|\boldsymbol{\nabla}\alpha|} = \frac{1}{|\boldsymbol{\nabla}\alpha|}\left(\frac{\partial\alpha}{\partial z}\boldsymbol{z} + \frac{\partial\alpha}{\partial r}\boldsymbol{r}\right) \tag{44}$$

$$t_r = -\frac{n_z}{n_r}\,t_z = -\left(\frac{\partial\alpha}{\partial z}\Big/\frac{\partial\alpha}{\partial r}\right)t_z \tag{45}$$

Moreover, thanks to the modulus of vector $\boldsymbol{t}$, the following expression provides the missing link:

$$t_z{}^2 + t_r{}^2 = 1 \Rightarrow t_z{}^2 = \frac{\left(\frac{\partial\alpha}{\partial r}\right)^2}{\left(\frac{\partial\alpha}{\partial z}\right)^2 + \left(\frac{\partial\alpha}{\partial r}\right)^2} \tag{46}$$

Using the above expressions, the projection of the friction force in the (r, z) coordinate system can be calculated and presented as:

$$f_{oxide,z} = \boldsymbol{f}_{oxide}\cdot\boldsymbol{z} = -C_f A_{int}\left(\frac{\partial\alpha}{\partial r}V_{m,int,z} - \frac{\partial\alpha}{\partial z}V_{m,int,r}\right)\frac{\frac{\partial\alpha}{\partial r}}{\left(\frac{\partial\alpha}{\partial z}\right)^2 + \left(\frac{\partial\alpha}{\partial r}\right)^2} \tag{47}$$

$$f_{oxide,r} = \boldsymbol{f}_{oxide}\cdot\boldsymbol{r} = +C_f A_{int}\left(\frac{\partial\alpha}{\partial r}V_{m,int,z} - \frac{\partial\alpha}{\partial z}V_{m,int,r}\right)\frac{\frac{\partial\alpha}{\partial z}}{\left(\frac{\partial\alpha}{\partial z}\right)^2 + \left(\frac{\partial\alpha}{\partial r}\right)^2} \tag{48}$$

Friction force model development

In this sub-section, we discuss the choice of the best approximation method to calculate the interfacial area density in each interfacial cell and the selection of an appropriate friction coefficient value.

- Selecting an interfacial area density approximation method

The interfacial area density can be approximated by the following expressions in Table 8, found in the works carried out by Egorov et al. [74].

Table 8: Interfacial area density approximations A

A	B	C
$\lvert \nabla\alpha_l \rvert$	$2\alpha_l \lvert \nabla\alpha_l \rvert$	$6\alpha_l(1-\alpha_l)\lvert \nabla\alpha_l \rvert$

These expressions were programmed within the framework of a UDF, where the gradient of the volume fraction in each cell was obtained by an inbuilt ANSYS Fluent macro C_VOF_G. After comparing the accuracy of the various approximation methods (Annex 4), approximation C was deemed the most suitable choice for calculation of the interfacial area density.

- Selecting coefficient C_f

An important parameter of the model is the coefficient C_f which is adjustable and subject to case under study. A primary study was performed to gain an idea of its likely range of value. For this purpose, an analogy with a flat-plate boundary layer was considered (Figure 26).

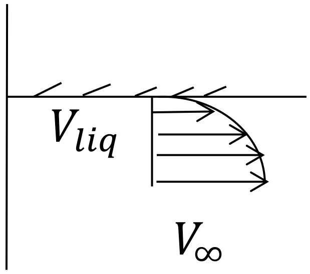

Figure 26: Boundary layer at a flat-plate

For such a flow, literature [76] shows that the shear-stress at the surface of the plate can be calculated using Eq. 49, where f_c , V_∞ and S are respectively the friction coefficient, the liquid velocity far from the wall and the surface area. Moreover, the friction coefficient is related to the Reynolds number for turbulent flow as indicated in the correlation (Eq. 50).

$$F_l = \frac{f_c}{2}\rho_f {V_\infty}^2 S \tag{49}$$

$$\frac{f_c}{2} = 0{,}037{Re_L}^{-0{,}2};\ Re_L = \frac{\rho_f V_\infty L}{\mu_f} \tag{50}$$

As described earlier in Eq. 42, the friction force due to the oxide layer is: $f_{oxide} = C_f S V_{m,int}$. An analogy with Eq. 49, provides the following relation between the coefficients C_f and $\frac{f_c}{2}$ in Eq. 51. Using Eq. 50 and Table 9, the friction coefficient $\frac{f_c}{2}$ is calculated to be equal to 0.0044. This in turn provides us with a value of $\sim 1700\ kg\ m^{-2}s^{-1}$ for the coefficient C_f from Eq. 51.

$$C_f = \frac{f_c}{2}\frac{\rho_f {V_\infty}^2}{V_{m,int}} \tag{51}$$

Table 9: IJL's induction furnace characteristic parameters

Characteristic length L	(m)	0.05
Aluminum alloy density ρ_f	$(\mathrm{kg.\,m^{-3}})$	2379
Dynamic viscosity μ_f	$(\mathrm{mPa.\,s})$	1.15
Liquid metal velocity V_∞	$(\mathrm{m.\,s^{-1}})$	0.4
Interface liquid velocity $V_{m,int}$	$(\mathrm{m.\,s^{-1}})$	0.001

With an idea of expected coefficient values, tests were carried out using a range of these values. Figure 27 shows velocity vectors near the interface for two coefficient values.

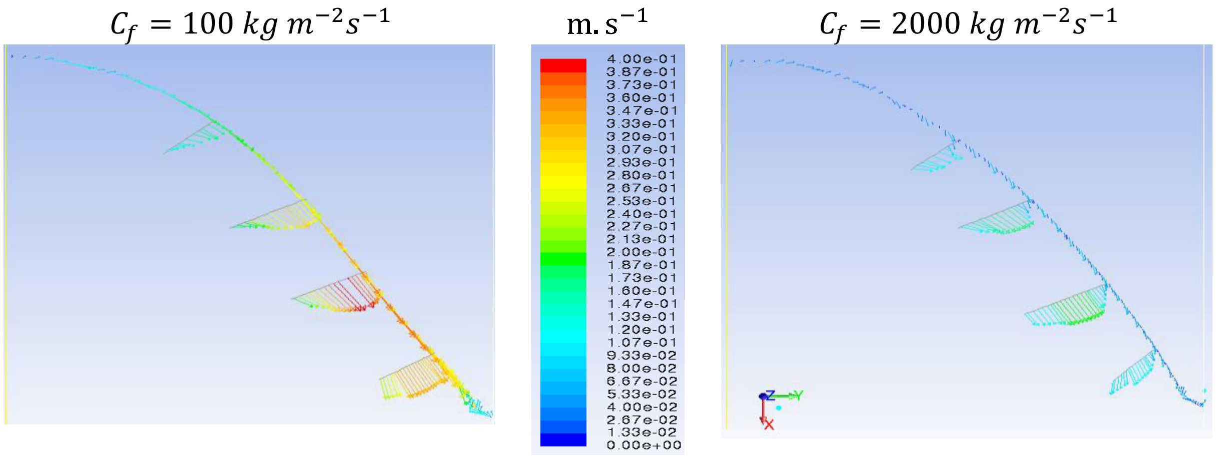

$C_f = 100\ kg\ m^{-2}s^{-1}$

$\mathrm{m.\,s^{-1}}$

$C_f = 2000\ kg\ m^{-2}s^{-1}$

Figure 27: Velocity profiles near interface as a function of friction coefficient

The velocity at the interface expectedly tends towards zero for the higher coefficient and leads to the formation of a boundary layer near the interface. This confirms that the free surface covered by an oxide layer behaves as a pseudo deformable wall. As shown in Figure 28, for friction coefficient values starting around 1200 $\mathrm{kg.m^{-2}.s^{-1}}$, an asymptotic behavior (dotted red line) of the shear stress at the interface is observed. The asymptotic behavior allows the selection of a suitable value of the friction coefficient as 1500 $\mathrm{kg.m^{-2}.s^{-1}}$ for all future use.

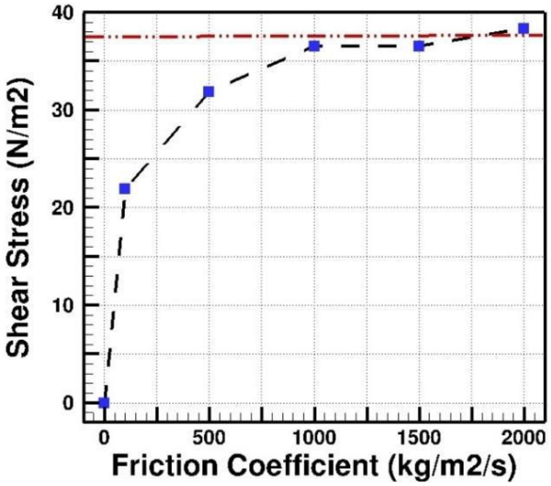

Figure 28: Oxide layer tangential shear stress as a function of the friction coefficient

3.3 Boundary conditions

An overall computational domain ten times the size of the coil encloses the crucible and the coil (Figure 29), which is big enough for the magnetic lines to close without any constraints.

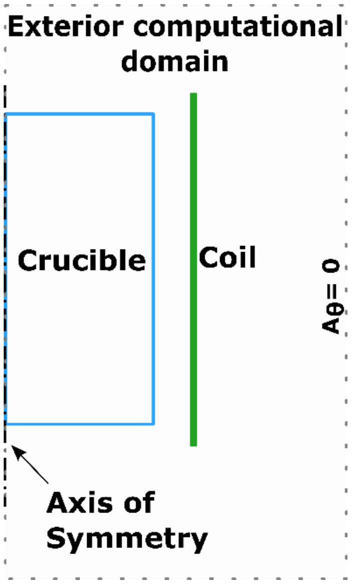

Figure 29: Representation of the induction furnace in the numerical model

A zero value of the vector potential A_θ on exterior boundaries of the computational domain was imposed as a boundary condition. Obviously a Neumann boundary condition on the axis of the crucible was imposed for all the electromagnetic and hydrodynamic variables. At the crucible walls, a no slip boundary condition was used resulting in a zero liquid metal velocity and the mesh has been refined to reach z^+ value of the first cell close to 1.

An initial value of zero bath velocity, zero turbulent kinetic energy and a very small initial dissipation rate equal to 0.002 s^{-1} were applied. Moreover, any presence of additional supports, shields or yokes warrant careful consideration. Later in section C.2.2.2.1, we will describe an example of such an additional geometrical element in our model.

3.4 Numerical model implementation

Besides the geometric description of the setup, the necessary input parameters for the numerical model are: (i) the liquid metal filling in the crucible, (ii) the intensity and the frequency of the current circulating in the inductor coils, and, (iii) the density, dynamic viscosity and electrical conductivity of the liquid metal at the operating temperature.

A transient calculation is performed until a steady state hydrodynamic regime is achieved. We use a 2nd order upwind numerical scheme for the resolution of the momentum and the turbulence equations and a 1st order upwind scheme for the magnetic vector potential equations.

The numerical model (ANSYS Fluent and UDFs) resides in one single framework (Figure 30). At each time step of the calculation, the Lorentz force distribution calculated by Induc 14.0.0 is supplied to the metal bath calculation. The oxide layer friction force UDF calculates the additional external force term. The updated free surface deformation is then provided back to Induc 14.0.0 to continue the next time step of the strongly coupled modeling. The final simulation results are in the form of fields of velocity, turbulence, Lorentz force etc. along with the free surface profile.

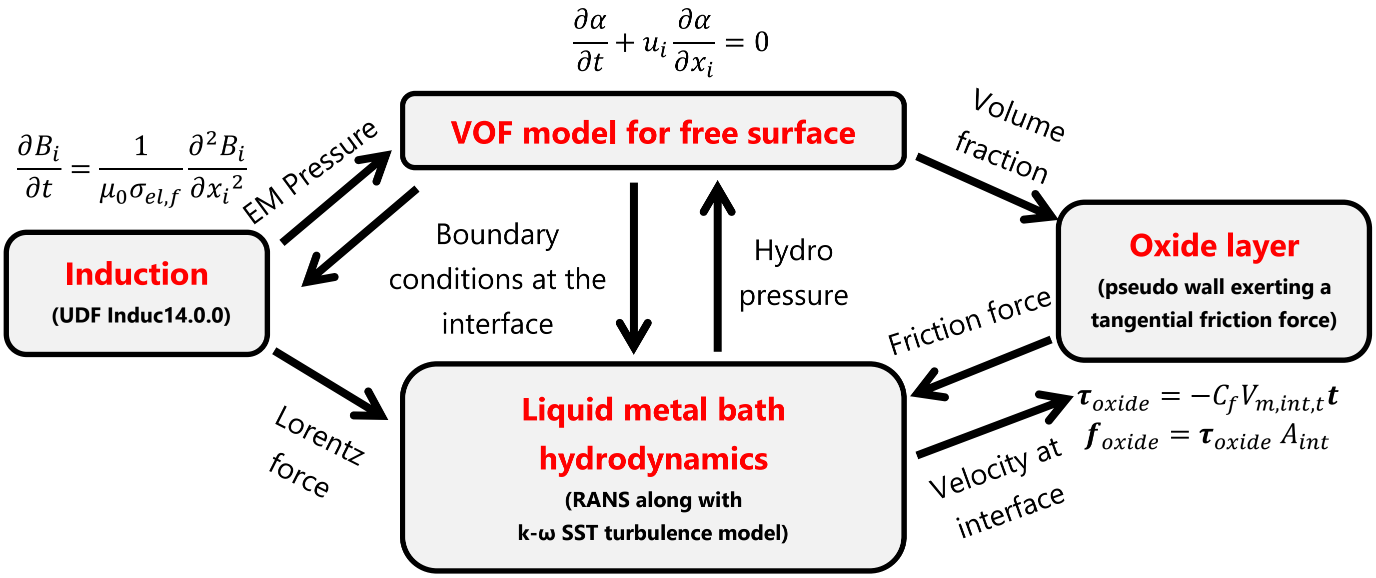

$$\frac{\partial \rho}{\partial t} + \frac{\partial (\rho u_j)}{\partial x_j} = 0$$

$$\frac{\partial (\rho u_i)}{\partial t} + \frac{\partial (\rho u_i u_j)}{\partial x_j} = -\frac{\partial p}{\partial x_i} + \mu_{eff} \frac{\partial^2 (u_i)}{\partial x_i \partial x_j} + \rho g_i + f_{Lorentz,i} + f_{oxide,i}$$

Figure 30: Summary of MHD model

Part B: Inclusion Behavior

In this part, to start with, we present an overview and a literature survey of the phenomena which govern the inclusion behavior in an induction stirred bath. The modeling technique employed is then described with an emphasis on the Population Balance Method (PBM).

1. Fundamentals

This chapter first introduces inclusions, their types and distribution, frequently encountered in liquid aluminum processing. Literature survey on experimental and numerical studies of inclusion behavior is then discussed. Later we discuss some important parameters and mechanisms which apply to inclusion (or particle) hydrodynamics in the bulk and near the interfaces. We also discuss interactions between inclusions leading to aggregation or break-up.

1.1 Description of inclusion population in aluminum alloys

The inclusions are microscale particles of a different phase with respect to the metallic phase, which remain solid in the liquid aluminum bath. After mechanical treatments and solidification, these particles are dispersed in the metal and may damage the quality of the end product. Figure 31 presents the size and the frequency of some types of inclusions occurring in aluminum alloys, extracted from Altenpohl's handbook on aluminum [77]. Three broad categories are notable, with respective sources of origin: A – inclusions formed during the liquid aluminum processing through electrolytic smelting (carbides) or recycling (oxides), B – alloy treatments in the casthouse (oxides and borides) and C – during liquid metal transfer into channels (such as entrained oxide layers). The metal properties are strongly influenced by the number density and the size of the inclusion populations.

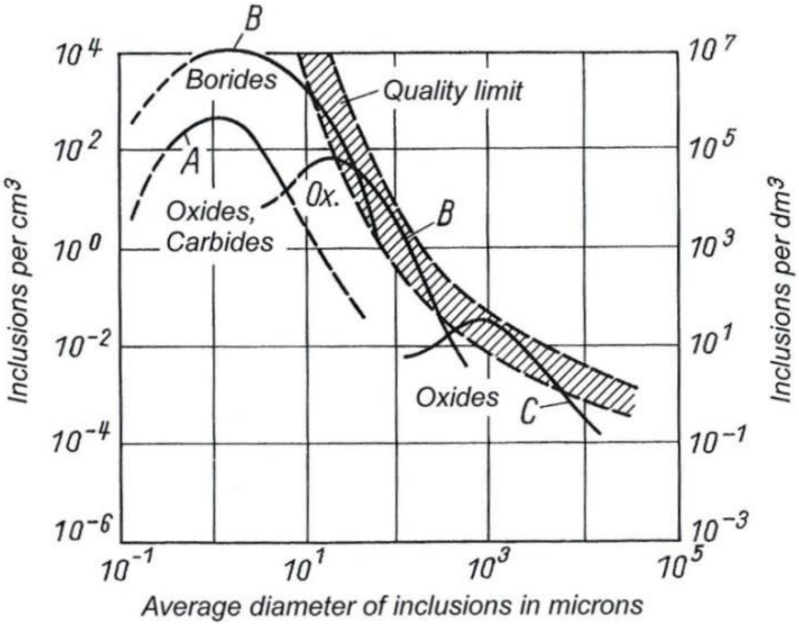

Figure 31: An example of quantitative description of inclusions in cast aluminum [77]

Inclusions in the melt have been traditionally analyzed post solidification of the melt. Meanwhile filtering and in-line techniques of determining inclusions properties for aluminum alloys, while the metal is still in its liquid phase, were introduced in the last two decades. Today techniques such as PoDFA# and LiMCA¤ are regularly used by casthouse quality enforcers to identify different types of inclusions and their properties: chemical composition, number density, morphology and particle size distribution (psd). Table 10 presents the principal types of inclusions found in molten aluminum along with some of their properties [3]. We only provide the type, usual dimensions and density of these inclusions. Their source of origin can vary, such as oxidation at the free surface for oxide film inclusions, or crucible erosion for refractory inclusions, or even melt treatment processes which may leave behind salt inclusions.

Table 10: Inclusions in aluminum casthouse [3]

Inclusion category	Inclusion name	Dimensions (µm)	Density ($kg.m^{-3}$)
Oxide films	Al_2O_3 (Oxide film)	Thickness ~ 1; Length: (250 ; 500)	3900
Carbides	Al_4C_3 (sphere)	0.5 to 3 (small) 3 to 25 (big)	2360
Mg oxides	MgO & $MgAl_2O_4$ (cuboids)	0.5 to 300	3580
	$MgAl_2O_4$ (spinel)	0.1 to 300	3600
Refractory	Graphite	0.5 to 30	2250
	SiO	20 to 5000	2660
Melt treatments	Salts (sphere)	-	-
Refining	TiB_2	1 to 30	4500

In our study we only treat spherical $MgAl_2O_4$ inclusions (see Figure 2), which are formed due to oxidation of magnesium during liquid aluminum processing. These inclusions are denser than the aluminum alloys ($\rho_p = 3600\ kg.m^{-3}$), while their size can vary in a wide range from 1 to 300 µm.

The particle size distribution (psd) for these inclusions was reconstructed using the experimentally measured data at Constellium. For a given sample size, the number of inclusions was counted and distributed into intervals with particle size as the distribution coordinate. This distribution was then fitted (Annex 5) to a log-normal distribution and ultimately used as an important numerical model input. We will introduce this psd later in section C.2.2.2.4.

¤ LiMCA stands for Liquid Metal Cleanliness Analyzer. Refer Guthrie and Doutre [78] for more information.
PoDFA stands for Porous Disc Filtration Apparatus. Refer Doutre et al. [79] for more information.

1.2 Literature survey on inclusion behavior in metallurgical processes

In the aluminum industry, some work has been done to understand and predict the inclusion behavior in liquid metal processes but has been primarily focused on gas stirred ladles. Later in this section we will focus on some examples treating the inclusion dynamics in induction furnaces.

Johansen et al. [80] numerically studied the inclusion transport from the free surface in a rotor stirred reactor for an aluminum bath. In his PhD thesis at Institut Jean Lamour, Mirgaux [81] studied a gas stirred aluminum ladle, where inclusion aggregation as well as inclusion flotation by the gas bubbles were considered in a CFD – Population Balance Method (PBM) coupled model. Also, Pauty et al. [82] studied a holding furnace where particle tracking was performed. A similar study was also carried out by Instone et al. [83] who considered only the buoyant forces and the fluid flow in a gas–fired furnace. In these studies, the furnace geometry and furnace emptying process play a major role in the inclusion dynamics. Recent studies show a diverse application of electromagnetic processing in the aluminum sector. While some have focused on increasing the dispersion of particles in the melt, other researchers are finding novel ways to remove them from the melt. For example, Nastac et al. [84] modeled the introduction of nanoparticles to reinforce the metal matrix composite, processed inside an induction furnace. Electromagnetic filtration of molten aluminum via application of an external EM field on the channels was numerically studied by Shu et al. [85], which was complemented with post solidification verification of a generally increased removal efficiency thanks to the EM effect on the particles. Some authors such as Kennedy et al. [86] have also numerically (FEM) and experimentally studied the impact of inductor coil geometries on the EM separation of particles from a melt and offer improved solutions through model designed filtration designs. Meanwhile Shimasaki and Taniguchi [87] presented a new inclusion separation experimental setup combining a liquid cyclone and an induction coil.

In the steelmaking sector, in contrast, modeling of inclusion populations in gas-stirred ladles has received a much wider attention by the metallurgists. Among them, Claudotte [88] modeled using PBM an inclusion population in a gas-stirred steel ladle while taking aggregation, nucleation and crystalline growth of inclusions into consideration. Bellot et al. [89] also coupled CFD and PBM to simulate a gas stirred ladle. In addition to inclusion aggregation they also considered inclusion flotation by the gas bubbles and inclusion transport by convection and sedimentation. An example of induction heating in steelmaking can be found in the work carried out by Wang et al. [90]. They numerically investigated (using the Euler-Lagrange approach) the non-metallic inclusion behavior of sizes less than 50 µm in continuous casting tundish within a channel type induction furnace and confirmed that the electromagnetic migration governs a large fraction of the inclusion transport.

The nature of the metal flow in an induction furnace is very different from that of a gas–fired furnace as the melt is continuously and strongly stirred by the EM forces, even during the casting step. The impact is illustrated in Figure 32, where the relative index of inclusions exiting a furnace is reported for several casts done with an induction furnace *A* or a gas–fired furnace *B*. The figure reports the general trend of the inclusion content during the entire casting time and hence during the emptying of the furnace, without comparing the metal cleanliness at the exit of each processing furnace. Therefore, it must be noted that the gas-fired treatment (blue zone) has an advantage over the induction furnace (red zone). Nevertheless, for certain alloys, the induction melting furnace remains the preferred technology and edges out the gas-fired furnace as it limits the liquid metal oxidation during the melting process.

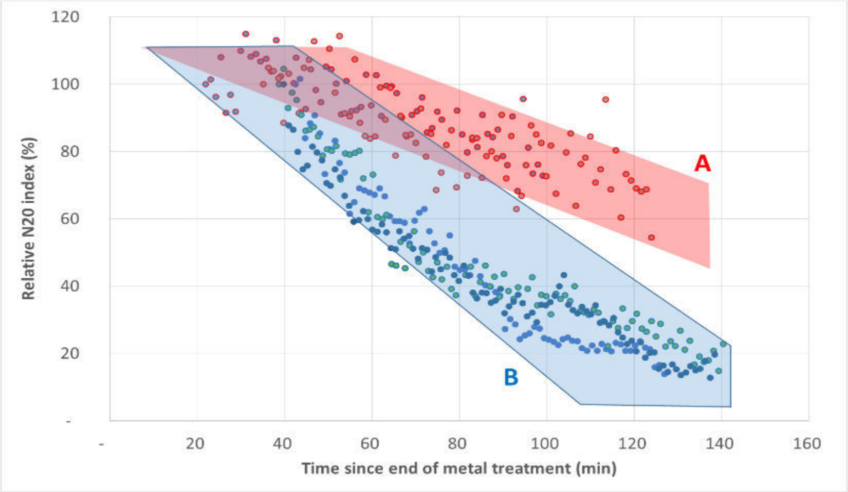

Figure 32: Relative LiMCA N20 index versus time measured during casts from an induction furnace *A* and a gas–fired furnace *B*, after an Ar-Cl_2 metal treatment [91]

Leenov and Kolin [92] established the theoretical concept behind the influence of EM fields on particles in conductive flows. They demonstrated that a non-conductive particle migrates through the melt in a direction opposite to the induced Lorentz forces. Several techniques based on this electromagnetic separation have been developed and applied in metal processing such as imposed DC or AC current in a melt, traveling magnetic fields, stationary or alternating magnetic fields, or a combination of the above. Sun et al. [93] conducted numerical analyses to predict inclusion removal from a melt, either by imposing a strong magnetic field or by imposing a strong DC current. Particle tracking was performed using the Lagrangian technique and the results show that the imposed DC current strongly favors the removal efficiency. Another interesting example is proposed by Taniguchi and Brimacombe [94], who numerically investigated the rate of particle deposition in the turbulent molten flow subjected to a pinch force, i.e. application of an AC current in a channel-induction furnace. Zhang et al. [95] reviewed these processes and provided a summary of available EM separation techniques. Inversely, Bolcato et al. [96] studied the behavior of conducting particles in a non-conducting fluid. Although it was only a proof of concept, the brief experimental work provided some interesting information on the particle velocity and its general movement in the fluid.

Experimental study of inclusions in induction furnaces

Notwithstanding, very few researchers have actually focused on inclusion behavior in an induction furnace. Over the years, some experimental investigations were performed, but primarily post-solidification, and due to the obvious reason of the liquid metal opacity, it has been difficult to correctly discern the history of inclusion dynamics prior to solidification.

El-Kaddah et al. [97] developed an experimental EM filtration device for refining molten aluminum. Cremer and Driole [98] studied the oxide inclusion behavior in molten steel in a lab scale IMF, whereby experiments were performed using radioactive tracers. Qualitative observations were made regarding the effect of the current frequency on the locations of inclusions post solidification and as such three regions were identified: the bulk, near the free surface and near the crucible walls. The maximum population concentration was generally found near the walls.

Sadoway and Szekely [99] tried to measure the flow structures in a transparent molten salt (LiCl-KCl eutectic) stirred in an IMF. However, the results obtained were not in agreement with the usual location of the bath recirculation zones and the order of magnitude of melt velocities. This was justified by the extensive natural convection from the cold walls to the hot bulk regions. Although the idea of working with transparent conductive fluids would have been very useful, unfortunately this drawback made it unfit for any further in-line measurement of inclusion dynamics. Only very recently, Scepanskis et al. [100] have proposed a novel technique of in-line inclusion dynamics study using neutron imagining. This was performed in a rectangular vessel (10 cm x 10 cm) nestled in a rotating magnet installation, where the induced flow is very similar to the one found in induction furnaces. This technique can be applied to opaque melts (gallium in their case) and is thus very useful for inclusion dynamics study. The initial results are very optimistic and numerical confrontation is currently underway.

Modeling inclusions in induction furnaces

The numerical modeling of inclusions has been mostly restricted to a Lagrangian technique where inclusions were tracked within the bath. Ilegbusi and Szekely [101] were probably the pioneers in modeling the particle transport in an induction stirred bath. While they only took drag and buoyant forces into account, they included the fluctuating velocity component when calculating the drag force exerted by the fluid on the particles. They concluded that turbulence plays an important role in particle transport, especially if the fluctuating velocity is of the same order as the settling velocity.

More recently Bojarevics et al. [102] investigated particle tracking in a small melt levitated in a cold crucible. They used two techniques for modeling particle dynamics: The Lagrangian technique and the Drift Concentration Method (DCM) (Eulerian approach) [103] [104]. The two methods were found to give similar results wherein the small particles (1 – 10 μm) remain in the bulk while bigger particles (100 μm) are attracted and then trapped by the EM migration forces within the EM skin. Takahashi and Taniguchi [105] also modeled the inclusion dynamics in an induction stirred furnace using the DCM, and followed it up with post solidification experimental verifications, which agreed well with the numerical trends. A higher EM migration towards the wall with an increase in the coil current was duly noted. It was also concluded that additional mechanical stirring delayed this migration.

Kirpo [37] used the Lagrangian technique to model the particle behavior in a LES (Large Eddy Simulation) resolved MHD flow, while taking into account drag, buoyancy, lift and EM forces for particle motion. Scepanskis et al. [45] added to Kirpo's work by treating only a particle cloud situated initially at the bath free surface. The acceleration and the virtual mass forces were also treated and the relative importance of each force was portrayed using a statistical analysis. Wang et al. [106] also worked on separation of non-metallic inclusions from molten steel in a small lab scale induction furnace. The Lagrangian technique for tracking particles showed that at least 90 % of the inclusions were transported to the vicinity of the crucible walls, where a simple solidification model simulated the entrapment of these inclusions.

To conclude, we note that among the induction related works, a general consensus exists over the important role of inclusion migration towards the EM skin depth. It was also observed that while the smaller inclusions were found to mainly follow the bath flow structures and thus take a long time to sediment or migrate towards the wall, the larger inclusions on the other hand, quickly migrate due to the EM influence. Most of the numerical studies used the Lagrangian particle tracking technique while some also employed the drift concentration technique. However, the particle interactions leading to agglomeration between inclusions in an induction stirred bath is a topic which has received little attention. The aim of this work is to describe the impact of the bath magnetohydrodynamics on inclusions in an induction furnace, while considering the inclusion interactions. This is to be performed using a combination of the drift concentration technique and the PBM.

1.3 Inclusion dynamics during liquid metal processing

The behavior of a dispersed multiphase flow can be classified according to the inclusion volume fraction α_p. As summarized in Figure 33 [107] [108], for diluted dispersed phase, the inclusion volume fraction is very low ($\alpha_p < 10^{-6}$), and therefore the influence of the inclusions on the macroscopic flow of the continuous phase may be neglected. While modeling this multiphase flow regime, a one-way coupling is employed, whereby the inclusion transport is calculated as a post-processing of the fluid dynamics calculation of the continuous phase.

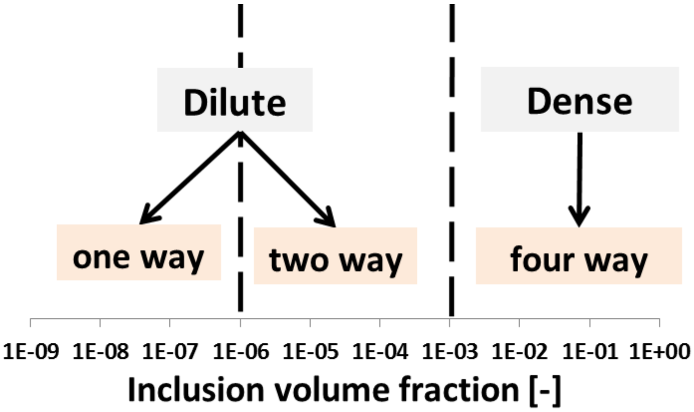

Figure 33: Classification of multiphase flows according to the volume fraction of inclusions

In regimes with higher volume fraction ($10^{-6} < \alpha_p < 10^{-3}$), the influence of the motion of the inclusions on the bath hydrodynamics may not be neglected and thus while modeling, a two-way coupling is used. On the other hand, in dense regimes ($\alpha_p > 10^{-3}$), the inclusions are too close to be treated as isolated regarding the multiphase flow and thus the bath hydrodynamics – inclusion interaction as well as inclusion – inclusion interactions come into play, resulting in a four way coupling technique. In most of the aluminum processing, the inclusion concentration is found to be close to or lower than 10^{-6}, and thus our model adopts the one-way coupling.

Dimensionless numbers must be introduced to characterize the dynamics of the fluid flow around the particle and the inertia of the inclusions. They are defined in the following paragraph where we consider particles as spherical. Eq. 52 gives the Reynolds number for a particle Re_p dragged by the flow of the continuous phase. d_p, u_f and u_p respectively represent the inclusion diameter, the fluid and particle mean velocities. This gives information on the regime of the flow around the particle and depends on the fluid properties (ρ_f, μ_f).

$$Re_p = \frac{\rho_f d_p |u_f - u_p|}{\mu_f} \tag{52}$$

We term a flow regime as Stokes flow past a particle if $Re_p \ll 1$, often indicating very small particle size. Furthermore, the momentum response time is the time required for a particle to respond to a bath velocity gradient. In order to derive this response time, the equation of motion while considering the drag and the added mass forces is written. The solution to this equation, for Stokes flow, gives us the expression in Eq. 53.

$$\tau_p = \frac{(\rho_p + 0.5\rho_f){d_p}^2}{18\mu_f} \; (if Re_p \ll 1\,) \tag{53}$$

Stokes number St_p is the ratio of the inclusion response time and the characteristic time scale of the flow. The characteristic time scale of a turbulent flow can be taken as that equals to the Kolmogorov time scale: $\tau_\eta = (\frac{\nu_f}{\varepsilon})^{0.5}$, which provides an expression for St_p in Eq. 54.

$$St_p = \frac{\tau_p}{\tau_\eta} = \frac{(\rho_p + 0.5\rho_f){d_p}^2}{18\mu_f}\left(\frac{\nu_f}{\varepsilon}\right)^{-0.5} \tag{54}$$

If $St_p \ll 1$, the particles are considered as non-inertial and thus the inclusions can respond to any flow velocity gradient, resulting in similar inclusion – fluid trajectories. Otherwise if St_p is not negligible with respect to 1, the inclusions do not have the time to respond to the fluid perturbations, often leading to the exit of the inclusions from the eddies (this is the so-called crossing trajectory effect).

The inclusion transport due to the velocity fluctuations is influenced by the particle size and the turbulent length scale. If the inclusion of size d_p is smaller than the Kolmogorov scale $\eta_k = \left(\frac{\nu^3}{\varepsilon}\right)^{0.25}$, the inclusion does not interfere with the turbulence pattern of the flow. However, if the inclusion is bigger than the Kolmogorov scale, then the scale of the smaller eddies and that of the inclusion overlap each other and thus the inclusion may alter the local flow turbulence.

1.3.1 Inclusion-fluid interaction

A description of the motion of an inclusion in a flow requires considering relevant forces acting on the inclusion. In the following paragraph, we only discuss the drag, the buoyancy and the electromagnetic migration forces, which can be introduced as drift velocities in a Eulerian approach. We neglect the lift force and forces related to transient relative velocities (virtual mass and Basset forces [107] [108]).

Drag force

The drag force [108] exerted by the surrounding fluid on the particle is expressed in Eq. 55. C_D and $|\boldsymbol{u_f} - \boldsymbol{u_p}|$ respectively represent the drag force coefficient and the fluid–particle relative velocity.

$$\boldsymbol{F_p^D} = \frac{1}{2}\rho_f C_D \frac{\pi {d_p}^2}{4}|\boldsymbol{u_f} - \boldsymbol{u_p}|(\boldsymbol{u_f} - \boldsymbol{u_p}) \tag{55}$$

The drag coefficient depends on the particle size and morphology and the surrounding fluid flow characteristics. While considering only spherical particles, we examine the impact of the particle

Reynolds number on the drag force coefficient. Figure 34 illustrates the variation of the drag force coefficient with Reynolds number for a spherical particle.

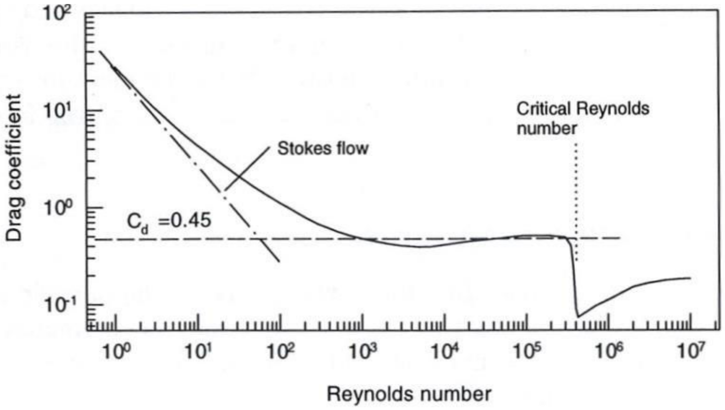

Figure 34: Standard drag curve [107]

For Stokes regime, the drag force coefficient is inversely related to the Reynolds number: $C_D = 24/Re_p$. We then enter a zone of relatively little variation, $750 < Re_p < 3 \cdot 10^5$, before an abrupt decrease beyond the critical Reynolds number. Several studies have been performed to measure the particle drag coefficients and the results are spread over the standard drag curve. However, a correlation suitable for $1 < Re_p < 800$ is expressed in Eq. 56.

$$C_D = \frac{24}{Re_p}\left(1 + 0.15{Re_p}^{0.687}\right) \tag{56}$$

In our model, while calculating the drift velocity corresponding to the drag force, we only consider the drag force coefficient corresponding to the Stokes regime: $\mathrm{C_D} = 24/\mathrm{Re_p}$ since $\mathrm{Re_p}$ numbers remain low for a majority of the particles.

Buoyancy force

In Eq. 57, the gravity and the Archimedes forces give us the net buoyancy force acting on the particle, which is basically due to the difference of densities. For equal densities, the particle will be subjected to neutral buoyant force.

$$\boldsymbol{F_p^B} = \frac{\pi {d_p}^3}{6}\boldsymbol{g}\left(\rho_p - \rho_f\right) \tag{57}$$

Electromagnetic force

According to Leenov and Kolin [92], a particle whose electrical conductivity is different from that of the metal experiences a reaction force to the Lorentz forces $\boldsymbol{F_{Lorentz}}$ induced in the metal bath by the EM field. As illustrated in Figure 35, when the electrical conductivity of the particle is different from that of the surrounding fluid, the presence of the particle introduces a local inhomogeneity resulting in a pressure gradient, thereby leading to an additional volumetric force acting on the particle.

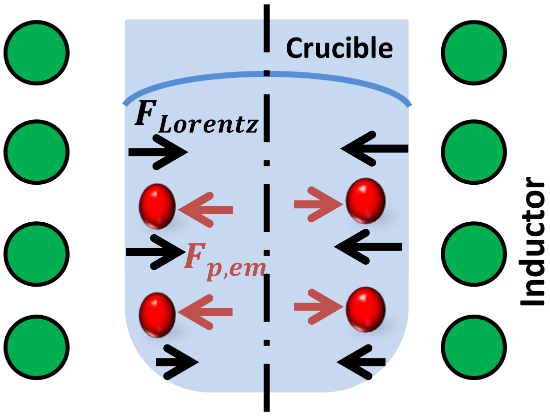

Figure 35: EM influence on inclusions

For a spherical particle, this force is expressed in Eq. 58, where $\sigma_{el,f}$ and $\sigma_{el,p}$ represent the electrical conductivities of the fluid and the particle.

$$\boldsymbol{F_p^{em}} = -\frac{3}{2}A\left(\frac{\sigma_{el,f} - \sigma_{el,p}}{2\sigma_{el,f} + \sigma_{el,p}}\right)\frac{\pi d_{p,i}{}^3}{6}\boldsymbol{F_{Lorentz}} \tag{58}$$

Eq. 58 further simplifies to $\boldsymbol{F_p^{em}} = -\frac{3}{4}A\frac{\pi d_{p,i}{}^3}{6}\boldsymbol{F_{Lorentz}}$ when considering a non-conducting particle ($\sigma_{el,p} = 0$). Over the past few years, there is a debate on the value of coefficient A. Most of the authors referring to the original work of Leenov and Kolin take its value as equal to 1, while Bojarevics [102] and Etay [109] argue that the work of Leenov and Kolin was only concerned with DC fields and that A = 2 for AC fields. In our current work, we have used A = 1, until further clarification on the subject.

1.3.2 Turbulent deposit of inclusions at interfaces

In turbulent flows, the statistical approach consists of decomposing the instantaneous fluid velocity u_i into two: the mean velocity $\bar{u}_i$ and the fluctuating velocity $u_i{}'$ (see section A.3.2.1.1). The particle velocity may be written similarly:

$$u_{p,i} = \bar{u}_{p,i} + u_{p,i}{}' \tag{59}$$

In regions adjacent to a wall or a free surface, the particles may be deposited on these boundaries, through two mechanisms: (i) due to the mean slip velocity (sedimentation or EM effect in our case), and, (ii) due to the turbulent fluctuations. The total deposit velocity is assumed to be the sum of these two contributions.

Over the years, the turbulent deposition of aerosols was thoroughly examined by the researchers in the energy and medical industries. On the other hand, the turbulent deposition of hydrosols has attracted very little attention. Duval and his team [110], [111] at Ecole Centrale Paris have studied during the PRINCIPIA project the turbulent deposition along two main approaches.

The first method uses the semi-analytic method proposed by Fan et Ahmadi [112] who studied the deposition in a channel reactor. Based on this approach, Xayasenh [110] simulated the turbulent deposition of particles in liquids at solid walls and proposed a law for turbulent deposit velocity v_d (i.e. the flux of deposition divided by the concentration of particles) as described in Eq. 60.

$$\frac{v_d}{u^*} = 9.3 \cdot 10^{-4}(\frac{d_p}{l^*})^{1.68} \tag{60}$$

$u^* = \sqrt{\frac{\tau_{wall}}{\rho_f}}$ and $l^* = \frac{\nu_f}{u^*}$ respectively represent the wall friction velocity and characteristic length scale at the wall.

The second approach combines the Direct Numerical Simulation (DNS) of a flow in proximity of an interface and the Lagrangian tracking of suspended particles. In this method, the particles are treated as points and supposed smaller than the Kolmogorov's length scale. The homogeneous and isotropic turbulence is generated in a forcing zone slightly away from the interface, corresponding to the equilibrium zone of a boundary layer. While the turbulence diffuses towards the interface, the transport of particles is therefore solely governed by the fluctuating particle velocity $u_{p,i}'$.

The complete study was carried out for a liquid free surface [110] and it was concluded that direct interception is the main deposition mechanism. The turbulent deposition rate can be expressed as:

$$\frac{v_d}{u_\eta} = 0.045(\frac{d_p}{\eta_k}) \tag{61}$$

$u_\eta = (\nu\varepsilon)^{0.25}$ and η_k respectively represent the Kolmogorov's free surface velocity and its corresponding length scale.

For a solid wall, the RMS of the fluctuations of the normal velocity to the wall follows a quadratic law as a function of the wall distance [113]: $u_\perp \cong {y^+}^2$. Although, the simulations for this configuration are currently underway, a generalized law similar to the one for direct interception deposit is expected, where C is a constant which must be defined:

$$\frac{v_d}{u_\eta} = C\left(\frac{d_p}{\eta_k}\right)^2 \tag{62}$$

1.3.3 Interactions between inclusions

As illustrated in Figure 36, collisions between inclusions can lead to aggregation and a change in the size distribution in the population of inclusions in the bath. *Aggregation* is the process by which two or more particles enter an efficient collision and then adhere to one another to form an aggregate, while keeping some of their initial individual properties (density for example). At the inclusion scale, a physico-chemical process such as diffusion may lead to the development of a cemented neck between the participating inclusions. The restructuring of the morphology of the inclusions with altered internal properties may then be termed as *Agglomeration*. Coagulation on the other hand would be a complete reconstruction of two particles to create a new one, with entirely new internal properties. In all these processes mass and volume of the dispersed phase are obviously conserved.

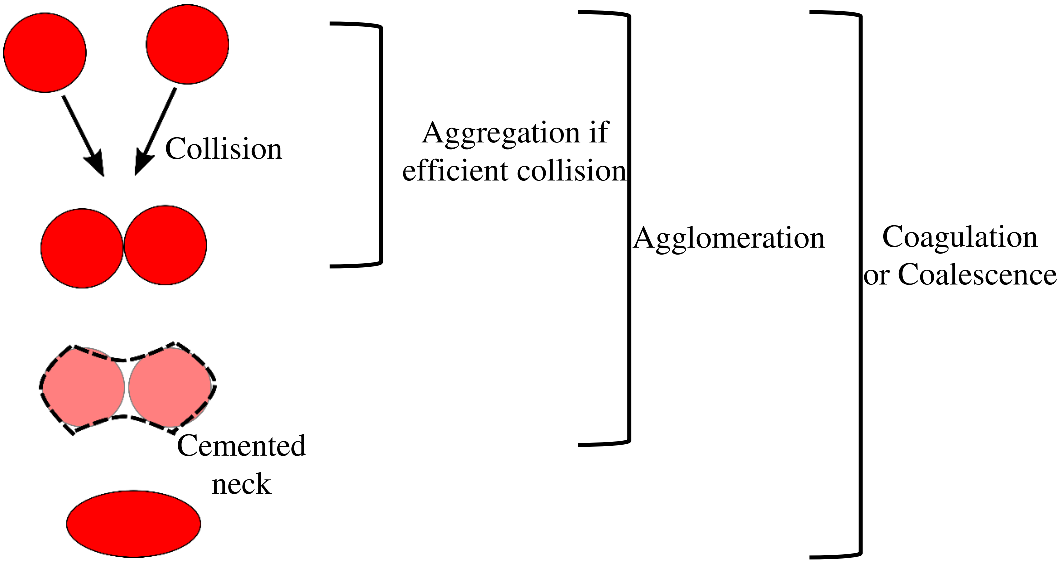

Figure 36: From collision to coagulation

In our case, we treat only the aggregation. In addition, since the particle concentration is considered as dilute, the inter-particle collisions are considered as binary collisions. Furthermore, due to the turbulent shear stress, an aggregate may also undergo a break-up and lead to two or more particles (otherwise termed as fragmentation of aggregates).

Two inclusions i and j can meet due to a difference in their respective velocities, which in turn depends on their size and properties (density for example) and their local surrounding fluid flow conditions. The probability of collision depends on the driving forces and is usually expressed as an aggregation kernel β^{agg}in $m^3.s^{-1}$. The authors during Pratsolis project [114] provide an overview of aggregation processes, with an interesting review of numerical and experimental studies. In his PhD thesis, Claudotte [88] also discusses these inclusion interactions and describes the aggregation kernels.

In the following section, we briefly discuss four phenomena: (i) Brownian collisions, (ii) Laminar and Turbulent collisions, (iii) Gravitational collisions, and, (iv) Aggregate fragmentation. We also discuss their relative collision kernels, which numerically describe the frequency with which two inclusions can meet.

Brownian collisions

At a very small length scale (submicron) the suspended particles are subjected to a random movement or otherwise termed as Brownian motion. The difference in each particle's velocity arises from the Brownian effect, characterized by relative thermal agitation. This can lead to collisions and hence aggregation. However, we do not consider sub-micron scale inclusions in our inclusion population and therefore do not treat Brownian collisions.

Laminar and Turbulent collisions

In a laminar shear flow, two particles in different streamlines may collide and the corresponding collision frequency ${\beta_{ij}}^{lam}$ is expressed in Eq. 63.

$${\beta_{ij}}^{lam} = \frac{4}{3}\dot{\gamma}{d_{p,ij}}^3 \tag{63}$$

Where $\dot{\gamma} = \frac{du}{dx}$ and $d_{p,ij} = 0.5(d_{p,i} + d_{p,j})$ respectively represent the shear rate and the collision diameter. The collision diameter is defined as the shortest distance between the centers of the two particles in question.

However, the flow being turbulent in our case, the probability of turbulent collisions (Figure 37 (a)) is expected to be much higher in comparison to the potential collisions in a laminar flow. Thus the laminar collision kernel may be neglected with respect to the turbulent collision kernel.

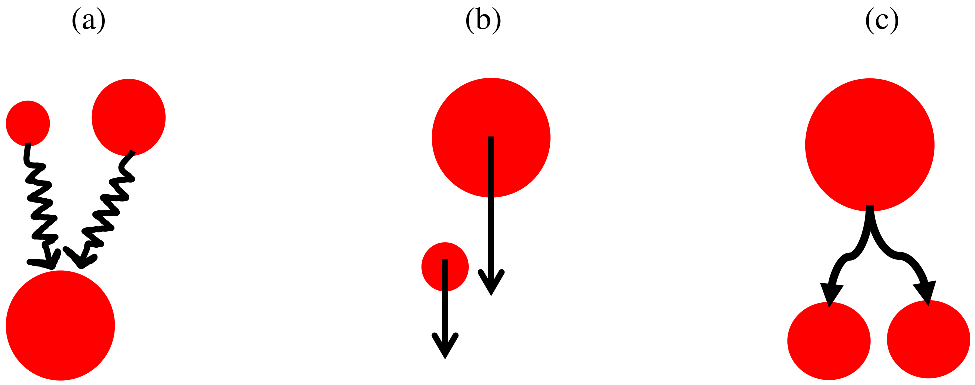

Figure 37: (a) Turbulent collisions, (b) Differential sedimentation collisions, (c) Break-up

Over the years, researchers have provided various ways of describing the turbulent collision kernels. Here, we cite three important models: Saffman and Turner (1956) [115] model for small non-inertial particles, Abrahamson (1975) [116] model for higher inertia particles and finally a more recent model by Zaichik et al. (2010) [117], which is not restricted to the particle size nor the Stokes number.

The Saffman and Turner model is valid for particles smaller than the Kolmogorov's length scale $d_p < \eta_k$, with very low-inertia particles $St_p \ll 1$. This basically assumes that the aggregation process takes place in the eddies in local shear flow conditions. The turbulent collision kernel ${\beta_{ij}}^t$ (Eq. 64) is a function of the shear rate $\left(\frac{\varepsilon}{\nu_f}\right)^{0,5}$ and the collision diameter $d_{p,ij}$, and is expressed similarly to the laminar kernel.

$$ {\beta_{ij}}^t = 1.3{d_{p,ij}}^3 \left(\frac{\varepsilon}{\nu_f}\right)^{0,5} \tag{64} $$

The Abrahamson model analyzes the case where the particle motion does not follow the fluid motion at all and is thus valid for high inertia particles. In other words, an infinite inertia case is treated, where a particle's velocity is completely uncorrelated from another particle's velocity as well as with the fluid. The calculation of the collision kernel is then similar to that found in the gas kinetic theory. The criterion which satisfies this is: ${d_{p,i}}^2 > \frac{15\mu_f \overline{{u'_f}^2}}{\rho_p \varepsilon}$, where $\overline{{u'_f}^2}$ is the mean squared velocity fluctuation of the fluid. The collision kernel is given by Eq. 65:

$$ {\beta_{ij}}^t = (8\pi)^{0,5}{d_{p,ij}}^2 \left(\overline{{u'_{p,\imath}}^2} + \overline{{u'_{p,\jmath}}^2}\right)^{0,5} \tag{65} $$

$\overline{{u'_{p,\iota}}^2}$ is the mean squared velocity fluctuation of particle of size i, which can be estimated from the mean squared fluid velocity fluctuation.

$$\overline{{u'_{p,\iota}}^2} = \frac{\overline{{u'_f}^2}}{1 + 1.5\frac{\tau_p \varepsilon}{\overline{{u'_f}^2}}} \tag{66}$$

The Zaichik et al. model is valid for all particle sizes (from particles of Kolmogorov length scale to much bigger size ~ integral scale).

$$\beta_{ij}{}^{t} = 4\sqrt{\pi} d_{p,ij}{}^{2}\, V_{ij}{}^{t} \tag{67}$$

$V_{ij}{}^{t}$ (in $\mathrm{m.s^{-1}}$) represents the total turbulent collision rate between two particles with sizes i and j (described in Annex 6). We have selected this model as it covers the entire range of particle sizes.

Gravitational collisions

As illustrated in Figure 37 (b), two particles with different sizes or relative densities (with respect to the fluid) sediment or float at different velocities. Therefore, a differential settling collision occurs when one particle sediments faster and catches up with the other one. The differential sedimentation collision kernel [108] is described in Eq. 68, considering Stokes sedimentation:

$$\beta_{ij}^{sed} = \frac{2\pi g}{9\mu_f}\left|\rho_f - \rho_P\right| \left|\left(\frac{d_{p,i}}{2}\right)^2 - \left(\frac{d_{p,j}}{2}\right)^2\right| d_{p,ij}{}^{2} \tag{68}$$

Fragmentation

The break-up of an aggregate (Figure 37 (c)) can occur thanks to the local flow conditions due to the shear stress exerted by the turbulent fluid flow. In Eq. 69, β_i^{frag} is the fragmentation kernel for a particle size i, similar to the expression provided by Soos et al. [118].

$$\beta_i^{frag} = \alpha^{frag}\left(\frac{\varepsilon}{\nu_f}\right)^{0,5}\left(\frac{d_{p,i}}{d_{p,0}}\right)^3 \tag{69}$$

The kernel is proportional to the turbulent flow shear rate, and is a cubic function of the dimensionless particle size. In this model, the aggregate is constituted of primary particles $d_{p,0}$ and when undergoing fragmentation, the aggregate cannot break-up into particles smaller than the primary particle size.

Various attributes of this phenomenon are still open to discussion, such as the strength of cohesion forces between two participating particles of the agglomerate [114], which in turn leads to the idea of the efficiency of the fragmentation process. The constant α^{frag} represents this efficiency which will depend on the type of inclusions under consideration and their corresponding mechanical resistance to a break-up. Another open discussion is the final result of the break-up. In our case, we assume that the breaking-up of a particle gives birth to two equal sized daughter particles [118].

2. Numerical modeling of inclusion behavior

This chapter first defines the Population Balance Equation (PBE), followed by its solution using numerical methods. Later we present the inclusion transport modeling as well as the modeling of the mesoscopic interactions among inclusions. Lastly we discuss some numerical implementation related details.

In the last chapter, we noted that the inclusion dynamics in literature was mostly modeled using the Lagrangian technique. This technique treats the particle as a single point with an individual particle velocity determined by the acting forces and as a result, calculates the trajectory for each particle. For highly dispersed particle phase, the continuous phase is first calculated followed by the particle trajectory calculation. However, for a large population of particles, this type of computation results in a very high calculation load. Furthermore, as our main aim is the macroscopic behavior of the system with a particular interest in determining the evolution of the internal properties of the inclusion population (not the individual inclusion dynamics), we turn our focus towards the Population Balance Method (PBM). The inclusion transport may be described using the Eulerian approach similar to the work performed by Bojarevics et al. [102]. The proposed Drift Concentration Model represents the transport of the inclusion number density akin to the transport of a scalar. Therefore, our inclusion behavior model combines the Drift Concentration Model with PBM. The above was performed by plugging in-house User Defined Functions (UDFs) to the ANSYS Fluent platform. MHD simulation provided results in the form of Lorentz force, mean velocity and turbulence fields which were then used while modeling the inclusion behavior in the bath.

A low inclusion concentration does not impact the bath hydrodynamics and hence a one-way numerical coupling method was selected. In our numerical model, we considered two broad categories of phenomena: (i) Inclusion transport, and, (ii) Inclusion interactions. An inclusion population may be transported due to the surrounding continuous phase characteristics. Hence the melt flow may drag the inclusions, or they might sediment or float due to the gravitational separation. Furthermore, in the current case of induction stirring, the inclusion population is also subjected to the electromagnetic migration. Additionally, in our model, inclusions may be captured at the interfaces due to sedimentation, electromagnetic migration and turbulent deposit. Meanwhile inclusion interactions are described through aggregation of inclusions due to collisions or fragmentation due to the flow shear.

2.1 Population Balance Equation

The population balance equation is a generalized transport equation of the number density of a particle population and accounts for various ways in which a population with a specific set of properties may appear or disappear [119]. The PBM treats both convective processes as well as the interactive processes, at the individual particle scale within the particle population setting.

In order to define the Population Balance Equation (PBE), we need to define some of the following variables. The internal property ξ of the inclusion characterizes the inherent traits of the inclusions such as the size or the composition of the inclusions (or even the age or a morphology parameter of an inclusion). The set of internal properties $(\xi_1, \xi_2, \ldots \xi_m)$ defining an inclusion population constitutes the internal coordinate domain Ω_ξ, while the factors influencing the evolution in the physical space x_i constitute the external coordinate system Ω_x. Therefore, the population may evolve in a maximum of $3 + 1 + m$ dimensions, corresponding to the physical space, the temporal space and m internal properties space.

We define the number density of inclusions $n(\xi,x,t)$ as the average number of particles with ξ properties at an instant t and located at a position x in the physical space. In Eq. 70, the total number of particles in the system would be given by the integral over the domains Ω_ξ and Ω_x.

$$N_T = \iint_{\Omega_\xi \Omega_x} n(\xi, \mathrm{x}, \mathrm{t}) \, \mathrm{d}V_\xi \mathrm{d}V_\mathrm{x} \tag{70}$$

The PBE in its continuous form [120] can be expressed in Eq. 71, whereby the evolution of the particle number density is a function of the evolution rate of the external coordinates $\dot{\chi}(\xi,\mathrm{x},,\mathrm{t})$ and the evolution rate of the properties of the particles $\dot{\xi}(\xi,\mathrm{x},\mathrm{t})$.

$$\frac{\partial n(\xi, \mathrm{x}, \mathrm{t})}{\partial t} + \mathrm{div}_\xi\big(n(\xi, \mathrm{x}, \mathrm{t})\dot{\xi}\big) + \mathrm{div}_\mathrm{x}(n(\xi, \mathrm{x}, \mathrm{t})\dot{\chi}) = \mathrm{H} = \mathrm{B} - \mathrm{D} \tag{71}$$

The evolution rate of the external coordinates describes the inclusion population transport which is governed by the instantaneous particle velocity $\boldsymbol{u_p}$. We only consider here the particle transport governed by the mean particle velocity $\overline{\boldsymbol{u}}_{\boldsymbol{p}}$ and do not take the inclusion transport (dispersion) due to turbulent diffusion into account. H represents the net (birth – death) new populations of particles (x, ξ) through mesoscopic inclusion interaction mechanisms or other source terms such as germination.

In our case, the primary internal coordinate, which defines the inclusion population and its evolution, is limited to the size of the inclusion [88]. $n(v_p)$ is a continuous univariate distribution most commonly called psd as particle size distribution (as illustrated in Figure 38), where v_p represents the inclusion volume.

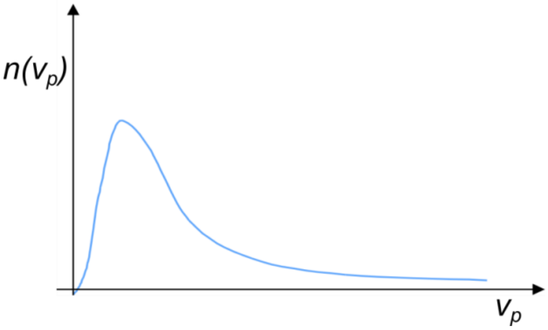

Figure 38: An example of a particle size distribution(psd)

Furthermore, we consider that the growth of inclusions through any mass transfer with the melt is negligible, removing the second term on the left of Eq. 71. This equation simplifies to a PBE with only particle volume v_p as the internal coordinate (Eq. 72).

$$\frac{\partial n(v_p)}{\partial t} + div(n(v_p)\bar{\boldsymbol{u}}_{\boldsymbol{p}}) = H \tag{72}$$

Thus the PBE describes how the populations of particles in the system evolves within the internal coordinate space (size) and their mean transport in the surrounding melt, while treating the rise of new populations of particles at the expense of the existing ones.

2.2 Numerical modeling of a Population Balance Equation

2.2.1 Class method

PBE may be solved using different numerical methods such as the Method of Moments (MOM) and the Class Method (CM). The method of moments consists in deriving the PBE equation (Eq. 72) into N_M transport equations of the N_M first moments of the psd n. These transport equations share the form of standard Eulerian equations and the method is amenable to implementation within the infrastructure of existing CFD codes. Variants of this method have been developed to improve the accuracy: Quadrature MOM [121] and Direct QMOM [122]. The Class Method is based on the discretization of the psd into M classes and the discretized PBE equation leads to a system of M transport equations which must be solved. Here, we only focus on the Fixed Pivot (FP) method, first proposed by Kumar and Ramkrishna [123], and then describe a variant of this method – Cell Average (CA) method proposed by Kumar et al. [124].

In conserving the total volume of the inclusion population in the system, the FP method [123] discretizes the complete range of the particle volume (and not diameter which is not conservative) into smaller intervals $[v_i, v_{i+1}]$ of pivot x_i, thereby meshing the internal coordinate space. This mesh may or may not be regularly spaced. As illustrated in Figure 39, the psd presented earlier is discretized using the volume intervals, described by a fixed pivot x_i and their bounds $v_i = \frac{x_{i-1}+x_i}{2}$.

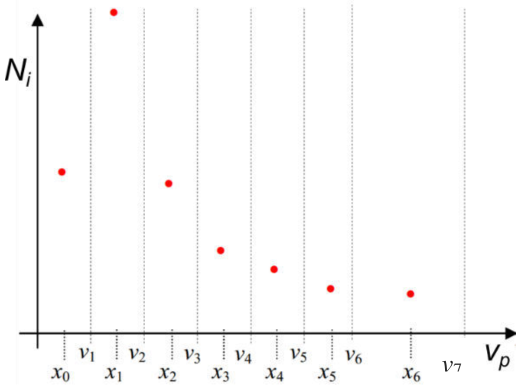

Figure 39: Discretization of the inclusion volume distribution into classes

The number density of inclusions N_i contained in each class i may then be written in Eq. 73 (number of inclusions of volume x_i per cubic meter of melt).

$$\forall i \in [1, M];\ N_i = \int_{v_i}^{v_{i+1}} n(v)\, dv;\ \ (N_i\ as\ \frac{\#\ of\ inclusions\ in\ class\ i}{m^3\ of\ Al\ bath}) \tag{73}$$

The PBE is integrated over each internal coordinate (size) class to give a coupled system of M non-homogenous transport equations. B_i is the net flux of inclusion population which has been given birth in the given class, while D_i accounts for the disappeared population flux from the class i.

$$\forall i \in [1, M];\ \frac{\partial N_i}{\partial t} + \frac{\partial}{\partial x_j}\left(N_i u_{p,i,j}\right) = H_i = B_i - D_i \tag{74}$$

2.2.2 Time splitting of PBE

An operator splitting technique [125] with respect to the time step is used for solving Eq. 74. This splitting decouples the non-homogenous partial differential equations and thereby allows us to separately treat the transport and the interactions of the inclusion population. It also provides the freedom in choosing the best numerical scheme for each type of problem.

$$\forall i \in [1, M];\ \frac{\partial N_i}{\partial t} + \frac{\partial}{\partial x_j}\left(N_i u_{p,i,j}\right) = 0 \tag{75}$$

$$\frac{\partial N_i}{\partial t} = H_i \tag{76}$$

At each time step, the decoupled homogenous system of equations 68 and 69 is solved in the following two steps. The first step (Eq. 77) comprises solving the left member, i.e. the convective transport of the inclusion population in each class N_i (max. M equations). This was performed by the in-built function DEFINE_UDS_FLUX of the ANSYS Fluent software as detailed in section B.2.3.2. This is followed by the second step (Eq. 78), which is concerned with the right member corresponding to the inclusion interactions in each class (net birth or death of inclusion populations by aggregation and fragmentation), while using the updated inclusion populations $N_i(t^*)$. This step was implemented at the end of step 1 using the function DEFINE_EXECUTE_AT_END of the ANSYS Fluent software. The entire time splitting operation is presented in Figure 40, where before time marching, a global mass balance verification is also performed.

$$\forall i \in [1, M];\ N_i(t^*) = N_i(t) - \frac{\partial}{\partial x_j}\left(N_i(t) u_{p,i,j}\right)\Delta t \tag{77}$$

$$N_i(t + \Delta t) = N_i(t^*) + H_i \Delta t \tag{78}$$

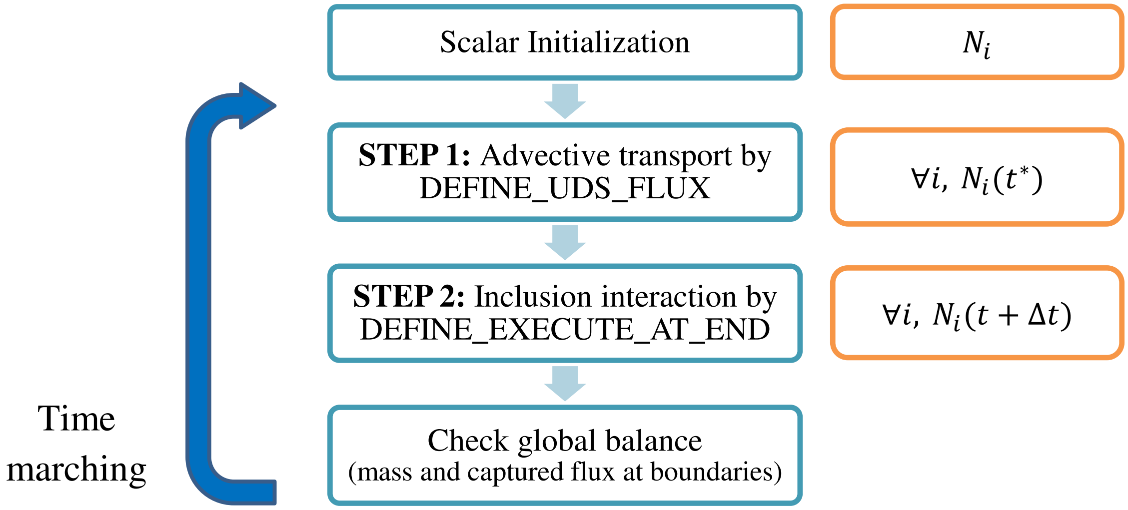

Figure 40: Numerical implementation of the model using time splitting technique

2.3 Transport of inclusions

2.3.1 Drift Concentration Method

The DCM [102] [104] describes the inclusion transport while assuming that the number density N_i is a continuous intensive variable of the inclusion phase. According to their pivot size x_i, the inclusion population of class i is transported with the inclusion mean velocity $\boldsymbol{u}_{p,i}$ calculated using the balance of forces in Eq. 79 – Eq. 81. The inclusions are supposed to have attained locally their terminal velocity with no further acceleration.

$$\forall i \in [1, M]; \sum \boldsymbol{F}_{p,i} = 0 \tag{79}$$

The involved forces (drag $\boldsymbol{F}_{p,i}^{D}$, buoyancy $\boldsymbol{F}_{p,i}^{B}$ and electromagnetic $\boldsymbol{F}_{p,i}^{em}$) acting on an inclusion were described in section B.1.3.1.

$$\boldsymbol{F}_{p,i}^{D} + \boldsymbol{F}_{p,i}^{B} + \boldsymbol{F}_{p,i}^{em} = 0 \tag{80}$$

$$\frac{\pi {d_{p,i}}^{3}}{6}\boldsymbol{g}(\rho_p - \rho_f) - \frac{1}{2}\rho_f C_D \frac{\pi {d_{p,i}}^{2}}{4}\left|\bar{\boldsymbol{u}}_{\boldsymbol{f}} - \boldsymbol{u}_{p,i}\right|(\boldsymbol{u}_{p,i} - \bar{\boldsymbol{u}}_{\boldsymbol{f}}) - \frac{3}{4}\frac{\pi {d_{p,i}}^{3}}{6}\boldsymbol{F}_{Lorentz} = \boldsymbol{0} \tag{81}$$

In Eq. 82 we obtain the particle drift velocity as the sum of the sedimentation velocity $\boldsymbol{u}_{sed,i}$ and the electromagnetic migration velocity $\boldsymbol{u}_{em,i}$.

$$\boldsymbol{u}_{p,i} - \bar{\boldsymbol{u}}_{\boldsymbol{f}} = \boldsymbol{u}_{sed,i} + \boldsymbol{u}_{em,i} = \frac{{d_{p,i}}^{2}}{18\mu_f}(\rho_P - \rho_f)\boldsymbol{g} - \frac{{d_{p,i}}^{2}}{24\mu_f}\boldsymbol{F}_{Lorentz} \tag{82}$$

Where $\bar{\boldsymbol{u}}_{\boldsymbol{f}}$ represents the mean melt velocity vector. By substituting the above expression in Eq. 75, we obtain Eq. 83.

$$\forall i \in [1, M]; \frac{\partial N_i}{\partial t} + \frac{\partial}{\partial x_j}\left(N_i(\bar{u}_{f,j} + u_{sed,i,j} + u_{em,i,j})\right) = 0 \tag{83}$$

2.3.2 Numerical treatment of inclusion transport using ANSYS Fluent and UDF

The above system of equations was solved using ANSYS Fluent, where the inclusion population in each class was defined as a scalar (User Defined Scalar – UDS), applicable only to the melt phase. In default mode, ANSYS Fluent solves the following transport equation (Eq. 84) for M scalars $\varphi_{l,k}$ defined for a given phase (for example phase *l* of a mixture).

$$\frac{\partial \alpha_l \rho_f \varphi_{l,k}}{\partial t} + div\left(\alpha_l \rho_f \varphi_{l,k} \boldsymbol{u}_{\boldsymbol{f}} - \alpha_l \Gamma_{l,k}\, grad(\varphi_{l,k})\right) = S_{l,k} \;\; ; k = 1, \ldots., M \tag{84}$$

Where α_l, ρ_f, $\boldsymbol{u}_{\boldsymbol{f}}$, $\Gamma_{l,k}$ and $S_{l,k}$ respectively correspond to the volume fraction, the density and the velocity of the metal, the diffusion coefficient and the source term of the scalar (which in this case is the liquid phase). Eq. 84 is similar to the inclusion transport equation (Eq. 83), with an altered convective term and zero diffusion coefficient. Therefore, in order to simulate Eq. 83 within ANSYS Fluent, a variable substitution is required, where the calculated scalar φ_i is defined as the number of inclusions in class *i* per kg of bath.

$$\varphi_i = \frac{N_i}{\alpha_l \rho_f}; \;\; (\varphi_i \; as \frac{\#\, of\ inclusions\ in\ class\ i}{kg\ of\ Al\ bath}) \tag{85}$$

Each scalar is initialized throughout the entire domain corresponding to aluminum bath, delimited by the crucible walls and the bath free surface. Taking the variable substitution into account, Eq. 83 may now be rewritten as described in Eq. 86.

$$\forall i \in [1, M]; \frac{\partial \alpha_l \rho_f \varphi_i}{\partial t} + \frac{\partial}{\partial x_j}\left(\alpha_l \rho_f \varphi_i (\bar{u}_{f,j} + u_{sed,ij} + u_{em,ij}\right) = 0 \tag{86}$$

Using the Green-Ostrogradsky theorem, the convective term in Eq. 86 is transformed to Eq. 87, where the integral over the control volume V_{cell} is written as the net flux across the cell faces.

$$\iiint_{Vcell} div\left(\alpha_l \rho_f \varphi_i \boldsymbol{u_{p,i}}\right) dV_c = \iint_{\Sigma} \varphi_i \, \alpha_l \rho_f \boldsymbol{u_{p,i}} \cdot \boldsymbol{dS} \tag{87}$$

The calculation of the net flux term was partly performed by a UDF plugged in to ANSYS Fluent. The UDF uses a specialized in-built function DEFINE_UDS_FLUX, whereby, for a given cell face inside the calculation domain, the face flux term $\alpha_l \rho_f \boldsymbol{u_{p,i}} \cdot \boldsymbol{dS}$ (in kg.s^{-1}) is calculated and fed to ANSYS Fluent. There onwards, using this face flux term, Fluent performs the remaining task of advecting the inclusion population.

At a given cell face of the domain, the calculation of the face flux term involves retrieving the velocity components from adjacent cell centers (c0 and c1), corresponding to each phenomenon (melt flow, sedimentation and electromagnetic migration). The face velocity is then calculated by averaging the values at the two cell centers to obtain a net face velocity vector. Finally, the UDF calculates the scalar product of the velocity vector with the surface normal vector, resulting in the face flux term. The technique is presented in Figure 41 (a).

At the domain boundaries, i.e. the bath free surface and the crucible walls, the face flux term is calculated by using the adjacent cell center velocity (u_{c0}). As illustrated in Figure 41 (b), if the face flux is directed outwards with respect to the domain boundary, then the inclusion populations were eliminated across the boundary. These populations were hence considered as *captured* due to sedimentation, electromagnetic migration or turbulent deposit. In reality, the fate of the inclusion populations once they are captured at the boundaries is unknown. However, in this dissertation, we consider them to be completely captured and removed from the domain and thus there is no release of inclusions.

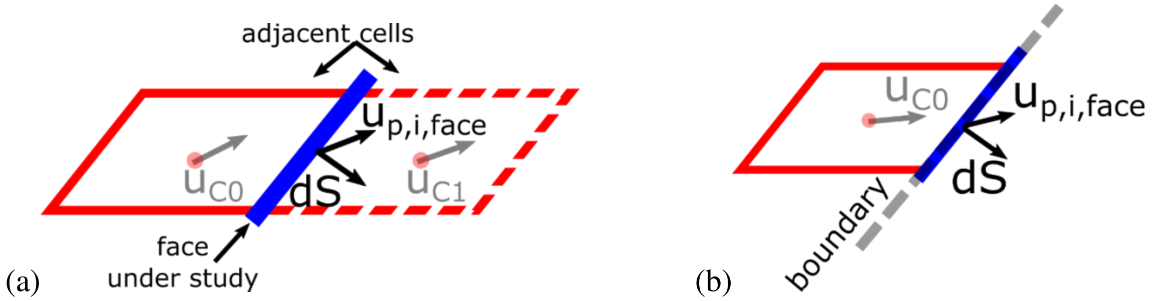

Figure 41: (a) Flux at a cell face in the bulk, (b) face flux at a boundary

The use of this UDF allows a much faster calculation as the transport term is partially calculated by Fluent. Additionally, contrary to an explicit scheme which may require very small time steps to ensure numerical stability, the implicit nature of the calculation offers numerical stability with reasonably large time steps.

2.4 Mesoscopic interactions

The inclusion interactions in our case are the combination of aggregation due to the efficient collisions between two particles and the fragmentation of the aggregates into two daughter inclusions of equal size. Eq. 76 may now be expressed as a sum of these two phenomena.

$$\forall i \in [1, M]; \frac{\partial N_i}{\partial t} = H_i = H_i^{agg} + H_i^{frag} \tag{88}$$

2.4.1 Aggregation

Smoluchowski [126] first gave the expression of H_i^{agg}, where the total birth B_i^a in a class $[v_i, v_{i+1}]$ subtracted by the total death D_i^a is expressed in its continuous form (Eq. 89).

$$\begin{aligned} H_i^{agg} &= \overbrace{\frac{1}{2}\int_{v_i}^{v_{i+1}} dv \int_0^{v} \beta^{agg}(v', v-v')n(v',t)n(v-v',t)dv'}^{B_i^a} \\ &\quad \underbrace{- \int_{v_i}^{v_{i+1}} n(v,t)dv \int_0^{\infty} \beta^{agg}(v',v)n(v',t)dv'}_{D_i^a} \end{aligned} \tag{89}$$

The integral concerning the death term is easily obtained as described in Eq. 90.

$$D_i^a = N_i \sum_{k=1}^{M} \beta_{ik}^{agg} N_k \tag{90}$$

The calculation of the birth term is trickier and requires the use of specific modeling techniques described in the following paragraphs. While calculating the birth term using the FP technique, the net flux of new inclusion population (characterized by the particle size v) within the size range of $[x_{i-1}, x_i\ ]$ is assigned to the nearby pivots and therefore both i^{th} and $(i-1)^{\text{th}}$ cells. These parts can be defined as a and b, where volume conservation dictates that $ax_{i-1} + bx_i = v$. Figure 42 (a) aptly illustrates this assignment of particle population flux (of size v) for the FP technique. It was noted in the literature that the FP technique gives rise to numerical diffusion [124] (over or under estimation of particle size distributions), when the number densities decrease very sharply (for example, if the distribution follows an exponential form). In order to reduce this numerical diffusion, Kumar et al. [124] have proposed the CA method, which is a slight variant of the FP technique. The CA technique improves the overall calculation accuracy by concentrating the newborn particle fluxes temporarily at the average mean volume.

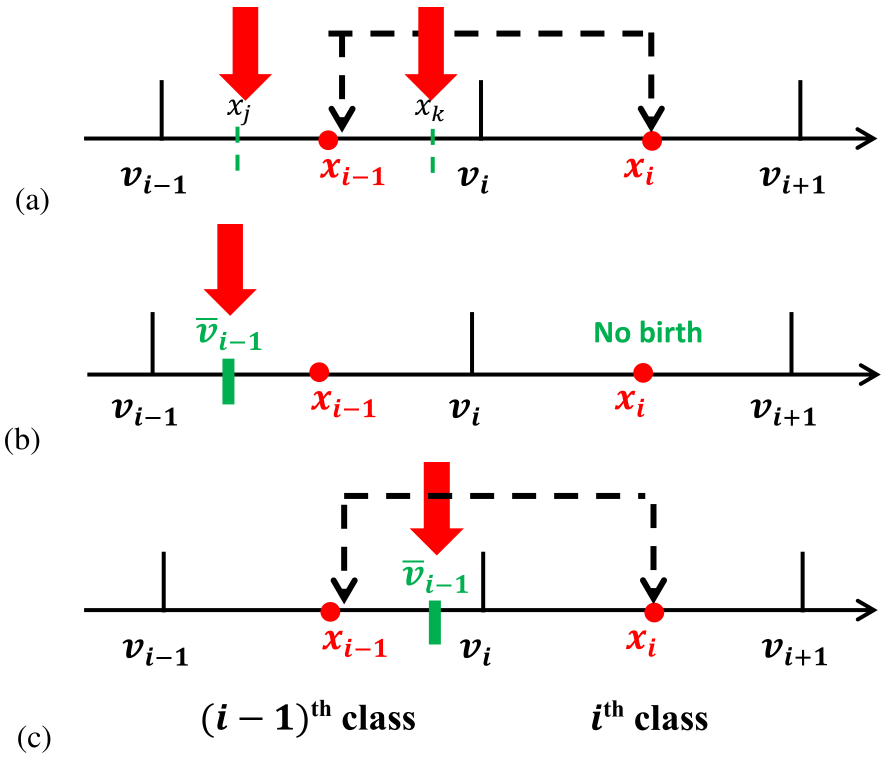

Figure 42: Assignment of particle flux (a) Fixed Pivot, (b, c) Cell Average techniques [124]

This is followed in the second step by a distribution of these particles to the neighboring pivots. For example, the average volume of the new particles born in (i-1) class due to the collisions between inclusion populations of sizes x_j and x_k is noted in Eq. 91.

$$\bar{v}_{i-1} = 0.5(x_j + x_k) \tag{91}$$

The contribution of birth in the nearby pivots will now differ and depend on the relative positioning of the average volume within the class interval. (i) if $v_{i-1} < \bar{v}_{i-1} < x_{i-1}$, then there will be no birth flux at the x_i pivot (Figure 42 (b)). (ii) if $x_{i-1} < \bar{v}_{i-1} < v_i$, then contributions will be distributed to both classes (Figure 42 (c)).

Coming back to the aggregation term in Eq. 89, using the CA technique, the birth contribution B_i^{agg}assigned to each class is described in terms of the collision kernel and the number densities participating in the binary collisions $j - k$ (Eq. 92). The total aggregate volume V_i^{agg} feeding the cell *i* is calculated by summing all the volume contributions of these binary collisions (Eq. 93). The average volume $\bar{v}_i$ of all newborn particles in the cell *i* is given by Eq. 93.

$$B_i^{agg} = \sum_{\substack{j,k \\ v_i \le (x_j + x_k) \le v_{i+1}}}^{j \ge k} \left(1 - \frac{1}{2}\delta_{j,k}\right) \beta_{jk}^{agg} N_j N_k \ \ (in\ \#.m^{-3}.s^{-1}) \tag{92}$$

$$\begin{gathered} V_i^{agg} = \sum_{\substack{j,k \\ v_i \le (x_j + x_k) \le v_{i+1}}}^{j \ge k} \left(1 - \frac{1}{2}\delta_{j,k}\right) \beta_{jk}^{agg} N_j N_k (x_j + x_k) \\ \bar{v}_i = V_i^{agg} / B_i^{agg} \end{gathered} \tag{93}$$

Finally, in Eq. 94, we express the birth due to aggregation term B_i^a as a function of the birth contributions at the neighboring pivots, the Heaviside step function $H(x)$ and the distribution function $\lambda_i^{\pm}(x)$.

$$\begin{aligned} B_i^a = {} & B_{i-1}^{agg} \lambda_i^- (\bar{v}_{i-1}) H(\bar{v}_{i-1} - x_{i-1}) \\ & + B_i^{agg} \lambda_i^- (\bar{v}_i) H(x_i - \bar{v}_i) \\ & + B_i^{agg} \lambda_i^+ (\bar{v}_i) H(\bar{v}_i - x_i) \\ & + B_{i+1}^{agg} \lambda_i^+ (\bar{v}_{i+1}) H(x_{i+1} - \bar{v}_{i+1}) \end{aligned} \tag{94}$$

$$H(x) = \begin{cases} 1; if\ x > 0 \\ 0.5; if\ x = 0; \\ 0; if\ x < 0 \end{cases} \lambda_i^{\pm}(x) = \frac{x - x_{i\pm1}}{x_i - x_{i\pm1}}$$

2.4.2 Fragmentation

The net birth due to fragmentation of inclusions may be written similarly to the aggregation term, where the first member B_i^f corresponds to the birth of new fragmented aggregates while the second corresponds D_i^f to the death of aggregates due to fragmentation.

$$H_i^{frag} = 2\underbrace{\int_{v_i}^{v_{i+1}} dv \int_0^{\infty} \beta^{frag}(v')n(v')\delta(v - \frac{v'}{2})dv'}_{B_i^f} - \underbrace{\int_{v_i}^{v_{i+1}} \beta^{frag}(v)n(v)dv}_{D_i^f} \quad (95)$$

In this expression, we suppose that the fragmentation of a particle gives birth to two identical particles. Moreover, a threshold diameter ($d_{p,c}$) was selected, beyond which the fragmentation of a particle in a given class is possible. This was performed by modifying the collision kernel whereby the efficiency of the fragmentation phenomena is zero if the inclusion size is below the threshold size (Eq. 96). The term representing the death of particles in a particular class is easily obtained and depends solely on the particle concentration of that class and the corresponding fragmentation kernel in Eq. 97.

$$\beta_i^{frag} = \begin{cases} 0; if\ d_{p,i} < d_{p,c} \\ \alpha^{frag}\left(\frac{\varepsilon}{\nu_f}\right)^{0,5}\left(\frac{d_{p,i}}{d_{p,c}}\right)^3; d_{p,i} \geq d_{p,c} \end{cases} \quad (96)$$

$$D_i^f = \beta_i^{frag} N_i \quad (97)$$

Concerning the birth term B_i^f, the same Cell Average algorithm is applied, which comprises three steps: (i) calculation of the net birth rate B_i^{frag} of the inclusion population in a class, which is a function of the fragmentation kernel and the population concentration in the participating classes (Eq. 98), (ii) calculation of the total net volume flux V_i^{frag} and the average volume of the newborn particle population $\bar{v}_i^{frag}$ (Eq. 99), and (iii) redistribution into the classes $(i-1, i, i+1)$ using the operators $\lambda_i^{\pm}(x)$ and the Heaviside function $H(x)$ (Eq. 100).

$$B_i^{frag} = 2\sum_{k=i}^{M} \beta_k^{frag} N_k \quad (98)$$

$$V_i^{frag} = 2\sum_{k=i}^{M} \beta_k^{frag} N_k \frac{x_k}{2} \quad (99)$$

$$
\begin{aligned}
\bar{v}_i^{frag} &= V_i^{frag}/B_i^{frag} \\
B_i^f &= B_{i-1}^{frag}\lambda_i^-\left(\bar{v}_{i-1}^{frag}\right)H\left(\bar{v}_{i-1}^{frag}-x_{i-1}\right) \\
&+B_i^{frag}\lambda_i^-\left(\bar{v}_i^{frag}\right)H\left(x_i-\bar{v}_i^{frag}\right) \\
&+B_i^{frag}\lambda_i^+\left(\bar{v}_i^{frag}\right)H\left(\bar{v}_i^{frag}-x_i\right) \\
&+B_{i+1}^{frag}\lambda_i^+\left(\bar{v}_{i+1}^{frag}\right)H\left(x_{i+1}-\bar{v}_{i+1}^{frag}\right)
\end{aligned} \tag{100}
$$

$$
H(x)=\begin{cases}1; if\ x>0\\ 0.5; if\ x=0\\ 0; if\ x<0\end{cases}\ ;\ \lambda_i^{\pm}(x)=\frac{x-x_{i\pm1}}{x_i-x_{i\pm1}}
$$

2.5 Global balance

As depicted in Figure 40, before time marching, a global mass balance of the inclusion phase was performed for verifying the calculation. For each class, the captured flux due to sedimentation at the crucible base ($\rho_p > \rho_f$) or bath free surface ($\rho_p < \rho_f$), is a sum of face fluxes across all faces on the boundary and is expressed in Eq. 101. Similarly, the captured flux due to EM migration at a boundary is given by the expression in Eq. 102. The total flux due to EM migration for each class is a sum of the fluxes due to migration across each boundary: $\Phi_{em,i} = \Phi_{em,bot,i} + \Phi_{em,side,i} + \Phi_{em,free,i}$.

$$
\forall i \in [1,M];\ \ \Phi_{sed,i} = \sum_{face}(\alpha_l\rho_f\varphi_i)u_{sed,i}Sx_i\rho_p\,;(in\ kg\ of\ inclusions.s^{-1}) \tag{101}
$$

$$
\forall i \in [1,M]; \forall j \in \{walls, free\ surface\}; \Phi_{em,j,i} = \sum_{face,j}(\alpha_l\rho_f\varphi_i)u_{em,i}S_jx_i\rho_p \tag{102}
$$

A global mass balance verification can be performed at the end of each time step, before time marching, as expressed in Eq. 103.

$$
\frac{dm}{dt} = \frac{m(t)-m(0)}{\Delta t} = \sum_{i=1}^{M}\Phi_{em,i} + \Phi_{sed,i} \tag{103}
$$

2.6 Conclusion

With the aim of modeling both transport of inclusions within the bath and mesoscopic interactions between inclusions (aggregation and fragmentation mechanisms) a PBM has been adopted. The class method was used to discretize the PBE into classes defined by the inclusion size. At the inclusion scale, the application of the fundamental dynamic equation led to the expression of the particle terminal velocity, and was used in the Drift Concentration Method for describing advection of the inclusion population. The redistribution of inclusions into classes as a result of interactions was expressed using the Cell Average method. Furthermore, the time splitting technique was applied to separate the transport and the interaction members of the PBE. Figure 43 summarizes the general flowchart of our inclusion behavior model.

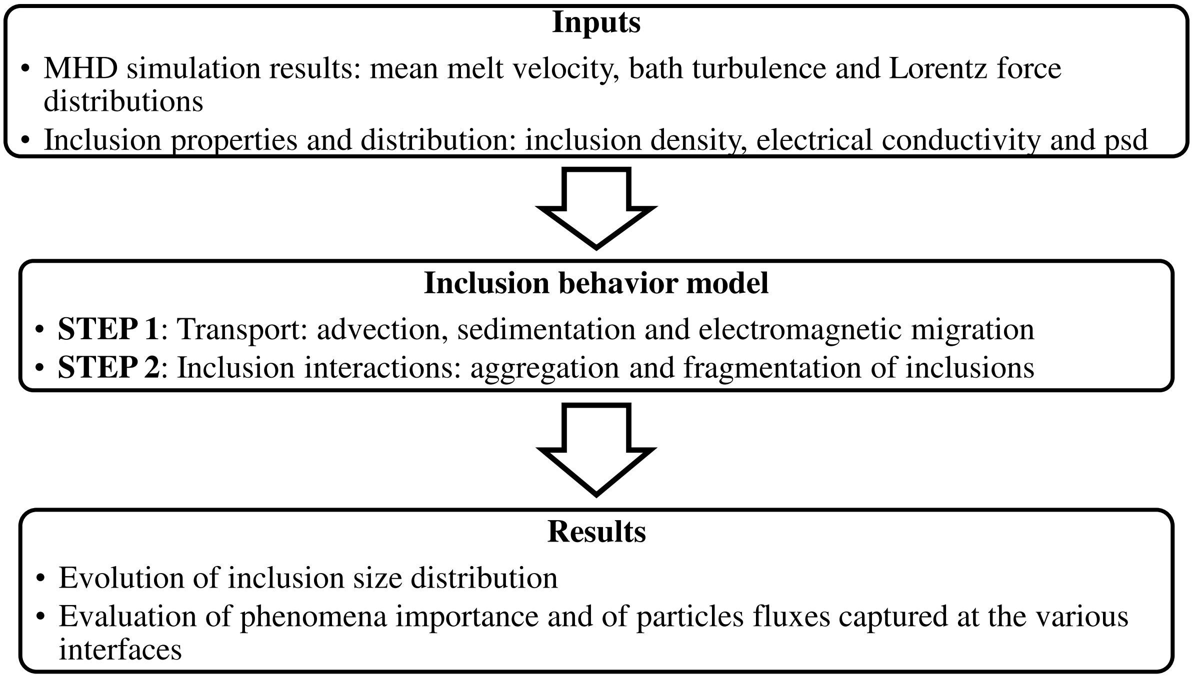

Figure 43: General outlay of the inclusion behavior model, TABInc2D

The complete inclusion behavior model was named TABInc2D (as Transport, Aggregation and Breakage of Inclusion in 2D) and uses extensive UDFs which were implemented along with the ANSYS Fluent code. The TABInc2D model follows the MHD model to predict the inclusion behavior in an induction stirred aluminum bath. The MHD simulation results in the form of mean velocity, turbulence and Lorentz force fields are provided to the inclusion model as input data. In addition to the MHD results, the type and distribution of the inclusion population are also required as numerical model input parameters.

Part C: Application

This chapter presents the application of the numerical tools described in Part A and Part B. First, we present the results obtained on a laboratory scale IMF and then, focus on an industrial scale IMF. Figure 44 illustrates the general outlay of the previously described MHD and inclusion behavior modeling tools.

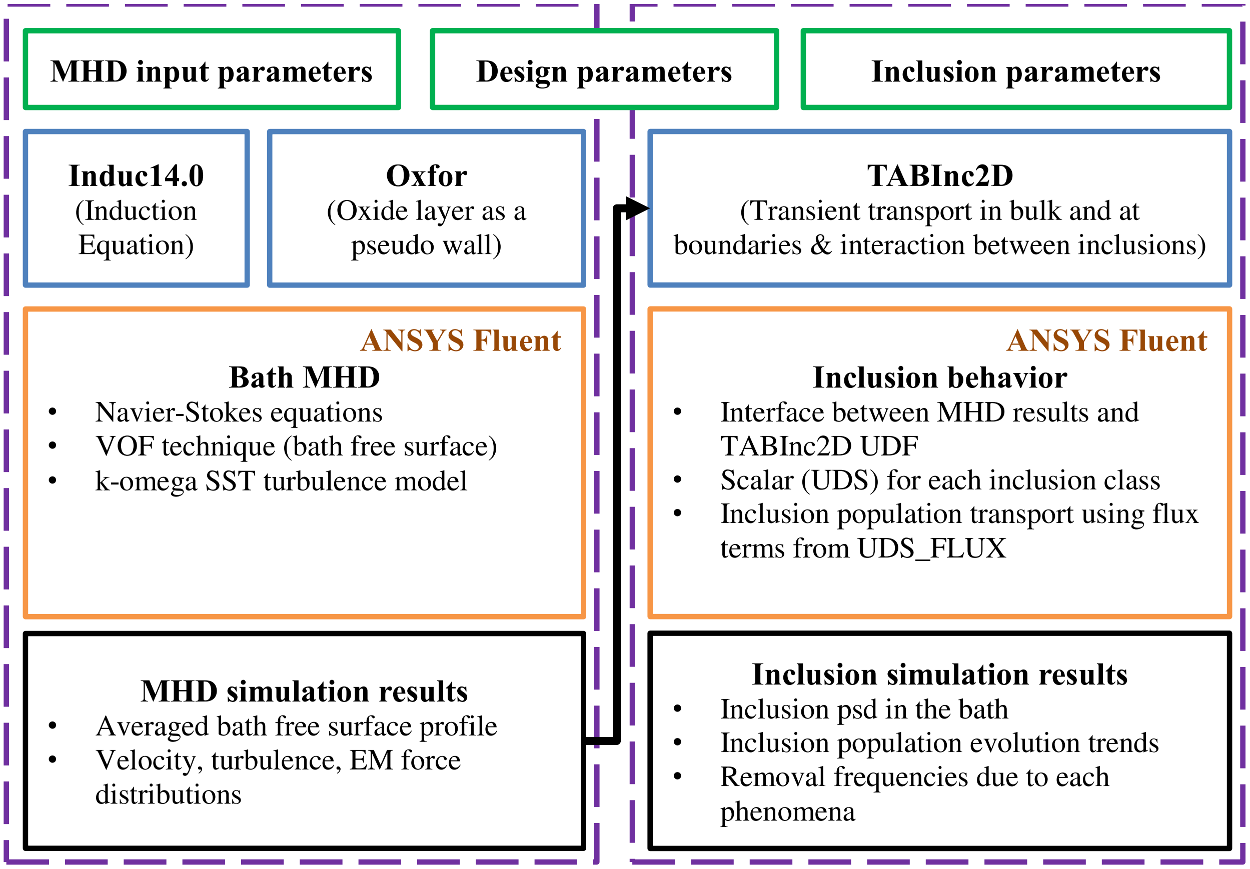

Figure 44: General outlay of the modeling tools

1. Application on a laboratory scale IMF

In this chapter, we present the results of the experimental campaign as well as the corresponding numerical simulation results performed on a laboratory scale IMF at IJL. After briefly presenting the measurement of the operating parameters, we will focus on the free surface deformation measurements. This is followed by the simulation results and a discussion.

1.1 Experimental measurements

Table 11 summarizes the details of all the laboratory scale experiments performed over the course of the project. Experiments 1 and 2 were devoted to the measurement of the magnetic field strength, which were performed in an empty crucible. The deformation of the free surface of the metal bath was investigated using either laser telemetry or structured light techniques.

Table 11: Experimental campaign details

Experiment n°	**Alloy**	**Measurement**	**Metal filling (%)**	**Generator power (kW)**
1a	-	Magnetic field	0	5
1b				5
2				10
3	Al-1050	Free surface deformation using telemetry	75	20
4		Free surface deformation using the structured light technique (and observation of the oxide layer fragmentation)	28	10
5			60	10
6				15
7				20
8			75	10
9				15
10				20
11	Al-5182		75	10
12				15
13				20
14	Al-7050	Observation of oxide layer	50	0 to 20
15	Al-5182		75	

Primarily, alloy Al-1050 (Annex 1) was used for these experiments (Experiments 3 to 10). Another aluminum alloy Al-Mg (Al-5182), with a high magnesium content was also used during the campaign (Experiments 11 to 13). Liquid metal filling level and generator power were varied to understand the effects of operating parameters on the free surface deformation. During Experiments 3 to 13, besides the free surface deformation measurements, parallel observations were also made regarding the possible fragmentation of the oxide layer. This latter point was also studied in more detail in a separate set of experiments (Experiments 14 – 15). Although we did not observe any fragmentation in the laboratory scale furnace, we present, in Annex 7, some of the obtained results.

1.1.1 Operating parameters

The liquid metal filling inside the crucible

Figure 45 illustrates the three filling levels inside the crucible. It is notable that the 28 % filling level is the closest to the symmetry plane of the inductor, followed by the 60 % level. The three levels correspond to 66 mm, 131 mm and 157 mm of filling with respect to the crucible bottom at z = 0 mm.

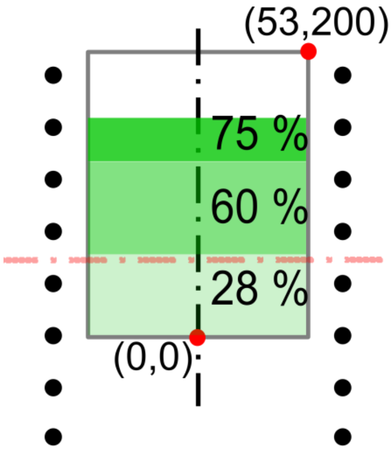

Figure 45: Liquid metal filling levels (r and z coordinates in mm)

The electrical parameters of the setup

The current intensity in the inductor was measured using the Rogowski's coil described in Section A.2.1.4.1 for which the results are tabulated later in Table 12. The current frequency was kept constant and equal to 3500 Hz. Meanwhile the strength of the axial magnetic field was measured using a Hall's effect Gaussmeter (Section A.2.1.4.2). This was performed along the symmetry axis of the inductor in absence of metal.

Figure 46 illustrates the centerline profile of the axial magnetic field strength measured for Experiments 1a and 1b (I = 990 A). A bell shape profile is observed with a maximum reached near the inductor's mid-plane. For each point of measurement, a relative deviation of around 4 mT was registered during the recording which lasted 4 to 5 seconds. To show reproducibility of the measurement, a second series was performed under same operating conditions. The two measured centerline profiles were found to be almost identical with similar relative deviations. These measured profiles will be compared later in Section C.0 with the predictions of the numerical model developed within the project.

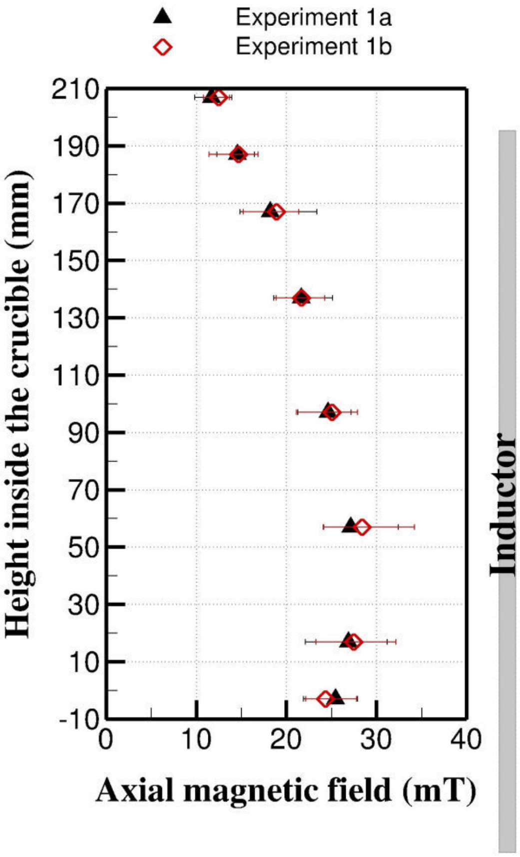

Figure 46: Measured axial magnetic field – Experiments 1a and 1b

1.1.2 Free surface deformation measurements by structured light technique

Free surface deformation was initially measured using laser telemetry (Annex 8). At a given instant, this non-intrusive technique allowed a rapid evaluation of the height of a single point of the free surface dome. Even though laser telemetry is a relatively easy to handle and cost effective technique, its application was limited by the thermal constraints. Moreover, this technique was not appropriate to perform any temporal evolution study of the dome. This led us to select the structured light technique which was not subjected to these limitations, while allowing access to a larger % of the free surface.

The structured light setup (described in Section A.2.2.2) was mounted on an optical bench support (Figure 47), which provided a degree of freedom along the z-axis for unidirectional translation of the complete setup. The optical system was calibrated to be 800 mm away from the reference plane at z = 0 mm. Around 100 mm of deformation along the z-axis, with respect to the reference plane could be measured.

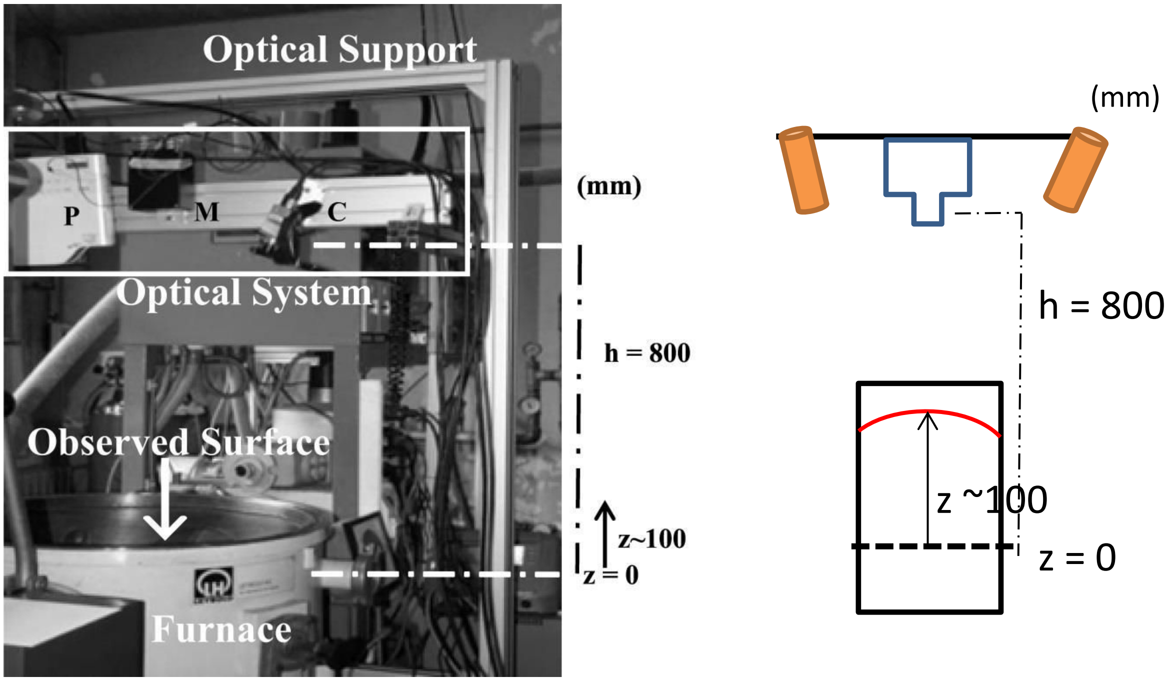

Figure 47: IJL IMF with mounted optical system (P: Projector, M: Modulator, C: Camera)

For the structured light campaign, the experimental operating parameters presented in Table 11– (Experiments 4 to 13) are completed in Table 12 by the measured current intensity.

Table 12: Structured light campaign operating parameters

Experiment n°	Alloy	Metal filling (%)	Generator power (kW)	Current intensity (A)*
4	Al-1050	28	10	1316
5		60	10	1278
6			15	1532
7			20	1756
8		75	10	1215
9			15	1507
10			20	1750
11	Al-5182	75	10	1217
12			15	1476
13			20	1700

(*±1% current intensity)

From raw images to relative height contours

Figure 48 presents an example of the grayscale raw image and the corresponding processed image of the deformed free surface recorded during Experiment 9. The processed image shows the 2D contours of the relative height of the image pixels as given by the software Fringe Analysis 4 [70].

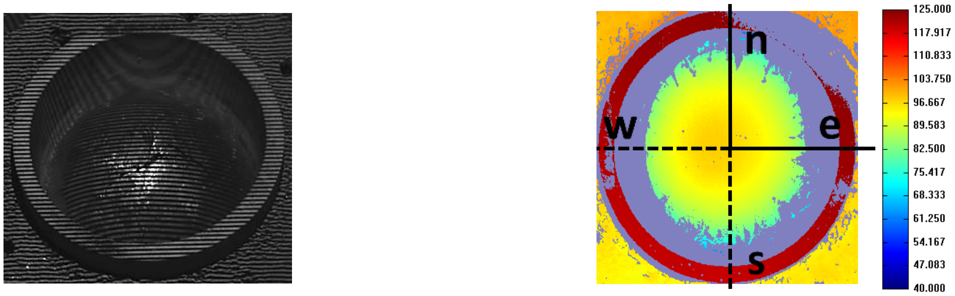

Figure 48: Raw and processed images of the deformed surface for Experiment 9

The structured light band projection is noted on the raw image. The processed image shows three major zones: (i) the red colored band, which reveals the crucible wall top, (ii) the central yellow-green disc, which represents the deformed free surface, and, (iii) the grey circle, which corresponds to the shadow of the crucible wall. No information for the near wall area is available since the reflected light and therefore fringe patterns were hidden by the walls (shadowed zone). Nevertheless, over the complete free surface, more than 60% was measured.

Axisymmetric shape of the dome

We now focus on the study of four sections (north, south, east and west) of the free surface profile. Figure 49 illustrates the south (**s**) cross-section of the free surface dome extracted from Figure 48.

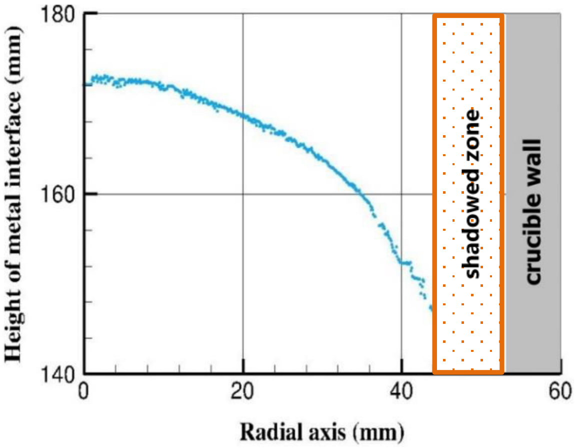

Figure 49: South cross-section of the deformed surface – Experiment 9

For such a small crucible (height of 200 mm), a very large deformation amplitude of almost 30 mm is observed in the figure. The high resolution (±0.1mm) of the captured images allows measurement of the miniscule height variations, indicating a slightly rough surface.

The other three cross-sections of the free surface are superimposed in Figure 50. Locally, we observe a near perfect coincidence of these cross-sections near the axis, while a slight difference among the cross-sections exists as we move towards the crucible wall (markedly beyond 30 mm of the radial axis). Nevertheless, an overall similarity is observed, thus establishing the quasi-axisymmetric shape of the dome.

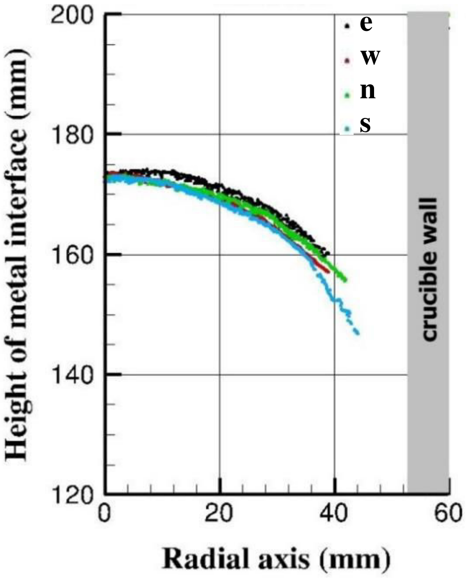

Figure 50: Interface height of the four radial sections – Experiment 9

Temporal fluctuations of the dome

The sequential hybrid method was used to follow the temporal fluctuations of the free surface at a low frequency of 0.03 Hz. Figure 51 represents the temporal evolution during 180 seconds of the vertical displacement (relative to the initial deformation) of four different points on the free surface during Experiment 9. The displacements vary between +2 mm and –0.5 mm. Even though this technique is quite accurate (±0.1mm), the low sampling frequency of 6 to 8 measurements is insufficient to establish any trend of the deformation fluctuations.

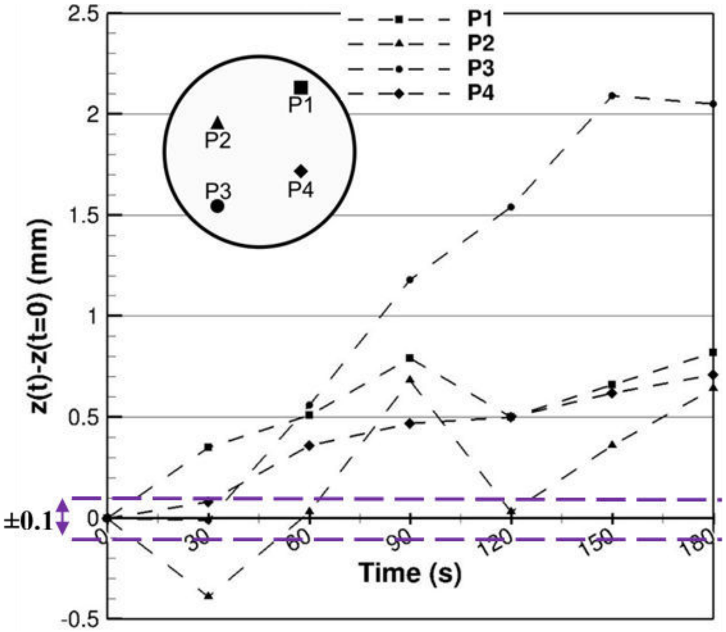

Figure 51: Relative temporal evolution (with t=0 as reference values) of the vertical displacement of four different points on the free surface extracted from data obtained using phase shift technique – Experiment 9

On the other hand, the results obtained from the single shot method (using only one camera) allow a temporal fluctuation study at a higher frequency of 1 Hz. Figure 53 presents the temporal evolution during 10 s of the vertical displacement of eight different points in Figure 52 of the free surface.

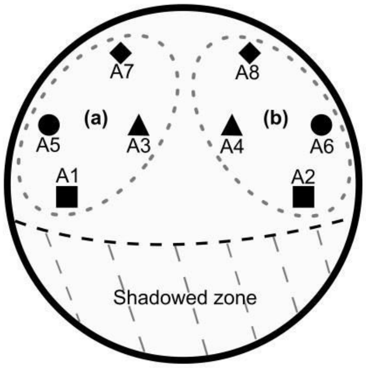

Figure 52: Positions on free surface – Experiment 9

The displacement values vary this time between ±1 mm. Since the fluctuations are within the precision range (±1 mm) of the technique, drawing any conclusions regarding the temporal fluctuation of the free surface is impossible.

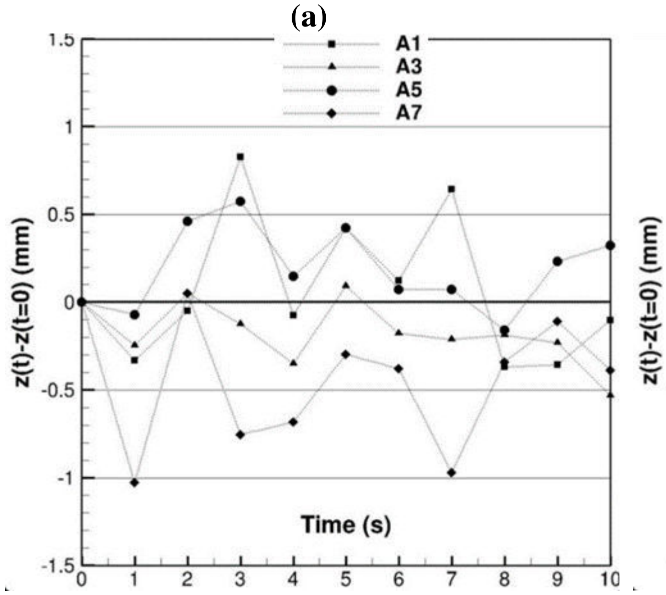

Figure 53: Relative temporal evolution of eight different positions using single shot technique – Experiment 9

Average dome

Figure 54 illustrates a spatially averaged dome profile obtained by averaging the four sections presented in Figure 50. Note that the average profile beyond 40 mm along the radial axis is only constituted of the measurements from the south section and therefore not representative of the entire dome. Additionally, the series of measurements performed using the hybrid sequential method provided the temporal fluctuations of the dome profile with a maximum deviation range of ±2 mm, which is also reported in Figure 54.

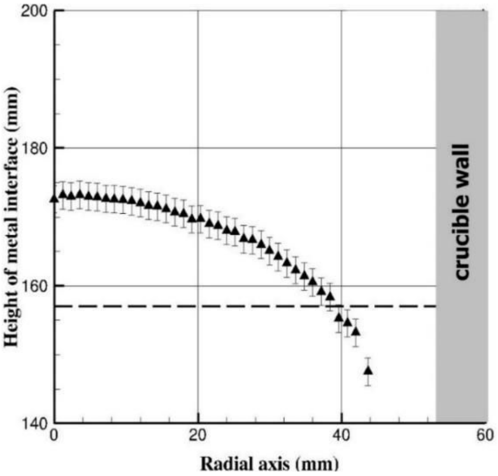

Figure 54: Average dome profile for Experiment 9 along with its deviation

The average dome profiles measured for the other sets of operating parameters are presented in Figure 55. We observed as expected that the measured deformation increases with the inductor current intensity for each liquid metal filling. Since the 60 % filling level is closer to the inductor symmetry plane, the liquid metal near the free surface experiences a higher magnetic induction. This explains why the elevation of the free surface at the axis is noticeably greater for the 60 % filling level in comparison to the 75 % filling level for comparable current intensities. For all cases, the deviation associated to the temporal fluctuations was found to be quite similar to that for Experiment 9, i.e.±2 mm.

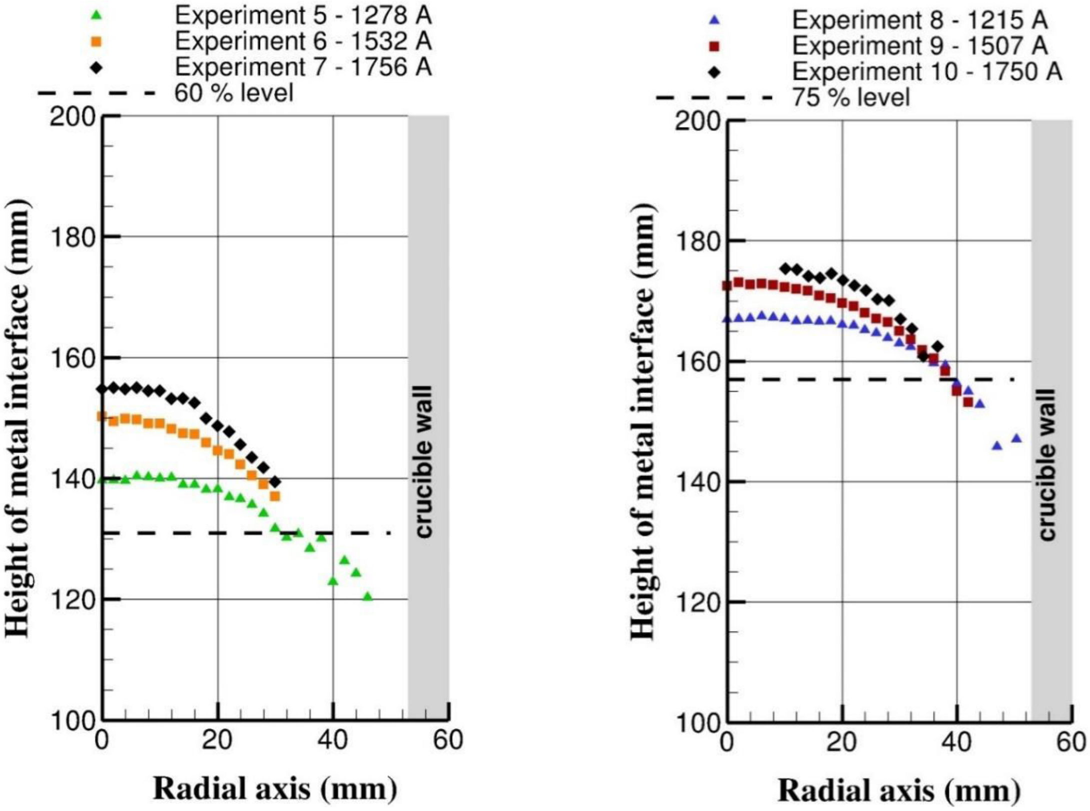

(a)

(b)

Figure 55: Average dome profile for (a) 60 % filling – Experiments 5 to 7, and (b) 75 % filling – Experiments 8 to 10

Table 13 summarizes the values of the vertical displacement (Δz) at the axis with respect to the initial filling level, measured during the structured light campaign. In Experiment 4, the optical system had to be recalibrated to accommodate the 28% crucible filling. Due to this, the crucible top wall reference system was absent on the processed image and therefore made the final dome profile very difficult to obtain. An estimation of the displacement of the interface is nevertheless given (in red) in Table 13. Apart from the regions in the proximity of the crucible wall, data for the height of the metal interface is also missing in the crucible center for Experiment 10 (maximum applied generator power). The data were therefore extrapolated up till the axis to find an approximate maximum height of the interface. The lack of measurement is readily explained by the high current intensity employed, leading to high thermal radiation from the free surface and thus the saturation of the camera sensor by the luminous intensity.

Table 13: Structured light campaign results
(correspond to numerical model initial conditions in Section C.1.2.1)

Experiment n°	**Alloy**	**Metal filling (%)**	**Initial filling level z_0 (mm)**	**Generator power (kW)**	**Current intensity # (A)**	**Vertical displacement of metal interface at the axis Δz * (mm)**
4	Al-10505	28	66	10	1316	22
5		60	131	10	1278	9
6				15	1532	19
7				20	1756	24
8		75	157	10	1215	10
9				15	1507	16
10				20	1750	22 *(extrapolated)*
11	Al-5182	75	156	10	1217	7
12				15	1476	12
13				20	1700	15

(# ±1% current intensity) (* ±2 mm height)

The data for Experiments 11 to 13, corresponding to the Al-5182 alloy, were also difficult to completely process due to the presence of a crumbled oxide layer covering the free surface (Annex 7). Nevertheless, an approximation (in red) of the vertical displacement of the metal interface for these cases was still made using the limited data available.

To better visualize the impact of the investigated operating parameters, we present in Figure 56 the evolution of the relative vertical displacement of the free surface at the axis ($\Delta z/z_0$) with respect to the initial filling level (60 % or 75 %), and the generator power. Not only do we see the usual trend of an increase in vertical displacement with an increase in the generator power, we also see the difference in trend due to the filling levels. As seen previously in Figure 55 (a) and Figure 55 (b), we observe in Figure 56 that the 60 % filling level cases undergo a larger vertical displacement (7 % to 19 %) compared to the 75 % filling level cases (6 % to 14 %). An example of similar behavior can be found in the work performed by Nakata and Etay [13] where the importance of the relative positioning of the coil with respect to the liquid metal free surface was highlighted.

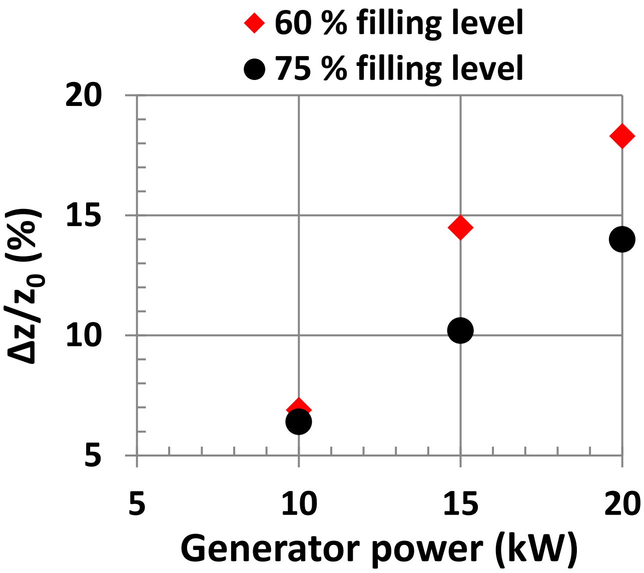

Figure 56: Evolution of the relative vertical displacement of the free surface at the axis as a function of the generator power and the initial filling level

1.2 Simulation results – Magnetohydrodynamics in IJL IMF

Figure 57 illustrates the 2D axisymmetric numerical model representation of the experimental setup. The three domains (coil, crucible and external) and the boundary conditions were described in section A.3.3. It is to be noted that the real crucible's round bottom was simplified and represented as rectangular bottomed crucible in the geometry.

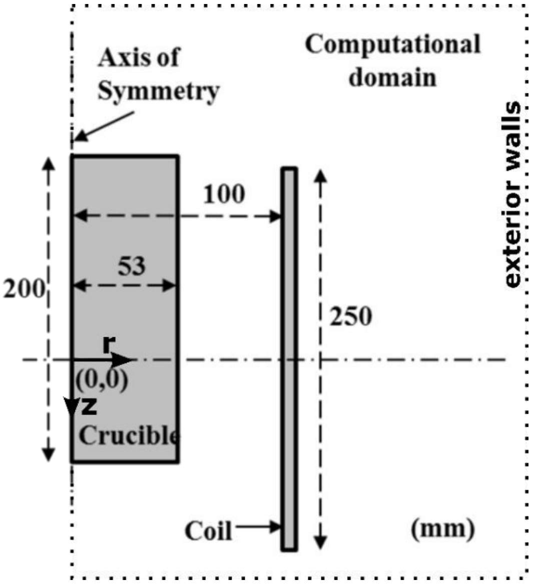

Figure 57: Representation of the IJL IMF in the numerical model (dimensions in mm)

1.2.1 Mesh and initial conditions

ANSYS Workbench – Design Modeler was used to create the geometry, followed by grid generation using *ANSYS Meshing*. Figure 58 illustrates a zoom on the crucible mesh, in which the structured outlay of the mesh can be observed. Since we did not use any wall functions, the mesh was refined near the crucible walls in order to resolve the inner boundary layer zones and in particular the laminar sublayer. The coil was also meshed in a structured manner. The outside computational domain, for simplicity, was meshed in an unstructured manner. Moreover, in order to avoid any discontinuities of the magnetic field lines across the crucible walls, a progressive mesh sizing was applied on the external side of the walls. The number of grid cells equals 21 200 in the crucible region, 250 in the coil and 7 382 in the outside region. The smallest cell size in the boundary layer of the crucible zone is of the order of 100 µm. The maximum skewness of the mesh is 0.75 in the unstructured computational domain, which is deemed satisfactory.

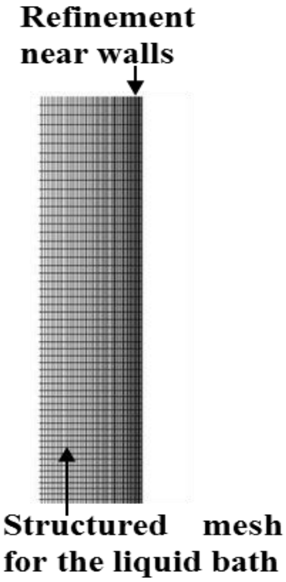

Figure 58: Zoomed up crucible mesh

The input parameters (electrical operating parameters and filling levels) used for the simulations presented in this section correspond to those of the experiments listed in Table 13. A fixed time stepping method was selected with a time step of 0.5 ms to obtain a Courant number lower than one. The average bath velocity, the free surface fluctuation and the recirculation zone positioning were monitored during the simulation in order to verify the establishment of a quasi-steady state regime. In the remainder of this section, we focus our analysis on the quasi-steady hydrodynamic regime reached after about 5 seconds.

1.2.2 MHD results

Simulations were performed for the conditions of Experiments 4 to 10 in Table 13. Amongst these simulations, results for only Experiments 5, 6, 8 and 9 are presented in the following paragraph, with a particular focus on Experiment 9. The steady state was never achieved in the case of Experiment 4, which may be linked to the low initial filling level and its relative positioning with respect to the inductor's mid-plane. The calculated free surface continued oscillating and the average melt velocity of the bath never stabilized, indicating an unsteady state. The calculations for Experiment 7 and Experiment 10, despite repeated attempts, diverged. This divergence may be a result of (i) the modeling of the geometrical setup of the crucible as a closed rectangular box[¤], and (ii) the very high current intensities (> 1700 A) in these two cases. During the first 0.5 s of these calculations, the high current intensities led to a transient and very large free surface deformation, further resulting in violent collisions of the free surface with the crucible top wall. Consequently, a large number of liquid metal drops were generated, where calculation of the various phenomena became very difficult and was accompanied by numerical divergence.

The numerical model was given the values of the thermo-physical properties of the aluminum alloy Al-1050 at the measured temperature of 1000 °C as described in Table 14.

Table 14: Al-1050 properties used in numerical model at 1000 °C

Property		**Value at 1000 °C**
Density	(kg.m^{-3})	2339
Dynamic viscosity	(mPa.s)	0.71
Surface tension	(N.m^{-1})	0.783
Electrical conductivity	(Ω^{-1}.m^{-1})	3.33x10^{6}

1.2.2.1 Simulation results concerning Experiment 9

Dome profile

Figure 59 presents the calculated time averaged free surface dome profile with and without the presence of the oxide layer. Without the oxide layer, the maximum height of the interface at the axis is 190 mm while the dome height is 62 mm. The dome undergoes a significant change with the addition of the friction force due to the oxide layer and reduces by almost 8 mm along the axis. Once the steady state was achieved, the maximum fluctuation range of the deformation was noted as ±1 mm.

[¤] The crucible was considered as a closed box to limit the computational domain of the multiphase flow (liquid metal – air).

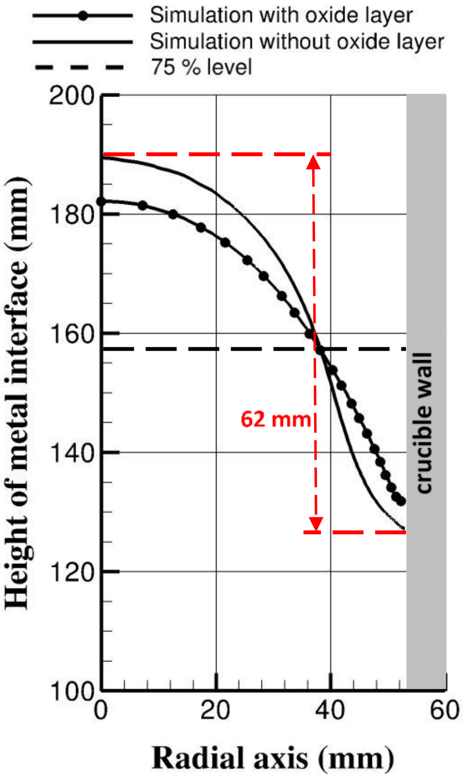

Figure 59: Dome profile calculated with and without the oxide layer friction force – Experiment 9

Bath hydrodynamics

In absence of the oxide layer, Figure 60 (a) and Figure 60 (b) respectively illustrate the turbulence intensity and the flow structures inside the liquid metal bath along with the distribution of the melt velocity. Figure 61 (a) and Figure 61 (b) show the same type of results in the presence of the oxide layer.

In both cases, the steady state flow is similarly organized into three recirculation zones: one within the dome, another in the central region of the bath and a third with a high vorticity and turbulence intensity in the bottom corner. Comparing Figure 60 (b) with Figure 61 (b), we note that the shear stress exerted by the oxide layer reduces the melt velocity, especially in the upper dome region. The turbulence intensity as a consequence is comparatively much lower in this region, as observed when comparing Figure 60 (a) with Figure 61 (a). The mean velocity and the turbulence intensity in the bath drop from 0.22 $\mathrm{m.s^{-1}}$ and 0.08 without the oxide layer to 0.16 $\mathrm{m.s^{-1}}$ and 0.06 in presence of the oxide layer.

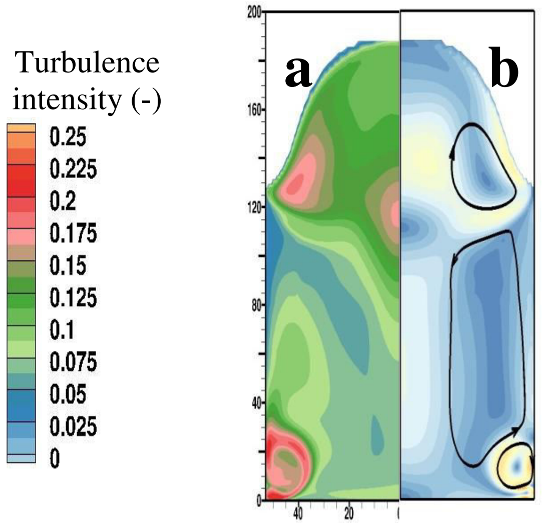

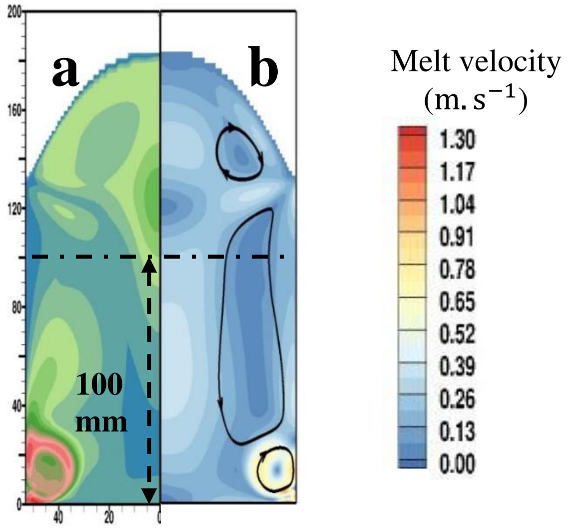

Figure 60: Bath hydrodynamics in absence of oxide layer – Experiment 9: (a) Turbulence intensity (-), (b) Melt velocity ($m.s^{-1}$)

Figure 61: Bath hydrodynamics in presence of oxide layer – Experiment 9: (a) Turbulence intensity (-), (b) Melt velocity ($m.s^{-1}$)

Figure 62 illustrates the radial profiles of the liquid metal velocity and the turbulence intensity along a section 100 mm above the crucible bottom, extracted from Figure 61. Only the region lying in the electromagnetic skin (4.5 mm) is presented. The liquid metal velocity increases to above $0.15\ m.s^{-1}$ before, as expected, decreasing in the boundary layer to zero at the crucible wall. As a result, the turbulence also tends towards zero at the wall, since turbulence in the inner boundary layer is resolved. The viscous sublayer is also reported.

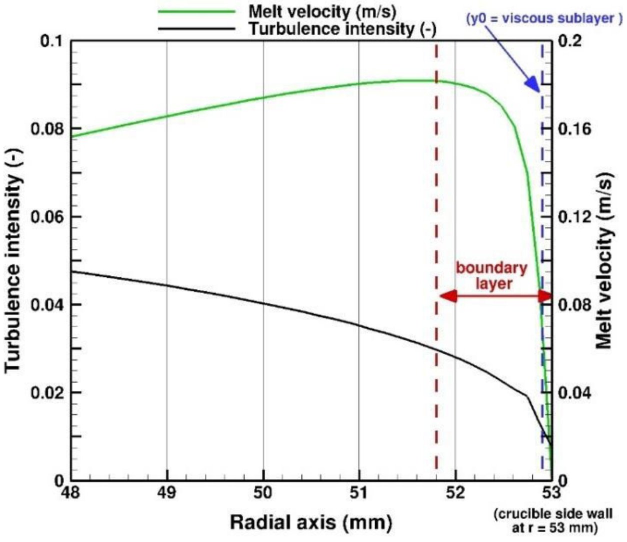

Figure 62: Radial profiles of the magnitude of the liquid metal velocity and the turbulence intensity along a section 100 mm from the crucible bottom, extracted from Figure 61

The crucible wall is subjected to a shear stress due to near wall flow, as presented in Figure 63 along with the corresponding near wall flow structure. The sign of the axial shear stress is governed by the near wall axial velocity direction. Zone 1 has negative shear stress indicating upward movement of the metal, while zone 2 has a positive shear stress indicating downward movement, which again inverses in the bottom corner of the crucible (zone 3). The magnitude of the shear stress is a function of the melt velocity and therefore is higher in the bottom crucible corner where the velocity attains high values.

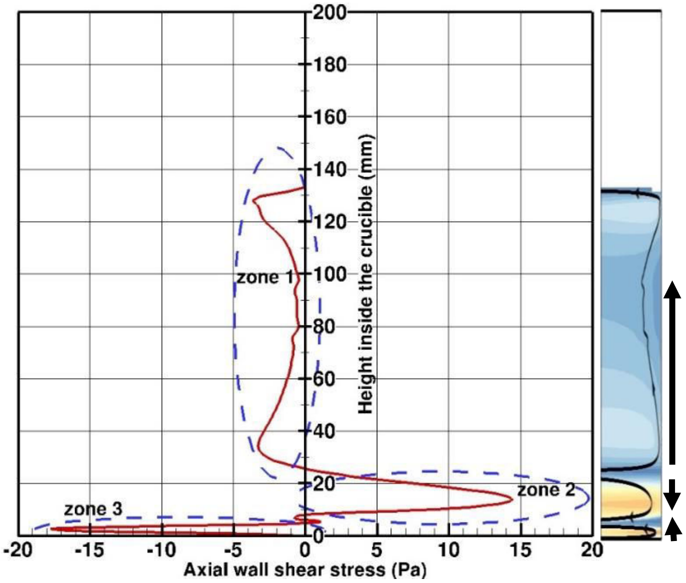

Figure 63: Wall shear stress along the crucible side wall – Experiment 9

Electromagnetics inside the bath

Figure 64 (a) and Figure 64 (b) respectively present the distributions of the induced current density and the Lorentz forces in the bath. It is noted that the induced current density is concentrated near the crucible wall and decreases rapidly to low values within 10 mm from the wall, which is in accordance with the theoretical concept of the electromagnetic skin effect. The Lorentz force follows the induced current density with its maximum magnitude near the crucible wall and is directed primarily towards the axis of symmetry of the metal bath. To better visualize the skin effect, the radial profiles of the Lorentz force and the induced current density along a section located 100 mm above the crucible bottom have been extracted and are presented in Figure 65. The skin depth may be approximated by finding the distance at which the current density satisfies the following expression [127]: $j_\delta = \frac{j_{max}}{e}$, where e is the mathematical constant equal to 2.72. From Figure 65, the skin depth is found equal to 4.5 mm, which is comparable to the skin depth calculated theoretically $\delta_{EM} = (\pi\mu_0\sigma_{el,f}f)^{-0.5}$= 4.27 mm.

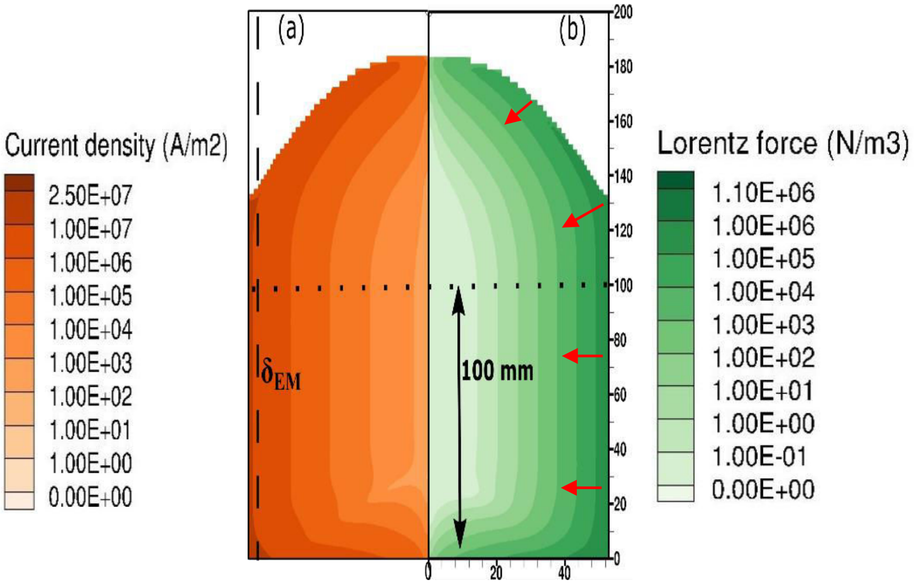

Figure 64: Bath electromagnetics – Experiment 9: (a) Induced current density distribution (A.m^{-2}), (b) Distribution of the magnitude of Lorentz force (N.m^{-3})

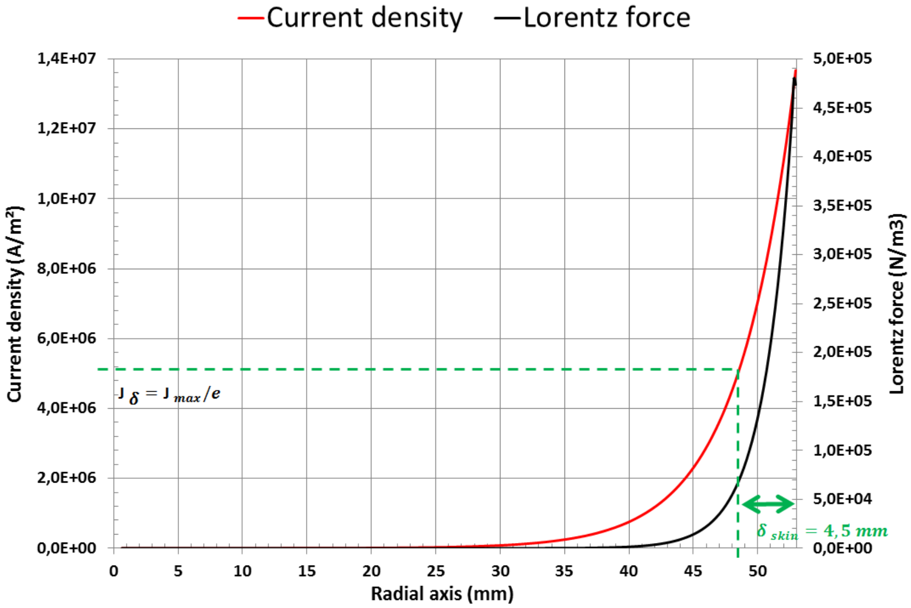

Figure 65: Radial profiles of the Lorentz force magnitude and the induced current density along a section 100 mm from the crucible bottom, extracted from Figure 64

1.2.2.2 Influence of the operating parameters

Figure 66 (a) and Figure 66 (b) illustrate the calculated dome profiles for Experiments 5&6 and Experiments 8&9 respectively. We see that an increase of 20 % in current intensity (from Experiment 5 to 6) led to an increase of almost 30 % in the respective dome height. Furthermore, as seen previously on the experimental data in section C.1.1.2, the calculated deformations for the

60 % filling level cases are relatively larger in comparison to those for the 75 % filling level cases, for similar generator power regimes.

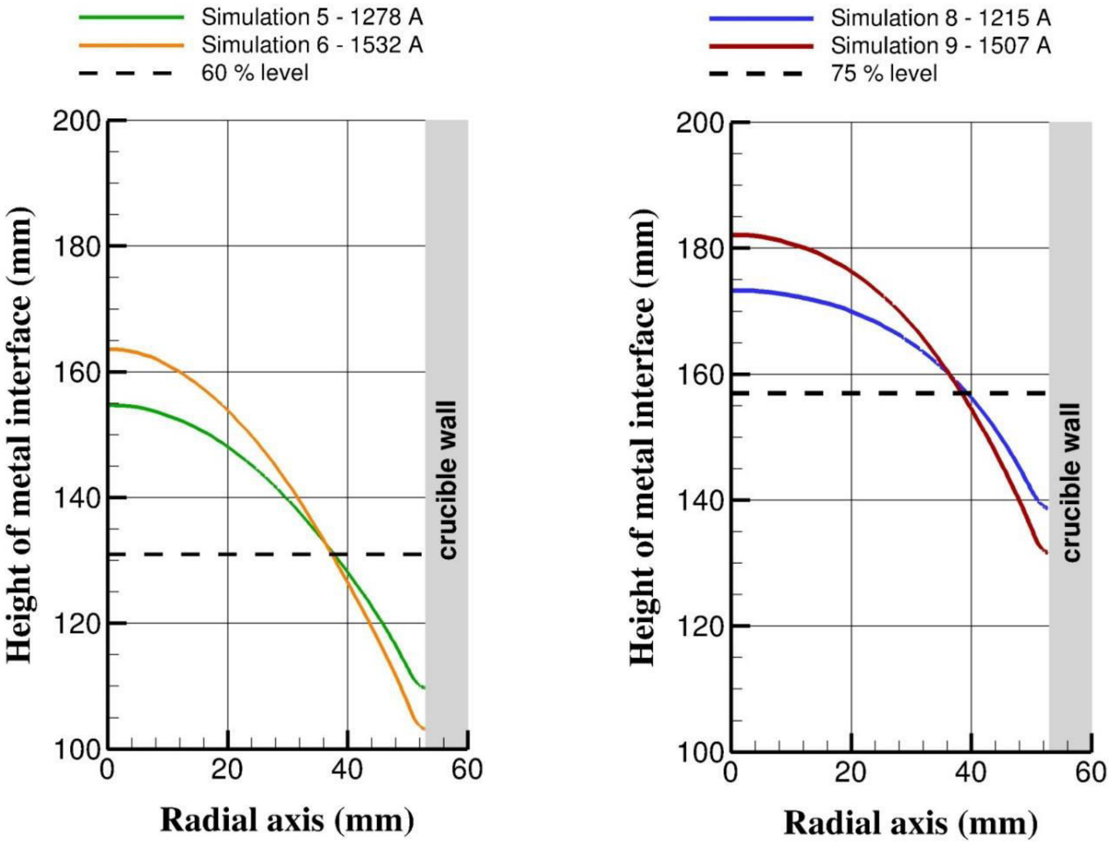

Figure 66: Calculated dome profiles: (a) 60 % filling level – Experiments 5&6, (b) 75 % filling level – Experiments 8&9

Figure 67 and Figure 68 present the magnitude of the mean melt velocity and turbulence intensity distributions in the bath calculated for various operating conditions. The presence of three recirculation zones (dome, middle and bottom corner) is constant across all these cases. Taberlet and Fautrelle [22] also noted a similar three loop flow pattern. However, this pattern is slightly different from other previously reported works [23] , [44], where a two loop flow structure (dome and middle) was usually described. Our simulation conditions show some consistence with cases in [22], specifically in terms of the operating current frequency. Moreover, in this work it was remarked that the flow pattern was insensitive to the coil current variations but may be influenced by the current frequency variations. Note that the geometrical simplification made in our model for the representation of the round cornered crucible as a rectangular corner could also be partly responsible for the extra recirculation zone.

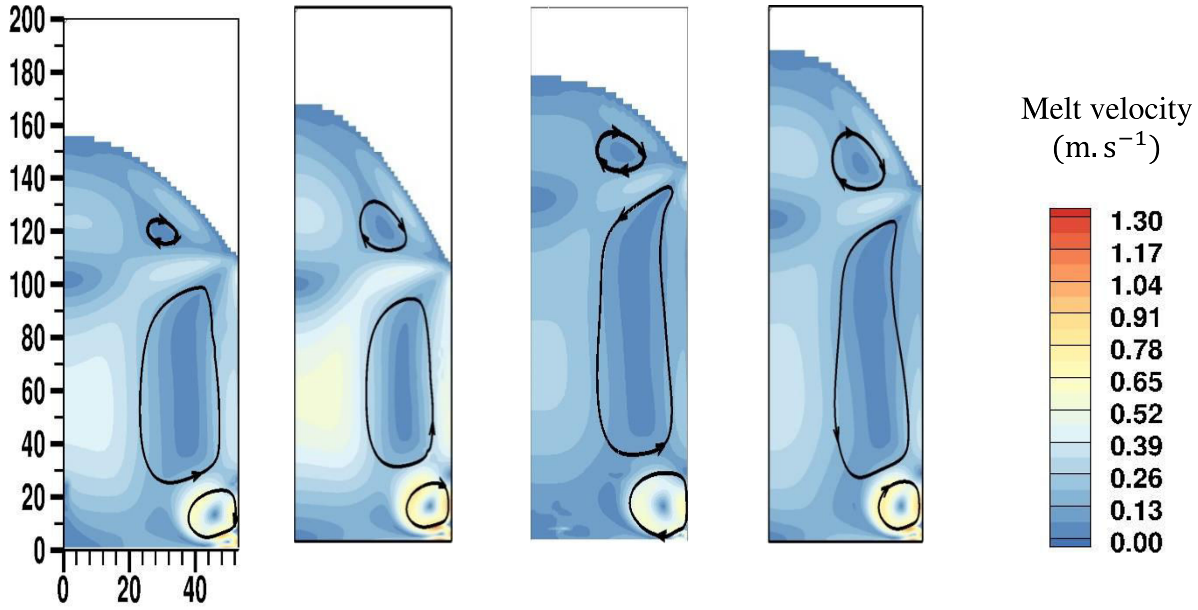

Exp.5 – 1278 A Exp.6 – 1532 A Exp.8 – 1215 A Exp.9 – 1507 A

Figure 67: Melt velocity magnitude distributions $(\mathrm{m.\,s^{-1}})$ for 60 % and 75% filling levels

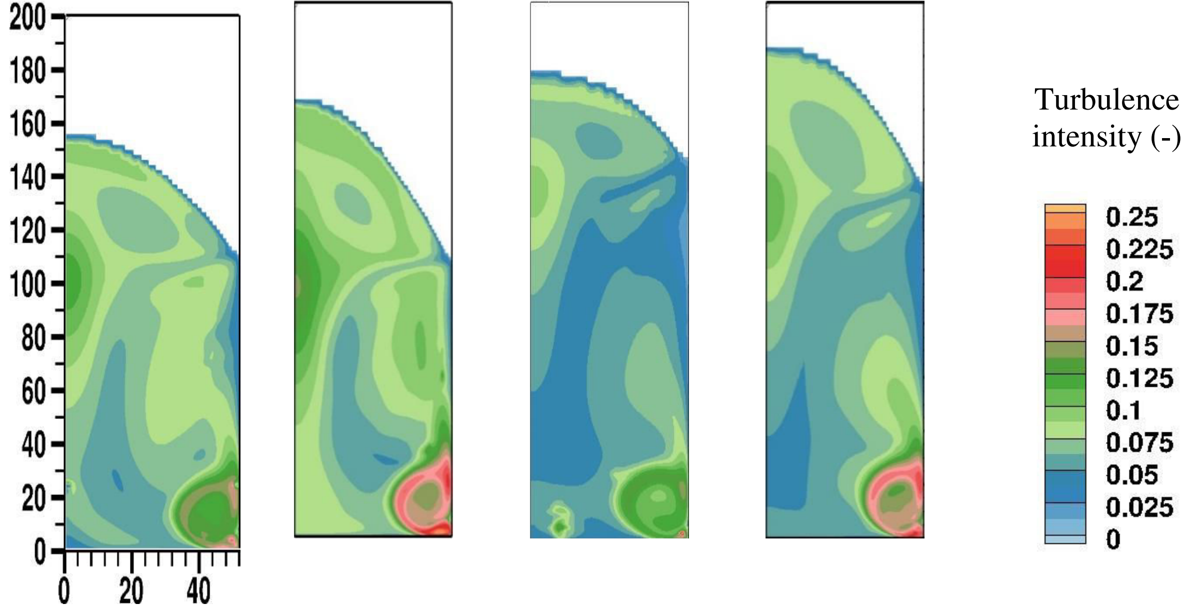

Exp.5 – 1278 A Exp.6 – 1532 A Exp.8 – 1215 A Exp.9 – 1507 A

Figure 68: Contours of the melt turbulence intensity (-) for 60 % and 75% filling levels

Across these four cases, a systematic presence of a very high velocity zone in the bottom corner of the crucible can be observed. On the other hand, the melt velocity under the dome zone is slightly higher than in the calmer middle zone. As indicated by Tarapore and Evans [20], this is expected as there is less liquid-solid contact area and therefore lesser drag forces in the dome zone.

Overall the bath turbulence ranges from low to moderate intensity (0.01 to 0.1), with a maximum in the bottom corner region (> 0.1). As a general rule, we observe that the turbulence intensity in the dome region is quite high compared to that in the middle zone. On the other hand, an even higher turbulence intensity is observed in the bottom corner region. Another interesting point to be noted is the apparent homogeneity of the turbulence intensity for the 60 % filling level cases compared to the 75 % level cases. Simultaneously we also observe a relatively higher melt velocity in the bulk region for the 60 % cases, which indicates a better stirred bath. The average turbulence dissipation rate, defined as $(\overline{\varepsilon^{0,5}})^2$, indicates the stirring power ($W.t^{-1}$) acting on the metal bath. This parameter along with the average melt velocity and the maximum Lorentz force is tabulated in Table 15. The orders of magnitude of the Lorentz force and the melt velocity are in accordance with the range seen in results for similar sized induction furnaces in the literature [44] [45] [37].

Table 15: Summary of simulation results for Experiments 5, 6, 8 and 9

	Exp.5	Exp.6	Exp.8	Exp.9
Average melt velocity magnitude ($m.s^{-1}$)	0.14	0.19	0.12	0.16
Max. Lorentz force magnitude ($N.m^{-3}$)	$0.8x10^6$	$1.0x10^6$	$0.7x10^6$	$1.0x10^6$
Stirring power ($W.t^{-1}$)	546	950	375	725

As we see in Figure 69, the melt velocity as well as the stirring power are increasing functions of the generator power (hence of the inductor current intensity). This is consistent with previous works such as those found in [20] and [37] where a linear trend was established between the melt velocity and the inductor current intensity. Similar to the trend seen in Figure 56 regarding the amplitude of the deformation of the free surface, we see a larger melt velocity and stirring power for the 60 % filling level as compared to the 75 % level. With a higher stirring power, the 60 % filling level case is thus more prone to satisfy the stirring objective of the IMF while simultaneously undergoing a much larger free surface deformation.

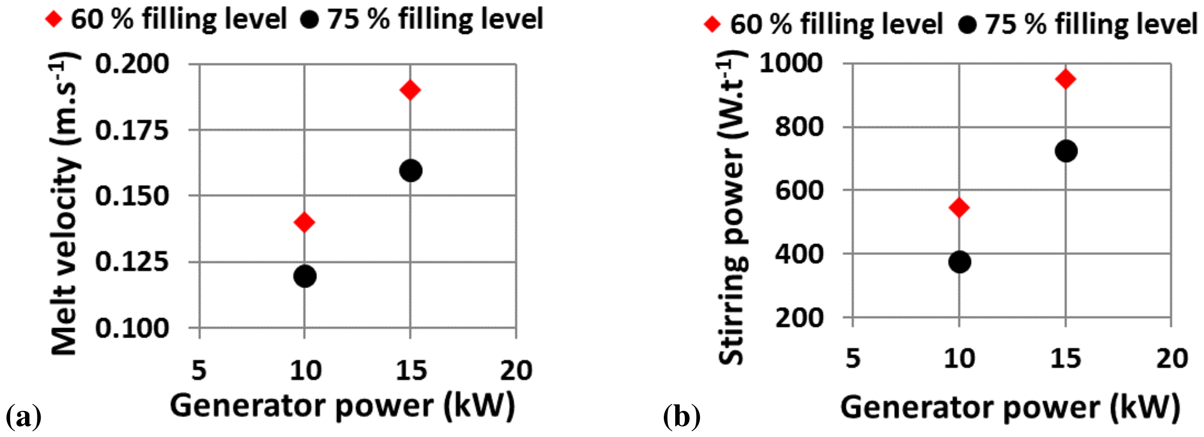

Figure 69: (a) The average melt velocity and (b) the stirring power as a function of filling levels and generator power

1.3 Experimental vs Simulation results

A comparison of the measured and calculated deformation of the free surface for the conditions of Experiments 5, 6, 8 and 9 is presented in Table 16. In this table, we have reported the height of the interface at the axis, the height of the interface at the axis with respect to the initial level and the dome height. The experimental dome height is unavailable since the triple point (air – bath – wall) at the crucible side wall was shadowed and thus remained unmeasured.

Table 16: Measured vs calculated results regarding the deformation of the free surface for Experiments 5, 6, 8 and 9

	Experiment 5		Experiment 6		Experiment 8		Experiment 9	
	Exp	**Sim**	Exp	**Sim**	Exp	**Sim**	Exp	**Sim**
Height of the interface at the axis (mm)	142	**154.5**	150	**162.5**	167	**173**	172.5	**182**
Height of the interface at the axis with respect to the initial metal level Δz (mm)	11	**23.5**	19	**31.5**	10	**16**	15.5	**25**
Dome height (mm)	-	**45**	-	**58.5**	-	**44**	-	**48**

Experimental and calculated free surface dome profiles are compared in Figure 70 (a) and Figure 70 (b). It must be remarked that the experimental data for Experiment 9 covers the simulation results for Experiment 8. For all cases, the measured and the calculated dome profiles are of comparable shape and size. However, it is clear that the model overestimates the free surface deformation amplitude by 6 to 12 mm at the axis, indicating a relative error ranging from 60 % to a little over 100 %.

The difference between the measured and the calculated dome profiles was examined by testing the following two hypotheses:

- ❖ How important is the representation of the inductor setup in the numerical model?
- ❖ Does the turbulence damping model near the metal bath free surface impact the dome profile?

It was found that the first point held an important role and is described hereunder. The second point was found to have a negligible effect on the dome profile and is presented in Annex 9.

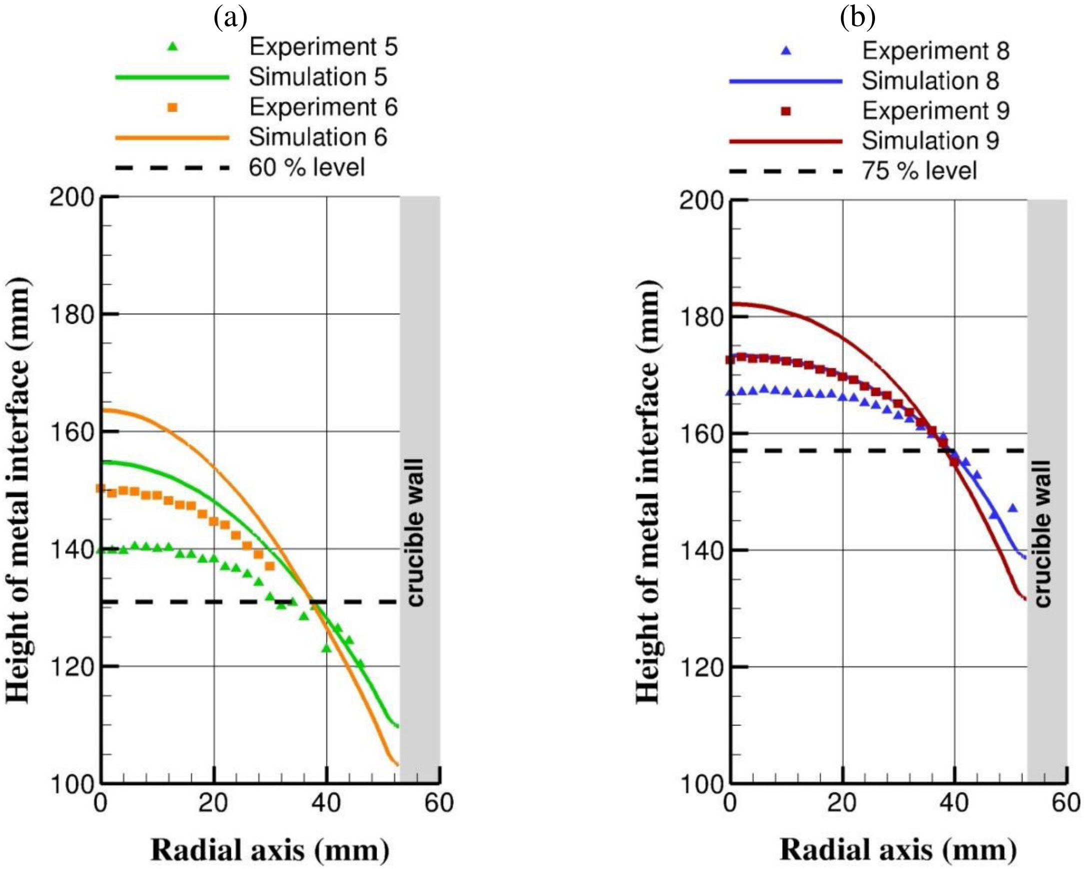

Figure 70: Measured vs calculated dome profiles for Experiments (a) 5&6 and (b) 8&9

Representation of the inductor setup in the numerical model

The difference between the real inductor setup as a disjointed 8 turn coil (Figure 13) and its representation in the numerical model as a continuous sheet (Figure 57) may lead to a difference between the real and the calculated magnetic field generated by the inductor. Since the electromagnetic forces acting on the liquid metal (whose magnitude is directly governed by the magnetic field) are one of the primary forces at work during the free surface deformation, a difference in the magnetic field may strongly impact the calculated free surface deformation of the metal bath.

A comparison between the centerline profiles of the axial magnetic field measured experimentally (already presented in Figure 46), calculated with our model and obtained using the theoretical expression of Nagaoka for conditions of Experiment 1 (empty crucible) is presented in Figure 71. The current intensity circulating inside the inductor was measured and equals 990 A at a frequency of 3500 Hz.

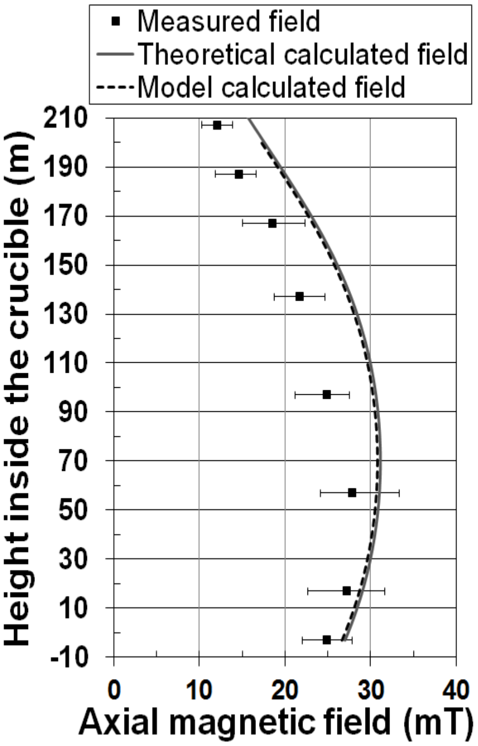

Figure 71: Centerline profile of the axial magnetic field in an empty crucible (Experiment 1): comparison between the measured, theoretical and simulated profiles

The theoretical centerline profile of the axial magnetic field in the case of an empty crucible can be approximated based on the Nagaoka's current sheet magnetic field expression [17], which is valid for a short finite continuous sheet.

$$B(z) = \frac{\mu_0 NI}{2H}\left(\frac{(-0.5H - z)}{\sqrt{(-0.5H - z)^2 + R^2}} - \frac{(0.5H - z)}{\sqrt{(0.5H - z)^2 + R^2}}\right) \tag{104}$$

In this expression μ_0, N, I, H and R are respectively the magnetic permeability constant, the number of coil turns, the current intensity in each turn, the inductor height and the inductor radius.

The theoretical field is very close to the one provided by the numerical model, which is consistent with the fact that both approaches suppose that the coil is a continuous sheet with uniformly distributed current intensity. In contrast, the measured field is found to be lower than the calculated magnetic field by 5 to 20 %. This difference between the real and the calculated magnetic field could possibly explain the difference between the measured and the calculated dome profiles. In order to narrow down the possible reasons of discrepancy, the measurement of the current intensity which is a major model input parameter was successfully verified using another Ampmeter. Furthermore, the absence of screening elements (which may influence the magnetic induction) around the inductor in the IJL induction furnace was verified. Therefore, the difference between the real inductor setup and its representation in the numerical model as a continuous sheet, and the resulting difference in the generated magnetic induction, is believed to be the main cause behind the overestimation of the calculated dome profile.

Previous researches concerning comparisons of measured and calculated dome profiles such as that by Li et al. [33], Kageyama and Evans [36], Bojarevics et al. [128], Kirpo [37] and Spitans et al. [44] provide interesting comparisons for various liquid metal processes. However, we usually notice only a few discrete measured points on the surface (up to 15), while measurement precision is often absent. However, in Kirpo's work which offers a more detailed measurement, we see an underestimation of the calculated vertical displacement (Δz) by a factor of at least two.

1.4 Preliminary conclusions drawn from IJL IMF

This section presented the results of an effective way to measure the 3D free surface deformation of a metal bath at high temperatures. The results confirmed the two-dimensional axisymmetric nature of the free surface inside our laboratory scale IMF. This justifies our 2D axisymmetric approach to numerical modeling. Moreover, the importance of the operating parameters (electrical parameters and filling level) was duly noted. Also, a much larger portion of the free surface was measured instantaneously, compared to the previous works found in the literature. Nevertheless, the study of the free surface fluctuations remained inconclusive.

We compared the calculated dome profiles with the measured dome profiles at the laboratory scale. Although they are of the same shape and order of magnitude, a relative error between the two results of 50 % to 100 % was noted and may possibly be attributed to the representation of the inductor in the numerical model. It was also remarked that the presence of the oxide layer, and consequently the friction force exerted on the bath, had an impact on both the free surface deformation (~ 25 %) and the bath hydrodynamics.

2. Application to an industrial scale IMF

After the application of the MHD model to a laboratory scale IMF in section C.1 and subsequent comparison with the experimental results, we scale up, in the present section, its application to an industrial scale furnace. The first part of the section deals with the hydrodynamics behavior of the metal bath. It includes in particular results concerning the deformation of the metal free surface, which are compared to measurements obtained using laser telemetry. The second part of the section focuses on the simulation of the inclusion behavior in the metal bath. There onwards, the phenomena controlling the inclusion dynamics and their capture at the interfaces are analyzed.

2.1 Introduction to the industrial scale IMF

An industrial furnace of a maximum capacity of 5 t was selected for its design allowing us to study various configurations. Figure 72 illustrates the schematic of the industrial scale IMF.

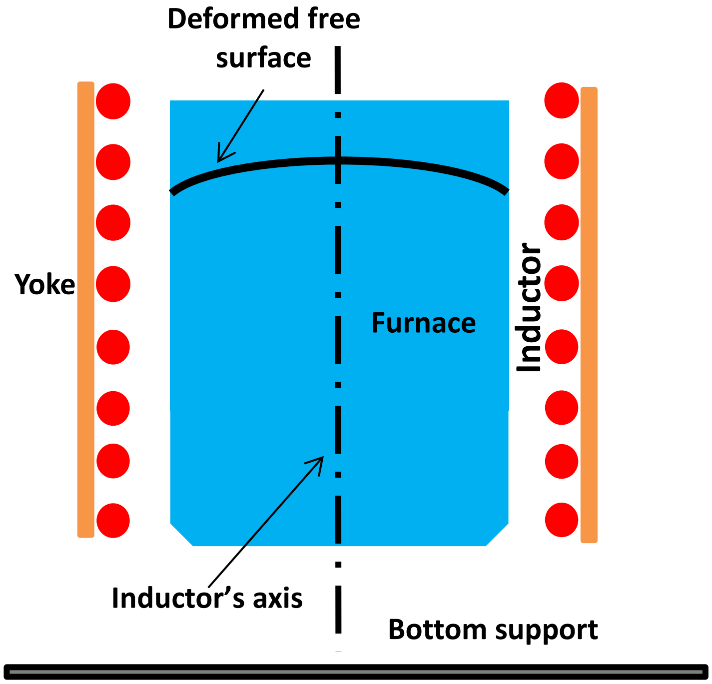

Figure 72: Schematics of the industrial scale IMF

An approximately 2.5 m high furnace with an inner diameter of a little over 1 m is surrounded by an inductor comprising around 60 coil turns. The top two coil turns of the inductor are short-circuited, which, as it will be seen later, may locally alter the magnetic induction and in some cases impact the bath free surface fluctuations at the crucible wall contact point. In contrast to the lab scale IMF, this installation also consists of lateral and bottom metallic elements, which interact with the generated magnetic induction and thus modify the driving forces in the melt.

The bottom element, made up of copper, constitutes a structural support almost 40 cm away from the crucible base. The lateral element, on the other hand, plays a complex role in the IMF setup. In our installation (Figure 73), the lateral element consists of a series of 12 distinct laminated ferromagnetic steel yokes connected to the outer frame, just beyond the inductor coils. These discrete elements are spaced from each other at a uniform distance. The set of yokes is used to guide the magnetic flux so as to concentrate the magnetic induction in the interior region of the crucible [129] [130]. Additionally, the yokes shield the external region of the furnace from the magnetic field. As previously illustrated in Figure 5, this sort of an arrangement is quite prevalent in the industry [12].

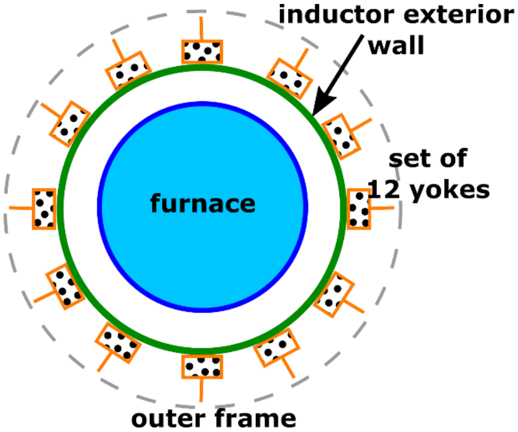

Figure 73: Top view of the industrial scale IMF – focus on magnetic yokes

2.2 MHD and free surface deformation

2.2.1 Experimental measurements

An experimental campaign was performed to measure the vertical displacement of some discrete points on the metal bath free surface using laser telemetry. Performed by Constellium, the campaign also comprised simultaneous measurements of the electrical parameters of the induction furnace. Alloy Al-2024 (which includes a high copper content) was used during these experiments (Table 17).

Table 17: Properties of Al-2024 at T = 750 °C *[57] [62]*

Density $(\mathrm{kg.m^{-3}})$	Dynamic viscosity $(\mathrm{Pa.s})$	Surface tension $(\mathrm{N.m^{-1}})$	Electrical conductivity $(\Omega^{-1}.\mathrm{m}^{-1})$
2416	1.04×10^{-3}	0.795	3.38×10^{6}

2.2.1.1 Operating parameters

We present the results of three experiments performed using different liquid metal filling, generator power and current frequency, as described in Table 18. Experiments A and C correspond to a stirring mode, with the maximum value of the generator power and a low current frequency (~ 60 Hz), while experiment B corresponds to a holding mode with nearly half of the maximum generator power and almost double the current frequency. The current intensity circulating in the inductor was measured using a Rogowski's coil.

Table 18: Operating parameters of the experimental campaign

Experiment	Metal filling (%)	Generator power (% of max.)	Current frequency (Hz)
A	73 %	100 %	62
B	73 %	50 %	131
C	57 %	100 %	59

2.2.1.2 *Free surface deformation analysis using laser telemetry*

As described in Annex 8, laser telemetry allows an easy approximation of the vertical displacement of a single point on the metal bath free surface. An external casing filled with an insulating material was designed to protect the telemeter setup from the severe thermal radiations (Figure 74). The telemeter was hung on to a metallic rail placed above the bath, allowing it to be displaced along a vertical cross section of the free surface dome. In this way, measurements were taken at several points (3 to 6) on the free surface during each experiment.

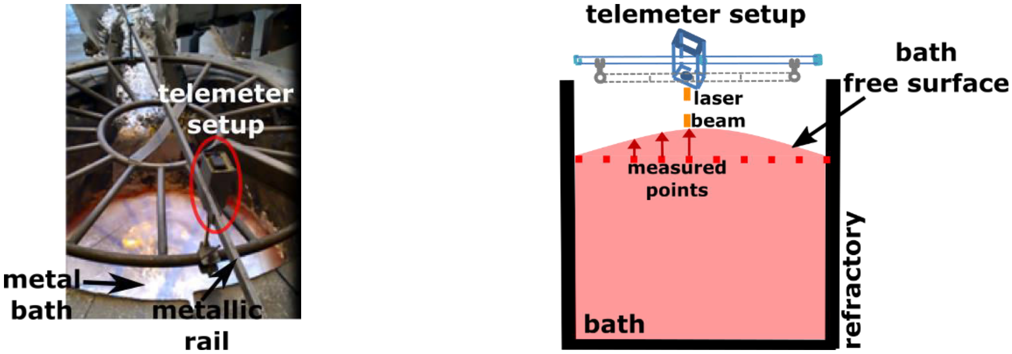

Figure 74: Implementation of laser telemetry on the industrial IMF

Figure 75 reports the data measured for the three experiments. In all the graphs of the following paragraphs, the scales of the horizontal and vertical axes were normalized with respect to the furnace radius.

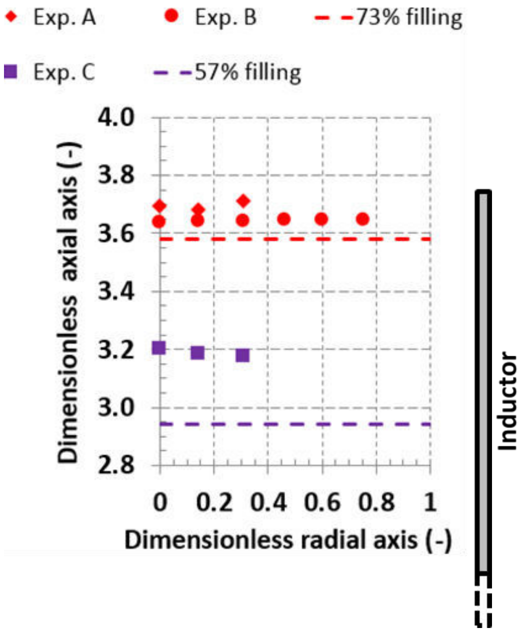

Figure 75: Laser telemetry results – industrial scale IMF

The laser telemetry measurements were not possible in the regions near the furnace wall for Exp. A and C, due to a high free surface deformation. On the other hand, Exp. B offered a much flatter free surface, which was therefore easier to measure, hence a greater number of measurement points. The deformation at the axis of symmetry is much larger for the 57 % filling level (Exp. C) compared to the 73 % filling level (Exp. A and B), which is consistent with the higher magnetic induction near the 57 % level. Also, as it might be expected, for the same filling level (73 %), a slight increase in the vertical displacement with an increase in the current intensity (from Exp. B to Exp. A) is noticeable. Later, these measurements will be compared to our model's predictions.

2.2.2 Numerical results

In the present section, we discuss the additional elements in the numerical representation of the industrial IMF, besides the usual modeling already presented in section A.3. A special emphasis is laid on the magnetic yoke modeling. MHD results are then presented and compared with the previously discussed experimental results.

Figure 76 illustrates the 2D axisymmetric numerical model representation of the industrial IMF.

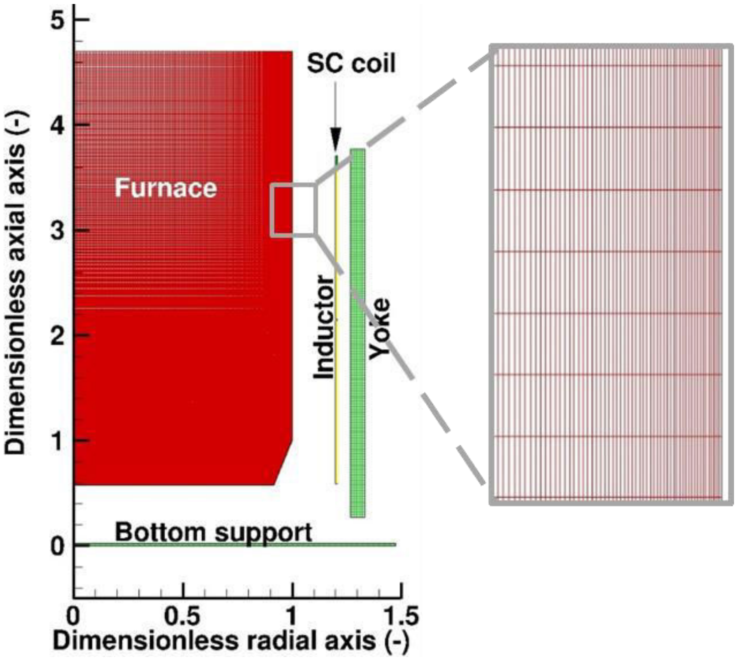

Figure 76: Representation of the industrial scale IMF along with a zoom of the wall-bounded mesh in the numerical model

The bottom support sheet and the short circuited coil turns were treated as conducting copper blocks. Similar to the method adopted for the lab scale IMF, the inductor was considered as an individual continuous sheet. The representation of the magnetic yokes will be described in a separate paragraph below. A global computational domain, ten times the size of the coils, was constructed. The boundary conditions on the external boundaries and the furnace walls remain unchanged as described in section A.3.3.The structured furnace mesh contained 125 730 cells with the smallest cell dimensions of 0.75 mm x 1.25 mm. The input parameters (electrical parameters and filling level) in the following simulations correspond to the operating parameters summarized in Table 18, while the physical properties of the liquid metal bath are described in Table 17.

2.2.2.1 Numerical modeling of the magnetic yokes

The magnetic yokes, as described in Figure 77, consist of a set of distinct vertical columns, arranged at a uniform spacing around the axis of the furnace. Due to the periodicity of the yoke geometry, an ideal numerical modeling approach would be to simulate one single yoke instead of the entire yoke assembly. However, this would lead to a complex 3D MHD modeling of the corresponding IMF [131]. In the present work, instead of considering the yokes as a set of distinct 3D elements, they were considered as a continuous sheet around the inductor in order to remain within the 2D axisymmetric modeling framework. The thickness of the continuous sheet was adjusted so that the total mass of the yokes remains conserved.

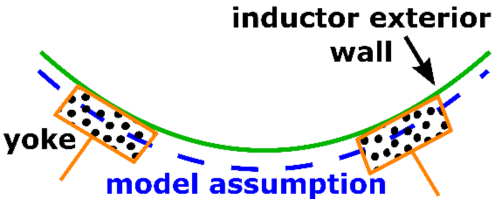

Figure 77: Geometrical representation of the yokes

Due to the very large permeability of the yokes ($\mu_{yoke}/\mu_0 \approx 100$ to 1000), as an initial approximation, we consider that the yoke permeability is infinite, which excludes any penetration of the magnetic field within the yokes. From the continuity condition of the tangential magnetic intensity ($\frac{B_{t,air}}{\mu_0} = \frac{B_{t,yoke}}{\mu_{yoke}}$) at the air-yokes interface, it follows that the tangential magnetic field at the yoke wall should be null ($B_t = 0$). Expressed in terms of the magnetic vector potential, the above condition implies the following two relations, which are imposed as boundary conditions along the yoke walls. This was implemented with the help of an additional macro DEFINE_PROFILE, programmed in a separate UDF.

$$\frac{\partial A_\theta}{\partial z} = 0 \quad \text{(for horizontal walls)}; \quad \frac{\partial A_\theta}{\partial r} = -\frac{A_\theta}{r} \quad \text{(for vertical walls)} \qquad (105)$$

In order to illustrate the yoke's magnetic effect, Figure 78 (a) shows the calculated near centerline profile of the magnetic field in an empty furnace for operating parameters corresponding to Exp. A. It is noted that the presence of the yoke increases the magnetic field by 10 % to 20 %. The magnetic field concentration effect due to the presence of the yoke, together with the shielding effect caused by the yoke, are also clearly visible on the computed magnetic field distribution presented in Figure 78 (b), where the yoke appears as a *hole* (i.e. B = 0) in the computational domain.

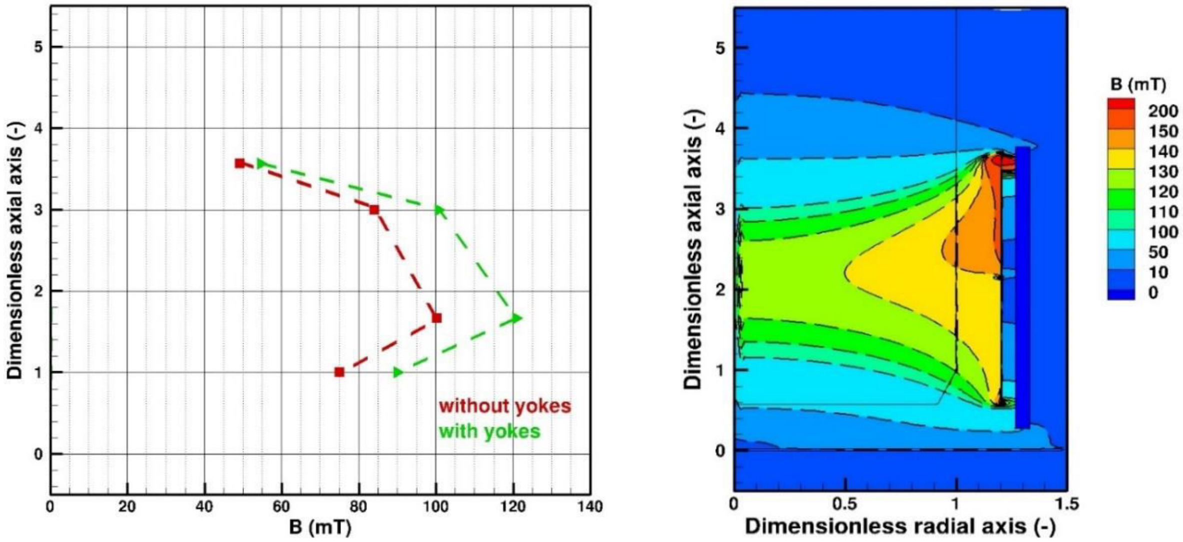

Figure 78: (a) Magnetic field strength at 0.1*$r_{furnace}$ from the furnace axis, (b) Effect of presence of a yoke on magnetic induction in an empty furnace

2.2.2.2 *Bath free surface – dome profile and fluctuations*

As presented in Figure 79, during the laser telemetry experiments, we observed large bath deformations in both Exp. A (higher filling level) and Exp. C (lower filling level), with a seemingly rippled surface in the former and a smooth surface in the latter. On the other hand, for Exp. B (high filling level but low power), the bath free surface remained almost undisturbed. Meanwhile video recordings illustrated vigorous surface fluctuations in the case of Exp. A confirming the rippled surface, while also confirming the much smoother fluctuation trend for Exp. C.


Exp. A
Exp. B
Exp. C

Figure 79: Experimental observations of bath free surface fluctuations during Exp. A, B and C

These experimental observations are in accordance with the calculated bath free surface fluctuations presented in Figure 80. This figure gives the fluctuations over a period of 6 s. We note large amplitude fluctuations along with an irregular profile of the dome for Exp. A, especially near the furnace wall. In contrast, we obtain for Exp. C, a smooth dome profile with smaller amplitude fluctuations. In these two stirring mode conditions, the large dome heights are a direct result of the high magnetic induction generated due to the high current intensity. The stronger fluctuations in Exp. A may possibly be related to instabilities resulting from the fact that the free surface when moving vertically regularly moves past the top of the upper coil. Similar to the experimental observations we see little to no fluctuations for the holding mode conditions in Exp. B. The 50 % drop in the generator power significantly reduces the magnetic induction, resulting in a very small deformation. For the stirring mode conditions, Figure 81 illustrates the variation with time of the height of the contact points of the free surface with the furnace axis and the side wall. This figure confirms the stability of the surface in Exp. C while illustrating the unstable surface for Exp. A.

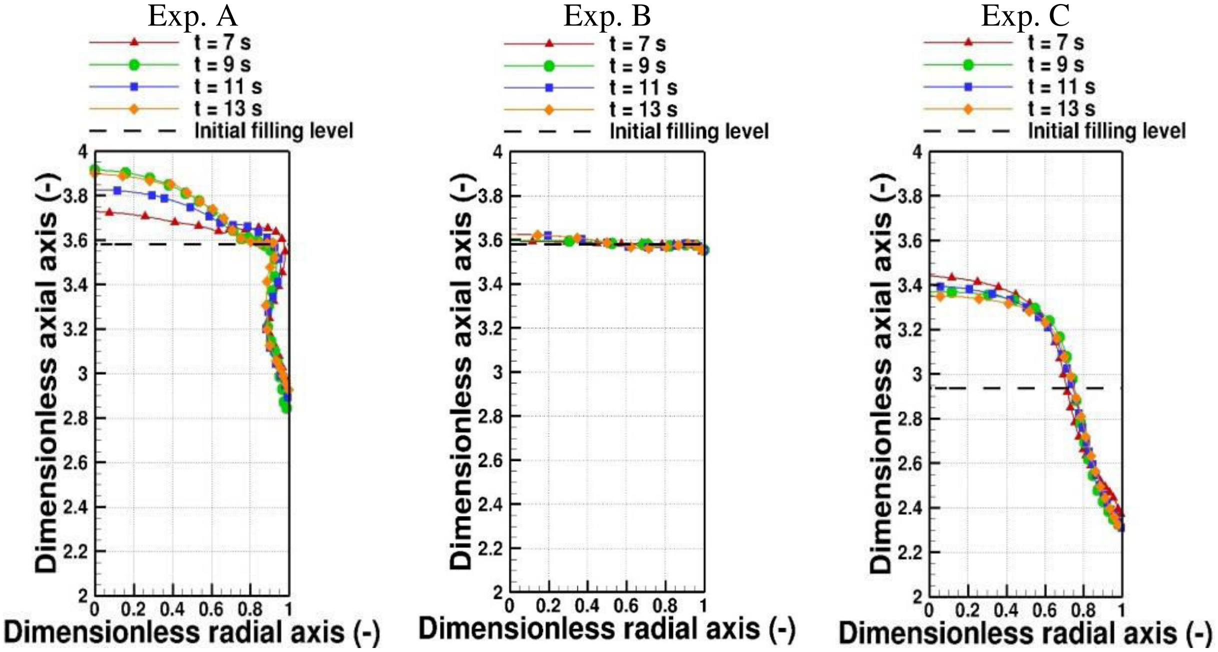

Figure 80: Calculated bath free surface fluctuations for experiments A to C over a period of 6 s

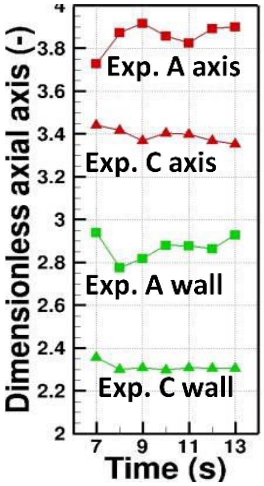

Figure 81: Fluctuation of axis and wall contact points during stirring conditions – Exp. A & C

The time averaged bath free surface profiles, along with the data measured using laser telemetry, are presented in Figure 82. The calculated amplitude of the free surface fluctuations is represented by a red line on the vertical axis. As noted previously, the calculated dome height (expressed in dimensionless height) is quite large in the stirring mode conditions – Exp. A (1) and Exp. C (0.9), while in the holding mode case – Exp. B the free surface is very slightly deformed (0.09).

Table 19 compares the measured and the calculated average vertical displacements of the bath free surface at the furnace axis with respect to the initial filling level, along with the maximum fluctuation range in red.

Table 19: Comparison of measured and computed free surface deformations at the furnace axis

		Exp. A	**Exp. B**	**Exp. C**
Measured vertical displacement	(mm)	68	34	161
Calculated vertical displacement (deviation)	(mm)	140 **(±20)**	38 **(±4)**	220 **(±10)**

The calculated and the experimental vertical displacements are almost identical for the holding mode (Exp. B). Meanwhile, the comparison for the stirring mode (Exp. A and C) shows a similar order of magnitude, but we note a marked overestimation of the vertical displacement by the model (the relative error is about 77 % for Exp. A and 36 % for Exp. C).

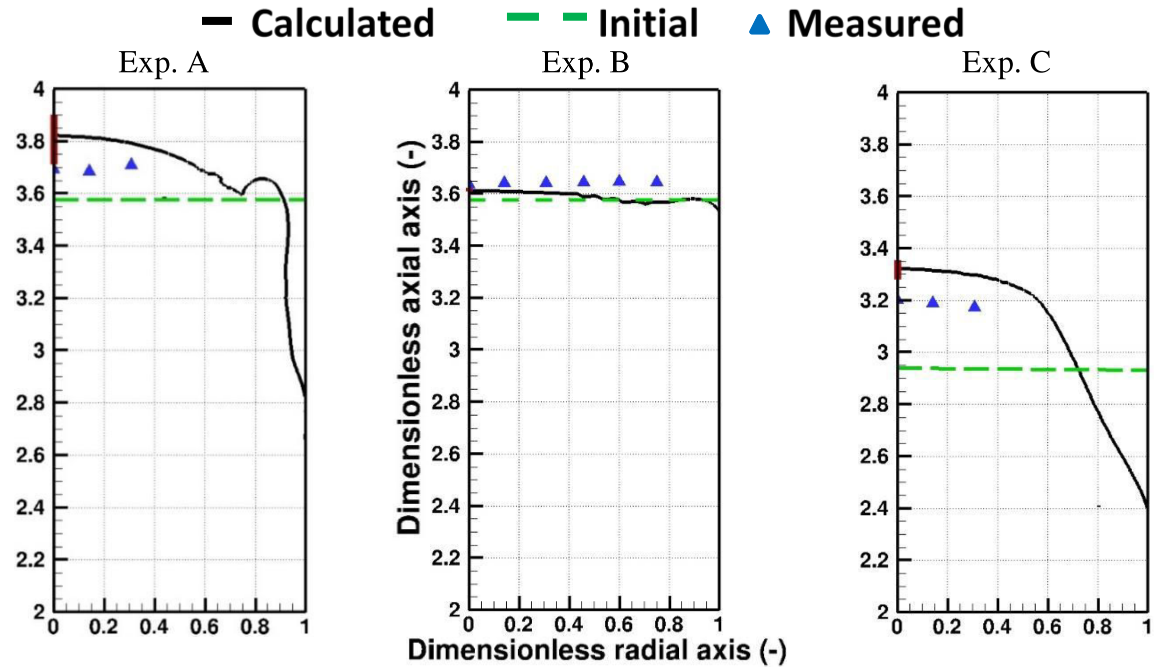

Figure 82: Time averaged free surface profiles for Exp. A to C

This discrepancy between the measured and the calculated vertical displacements could possibly be explained by a combination of several factors.

- ***Coil representation***

In section C.0, we discussed the impact of the coil representation in the numerical model on the bath free surface deformation and concluded that the choice to describe the coil as a continuous sheet of current is responsible for an overestimation of the vertical displacement of the bath free surface. The same argument is still valid in the present case.

- ***Yoke representation***

In section C.2.2.2.1, we discussed the numerical treatment of the magnetic yokes in our model. There, two very strong hypotheses were posited, whereby the first consisted in representing the set of 3D yokes as a 2D continuous sheet. The impact of this first hypothesis is unknown. Unfortunately, measurements of the magnetic induction in the industrial scale IMF could not be performed during the course of the present project. Such measurements could have helped us characterize the effect of the yokes and possibly adjust the yoke representation in our model. However, we may speculate that the 2D continuous representation of the set of yokes, which does not allow any gaps in between each yoke, may lead to an overall increase in the magnetic induction in the internal region of the inductor, leading to a larger deformation of the bath free surface. The second hypothesis consisted in taking the yoke permeability as infinite, which results in a zero magnetic field penetration in the yokes. In case of a finite permeability, some penetration into the yokes would occur, resulting in a reduction of the overall electromagnetic power available within the melt. Therefore, the infinite permeability is an extreme scenario which probably tends to maximize the magnetic induction within the melt and thus the displacement of the free surface.

- ***Laser telemetry measurement precision***

The laser telemetry measurements should be taken with a grain of salt. These measurements were performed in difficult industrial conditions, where an uncertainty on the exact positioning of the telemeter may play a role in adversely affecting the measurement precision.

- ***Other***

The metallic support grill for telemetry measurements (Figure 79), placed over the top of the furnace, may also interact with the EM forces and eventually alter the bath free surface deformation. However, this factor was considered beyond the scope of our study.

2.2.2.3 Bath hydrodynamics

Figure 83 illustrates the distributions of the melt velocity (along with the flow structure) and of the turbulence intensity in the bath for the three investigated conditions. Since a steady state was never achieved during the calculations for Exp. A, only instantaneous distributions of the melt velocity and the turbulence intensity are presented hereunder. Meanwhile, a steady state was attained for the other two operating conditions and therefore the reported distributions are stable results.

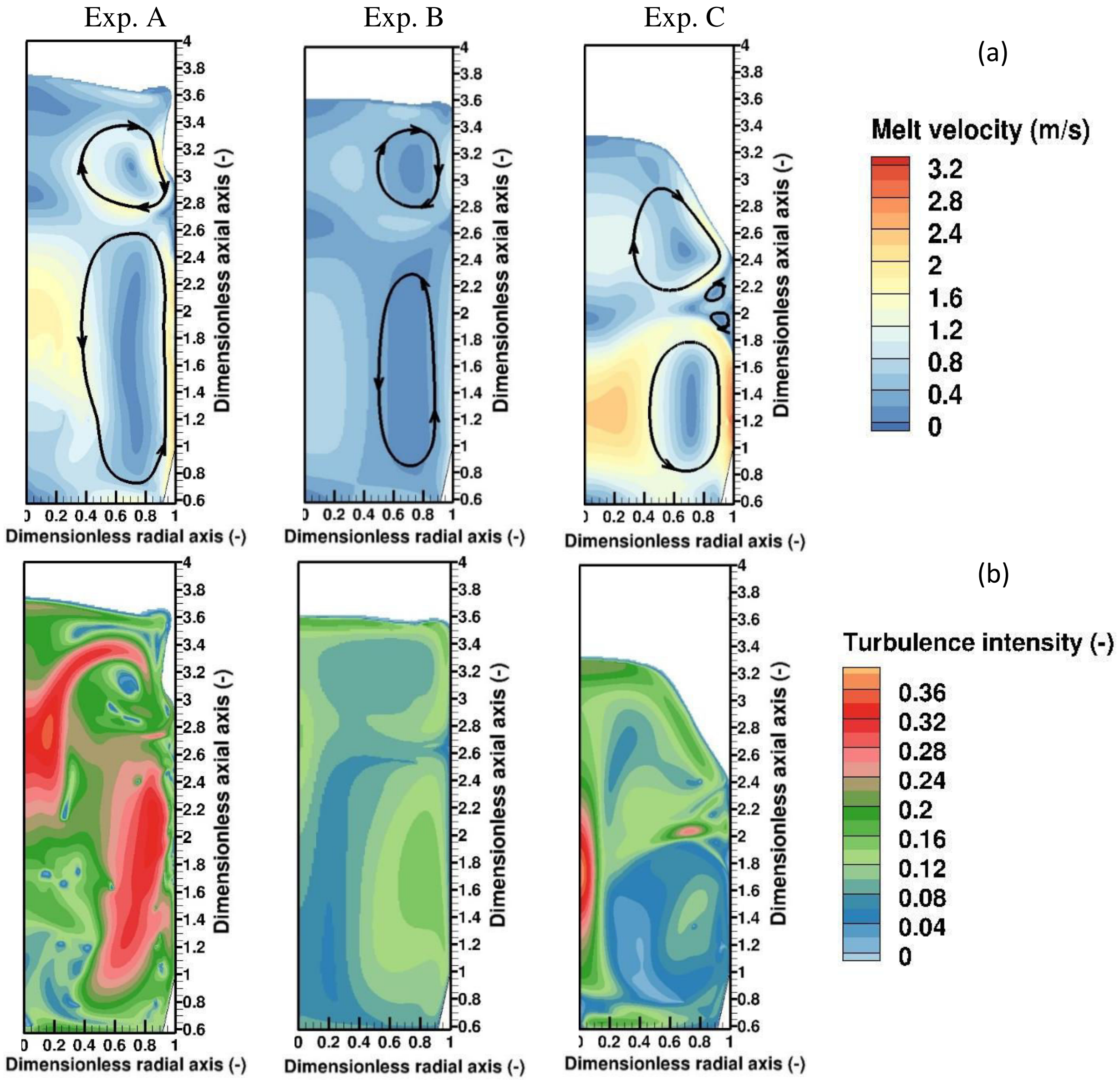

Figure 83: (a) Melt velocity and (b) Turbulence intensity distributions – industrial IMF

The presence of two main recirculation zones in each of the cases is observed, although the velocity fields are relatively different. Let us first compare the two stirring cases Exp. A and C. The melt velocity is very high in the central region of the bath in these two cases (reaching values of $2\ \mathrm{m.s^{-1}}$). Although the average melt velocity in the lower loop remains quite similar, the dome area is calmer for the stable Exp. C. The overall turbulence is much higher for Exp. A, as compared to Exp. C. A very high turbulence intensity zone (~0.3) near the furnace side wall for Exp. A is also noticeable. We observe some significant differences between the bath hydrodynamics of the stirring mode (Exp. A) and that of the holding mode (Exp. B). In Exp. B, we see very minor velocity gradients and the melt in the two recirculation zones is rotating at much lower velocities as compared to the stirred mode. Moreover, the flow is at least twice less turbulent as compared to the stirring mode, with calmer central bath regions. Table 20 summarizes the calculated bath magnetohydrodynamics results. In the two stirring modes, because of a similar current frequency and generator power, the ranges of values of the magnetic induction ~ 200 mT and the Lorentz forces ~ $8\mathrm{x}10^5$ N.m^{-3} are similar, albeit with different filling levels. The average melt velocity is around $0.45\ \mathrm{m.s^{-1}}$ with very high velocities (~ $2.5\ \mathrm{m.s^{-1}}$) in particular near the wall where Lorentz forces apply. Due to a higher current frequency in the holding mode (Exp. B), we observe a decrease in the EM skin depth. Also, the 50 % drop in the generator power significantly reduces the magnetic induction, which subsequently affects the melt velocity.

Table 20: Industrial scale MHD results

		Exp. A	**Exp. B**	**Exp. C**
		Stirring mode	Holding mode	Stirring mode
$\delta_{EM}/r_{furnace}$	(%)	5.8	4.0	5.9
Max. Magnetic induction	(mT)	200	100	200
Max. Lorentz force	(N.m^{-3})	$8\mathrm{x}10^5$	$2\mathrm{x}10^5$	$8\mathrm{x}10^5$
Turbulence intensity	(-)	[0;0.36]	[0;0.21]	[0;0.37]
Melt velocity	($\mathrm{m.s^{-1}}$)	[0;2.5]	[0;1.1]	[0;3]
Average melt velocity	($\mathrm{m.s^{-1}}$)	0.47	0.20	0.43

Spitans et al. [44] calculated the bath hydrodynamics in a 2 t industrial scale induction furnace. Another example of modeling of an industrial scale IMF can be found in the work performed by Henneberger et al. [132]. In both cases, the order of magnitude of the melt velocity is comparable to our results and the two loop flow structure is consistently present.

Finally, Figure 84 illustrates the profile of the shear stress due to the liquid metal flow along the lateral wall of the furnace. A maximum of around 50 Pa is observed near the bottom furnace corner in Exp. C. The order of magnitude is similar to what we may see in some liquid metal channels [133]. As the shear stress is directly related to the melt flow velocity, we see a higher stress for the two stirring mode cases compared to the holding mode. The change in the sign of the shear stress corresponds to the change in the flow direction, while zones with almost zero shear stress correspond to very quiet zones near the wall.

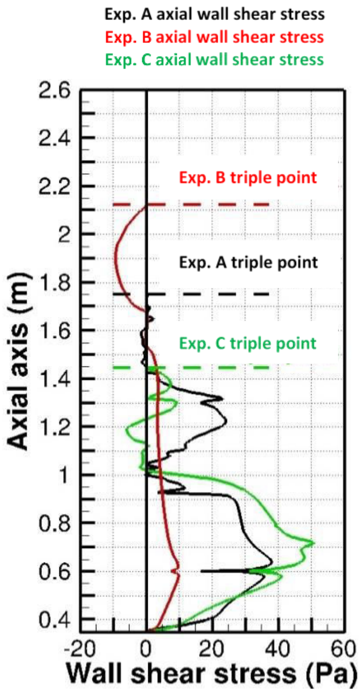

Figure 84: Computed shear stress along the lateral wall of the furnace

2.2.2.4 Dimensionless analysis of the induction furnace at lab and industrial scales

Table 21 provides another way of analyzing the relative importance of the phenomena at work in an IMF by evaluating some dimensionless numbers for both laboratory and industrial furnaces. We use the liquid aluminum properties found in Table 17 along with the thermal expansion coefficient for liquid aluminum $\beta=1\text{x}10^{-6}$ K^{-1} and the thermal diffusivity parameter $\alpha=2\text{x}10^{-5}$ $m^2.s^{-1}$.

Table 21: Dimensionless analysis of the induction furnace at laboratory and industrial scales

		Laboratory scale	**Industrial scale**
		Exp. 9	Exp. B
Characteristic length (diameter)	(m)	0.1	1
Average melt velocity	(m.s^{-1})	0.16	0.20
Max. Magnetic induction	(mT)	70	100
δ_{EM}	(m)	$4\text{x}10^{-3}$	$24\text{x}10^{-3}$
ΔT (assumed)	(K)	10	10
Shield parameter R_{ω}	(-)	625	1736

Magnetic Reynolds number Re_m	(-)	0.06	0.75
Hartmann number Ha	(-)	383	5477
Reynolds number Re	(-)	$4\text{x}10^{4}$	$5\text{x}10^{5}$
Stuart number N	(-)	4	63
Grashof number Gr	(-)	$6\text{x}10^{5}$	$6\text{x}10^{8}$
Gr/Re²	(-)	$4\text{x}10^{-4}$	$2\text{x}10^{-3}$
Marangoni number Ma	(-)	$1\text{x}10^{4}$	$1\text{x}10^{5}$
$\frac{Ma}{Re^2Pr}$	(-)	$4\text{x}10^{-4}$	$3\text{x}10^{-5}$

The shield parameter R_ω, previously defined in Eq. 2, indicates the distribution of the Lorentz forces in the bath. In the laboratory scale furnace, the shield parameter is valued at 625, indicating that the EM forces are confined within the EM skin depth. At industrial scale, the shield parameter is even larger (>1700), which indicates an even further concentration of the EM forces near the furnace walls.

The Magnetic Reynolds number is useful in ascertaining if the moving conducting fluid has an impact on the magnetic field through the rotational term in the induction equation (Eq. 12). The calculated Re_m is quite low (<<1) at laboratory scale while barely less than 1 for the industrial furnace. Having said this, the rotational term was in any case included in the UDF – Induc14 and was thus calculated along with the rest of the induction equation. From Table 21, its importance at the laboratory scale is negligible while it may play a minimal role in the industrial scale furnace.

Since we use the maximum magnetic induction found within the EM skin depth, we find that the Hartmann number is quite large (380 and 5500) at both scales, indicating the importance of the EM forces with respect to the viscous forces adjacent to the furnace walls. However, if the same is calculated at r/2 with a drastically reduced magnetic induction, the Hartmann number is either smaller than or of the order of unity, indicating the importance of viscous forces away from the furnace wall.

The Reynolds number of the bath in both cases is of the order of 10^4 indicating a turbulent bath flow. The Stuart number or the interaction parameter is the ratio of the EM forces and the inertial forces. In both furnaces, the Stuart number is greater than unity near the wall, while N<<1 away from the wall, which follows the shield parameter indicating the concentration of EM forces near the wall.

Coming to the aspect of heat transfer in the bath, we had previously hypothesized that due to the strong turbulence, the bath temperature is homogeneous and thus the energy equation is not solved. Supposing a temperature gradient of 10 K, the ratio of buoyancy to inertial forces indicated by Gr/Re^2 is much smaller than unity in both furnaces, supporting our hypothesis. However, at the industrial scale, the natural convection forces may play some role in zones with lower Reynolds number (near the free surface or the central bath zones). The calculation of the ratio $\frac{Ma}{Re^2Pr}$ clearly demonstrates that the Marangoni effect does not plat any role in the macroscopic fluid flow in both laboratory and industrial furnaces.

2.3 Inclusion behavior – modeling results

In the following section, the stationary MHD results are used as a base to calculate the transient evolution of the inclusion population in the holding mode (Exp. B) operation of the industrial furnace. Before going any further, we discuss hydrodynamic conditions which play a primordial role in the turbulence aggregation kinetics of the inclusions. Figure 85 presents the contours of the turbulence dissipation rate, the Kolmogorov length scale and the turbulence kinetic energy.

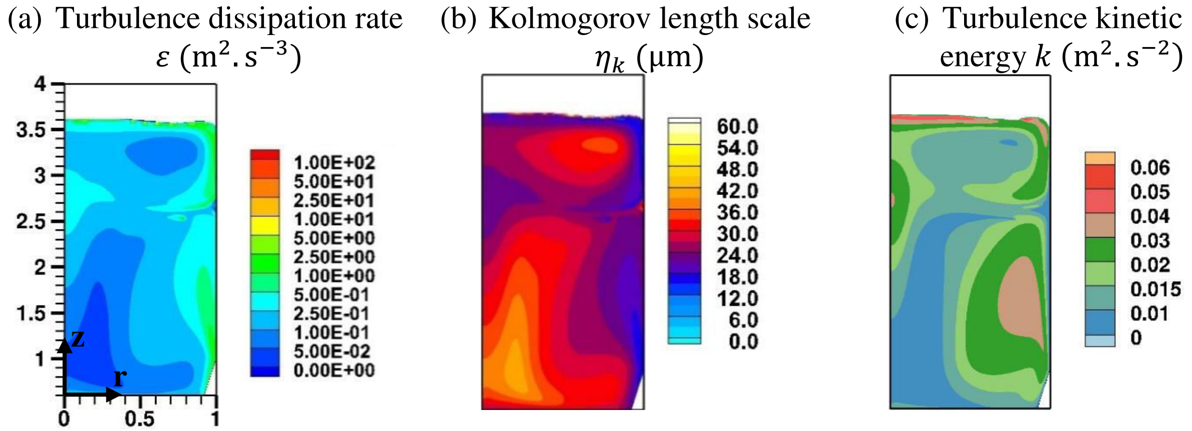

(a) Turbulence dissipation rate ε $(\mathrm{m^2.s^{-3}})$

(b) Kolmogorov length scale η_k (µm)

(c) Turbulence kinetic energy k $(\mathrm{m^2.s^{-2}})$

Figure 85: (a) Turbulence dissipation rate, (b) Kolmogorov length scale and (c) turbulence kinetic energy for Exp. B

The Kolmogorov length scale determines whether or not the agglomeration takes place in the smallest eddies in the local shear flow condition. In an affirmative case, the aggregation frequency is explicitly a function of the local turbulence dissipation rate. We notice that the Kolmogorov length scale varies from 5 µm in the high turbulence zones to almost 60 µm in the low turbulence zones. The length scale remains larger than 20 µm in the majority of the bath.

The maximum turbulence dissipation rate for Exp. B is 15 $\mathrm{m^2.s^{-3}}$, with a zone of high turbulence dissipation near the furnace wall regions readily explained by the source of kinetic energy (Lorentz force) in the electromagnetic skin and by the friction in the viscous sublayer. The zones with higher turbulence kinetic energy (near the bath free surface and within the bottom recirculation zone), indicative of high velocity fluctuations, play a role in determining the aggregation kernel, especially in the case of the larger inertial particles. All these regions may favor the inclusion collisions and hence aggregation.

Table 22 presents some other characteristic values and dimensionless numbers for the modeling of particle transport and interactions deduced from the MHD simulation. These are the maximum sedimentation and electromagnetic migration velocities which particles of a given size may attain. Moreover, the ranges of the Reynolds number and the Stokes number for the particle are also tabulated for three particle sizes – 10, 50 and 150 µm.

Table 22: MHD results for Exp. B – inclusion behavior model preprocessing

	Particle size (µm)		
	10	50	150
Max. sedimentation velocity $\mathbf{u}_{\mathbf{sed,i}}$ $(\mathrm{m.s^{-1}})$	6.20x10^{-5}	1.55x10^{-3}	1.40x10^{-2}
Max. EM migration velocity $\mathbf{u}_{\mathbf{em,i}}$ $(\mathrm{m.s^{-1}})$	8.00x10^{-4}	2.00x10^{-2}	1.80x10^{-1}
Reynolds number for the particle $\mathrm{Re_p}(-)$	(1x10^{-3}; 2x10^{-2})	(2x10^{-1}; 3x10^{0})	(5x10^{0}; 7x10^{1})
Stokes number for the particle $\mathrm{St_p}(-)$	(4x10^{-3}; 2x10^{-1})	(1x10^{-1}; 4x10^{0})	(9x10^{-1}; 4x10^{1})

The sedimentation and EM migration velocities steadily increase with the particle size due to their quadratic dependence. The EM migration is about 10 times the sedimentation velocity influencing the inclusion transport primarily in the electromagnetic skin depth adjacent to the furnace wall. Thus, there is already a strong indication that the high values of the EM migration velocities near the furnace wall, compared to the sedimentation velocities (and even the mean melt velocities in the boundary layer) may result in a high inclusion capture rate due to the electromagnetic forces. The Reynolds number is larger than unity for the 150 µm sized particle in the entire bath, indicating that the Stokes regime is not satisfied in any of the control volumes in the bath. Therefore, in order to improve on the precision of the inclusion transport, our choice for the drag coefficient $(\mathrm{C_D} = 24/\mathrm{Re_p})$ would require a correction by use of Eq. 56. On the other hand, the inertial nature of the big sized particle $(\mathrm{St_p} > 1)$ does not impact the aggregation calculation since the validity of Zaichik et al. [117] model extends to particles whose size is larger than the Kolmogorov length scale and the arbitrary particle fluid density ratio.

Initial $MgAl_2O_4$ particle size distribution (psd)

As indicated earlier in section B.1.1, our study was restricted to the spinel type inclusion of $MgAl_2O_4$, considered as a sphere. We have used a log-normal law to model (Annex 5) the initial particle size distribution [91] with a total concentration equal to $5.2\text{x}10^{-3}$ kg. m^{-3} corresponding to 2 ppm of total mass content. In real Al baths, other inclusion types coexist with $MgAl_2O_4$ amounting to a total inclusion concentration of 2 ppm. However, in the current calculations we assume that all inclusions in the bath behave as $MgAl_2O_4$ type inclusion.

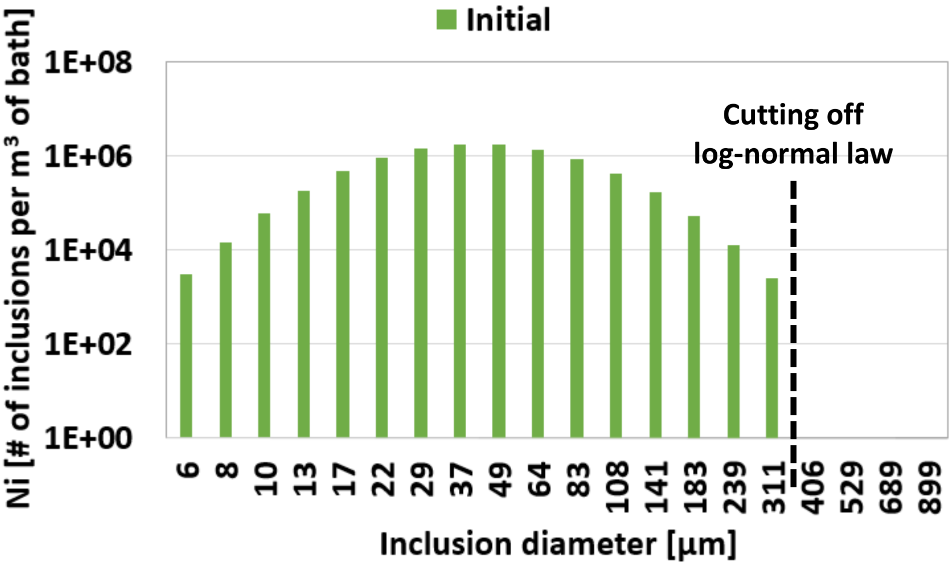

Figure 86: Adopted initial inclusion psd – 2 ppm

The distribution was cut off at 311 µm, but the maximum pivot size used is 899 µm in order to leave the last few classes empty for a coherent calculation of the fixed pivot technique.

2.3.1 Simulation and analysis of inclusion behavior in Experiment B

This section focusses on the inclusion behavior for operating parameters corresponding to Exp. B, during which the following conditions were considered:

- Inclusion transport:
  - melt flow, sedimentation and EM migration
  - no turbulent deposit at the interfaces nor any turbulence dispersion in the bath
- The inclusion interaction was limited to the aggregation of particles¤

2.3.1.1 Inclusion behavior

Evolution of psd

The number densities of inclusion populations N_i are calculated at each pivot class i, at each time step and within each cell volume of the aluminum bath. It allows us to study the evolution of the average particle size distribution over the entire bath volume, with respect to time, as reported in Figure 87. It clearly highlights a strong reduction of the population within the bath after a few minutes of treatment regardless of the inclusion size.

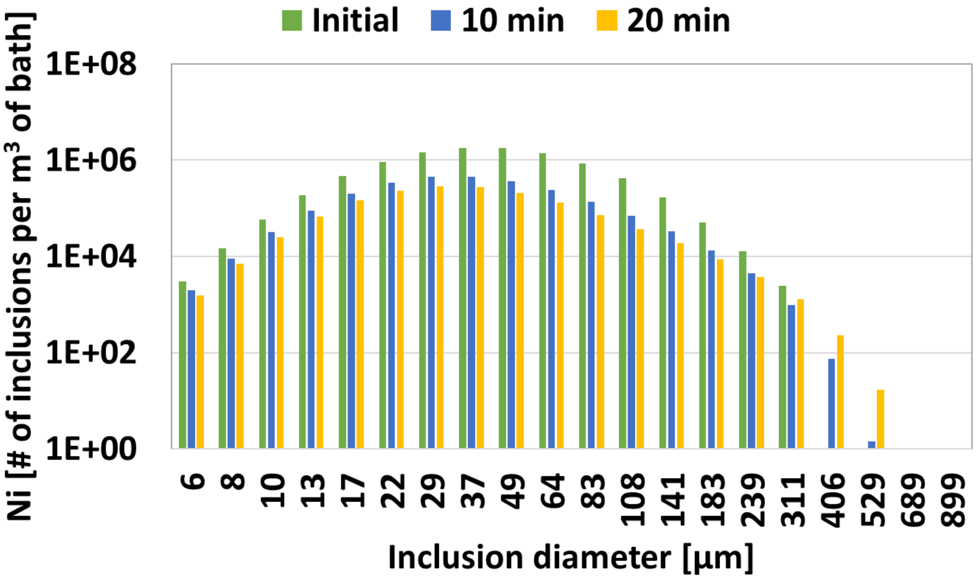

Figure 87: Evolution of inclusion psd for Exp. B – 2 ppm

The inclusion removal appears to be more effective for large sized inclusions. For instance, we notice a 50 % decrease of the number density for 10 µm inclusions after 20 minutes while 141 µm inclusions have been removed to the tune of 90 %. However, the individual participation of each phenomenon, especially the obscured inclusion aggregation can-not be analyzed using this figure. We discuss it later, especially with the help of removal frequency for each phenomenon.

¤ The mechanism of fragmentation requires data concerning the adhesion forces at the scale of an aggregate, which unfortunately remain unknown. Our work, thus, does not take into account this phenomenon while modeling the inclusion behavior in the bath. Nevertheless, an additional study was performed to understand the aggregation-fragmentation equilibrium, described in section C.2.3.1.3.

Evolution of the total number and mass of inclusion population

Figure 88 illustrates the striking drop of the total mass of the inclusion population in the bath to only 14 % of the initial total mass after 20 minutes of processing time. On the other hand, Figure 89 presents the total number of inclusions in the bath which duly follows the mass evolution curve and drops down to 16 % of the initial total number of inclusions.

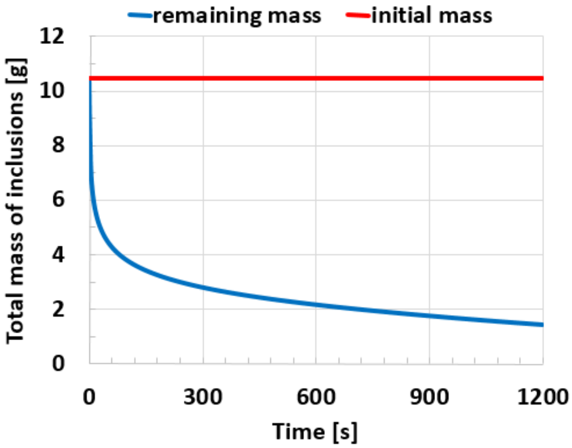

Figure 88: Evolution of total mass of the inclusion population in the bath for Exp. B – 2 ppm

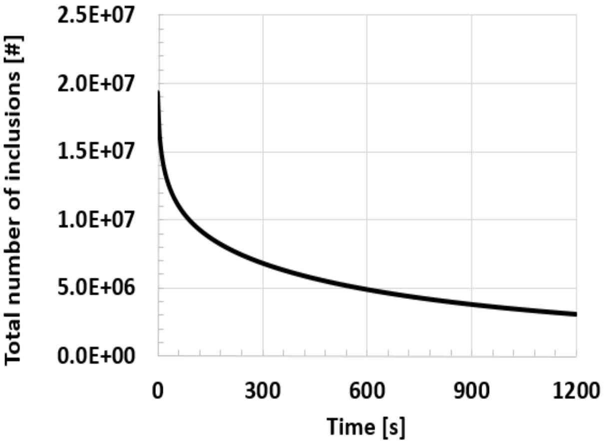

Figure 89: Evolution of total number of inclusions in the bath for Exp. B – 2 ppm

In Table 23, the global balance at 20 minutes of processing time is presented. The mass balance is verified, evident by the negligible relative error of the order of 10^{-7}. The various contributions of each removal phenomenon at different interfaces are also tabulated. The trend in Figure 88 can be analyzed by the relative role of the two removal mechanisms i.e. gravitational and electromagnetic separation. For the inclusion type and the initial psd currently being considered, only 3.42 % of the captured inclusions are removed as a result of the sedimentation at the furnace bottom. It confirmed that the electromagnetic force is comparatively very strong. The electromagnetic force is primarily confined in the EM skin depth adjacent to the furnace side wall, leading to almost all inclusion removal due to EM migration (99.30 %) occurring at this wall. Obviously this level of removal is valid for the considered inclusion type and is susceptible to change with the inclusion properties.

Table 23: Verification of global balance for Exp. B – 2 ppm at 20 min of processing time

Global balance				
Time	1200.00	[s]		
Initial total mass of the inclusion population in the bath	10.4773	[g]	100.00	[%]
Total mass of the inclusion population left in the bath	1.4546	[g]	13.88	[%]
Total mass of the inclusion population *captured*	9.0227	[g]	86.12	[%]
Error $\Delta m/m_0$	-5.6E-07	[-]		

Contributions of each phenomenon to inclusion population capture				
Total captured due to EM migration	8.7145	[g]	96.58	[%]
Furnace side wall	(8.6533)	[g]	(99.30)	[%]
Bath interface	(0.0026)	[g]	(0.03)	[%]
Furnace bottom wall	(0.0587)	[g]	(0.67)	[%]
Total captured due to gravitational separation at bottom wall	0.3082	[g]	3.42	[%]

Contours of different inclusion size populations at different processing times

Figure 90 illustrates the distribution contours of the number density for two inclusion sizes (13 μm and 49 μm) at three different processing times (20 s, 60 s and 600 s).

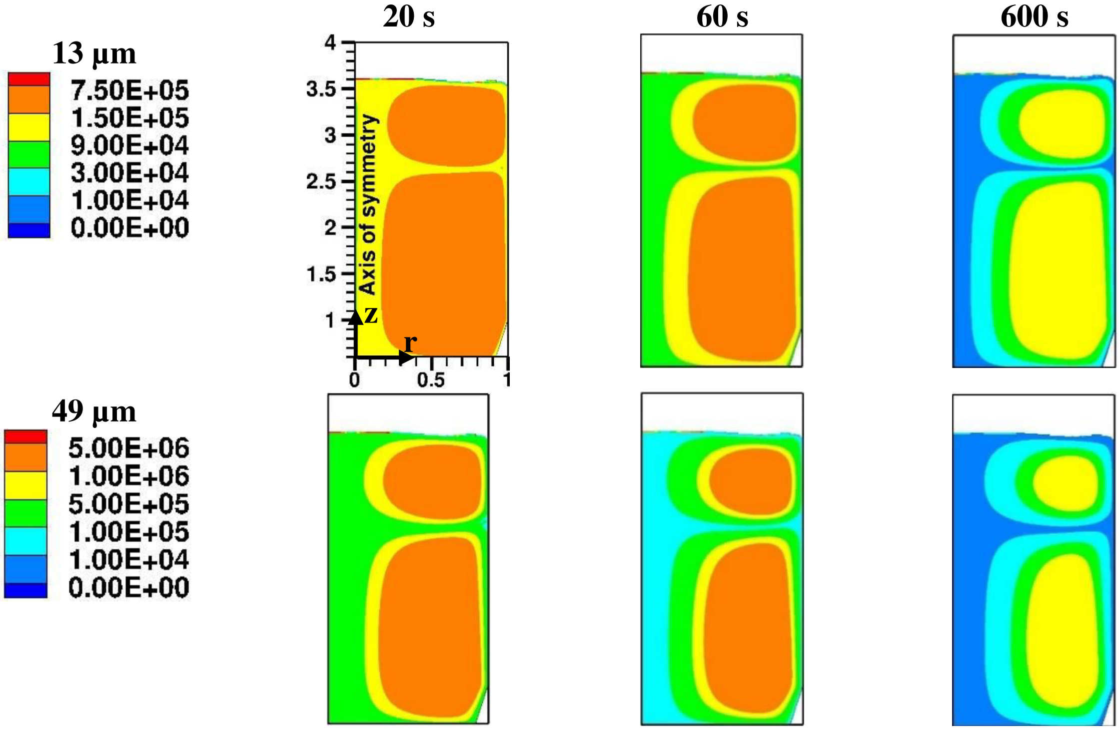

Figure 90: Temporal evolution of number density (# of inclusions per m^3 of melt) distribution contours for two inclusion sizes for Exp. B – 2 ppm

Compared to the uniform initial distribution, we now observe that the particle concentration in the bath is distributed inhomogeneously. This important result shows evidence of the need to couple the population balance model to the computational fluid dynamics. With the contours at different time intervals, we can see that the particles in the centers of the two recirculation zones remain within the bath while the particles at the outer periphery of the recirculation zones may enter the electromagnetic skin, where they are dragged by the EM drift velocity towards the wall. An important part of the population is then removed at the side wall. Therefore, a continuous decrease of particle concentration with respect to time is noted, which is in accordance with the already discussed global mass removal trend.

Evolution of the average and the average Sauter diameters of the inclusion population

Figure 91 presents the continuous approximation of the previously reported evolution (Figure 87) of the inclusion psd. Additionally, the inset figure shows the time evolution of the average diameter and the average Sauter diameter of the inclusion population in the bath.

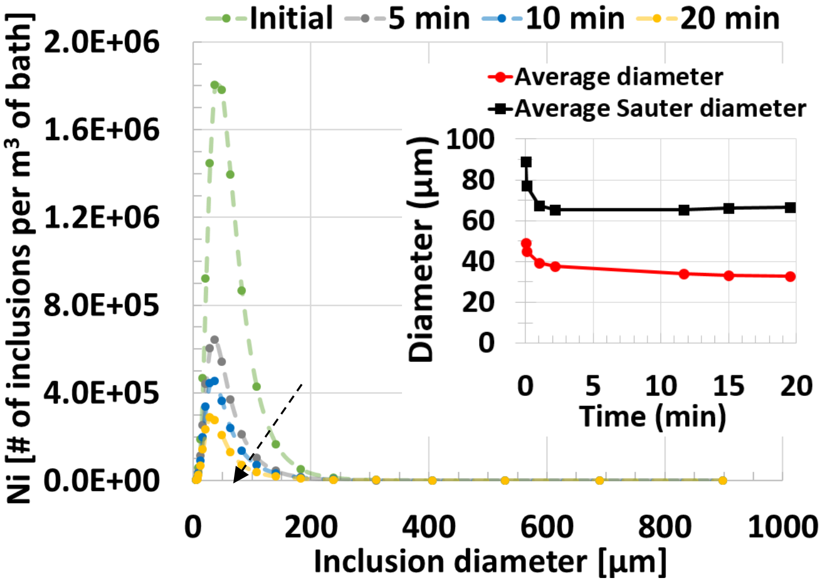

Figure 91: Evolutions of inclusion psd, average diameter and average Sauter diameter

The average diameter $\bar{d}$ and the average Sauter diameter $\overline{d_{32}}$ are expressed in Eq. 106. The average Sauter diameter is defined as the ratio of the third to the second moments of the psd, while the ratio of the first moment to the total inclusion concentration in the bath gives the average diameter.

$$\bar{d} = \frac{1}{V_{bath}} \int_{V_{bath}} \left(\frac{\sum_{i=1}^{M} N_i d_{p,i}}{\sum_{i=1}^{M} N_i} \right) dV \; ; \; \overline{d_{32}} = \frac{1}{V_{bath}} \int_{V_{bath}} \left(\frac{\sum_{i=1}^{M} N_i \, d_{p,i}^3}{\sum_{i=1}^{M} N_i \, d_{p,i}^2} \right) dV \qquad (106)$$

As indicated with the help of an arrow, it is clear that with time, the inclusion psd is decreasing in amplitude as well as in its width. This follows the previously discussed overall removal of the inclusion population along with a preferential removal of the larger sized particles.

A correlation with the trend seen in the inset figure may be established. The average diameter continues to decrease (to ~ 33 µm) corresponding to the removal of the inclusions and thereby illustrating the remaining population being primarily contained in the smaller classes. The mean

Sauter diameter attains a quasi-constant value of 65 µm after a time period of around 2 minutes indicating a constant change of the skewness of the curve (third moment) with respect to the variance (second moment) of the psd. It can once again be explained by a more intense elimination of large size particles with respect to the smaller ones.

Removal frequency for each phenomenon

The previous results make the analysis of the aggregation events with respect to the capture events difficult, since the magnitude of aggregation of inclusions is masked by the inclusion removal due to sedimentation and electromagnetic migration. To this end, Figure 92 shows the class wise inclusion removal frequency (#.s^{-1}) for each phenomenon at an intermediate process time of 30 seconds. The removal frequencies (Eq.107) were calculated at all furnace walls and the bath free surface, for the EM migration effect, at the furnace bottom wall for the sedimentation effect and averaged over the entire bath for the aggregation phenomenon.

$$\begin{gathered}
\forall i \in [1, M]; j \in \{walls, free\ surface\}; \Psi_{em,j,i} = \int_{face_j} (\alpha_l \rho_f \varphi_i) u_{em,i} dS_j \\
\forall i \in [1, M]; bottom\ wall;\ \Psi_{sed,i} = \int_{face_{bottom}} (\alpha_l \rho_f \varphi_i) u_{sed,i} dS \\
\forall i \in [1, M]; \Psi_{agg,i} = \int_{V_{bath}} H_i^{agg} dV
\end{gathered} \tag{107}$$

The positive or the negative signs respectively demonstrate the net birth or the net death of inclusions due to aggregation occurring in that particular class. Therefore, the psd up until the inclusion size of 108 µm, suffers with a net removal of inclusions, and may reach a rate of 10^3 inclusions per second. On the other hand, the inclusion populations beyond this class register a net generation, albeit at a much slower rate for the largest sizes (< 1 #.s^{-1}).

The quadratic size dependence of the sedimentation $\boldsymbol{u_{sed,i}} = ({d_{p,i}}^2(\rho_P - \rho_f)\boldsymbol{g})/18\mu_f$ and electromagnetic drift $\boldsymbol{u_{em,i}} = (-{d_{p,i}}^2 \boldsymbol{F_{Lorentz}})/24\mu_f$ velocities explains the fact that larger particles are more easily transported than the smaller ones. For small inclusion sizes (< 30 µm), the removal frequency due to the EM migration is of the same order of magnitude or even smaller than aggregation, resulting from the small migration velocities for these sizes. In the remainder of the psd till 311 µm, the inclusion removal due to the EM migration near the interfaces outpaces the total aggregation in the bath. Meanwhile the inclusion sedimentation remains a negligible phenomenon for all sizes. The population in larger classes (> 400 µm), which were initially absent in the bath, are generated due to aggregation at a relatively faster pace than their removal due to

EM effect. This may be a result of the aggregation occurring in bath zones favoring collisions, away from the near wall or free surface areas where the EM field is concentrated.

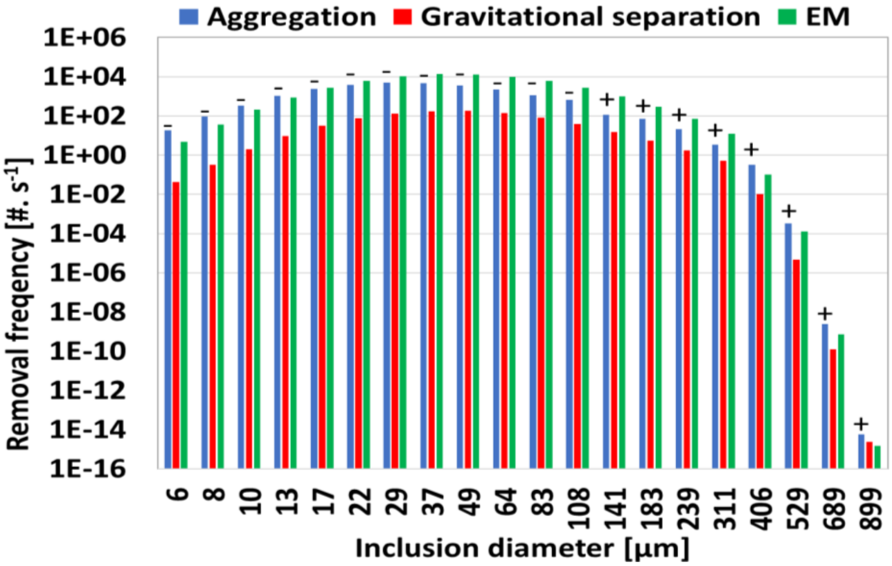

Figure 92: Frequencies of the three events at time of 30 s – Exp. B – 2 ppm

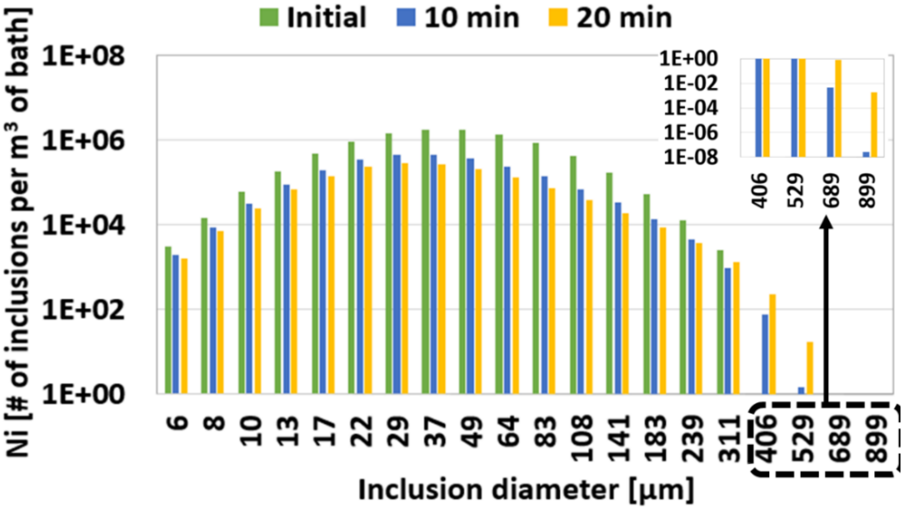

Figure 93: Focus on larger classes of inclusion psd for Exp. B – 2 ppm

In Figure 93, we continue to see the same trend of higher aggregation rate at the process time of 20 minutes. A closer look at the psd along with a zoom of the last few classes (see inset figure) reveals an increase of the number density of the large sized particles (>300 µm) with respect to the intermediate time period of 10 minutes, even though the concentrations remain extremely low at less than 1 inclusion per m^3 of melt for the largest sizes (> 600 µm).

Table 24 describes the characteristic time (Eq. 108) for each of the discussed phenomenon, illustrating the time required to separate inclusions from the bath, considering the removal frequency (Ψ_i) calculated at a given process time.

$$\forall i \in [1, M];\ \tau_{em,i} = \frac{N_{i,bath} V_{bath}}{\Psi_{em,i}};\tau_{agg,i} = \frac{N_{i,bath} V_{bath}}{\Psi_{agg,i}};\ \tau_{sed,i} = \frac{N_{i,bath} V_{bath}}{\Psi_{sed,i}} \tag{108}$$

For the 13 μm inclusions, the characteristic time for aggregation is slightly smaller than the EM migration, suggesting a competition between the two phenomena. But these two phenomenon cannot be considered as competitive but complementary mechanisms since small inclusions collide to form larger aggregates which are more easily transported by electromagnetic forces. Hence the characteristic time for EM migration remains quite small for the rest of the tabulated inclusion sizes (< 3 minutes i.e. smaller than the operation time). Hypothetically, if the inclusions were to be removed only by sedimentation, the process time required would be to the tune of several hours or even days for the smallest inclusions.

Table 24: Characteristic time for each phenomenon for Exp. B – 2 ppm (at t = 30 s)

Inclusion size μm	τ_{em} min	τ_{agg} min	τ_{sed} min
13	6.4	5.4	3 587
49	2.8	10.4	3 171
141	2.3	20.5	2 133
311	1.7	6.3	451

2.3.1.2 Calculation of the turbulent collision kernel

Let us examine the aggregation kernel (in $\mathrm{m^3.s^{-1}}$) due to turbulent collisions calculated through two different models proposed by Saffman and Turner [115] and Zaichik et al. [117] previously discussed in section B.1.3.3. Figure 94 compares the two turbulent collision rates for binary collisions between 6 μm and 8 μm particles (a) and between 108 μm and 141 μm particles (b). The kernel β^t is given as a function of the turbulent dissipation rate ε in the range (10^{-3} to 15 $\mathrm{m^2.s^{-3}}$) encountered in the aluminum bath. The corresponding particle Stokes numbers are also indicated. The Saffman and Turner kernel (Eq. 64) is a function of the particle diameter and the turbulence dissipation rate. When expressed in the logarithmic scale, the kernel is clearly represented by a straight line, as illustrated in Figure 94 (red lines). On the other hand, the Zaichik et al. kernel (Annex 6) additionally depends on the velocity fluctuations as well as the inertia of the particle. Therefore, the markers (black square) correspond to the kernel values calculated for respective turbulence values in each grid cell of the bath.

(a) Interaction between 6 µm and 8 µm particles

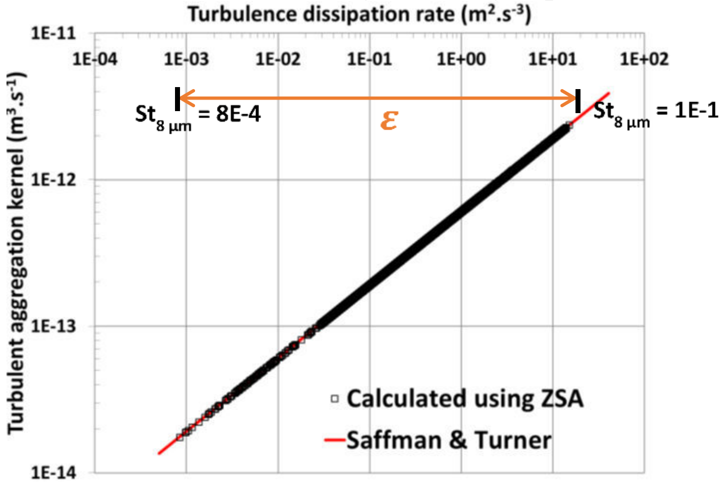

(b) Interaction between 108 µm and 141 µm particles

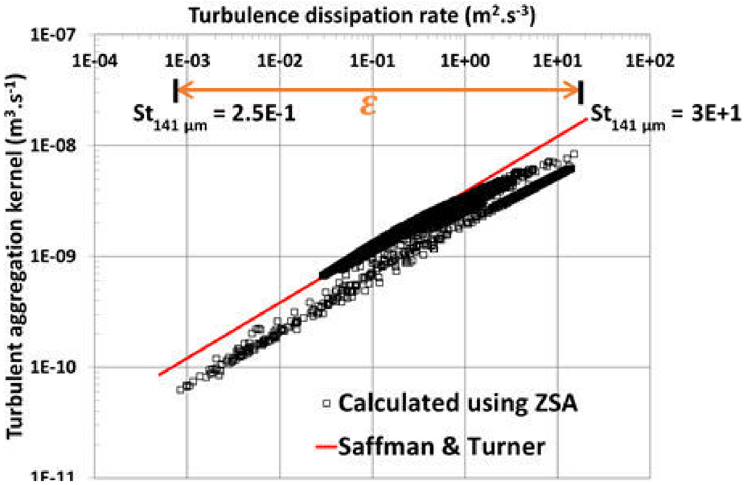

Figure 94: Comparing turbulent collision kernels calculated using Zaichik et al. and Saffman and Turner models for interactions between particle sizes (a) 6–8 µm, and, (b) 108–141 µm

The kernel calculated by the Zaichik et al. for the smaller particles (6 and 8 µm) is almost identical to that given by the Saffman and Turner model, since the particles are non-inertial ($\mathrm{St_p} < 1$). For the larger inclusions (108 and 141 µm) the Stokes number is larger than 1 in most of the bath cells and their sizes are larger than the Kolmogorov length scale, meaning that the Saffman and Turner model is not valid anymore. As a consequence, the Zaichik et al. model exhibits values often half or even a third of those calculated by the Saffman and Turner model.

2.3.1.3 A focus on aggregation and fragmentation of an inclusion population

In this section, we compare some results obtained from two different simulations according to Eq. 109 where: (i) inclusion may only aggregate, and, (ii) inclusion may aggregate as well as fragment.

In these two cases, the inclusion population is only transported by the average melt velocity, by forcing the sedimentation and the electromagnetic migration velocities to zero.

$$\begin{aligned} &\text{(i)} \quad \forall i \in [1, M]; \ \frac{\partial N_i}{\partial t} + \frac{\partial}{\partial x_j}\left(N_i \bar{u}_{f,j}\right) = H_i^{agg} \\ &\text{(ii)} \quad \forall i \in [1, M]; \ \frac{\partial N_i}{\partial t} + \frac{\partial}{\partial x_j}\left(N_i \bar{u}_{f,j}\right) = H_i^{agg} + H_i^{frag} \end{aligned} \qquad (109)$$

Only aggregation of the inclusion population

The process of aggregation when modeled all alone using Eq. 109 (i), is a quadratic process where the aggregation frequency continues to grow exponentially. Ultimately, this exponential growth of particle size may lead to a divergence and an erroneous calculation with very large inclusion concentrations in the last few classes of the psd. In order to ensure a mass balance, the fixed pivot technique requires a negligible number density in the last class M. This is contrary to the situation illustrated in Figure 95, where at the end of 30 minutes of aggregation, very large inclusion concentrations (~10^3 $\#.\mathrm{m}^{-3}$) have taken birth in the last few classes of the distribution.

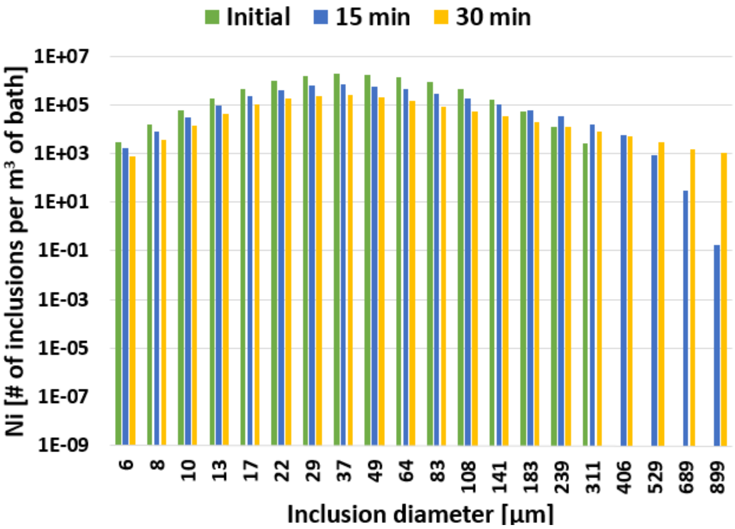

Figure 95: Evolution of inclusion psd when considering only aggregation for Exp. B – 2 ppm

Simultaneous aggregation and fragmentation of the inclusion population

To further study the inclusion interaction, the fragmentation process was taken into account (Eq. 109 (ii)). However, to describe the fragmentation kernel in Eq. 96, two hypotheses were made where the threshold diameter $d_{p,c}$ was selected as 108 µm, and the fragmentation efficiency α^{frag}~10^{-7} was adjusted so as to have a similar order of magnitude when compared to the aggregation kernel in the 108 µm class. These two hypotheses may not entirely represent the real physical processes occurring in the bath. Figure 96 presents the inclusion distribution for a much larger time duration (> 1 hour) while considering the two phenomena. The inclusion populations in the last few classes have undergone simultaneous fragmentation and aggregation, resulting in very small concentrations in the tail of the psd. A general stabilization of the process seems to be established where any aggregation of smaller particles into the large classes is countered by an equally strong fragmentation of the newly formed particles leading to a steady-state psd [134] [135]. Figure 97 summarizes these two cases by showing the evolution of the average diameter (black curves) and the average Sauter diameter (red curves).

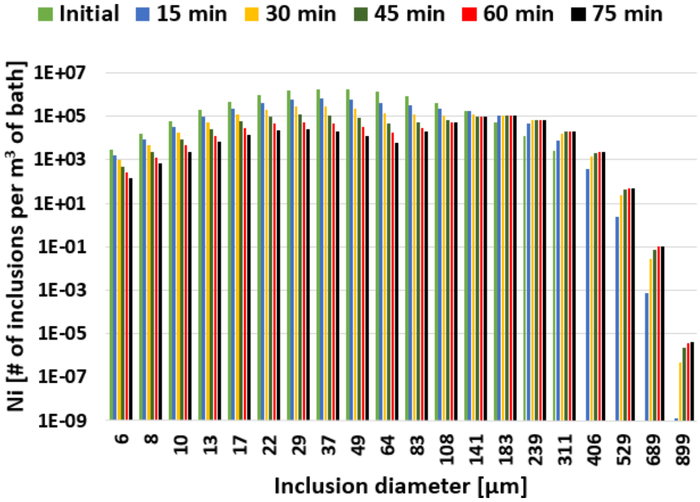

Figure 96: Evolution of inclusion psd considering both aggregation and fragmentation for Exp. B – 2 ppm

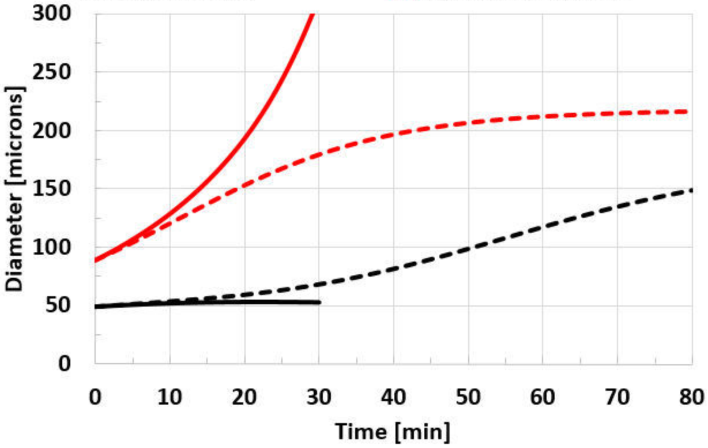

Figure 97: Comparing aggregation and fragmentation phenomena through inclusion population average diameters

The average Sauter diameter grows exponentially to 300 µm within 30 minutes of process time when only aggregation was considered because of the shift of the psd towards the large classes. However, the same attains an almost constant value ~215 µm, illustrating the relative canceling of the two phenomena and thus stability of the concentrations when fragmentation is also considered.

2.3.2 Effect of the total initial inclusion concentration

The initial psd was augmented ten times (20 ppm) compared to that studied in the previous section. The initial total mass of the inclusion population is hence equal to 104.8 grams. Figure 98 gives the initial psd for the two inclusion concentrations under study, with a logical difference of one order of magnitude between the N_i values. Figure 99 illustrates the evolution of the remaining mass fraction of the inclusion population in the bath for the two concentrations.

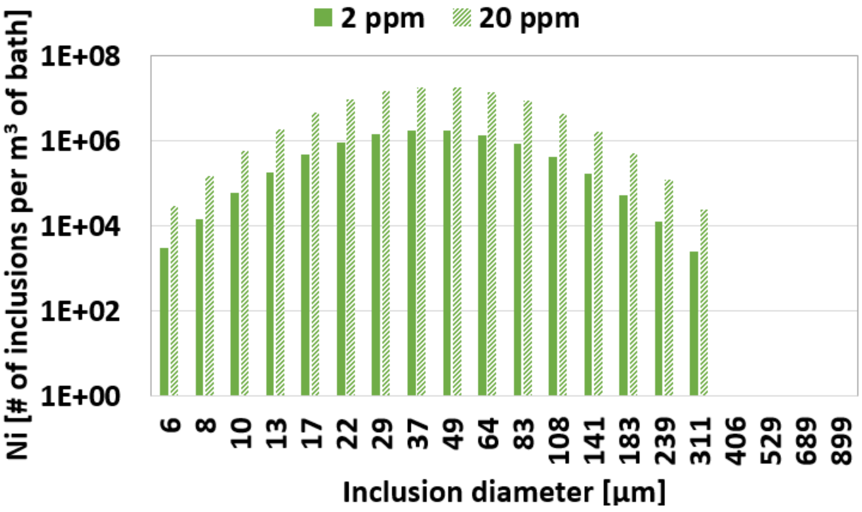

Figure 98: Initial inclusion psd for Exp. B – 2 ppm vs 20 ppm

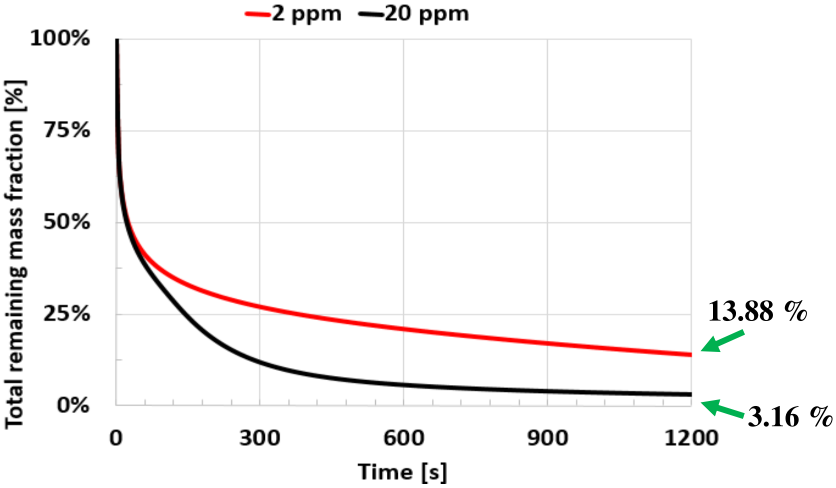

Figure 99: Evolution of remaining mass fraction of inclusion population with respect to time

At the end of 20 minutes, the 2 ppm case is left with almost 14 % of the initial mass while the 20 ppm case is almost empty with only 3% of the mass left in the bath. The total inclusion removal rate in the 20 ppm case (1.6x10^5 $\#.\mathrm{m}^{-3}.\mathrm{s}^{-1}$) is slightly more than ten times the rate in the 2 ppm case (1.4x10^4 $\#.\mathrm{m}^{-3}.\mathrm{s}^{-1}$), indicating an almost linear dependence of the global captured mass flux with respect to the inclusion concentration. From the pie charts in Figure 100, it seems that the sedimentation is almost twice as more effective for higher inclusion concentration, while the EM migration towards the boundaries remains the dominant removal phenomenon (~ 94 %) and almost singularly at the furnace side wall.

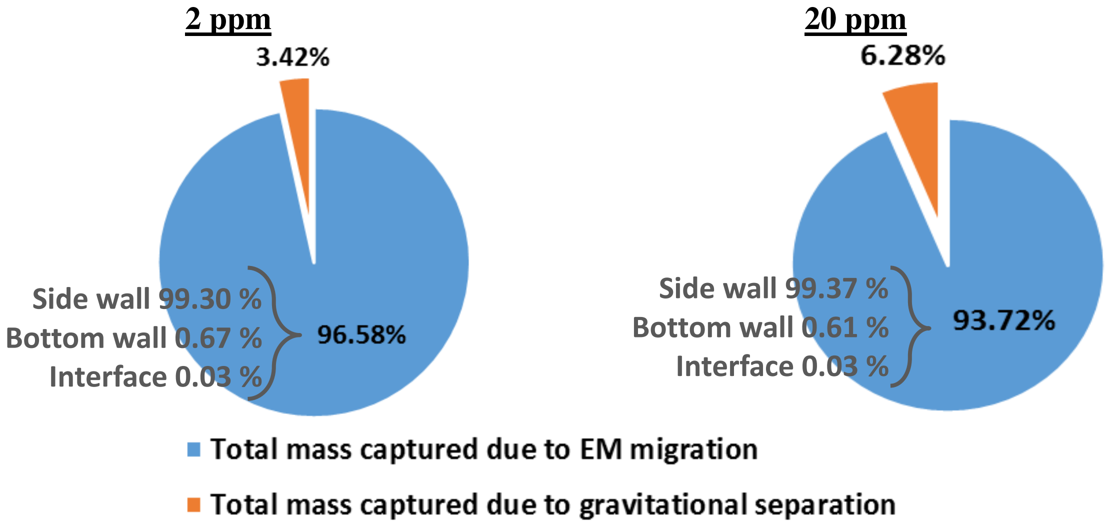

Figure 100: Contribution of each phenomenon to inclusion population capture – Exp. B for 2 ppm and 20 ppm concentrations

Effect of inclusion concentration on the removal frequency

Figure 101 compares the removal frequencies of each inclusion size for the three phenomena for inclusion concentrations of 2 and 20 ppm. Since the removal frequencies depend on the inclusion density in the bath, any increase of concentration will reflect on its removal rate. The EM migration effect seemingly becomes at least ten times more potent in removing the inclusions, while sedimentation although higher than in the 2 ppm case, still lags behind the other two phenomena.

The aggregation, however, sees a growth of almost hundred times since the removal frequency depends on the square of the inclusion concentration, resulting in a much higher rate of aggregation (Eq. 92). This follows the results seen in Figure 99, where a higher total inclusion removal rate was demonstrated for the 20 ppm case. An increase in the rate of aggregation of smaller inclusion sizes into larger sizes results in a more favorable elimination by the electromagnetic effect or by the gravitational separation. The inset figure shows the above trends regarding the removal frequencies for two inclusion sizes – 49 and 311 µm.

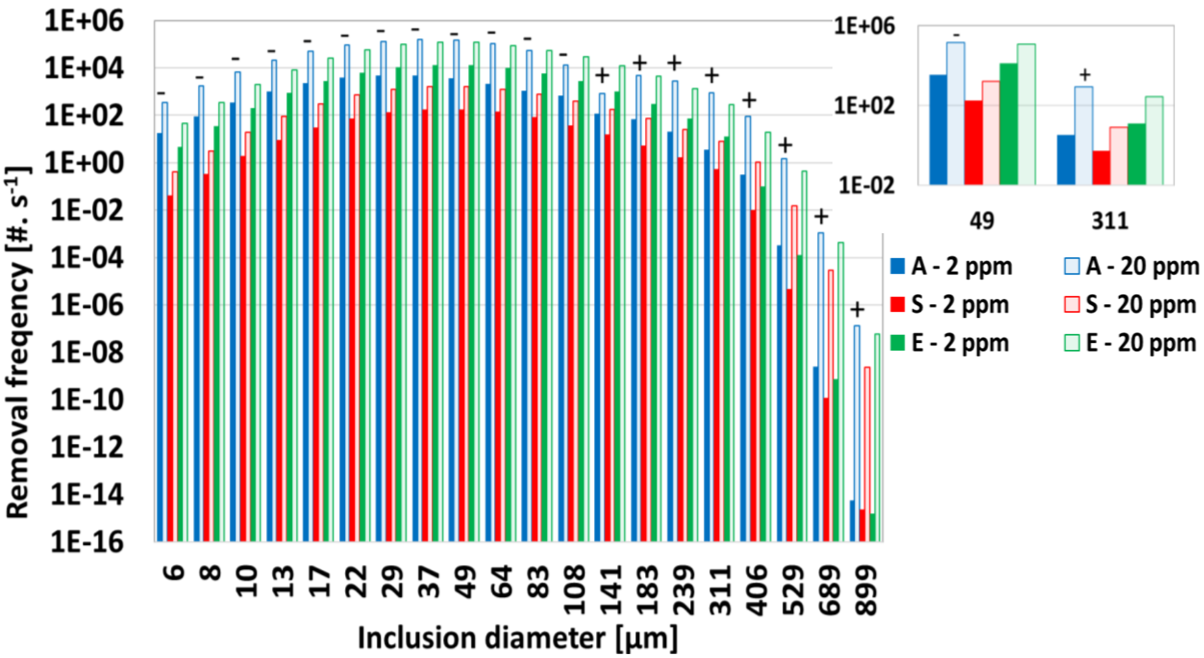

Figure 101: Comparison of removal frequencies of different phenomena at time of 30 s for two initial inclusion population concentrations

2.4 Conclusion on application on an industrial scale IMF

The application of the developed tools (both numerical and experimental) was performed on an industrial scale IMF. The obtained results fall into two broad categories of MHD and Inclusion behavior.

Magnetohydrodynamics in an industrial scale IMF

The bath free surface in the furnace was observed and measured using laser telemetry. The technique satisfactorily approximated the vertical displacement and was able to reproduce the general dome shape of the bath free surface. The surface fluctuations were also observed using video recordings which were later used to identify and confirm the different stirring modes.

The numerical model, developed and validated at the laboratory scale, was adapted to suit the complex industrial IMF design. An additional description of the magnetic yokes was required to model its significant impact on the magnetic induction. The experimental campaign provided the vital operating parameters as input parameters and as such three cases were simulated, corresponding to stirring and holding modes with different filling levels. The resulting hydrodynamics was found to be in agreement with literature for similarly sized IMFs. Moreover, the measured free surface was found to be comparable to the calculated free surface deformation, with certain discrepancy. The observed error was judged to be a sum of three main reasons: (i) the coil representation as a thin continuous block instead of separated coil turns, (ii) the magnetic yoke representation as a continuous sheet of ferromagnetic metal surrounding the inductor neglecting its real and complex 3D design, and (iii) the limitation of the laser telemetry technique and hence the measurements.

Inclusion behavior in an industrial scale IMF

The MHD results were used as a base in order to calculate the inclusion behavior considered to be a one-way interaction (which mean no influence of the particles on the macroscopic fluid flow). The Population Balance Method along with the Drift Concentration Method was used to model the transport as well as the interaction of spinel inclusion population (denser than aluminum) during the holding mode operation of the IMF.

The model shows that most of the $MgAl_2O_4$ (spinel) type inclusion population is quickly captured at the furnace walls due to electromagnetic migration. However, the strong assumption of a 100 % efficiency of the inclusion capture at the walls with no release may explain the large percentage (~85 %) of particle removal after a process time of 20 minutes. By increasing the concentration ten times, the particle removal efficiency further increases and almost 97 % of the inclusion population was deemed as captured.

An additional study of the inclusion interaction phenomena illustrates that the aggregation all alone is naturally diverging and can be stabilized (and reach a steady-state) by a simultaneous fragmentation of the inclusion population. However, the closure parameters of the fragmentation model remain unknown and are currently adjusted in our model to hold down the population birth and death rates to similar order of magnitudes.

Conclusion & Future Outlook

Conclusions

The principal objective of our work was to study the behavior of a non-metallic inclusion population in an induction melting furnace (IMF) and to provide a tool-box for future modeling of such installations. This was achieved by separately modeling the magnetohydrodynamics and the inclusion behavior in the IMF. Two corresponding numerical tools were thus developed, which are summarized as follows.

- ***Modeling the MHD phenomena***

A strong electromagnetics – hydrodynamics coupling was employed in the MHD numerical model, initially developed by SIMAP laboratory in Grenoble. The tool was based on the ANSYS Fluent software, which calculated the bath hydrodynamics and the free surface deformation in a 2D axisymmetric representation of the IMF, whereas a customized User Defined Function (UDF) solved the induction equation. The impact of the oxide layer (in the form of a friction force) on the bath free surface deformation and the bath hydrodynamics was additionally modeled assimilating it as a pseudo-wall, thanks to a UDF plugged into the ANSYS Fluent platform. The main model input parameters were the inductor current intensity and the initial filling level, obtained from an experimental campaign. Once the MHD model was validated at the laboratory scale (~4 kg of metal), it was scaled up to describe an industrial furnace (few tons of metal) with complex design features. Magnetic yokes present in that furnace were modeled by introducing specific boundary conditions using an additional UDF.

- ***Modeling the inclusion behavior***

The inclusion population behavior model comprised a UDF – TABInc2D (Transport, Aggregation and Breakage of Inclusion in 2D) which interfaced directly with ANSYS Fluent. A one-way fluid-particle interaction was considered due to the highly diluted particle concentration in the Al bath. The steady state MHD results were used as input data in order to calculate the transient inclusion behavior. In addition to the MHD results, the inclusion type (spinel $MgAl_2O_4$), its properties (denser than liquid aluminum and electrically non-conducting) and the particle size distribution (psd) were the other model input parameters. A combination of the Drift Concentration Method and the Population Balance Method was used to respectively model the mean transport of inclusions within the bath and the inclusion interactions such as turbulent aggregation and fragmentation. The time splitting technique was applied to separate the transport and the interaction members of the PBE (solved using a class method), to alleviate the complex calculations.

We obtained several key experimental and numerical simulation results, for both magnetohydrodynamics and inclusion behavior. They are summarized in the following paragraphs.

- ***Results from the experimental study of MHD***

The numerical modeling of magnetohydrodynamics was successfully complemented by an experimental work, at both laboratory and industrial scales. At the laboratory scale, a contactless structured light technique was used to measure the bath free surface, resulting in an instantaneous 3D dome profile. This has confirmed its axisymmetric nature, justifying our 2D axisymmetric assumption. The application of this technique is of particular note since it addressed the inadequacies of the earlier techniques, noticeably by performing precise and dynamic measurements of a much larger portion of the bath surface kept at high temperatures. The laser telemetry technique was implemented at the industrial scale to measure the bath surface. The combination of a lower technique accuracy and the relatively constrained access around the industrial setup led to satisfactory albeit less precise measurements of the bath surface vertical displacements. Hence the performance of the MHD numerical tool was evaluated by comparing the model results with the experimental results at both scales.

- ***Results from the numerical simulations of MHD***

At the laboratory scale, the simulation results illustrated that the oxide layer had an important impact on the dome profile. The friction induced by the oxide layer noticeably reduced the calculated maximum height of the interface at the axis by almost ~25 % for the reference case. It also lowered the overall melt velocity. The comparison of the calculated dome profiles with the measured dome profiles demonstrated a similar shape and order of magnitude for all cases considered in our study. The relative error of over 50 % between the measured and the calculated vertical displacements may possibly be due to the simplified representation of the induction coil in the numerical model. At the industrial scale, three cases were simulated, corresponding to stirring and holding modes with varied operating parameters. The calculated bath hydrodynamics results at this scale were found to be consistent with previous studies found in the literature. Meanwhile, the telemetry measured vertical displacements of the free surface were comparable to the calculated results. The observed error, may be a result of the induction coil representation, the magnetic yoke representation, the limitation of the laser telemetry technique and the presence of the metallic support grill over the furnace.

- ***Results from the inclusion behavior simulations***

The inclusion behavior simulations were performed for the holding mode operation of the industrial IMF. The initial inclusion psd was based on the experimental data provided by the industrial partner. These simulations showed that the inclusion population quickly got captured at the furnace side wall, primarily due to the electromagnetic migration. The assumption of the complete inclusion capture at the furnace walls with no release explained the high inclusion removal efficiency. It was further demonstrated that an increase in the initial inclusion population concentration increased the removal efficiency due to the combination of the aggregation and the electromagnetic migration. The relative importance of each phenomenon was duly illustrated, whereby the characteristic removal time for the electromagnetic migration is shorter than those for aggregation and sedimentation. The fragmentation phenomenon was also studied and compared with aggregation, even though several of its parameters remain unknown and were therefore adjusted.

Future Outlook

The following themes could be explored in order to enhance our understanding of the multi-physics phenomena involved in the induction stirring process and to improve the assessment of the removal rate of inclusions.

Theoretical understanding

- Oxide layer

Despite modeling the impact of the oxide layer on the free surface deformation and the hydrodynamics, a correlation with the mechanical strength [60] of this layer could not be established. Additionally, we did not observe any oxide layer break-up during any of the experiments at the laboratory scale (Annex 7). Therefore, it could be interesting to further investigate these avenues as it may complete our understanding of the oxide layer break-up, the fragment engulfment and perhaps its transport by the turbulent flow within the bath.

- Fragmentation of inclusions

While calculating the inclusion fragmentation, three hypotheses were laid out: (i) an inclusion break-up gives birth to two equal sized daughter inclusions, (ii) the threshold diameter ($d_{p,c}$) was selected as 108 μm, and, (iii) the fragmentation efficiency (α^{frag}) was adjusted such that aggregation and fragmentation frequencies were similar for this range of size. These three hypotheses require further examination for an accurate modeling of the phenomenon.

- Fate of inclusions

The *no release* assumption of the inclusions at the furnace wall was only a first step towards modeling, and does not represent the real process occurring in the furnace. A near wall treatment should be added in order to model the phenomena such as wall agglomeration and potential release of inclusions back into the bath. Scepanskis [136] opens the way with a first analysis of the sintering mechanism between an inclusion and an aggregate already attached to the wall or directly with the furnace wall.

Experimental analysis

Additional experiments may throw light on some aspects:

- Magnetic induction in an industrial scale IMF

As it was performed on the laboratory scale IMF, magnetic induction measurements in the industrial scale IMF would show the impact of the presence of the magnetic yokes and thus may help improve the overall model accuracy while accounting for the magnetic yokes.

- Inclusion population in an industrial scale IMF

Usually the metal cleanliness is measured using LiMCA or PoDFA techniques in the liquid metal stream exiting the furnace. This obscures any history of the inclusion population during the process. A dynamic, real time measurement during the stirring or holding process may be able to provide a valuable insight into various phenomena acting on the inclusion population. Such an experimental campaign would allow a verification as well as improvement of the current numerical model. A particular attention should be paid (if technically possible) on the location of the deep sampling since the simulations have revealed a noticeable non-homogeneous inclusion concentration within the bath.

Additional numerical model features

- Turbulent deposit of inclusions at the interfaces

The work currently being carried out at the Ecole Centrale Paris, once completed will allow us to incorporate the updated correlation of the turbulent deposition rate at the interfaces. Even though the flux of turbulent deposition will remain many orders of magnitude lower than the flux of electromagnetic migration at the furnace walls, this may play a significant role near the bath free surface, especially in regions away from the electromagnetic skin.

- Transport of inclusions due to turbulence

The turbulence dispersion of the inclusions within the Al bath may be modeled by an additional diffusion term in the transport equation of N_i. This will probably have a negligible impact on the removal efficiencies and may only play a small role in transporting the inclusions trapped in the recirculation zones from the central regions of the bath towards the walls.

- Drag coefficient

The drag coefficient, used while deducing the particle velocity in the Drift Concentration Model, was only valid for the Stokes regime ($Re_p < 1$). An improvement on the calculation of the sedimentation velocity of the inclusions could be made by correcting this coefficient and adopting the coefficient valid for particle Reynolds number greater than unity.

- Other inclusion morphology

We only considered the spherical type of inclusion amongst several shapes which may exist in the bath. Modeling of inclusions with a different morphology may be initiated by modifying the drag coefficient and the EM migration velocity in the Drift Concentration Method. Turbulent kernels should also be modified for other inclusion shapes. In the future, this complex question could be tackled through the mesoscopic simulations of collisions between non-spherical particles using Lattice-Boltzmann Method coupled with discrete elements through flow penalization [137].

Résumé en Français

Objectif

L'objectif de ce travail est focalisé sur le comportement des inclusions au sein du four de maintien, dans lequel l'alliage d'aluminium est chauffé, fondu et brassé par induction. Le comportement prend ici plusieurs sens et s'attache à des échelles différentes : à l'échelle macroscopique du bain, il s'agit du transport dynamique des inclusions par le mouvement moyen de l'Al liquide ainsi que par l'ensemble des forces qui s'appliquent sur les inclusions, principalement la force électromagnétique et la force de séparation gravitaire. A l'échelle mésoscopique, il faut étudier l'interaction des particules entre elles (agglomération, fragmentation) et les interactions avec les parois. Les conditions particulières du chauffage par induction conduisent à des forces de brassages limitées à la peau électromagnétique (à proximité des parois du creuset) et à une déformation de la surface du bain qui pourrait conduire à des déchirements de la peau d'oxyde de surface. Le comportement des inclusions dans le bain (transport et interactions) dépend naturellement de ces conditions hydrodynamiques.

Etat de l'art

Jusque vers la fin des années 80, les travaux de recherche sur la propreté inclusionnaire étaient consacrés à l'acier, et partagés entre des études thermodynamiques (équilibres laitier - métal liquide - inclusion [138]), et les premiers calculs de réacteurs de métallurgie secondaire [139]. Ceci a donné naissance à des logiciels de calcul largement utilisés dans la sidérurgie pour prédire la composition des phases inclusionnaires stables [140]. La simulation des procédés de traitement du métal liquide s'est développée par ailleurs avec un degré de sophistication croissant (KTH de Stockholm [141] ; Université d'Urbana-Champaign [142]) ; c'est la base des travaux de l'équipe 301 de l'IJL. Les modèles existant, dont Zhang [143] a fait récemment paraître une revue assez exhaustive, ne traitent pas précisément du comportement et de la capture des particules aux interfaces (paroi réfractaire, surface laitier, bulles). Parmi les études expérimentales peu nombreuses dans ce domaine, citons celles, originales, de Taniguchi (Université de Sendai [144]) en maquettes froides ou chaudes sur le comportement des inclusions ; et les études de l'Université de Worcester [145], pionnières dans la simulation des poches de traitement de l'aluminium liquide. Les développements se sont poursuivis à l'Ecole des Mines de Nancy (IJL 301) dans le cadre du projet Cipal pour aboutir à un premier outil de simulation des inclusions dans les poches Alpur [81]. Récemment, les travaux de Scepanskis à Riga [136] ont permis d'étudier expérimentalement et numériquement l'effet important du champ électromagnétique sur le mouvement des inclusions dans le bain, et leur rapide transport vers la paroi du creuset.

Démarche et résultats

L'approche utilisée a pour objet de développer un modèle numérique pour, dans un premier temps, simuler le comportement magnétohydrodynamique du bain liquide dans le creuset et, dans un deuxième temps, prédire le comportement d'une population d'inclusions. Des campagnes expérimentales à l'échelle d'un four de laboratoire et d'une installation industrielle accompagnent cette approche théorique.

Ainsi, en tenant compte des conditions de symétrie du four à induction et des conditions opératoires, un modèle 2D axisymétrique en régime transitoire a été développé s'appuyant sur le code de CFD commercial ANSYS Fluent, tandis que de nombreuses fonctions utilisateurs ont été introduites pour simuler les phénomènes spécifiques comme l'induction électromagnétique, les bilans de population, l'agglomération etc. Puisque la concentration massique des inclusions solides demeure très petite (inférieure à 50 ppm), le mouvement de la population inclusionnaire affecte nullement l'écoulement de l'aluminium à l'échelle macroscopique. En conséquence, le calcul hydrodynamique et la simulation du comportement des inclusions peuvent être découplés, et s'effectuent en deux étapes successives.

Le modèle Magneto-Hydro Dynamique (MHD)

Le modèle MHD déployé s'attache à résoudre dans un unique maillage les phénomènes d'induction électromagnétiques, l'écoulement turbulent de l'alliage liquide, la déformation de la surface libre et la présence d'une couche de métal oxydée en surface du bain. Ce modèle s'appuie sur le module Induc_14.0 développé au SIMAP à Grenoble. Une publication [146] détaille le modèle mis en œuvre avec le système d'équations aux dérivées partielles à résoudre ainsi que les méthodes numériques choisies.

Le Modèle de Bilan de Population (MPB)

Nous avons choisi un modèle de bilan de population dans le but de simuler à la fois le transport des inclusions dans le bain d'Al et les interactions mésoscopique entre les inclusions (c.à.d. les mécanismes d'agrégation et de fragmentation). En effet le bilan de population est une approche efficace pour simuler le comportement d'une population de particules discrètes dans leur environnement local. Le comportement de la population d'inclusions, définie par une distribution de particules selon leur taille (N_i est le nombre d'inclusions dans la classe de taille i par m^3 d'Al liquide) est décrite par l'Equation de Bilan de Population suivante (EBP) :

$$\forall i, \quad \frac{\partial N_i}{\partial t} + \frac{\partial}{\partial x_j}\left(N_i u_{p,i,j}\right) = H_i \tag{1}$$

Dans l'équation (1), le transport macroscopique est représenté par le membre de gauche tandis que l'agrégation des particules est modélisée par le membre de droite. A l'échelle de l'inclusion, l'application de la relation fondamentale de la dynamique conduit à l'expression de la vitesse de glissement, c.à.d. la vitesse relative entre les inclusions de taille i et le métal liquide:

$$u_{p,i} - u_f = u_{sed,i} + u_{em,i} = \frac{d_{pi}^2}{18\mu_f}\left(\rho_p - \rho_f\right) g - \frac{d_{pi}^2}{24\mu_f} F_{em} \tag{2}$$

$u_{sed,i}$ et $u_{em,i}$ représentent respectivement la vitesse de Stokes et la vitesse de glissement électromagnétique. La résolution du système (1) est obtenue en appliquant une séparation des opérateurs selon le système:

$$\forall i, \quad \frac{\partial N_i}{\partial t} + \frac{\partial}{\partial x_j}\left(N_i\left(\vec{u}_f + \vec{u}_{sed,i} + \vec{u}_{em,i}\right)\right) = 0 \tag{3}$$

$$\forall i, \quad \frac{\partial N_i}{\partial t} = H_i = B_i - D_i \tag{4}$$

La première étape (Equation 3) résout l'équation de transport convective du scalaire N_i, en adaptant la vitesse de transport qui ne vérifie pas par nature une divergence nulle. La seconde étape (Equation 4) consiste à résoudre l'EBP dans chaque volume de contrôle du domaine en utilisant la méthode de pivot fixe de Kumar et Ramkrishna et une technique de moyenne pour réduire la diffusion numérique dans l'espace de la coordonnée interne. Le noyau d'agglomération combine le terme de collision turbulente et le terme gravitationnel.

Déformation de la surface du bain

Sous l'action des forces électromagnétiques, la surface libre du métal se déforme, et l'atmosphère d'air au-dessus du bain produit une peau d'oxyde très stable chimiquement à la surface du bain. La mesure expérimentale de cette déformation est un moyen de valider partiellement le calcul MHD. Nous avons donc mis en œuvre à l'échelle d'un four à induction de laboratoire la mesure dynamique de cette déformation selon une technique de lumière structurée, qui consiste à projeter sur la surface un motif en bandes contrastées. L'image de la déformation du motif sur la surface est enregistrée par une ou deux caméras vidéo, et une reconstruction de la surface est obtenue grâce au principe de triangulation.

Un exemple de comparaison du profil mesuré et calculé numériquement est apporté sur la Figure 1 qui souligne le rôle joué par la peau d'oxyde sur l'amplitude de la déformation.

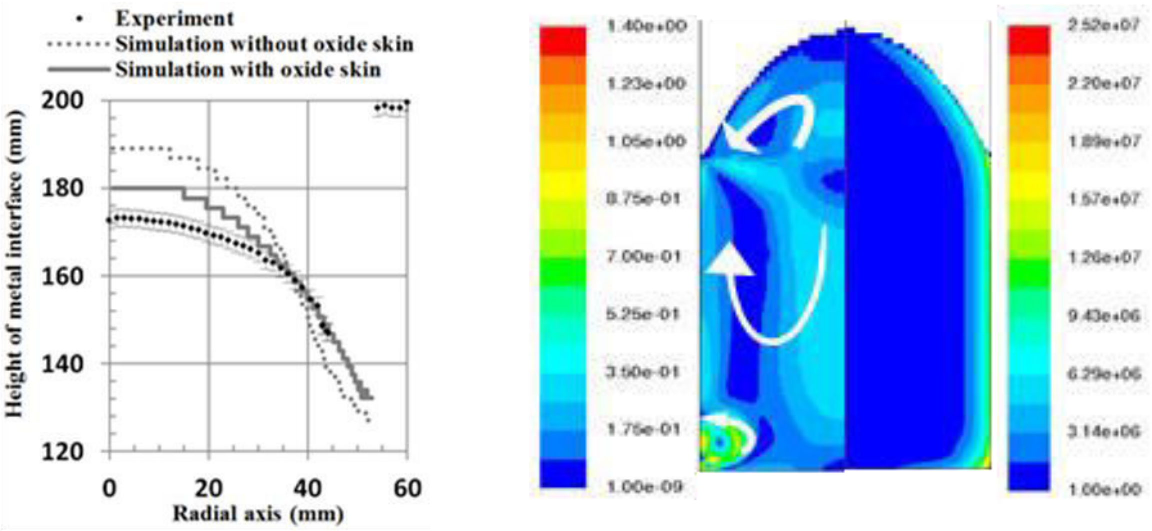

Figure 1 : Comparaison entre les profils du dôme calculés (avec ou sans peau d'oxyde) et mesuré (gche) et cartes de la vitesse moyenne et de la densité de courant induit calculées dans le four de laboratoire (dte).

Un travail identique a été mené à l'échelle industrielle avec une technique de mesure par télémètrie laser, plus simple à mettre en œuvre. Il montre que, même pour des fours à induction à l'échelle métrique, les déformations de la surface du bain sont conséquentes lors de conditions opératoires de fort brassage.

Simulation du comportement de la population d'inclusions

Un ensemble de simulations MHD et de bilans de populations a été réalisé pour une installation industrielle de Constellium, en prenant en compte scrupuleusement la géométrie du four à induction et les conditions opératoires qui prévalent à différentes périodes du traitement. Nous avons considéré dans le cas rapporté ici une population initiale d'inclusions de $MgAl_2O_4$ présentant une loi log-normale de distribution en taille et une concentration massique totale de 2 ppm.

Le modèle de bilan de population nous permet d'étudier l'évolution de la distribution en taille avec le temps de traitement, comme le montre la Figure 2.

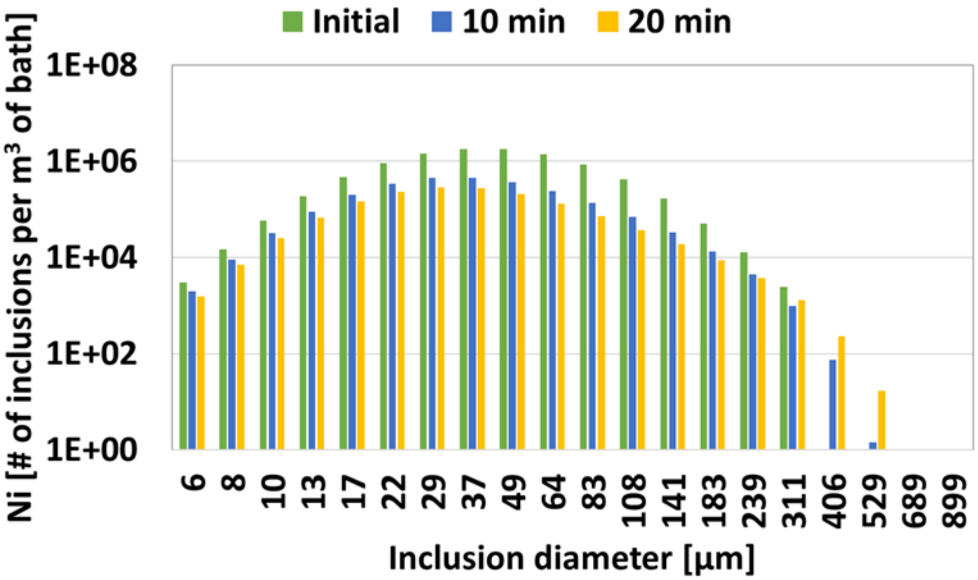

Figure 2 : Evolution avec le temps de la fonction de distribution en taille des inclusions

Les simulations montrent clairement une importante (échelle logarithmique) réduction de la population au sein du bain après quelques minutes de traitement, puisque dans l'exemple traité, seul 14% de la masse totale initial de particules demeurent dans le bain après 20 minutes de traitement. Cette réduction est plus effective pour les inclusions de forte taille, puisque par exemple on note une diminution de moitié de la densité d'inclusions de 10 µm, tandis que les inclusions de 141 µm ont été réduites de 90%.

La forte diminution de la masse totale inclusionnaire dans le bain liquide peut s'expliquer par le rôle relatif des deux mécanismes que sont la sédimentation et la séparation magnétique. Il apparait que les forces de Lorentz sont suffisamment intenses pour transporter les inclusions en direction de la paroi du creuset et participer, dans la simulation présentée, à plus de 90% à la réduction de la masse inclusionnaire.

Le transport de la population d'inclusions vers la paroi du creuset combine deux mécanismes, comme illustré par la Figure 3 pour deux tailles de particules et 3 différents instants. Les inclusions sont entrainées par le métal liquide en suivant les deux boucles de recirculations. Lorsque les inclusions approchent de la paroi et entrent dans la peau électromagnétique, elles sont entrainées fortement par la vitesse de glissement électromagnétique. Selon l'équation 2, la vitesse de glissement dépend du carré de la taille de la particule, ce qui explique facilement la sensibilité du processus global avec la taille. Le comportement des inclusions impactant la paroi n'est pas modélisée ici, et les mécanismes de cémentation, agrégation à la paroi sont sans doute un sujet très important à investiguer pour quantifier à terme l'efficacité réelle de la capture à la paroi.

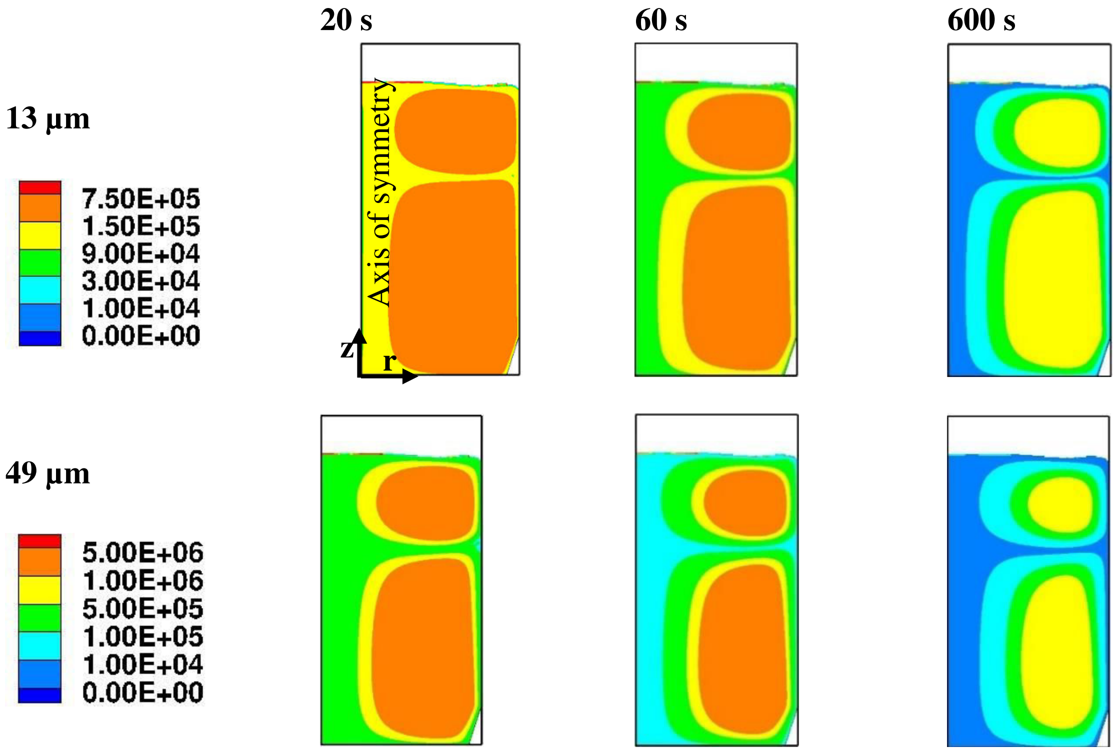

Figure 3: Evolution avec le temps de la densité numérale d'inclusions pour 2 tailles d'inclusions, 13 µm et 49 µm.

Perspectives

Des campagnes expérimentales de mesure de la composition inclusionnaire au cours du traitement sont nécessaires pour conforter les résultats apportés par cette modélisation. Par ailleurs l'hypothèse d'efficacité de la capture des inclusions à la paroi du creuset est à l'évidence trop forte, et une étude sur le comportement des inclusions à proximité de la paroi mérite d'être engagée, en prenant en compte les mécanismes de cémentation et d'agrégation éventuels à la paroi réfractaire du creuset. De plus, le réentrainement des inclusions piégées à la paroi lors de la coulée est un sujet qui mérite sans doute d'être engagé. Enfin, la non-sphéricité des inclusions, comme il en existe dans l'aluminium liquide (peau d'oxyde par exemple), pourrait être prise en compte dans les expressions de la force de trainée et de la force électromagnétique. Les expressions de noyaux de collision devraient être aussi modifiées grâce à un travail engagé à l'IJL utilisant un modèle de Boltzmann sur réseau couplé avec des frontières immergées.

References

[1] V. Warke, M. Maniruzzaman and M. Makhlouf, "Computer simulations for the removal of solid particles from molten aluminum in the rotating impeller degasser," *Light Metals,* p. 893, 2003.

[2] E. Waz, *Private communications on aluminum processing in a casthouse,* 2015.

[3] O. Mirgaux, "Modélisation de la purification de l'aluminum liquide par procédé de flottation en cuve agitée (PhD Dissertation)," INPL, Nancy, 2007.

[4] E. Lae, H. Duval, C. Riviere, P. Le Brun and J. Guillot, "Experimental and numerical study of ceramic foam filtration," *Light Metals,* p. 753, 2006.

[5] P. Davidson, An Introduction to Magnetohydrodynamics, Cambridge, UK: Cambridge University Press, 2001.

[6] M. S. Tillack and N. B. Morley, Magneto Hydro Dynamics. Standard Handbook for Electrical Engineers, McGraw Hill, 1998.

[7] H. Moffatt and W. Proctor, "Metallurgical Application of Magnetohydrodynamics," in *IUTAM 1982 - TMS*, Cambridge, 1984.

[8] S. Asai, "Recent development and prospect of electromagnetic processing of materials," *Science and Technology of Advanced Materials,* vol. 1, no. 4, p. 191, 2000.

[9] H. K. Moffatt, "Electromagnetic stirring," *Physics of Fluids A: Fluid Dynamics,* vol. 3, no. 5, p. 1336, 1991.

[10] V. Bojarevics and K. Pericleous, "Numerical Modelling for Electromagnetic Processing of Materials," in *Magnetohydrodynamics – Historical evolution and Trends*, Springer, 2007, p. 357.

[11] A. Mühlbauer, History of Induction Heating and Melting, Vulkan-Verlag GmbH, 2008, p. 202.

[12] O. Junker, "Induction Furnaces". USA Patent 2852587, 7 November 1955.

[13] H. Nakata and J. Etay, "Meniscus shape of molten steel under alternating magnetic field," *ISIJ International,* vol. 32, no. 4, p. 521, 1992.

[14] L. PetitNicolas, "Etude Expérimentale et Modélisation mathématique des cinétiques de nitruation et denituration des alliages Ni-Cr liquides (PhD Dissertation)," INPL, Nancy, 1996.

[15] J. Etay and Y. Fautrelle, "Controle Electromagnétique des interfaces libres," Technique de l'Ingenieur: re41, 2005.

[16] Y. Fautrelle, A. Sneyd and J. Etay, "Effect of AC magnetic fields on free surfaces," in *Magnetohydrodynamics - Historical Evolution and Trends*, Springer, 2007, p. 345.

[17] P. Lorrain and D. R. Corson, Electromagnetism: Principles and Applications, 2 ed., W.H. Freeman, 1978.

[18] J. D. Anderson, Computational Fluid Dynamics, McGraw-Hill Science, 1995.

[19] G. Yeoh and J. Tu, Computational Techniques for Multi-Phase flows, Butterworth-Heinemann, 2010.

[20] E. Tarapore and J. Evans, "Fluid velocities in induction melting furnaces: Part1. Theory and Laboratory Experiments," *Metallurgical Transactions B,* vol. 7B, p. 343, 1975.

[21] E. Tarapore, J. Evans and J. Langfeldt, "Fluid velocities in induction melting furnaces: Part2. Large scale measurements and predictions," *Metallurgical Transactions B,* vol. 8B, p. 179, 1977.

[22] E. Taberlet and Y. Fautrelle, "Turbulent stirring in an experimental induction furnace," *Journal of Fluid Mechanics,* vol. 159, p. 409, 1985.

[23] N. El-Kaddah, J. Szekely, E. Taberlet and Y. Fautrelle, "Turbulent recirculating flow in induction furnaces: A comparison of measurements with predictions over a range of operating conditions," *Metallurgical Transactions B,* vol. 17B, p. 687, 1986.

[24] C. Vives and R. Ricou, "Experimental study of continuous electromagnetic casting of aluminum alloys," *Metallurgical Transactions B,* vol. 16B, p. 377, 1985.

[25] C. Vives and R. Ricou, "Fluid flow phenomena in a single phase coreless induction furnace," *Metallurgical Transactions B,* vol. 16B, p. 227, 1985.

[26] A. Umbrashko, E. Baake, B. Nacke and A. Jakovics, "Modeling of the turbulent flow in induction furnaces," *Metallurgical and Materials Transactions B,* vol. 37B, p. 831, 2006.

[27] A. Bojarevics, A. Cramer, Y. Gelfgat and G. Gerbeth, "Experiments on the magnetic damping of an inductively stirred liquid metal flow," *Experiments in Fluids,* vol. 40, no. 2, p. 257, 2006.

[28] A. Cramer, S. Eckert and G. Gerbeth, "Flow measurements in liquid metals by means of the ultrasonic doppler method and local potential probes," *The European Physical Journal - Special topics,* vol. 220, p. 25, 2013.

[29] Y. Kolesnikov, C. Karcher and A. Thess, "Lorentz Force Flowmeter for Liquid Aluminum: Laboratory Experiments and Plant Tests," *Metallurgical and Materials Transactions B,* vol. 42, no. 3, pp. 441-450, 2011.

[30] D. Jian and C. Karcher, "Electromagnetic flow measurements in liquid metals using time-of-flight Lorentz force velocimetry," *Measurement Science and Technology,* vol. 23, no. 7, p. 074021, 2012.

[31] N. Dubovikova, Y. Kolesnikov and C. Karcher, "Experimental study of an electromagnetic flow meter for liquid metals based on torque measurement during pumping process," *Measurement Science and Technology,* vol. 26, no. 11, p. 115304, 2015.

[32] S. Argyropoulos, "Measuring velocity in high temperature liquid metals: a review," *Scandinavian Journal of Metallurgy,* vol. 30, p. 273, 2000.

[33] B. Li, J. Evans and D. Cook, "An improved mathematical model for electromagnetic casters and testing by a physical model," *Metallurgical Transactions B,* vol. 22B, p. 121, 1991.

[34] J. Etay, B. Dumont, J. Hamburger, R. Bolcato and R. Haettel, "Resistive probe for continuous measurement of electroconductive liquid levels facing electromagnetic fields," *Experiments in Fluids,* vol. 32, no. 4, p. 518, 2002.

[35] D. Perrier, Y. Fautrelle and J. Etay, "Experimental and theoretical studies of the motion generated by a two-frequency magnetic field at the free surface of a gallium pool," *Metallurgical and Materials Transactions B,* vol. 34B, p. 669, 2003.

[36] R. Kageyama and J. Evans, "A mathematical model for the dynamic behavior of melts subjected to electromagnetic forces: Part 1. Model development and comparison of predictions with published experimental results," *Metallurgical and Materials Transactions B,* vol. 29B, p. 919, 1998.

[37] M. Kirpo, "Modeling of Turbulence Properties and Particle Transport in Recirculated Flows (PhD Dissertation)," University of Lativa, Riga, 2008.

[38] F. Debray and Y. Fautrelle, "Free surface deformation frequencies of an electromagnetically excited mercury level," *Experiments in Fluids,* vol. 16, p. 316, 1994.

[39] Y. Fautrelle, D. Perrier and J. Etay, "Free surface controlled by magnetic fields," *ISIJ International,* vol. 43, no. 6, p. 801, 2003.

[40] J. Mohring, C. Karcher and D. Schulze, "Dynamic behavior of a liquid metal interface under the influence of a high-frequency magnetic field," *Physical Review E,* vol. 71, no. 4, p. 047301, 2005.

[41] R. Kageyama and J. Evans, "A Mathematical model for the dynamic behavior of melts subjected to electromagnetic forces: Part 2. Measurement of surface waves and comparison with predictions of the mathematical model," *Metallurgical and Materials Transactions B,* vol. 30B, p. 331, 1999.

[42] E. Baake, B. Nacke, A. Umbrashko and A. Jakovics, "Turbulent flow dynamics, heat transfer and mass exchange in the melt of induction furnaces," *COMPEL - The International Journal of Computation and Mathematics in Electrical and Electronic Engineering,* vol. 22, no. 1, p. 39, 2003.

[43] C. Courtessole and J. Etay, "Flows and mass transfers in two superimposed liquid layers in an induction furnace," *International Journal of Heat and Mass Transfer,* vol. 65, p. 893, 2013.

[44] S. Spitans, A. Jakovics, E. Baake and B. Nacke, "Numerical Modeling of Free Surface Dynamics of Melt in an Alternate Electromagnetic Field: Part I. Implementation and Verification of Model," *Metallurgical and Materials Transactions B,* vol. 44B, p. 593, 2013.

[45] M. Scepanskis, A. Jakovics, E. Baake and B. Nacke, "Solid inclusions in an electromagnetically induced recirculated turbulent flow: simulation and experiment," *International Journal of Multiphase Flow,* vol. 64, p. 19, 2014.

[46] D. Fugate and J. Hoburg, "Shape and stability computations of electromagnetically confined liquid metal boundaries," *Metallurgical Transactions B,* vol. 24B, p. 171, 1993.

[47] X. R. Zhu, R. A. Harding and J. Campbell, "Calculation of the free surface shape in the electromagnetic processing of liquid metals," *Applied Mathematical Modelling,* vol. 21, p. 207, 1997.

[48] O. Pesteanu and E. Baake, "The Multicell Volume of Fluid (MC-VOF) Method for the Free Surface Simulation of MFD Flows. Part I: Mathematical Model," *ISIJ International,* vol. 51, no. 5, p. 707, 2011.

[49] Y. Delannoy and C. Garnier, "Free Surface Shape in Induction Furnaces: Influences of the Stirring motion on the mean dome height," in *Proceeding at 5th International Conference of Electromagnetic Processing of Materials*, Sendai, Japan, 2006.

[50] J. Anson, R. Drew and J. Gruzleski, "The surface tension of molten aluminum and Al-Si-Mg alloy under vacuum and hydrogen atmospheres," *Metallurgical and Materials Transactions B,* vol. 30B, p. 1027, 1997.

[51] I. Egry, E. Ricci, R. Novakovic and S. Ozawa, "Surface tension of liquid metals and alloys - recent developments," *Advances in Colloid and Interface Science,* vol. 159, p. 198, 2010.

[52] N. Eustathopoulos, J. Joud, P. Desre and J. Hicter, "The wetting of carbon by aluminium and aluminium alloys," *Journal of Materials Science,* vol. 9, p. 1233, 1974.

[53] I. Bainbridge and J. Taylor, "The surface tension of pure aluminum and aluminum alloys," *Metallurgical and Materials Transactions A,* vol. 44, no. 8, pp. 3901-3909, 2013.

[54] L. Goumiri, J. C. Joud, P. Desre and J. M. Hicter, "Tensions superficielles d'alliages liquides binaires présentant un caractère d'immiscibilité: Al-Pb, Al-Bi, Al-Sn et Zn-Bi.," *Surface Science,* vol. 83, p. 471, 1979.

[55] C. Garcia-Cordovilla, E. Louis and A. Pamies, "The surface tension of liquid pure aluminium and aluminium-magnesium alloy," *Journal of Materials Science,* vol. 21, no. 8, p. 2787, 1986.

[56] L. Goumiri and J. Joud, "Auger electron spectroscopy study of aluminium-tin liquid system," *Acta Metallurgica,* vol. 30, no. 7, p. 1397, 1982.

[57] F. Frisvold, Filtration of Aluminium - Theory, Mechanisms and Experiments (PhD Dissertation), Trondheim: NTNU, 1990.

[58] J. Schoutens, "Some theoretical considerations of the surface tension of liquid metals for metal matrix composites," *Journal of Materials Science,* vol. 24, p. 2681, 1989.

[59] W. Kahl and E. Fromm, "Examination of the strength of oxide skins on aluminum alloy melts," *Metallurgical Transactions B,* vol. 16B, p. 47, 1985.

[60] M. Syvertsen, "Oxide skin strength on molten aluminum," *Metallurgical and Materials Transactions B,* vol. 37B, p. 495, 2006.

[61] M. Syvertsen, "Oxide skin strength measurements on molten aluminum - manganese alloys with and without salt on surface," in *Light Metals, TMS 2014*, 2014.

[62] S. Roach and H. Henein, "A new method to dynamically measure the surface tension, viscosity and density of melts," *Metallurgical and Materials Transactions B,* vol. 36B, p. 667, 2005.

[63] P. D. Desai, H. M. James and C. Y. Ho, "Electrical Resistivity of Aluminum and Manganese," *Journal of Physical and Chemical Reference Data,* vol. 13, no. 4, p. 1131, 1984.

[64] B. Drafts, "Methods of Current Measurement," Pacific Scientific OECO, 2004.

[65] S. Macintyre, "Magnetic Field Measurement (Chapter 48)," in *The Measurement, Instrumentation and Sensors Handbook on CD-ROM*, CRC Press, 1999.

[66] M. Amann and T. Bosch, "Laser ranging: a critical review of usual techniques for distance measurement," *Optical Engineering,* vol. 40, no. 1, p. 10, 2001.

[67] K. Maatta and J. Kostamovaara, "Profiling Of Hot Surfaces By Pulsed Time-Of-Flight Laser Range Finder Techniques," *Applied Optics,* vol. 32, no. 27, p. 5334, 1993.

[68] J. Geng, "Structured light 3D imaging – A tutorial," *Advances in Optics and Photonics,* vol. 3, no. 2, p. 128, 2011.

[69] F. Blais, M. Rioux and J. Beraldin, "Practical considerations for the design of a high precision 3D laser scanner system," *Proceeding SPIE, Optomechanical and Electro-Optical Design of Industrial Systems,* 14 November 1988.

[70] Holo3, Saint Louis, France. , "A structured light tutorial," [Online]. Available: www.holo3.com.

[71] J. Lacombe, Y. Delannoy and C. Trassy, "The role of radiation in modelling of argon inductively coupled plasmas at atmospheric pressure," *Journal of Physics D: Applied Physics,* vol. 41, no. 16, p. 165204, 2008.

[72] F. Menter, "Two-equation eddy-viscosity turbulence models for engineering applications," *AIAA Journal,* vol. 32, no. 8, p. 1598, 1994.

[73] ANSYS , "Fluent Theory guide".

[74] Y. Egorov, M. Boucker, A. Martin, S. Pigny, M. Scheuerer and S. Willemsen, "Validation of CFD codes with PTS-relevant test cases," European Commission - ECORA, 2004.

[75] C. Hirt and B. Nichols, "Volume Of Fluid (VOF) Method For The Dynamics Of Free Boundaries," *Journal of Computational Physics,* vol. 39, no. 1, p. 201, 1981.

[76] T. Von Karman, "On Laminar and Turbulent Friction," *National Advisory Committee for Aeronautics - NACA Technical Memorandum,* vol. 1092, 1946.

[77] D. Altenpohl, Aluminum: Technology, Applications, and Environment: a Profile of a Modern Metal: Aluminum from Within--the Sixth Edition, Aluminum Association, TMS, 1998.

[78] R. Guthrie and D. Doutre, "On-Line Measurements of Inclusions in Liquid Metals," in *International Seminar on Refining and Alloying of Liquid Aluminum and Ferro-Alloys*, Trondheim, Norway, August 1985.

[79] D. Doutre, B. Gariepy, J. P. Martin and G. Dube, "Aluminum cleanliness monitoring: methods and applications in process development and quality control," *Essential Readings in Light Metals: Cast Shop for Aluminum Production.,* vol. 3, p. 296, 1985.

[80] S. T. Johansen, S. Graadahl and T. F. Hagelien, "Entrainment of inclusions from the dross in stirred reactors for melt treatment," *Applied Mathematical Modelling,* vol. 28, no. 1, p. 63, 2004.

[81] O. Mirgaux, D. Ablitzer, E. Waz and J. Bellot, "Mathematical modeling and computer simulation of molten aluminium purification by flotation in stirred reactor," *Metallurgical and Materials Transactions B,* vol. 40B, p. 363, 2009.

[82] E. Pauty, B. Laboudigue and J. Etay, "Numerical simulation of the flow and the solid transport when tilting a holding furnace," *Metallurgical and Materials Transactions B,* vol. 31B, p. 207, 2000.

[83] S. Instone, A. Buchholz and G. Gruen, "Inclusion Transport Phenomena in Casting Furnaces," *Light Metals 2008,* p. 811, 2008.

[84] L. Nastac, D. Zhang, S. Jia and Y. Xuan, "Advances on Experimental and Numerical Modeling of Al-based Alloys and Nanocomposites Fabricated via Ultrasonic and Electromagnetic Processing," in *Proceedings of EPM2015, 8th International Conference on Electromagnetic Processing of Materials*, Cannes, 2015.

[85] D. Shu, J. Wang and B. Sun, "Online Electromagnetic Filtration of Molten Aluminum Using a Multistage Separator System," *Journal for Manufacturing Science and Production,* vol. 15, no. 1, pp. 89-92, 2015.

[86] M. W. J. A. B. a. R. E. A. Kennedy, "Impact of Coil Geometry on Magnetohydrodynamic Flow in Liquid Aluminium and Its Relevance to Inclusion Separation by Electromagnetophoresis," *Journal for Manufacturing Science and Production,* vol. 15, no. 1, pp. 69-78, 2015.

[87] S. Shimasaki and S. Taniguchi, "Separation Efficiency of Inclusion Particles from Liquid Aluminum by Electromagnetic Cyclone Separator," in *Proceedings of EPM2015, 8th International Conference on Electromagnetic Processing of Materials*, Cannes, 2015.

[88] L. Claudotte, "Prédiction de la taille et de la composition des inclusions dans une poche d'acier liquide: étude numérique (PhD Dissertation)," Université de Lorraine, Nancy, 2010.

[89] J. P. Bellot, V. De Felice, B. Dussoubs, A. Jardy and S. Hans, "Coupling of CFD and PBE Calculations to Simulate the Behavior of an Inclusion Population in a Gas-Stirring Ladle," *Metallurgical and Materials Transactions B,* vol. 45B, p. 13, 2014.

[90] Q. Wang, F. Qi, B. Li and F. Tsukihashi, "Behavior of Non-metallic Inclusions in a Continuous Casting Tundish with Channel Type Induction Heating," *ISIJ International,* vol. 54, no. 12, pp. 2796-2805, 2014.

[91] E. Waz, A. Bansal, P. Chapelle, Y. Delannoy, J. P. Bellot and P. L. Brun, "Modeling of Inclusion Behavior in an Aluminum Induction Furnace," in *Light Metals 2016*, John Wiley & Sons, 2016.

[92] D. Leenov and A. Kolin, "Theory of electromagnetophoresis. I. Magnetohydrodynamic forces experienced by spherical and symmetrically oriented cylindrical particles," *The Journal of Chemical Physics,* vol. 22, no. 4, p. 683, 1954.

[93] Z. Sun, M. Guo, J. Vleugels, O. Van der Biest and B. Blanpain, "Numerical calculations on inclusion removal from liquid metals under strong magnetic fields," *Progress In Electromagnetics Research,* vol. 98, p. 359, 2009.

[94] S. Taniguchi and J. K. Brimacombe, "Application of pinch force to the separation of inclusion particles from liquid steel," *ISIJ international,* vol. 34, no. 9, p. 722, 1994.

[95] L. Zhang, S. Wang, A. Dong, J. Gao and L. N. W. Damoah, "Application of Electromagnetic (EM) Separation Technology to Metal Refining Processes: A Review," *Metallurgical and Materials Transactions B,* vol. 45B, p. 2153, 2014.

[96] R. Bolcato, J. Etay, Y. Fautrelle and H. K. Moffatt, "Electromagnetic billiards," *Physics of Fluids A: Fluid Dynamics,* vol. 5, no. 7, p. 1852, 1993.

[97] N. El-Kaddah, A. D. Patel and T. T. Natarajan, "The electromagnetic filtration of molten aluminum using an induced-current separator," *JOM,* vol. 47, no. 5, p. 46, 1995.

[98] P. Cremer and J. Driole, "Effects of the electromagnetic stirring on the removal of inclusions of oxide from liquid steel," *Metallurgical Transactions B,* vol. 13B, p. 45, 1982.

[99] D. R. Sadoway and J. Szekely, "A new experimental technique for the study of turbulent electromagnetically driven flows," *Metallurgical and Materials Transactions B,* vol. 11B, p. 334, 1980.

[100] M. Ščepanskis, K. Thomsen, A. Jakovičs, T. Beinerts, M. Sarma, R. Nikoluškins and A. Bojarevičs, "How to make liquid metal transparent? A neutron radiography method for scaled down metallurgical equipment," in *Proceedings of the 1st Thermal and Fluid Engineering Summer Conference*, New York, 2015.

[101] O. J. Ilegbusi and J. Szekely, "On the flow criteria for suspending solid particles in inductively stirred melts: Part I. newtonian behavior," *Metallurgical Transactions B,* vol. 19B, p. 557, 1988.

[102] V. Bojarevics, K. Pericleous and R. Brooks, "Dynamic model for metal cleanness evaluation by melting in a cold crucible," *Metallurgical and Materials Transactions B,* vol. 40B, p. 328, 2009.

[103] K. A. Pericleous and S. N. Drake, "An algebraic slip model of PHOENICS for multi-phase applications," in *Numerical simulation of fluid flow and heat/mass transfer processes*, Springer Berlin Heidelberg, 1986, p. 375.

[104] M. Cross, T. N. Croft, G. Djambazov and K. Pericleous, "Computational modelling of bubbles, droplets and particles in metals reduction and refining," *Applied mathematical modelling,* vol. 30, no. 11, p. 1445, 2006.

[105] K. Takahashi and S. Taniguchi, "Electromagnetic separation of nonmetallic inclusion from liquid metal by imposition of high frequency magnetic field," *ISIJ international,* vol. 43, no. 6, p. 820, 2003.

[106] S. Wang, L. Zhang, Y. Tian, Y. Li and H. Ling, "Separation of non-metallic inclusions from molten steel using high frequency electromagnetic fields," *Metallurgical and Materials Transactions B,* vol. 45B, p. 1915, 2014.

[107] C. T. Crowe, J. D. Schwarzkopf, M. Sommerfeld and Y. Tsuji, Multiphase Flows with Droplets and Particles, CRC Press, 1997.

[108] M. Sommerfeld, Theoeretical and Experimental modelling of particulate flow: overview and fundamentals. Lecture Series 2000-06, Von Karman Institute of Fluid Dynamics, Belgium, 2000.

[109] J. Etay, Private Communication.

[110] A. Xayasenh, "Étude numérique du dépôt turbulent de particules non-browniennes en suspension dans un liquide: application aux inclusions dans l'acier liquide (PhD Dissertation)," Ecole Centrale Paris, 2013.

[111] M. Dupuy, A. Xayasenh, E. Waz and H. Duval, "Analysis of non-Brownian particle deposition from turbulent liquid-flow," *AIChE Journal,* vol. 62, no. 3, p. 891, 2015.

[112] F. Fan and G. Ahmadi, "Analysis of particle motion in the near-wall shear layer vortices – Application to the turbulent deposition process," *Journal of Colloid and Interface Science,* vol. 172, p. 263, 1995.

[113] H. Ounis, G. Ahmadi and J. McLaughlin, "Brownian particle deposition in a directly simulated turbulent channel flow," *Phys. Fluids A,* vol. 5, no. 6, p. 1427, 1993.

[114] M. Signorino, G. Baldi, A. A. Barresi, M. Cournil, J. J. Derksen, F. Gruy, E. Hollander, M. Kraume, D. Marchisio, A. Paschedag, M. Vanni, H. E. A. Van den Akker and A. Varone, "Agglomeration in Pratsolis Project".

[115] P. Saffman and J. S. Turner, "On the collision of drops in turbulent clouds," *Journal of Fluid Mechanics,* vol. 1, no. 1, p. 16, 1956.

[116] J. Abrahamson, "Collision rates of small particles in a vigorously turbulent fluid," *Chemical Engineering Science,* vol. 30, no. 11, p. 1371, 1975.

[117] L. I. Zaichik, O. Simonin and V. M. Alipchenkov, "Turbulent collision rates of arbitrary-density particles," *International Journal of Heat and Mass Transfer,* vol. 53, no. 9, p. 1613, 2010.

[118] M. Soos, L. Wang, R. O. Fox, J. Sefcik and M. Morbidelli, "Population balance modeling of aggregation and breakage in turbulent Taylor–Couette flow," *Journal of Colloid and Interface Science,* vol. 307, no. 2, p. 433, 2007.

[119] D. Ramkrishna, Population balances: Theory and applications to particulate systems in engineering, Academic press, 2000.

[120] D. Ramkrishna and M. R. Singh, "Population balance modeling: Current status and future prospects," *Annual Review of Chemical and Biomolecular Engineering,* vol. 5, p. 123, 2014.

[121] D. L. Marchisio, R. D. Vigil and R. O. Fox, "Quadrature method of moments for aggregation–breakage processes," *Journal of Colloid and Interface Science,* vol. 258, no. 2, p. 322, 2003.

[122] D. L. Marchisio and R. O. Fox, "Solution of population balance equations using the direct quadrature method of moments," *Journal of Aerosol Science,* vol. 36, no. 1, p. 43, 2005.

[123] S. Kumar and D. Ramkrishna, "On the solution of population balance equations by discretization—I. A fixed pivot technique," *Chemical Engineering Science,* vol. 51, no. 8, p. 1311, 1996.

[124] J. Kumar, M. Peglow, G. Warnecke, S. Heinrich and L. Mörl, "Improved accuracy and convergence of discretized population balance for aggregation: The cell average technique," *Chemical Engineering Science,* vol. 61, no. 10, p. 3327, 2006.

[125] F. Anker, S. Ganesan, V. John and E. Schmeyer, "A comparative study of a direct discretization and an operator-splitting solver for population balance systems," *Computers & Chemical Engineering,* vol. 75, p. 95, 2015.

[126] M. Smoluchowski, "Versuch einer mathematischen Theorie der Koagulationskinetik kolloiderLösnngen," *Zeitschrift fuer physikalische Chemie,* vol. 92, p. 129, 1917.

[127] Z. Popovic and B. Popovic, Introductory Electromagnetics, New Jersey: Prentice Hall, 1999.

[128] V. Bojarevics, R. Harding, K. Pericleous and M. Wickins, "The development and experimental validation of a numerical model of an induction skull melting furnace," *Metallurgical and Materials Transactions B,* vol. 35B, p. 785, 2004.

[129] V. V. Yashchuk, S. Lee and E. Paperno, "Magnetic shielding," in *Optical Magnetometry*, 1st ed., D. Budker and D. Kimball, Eds., Cambridge University Press, 2013, p. 225.

[130] M. Zucca, G. Crotti, O. Bottauscio, X. Li, M. Di Pardo and M. Chiampi, "Three-dimensional modeling for magnetic field shielding in a high electric power process," *Journal of Applied Physics,* vol. 99, no. 8, p. 08P503, 2006.

[131] D. van Riesen, G. Henneberger and C. Kaehler, "Comparison of different formulations for eddy-current computations in an induction furnace," *Progress in Electromagnetic Research Symp,* p. 623, 2004.

[132] G. Henneberger, P. K. Sattler, D. Shen and W. Hadrys, "Coupling of magnetic and fluid flow problems and its application in induction melting apparatus," *IEEE Transactions on Magnetics,* vol. 29, no. 2, p. 1589, 1993.

[133] A. Kumar, S. K. Ajmani and A. R. Pal, "Optimal configuration of blast furnace slag runner to reduce fluid flow stresses at wall using mathematical modelling," *Ironmaking and Steelmaking,* vol. 37, no. 1, p. 9, 2010.

[134] M. Kostoglou and A. Karabelas, "On the self-similarity of the aggregation–fragmentation equilibrium particle size distribution," *Journal of Aerosol Science,* vol. 30, no. 2, p. 157, 1999.

[135] R. Vigil, "On equilibrium solutions of aggregation–fragmentation problems," *Journal of Colloid and Interface Science,* vol. 336, no. 2, p. 642, 2009.

[136] M. Ščepanskis, "The Modelling of the Behaviour of Solid Inclusions in the EM Induced Recirculated Turbulent Flows of Liquid Metal (PhD Dissertation)," University of Latvia, Riga, 2014.

[137] J. Ngoma and J. Kroll-Rabotin, "Numerical study of aggregation dynamics with a Lattice Boltzmann Method coupled with discrete elements through flow penalization," in *International Conference on Multiphase Flow*, Florence, 2016.

[138] H. Gaye, C. Gatellier, M. Nadif, P. Riboud, J. Saleil and M. Faral, "Slags and inclusions control in secondary steelmaking," *Revue de Métallurgie,* vol. 85, p. 759, 1987.

[139] J. Szekely, T. Lehner and C. Chang, "Flow phenomena,mixing and mass transfer in argon-stirred ladles," *Ironmaking and Steelmaking,* vol. 6, p. 285, 1979.

[140] H. Gaye, J. Lehmann, P. Rocabois and F. Ruby-Meyer, "Computational thermodynamics and slag modelling applied to steel elaboration," *Steel Research,* vol. 72, p. 446, 2001.

[141] M. Hallberg, P. Jönsson, T. Jonsson and R. Erikson, "Process model of inclusion separation in a stirred steel ladle," *Scandinavian Journal of Metallurgy,* vol. 34, p. 41, 2005.

[142] J. Aoki, B. Thomas, J. Peter and K. Peaslee, "Experimental and theoretical investigation of mixing in a bottom gas-stirred ladle," in *AISTech*, 2004.

[143] L. Zhang, "Transport phenomena and CFD application during process metallurgy," in *Advanced Processing of Metals and Materials: Iron and Steel Making*, 2006.

[144] T. Kato, S. S. Shimasaki and S. S. Taniguchi, "Water model experiments for hydrodynamics forces acting on inclusion particles in molten metal under turbulent conditions," in *Jim Evans Honorary Symposium, TMS 2010*, 2010.

[145] V. Warke, S. Shandar and M. Makhlouf, "Mathematical modelling and computer simulation of molten aluminium cleaning by the rotating impeller degasser," *Journal of Materials Processing Technology,* vol. 168, 2005.

[146] A. Bansal, P. Chapelle, Y. Delannoy, E. Waz, P. Le Brun and J. Bellot, "Experimental and Numerical Analysis of the Deformation of a Liquid Aluminum Free Surface Covered by an Oxide Layer During Induction Melting," *Metallurgical and Materials Transactions B,* vol. 46, p. 2096, 2015.

[147] The Aluminum Association, "International Alloy Designations and Chemical Composition Limits for Wrought Aluminum and Wrought Aluminum Alloys," The Aluminum Association, 2009.

[148] O. Ubbink, "Numerical prediction of two fluid systems with sharp interfaces (PhD Dissertation)," Imperial College of Science, London, 1997.

[149] D. Youngs, "Time dependent multi-material flow with large fluid distortion," *Numerical Methods for Fluid Dynamics,* p. 273, 1982.

Annex

Annex 1: Composition and properties of Aluminum alloys

Table 25: Composition of aluminum alloys [147]

	Si	Fe	Cu	Mn	Mg	Cr	Ni	Zn	Ti	Zr
1050	0.25	0.4	0.05	0.05	0.05	…	…	0.07	0.05	…
2024	0.15	0.2	3.7-4.5	0.15-0.8	1.2-1.5	0.1	…	0.25	0.15	…
5182	0.2	0.35	0.15	0.20-0.50	4.0-5.0	0.1	…	0.25	0.1	…
7050	0.12	0.15	1.7-2.4	0.04	1.7-2.6	0.04	0.03	5.7-6.9	0.06	0.05-0.12

Table 26: Physical properties of aluminum alloys

Alloys	T (°C)	Density [62] (kg.m^{-3})	Dynamic viscosity [62] (Pa.s)	Electrical conductivity [63] (Ω^{-1}.m^{-1})	Surface tension coefficient [57] (N.m^{-1})
1050	660 (T_m)	2390	1.28E-03	4.04E+06	0.868
	700	2379	1.15E-03	3.97E+06	0.865
	1000	2339	7.10E-04	3.33E+06	0.783
	Law f(T)	$\rho(T) = \rho(T_m) - 0.15(T - T_m)$	-	$\sigma_{EL}(T) = 5.91\text{x}10^6 - 2.03\text{x}10^3\text{T}$	$\gamma(T) = \gamma(T_m) - 0.25\text{x}10^{-3}(T - T_m)$
2024	750	2416	1.04E-03	3.38E+06	0.795
5182	700	2337	1.15E-03	3.53E+06	0.860
7050	700	2522		3.77E+06	

Annex 2: Experimental techniques for free surface deformation study

Table 27: Summary of experimental techniques available for the measurement of a deformable surface

Technique	Strengths	Limitations
Laser telemetry	- Easy application - Varied range - Good data acquisition rate	- Limited precision - Single point measurement
Interferometry	- Very high precision	- High cost - Reflective surfaces only
Laser triangulation	- Simple and accurate - Independent of illumination - High data acquisition rate	- Laser safety - Reconstruction of image – algorithm required
Structured light	- Accurate pattern projection - High data acquisition rate	- Reconstruction of data images
Photogrammetry and Stereoscopy	- Simple application	- Algorithms required - Lower data acquisition rate
Electrical potential probe	- Good accuracy	- Interference with EM field - Intrusive and low temperature range
Thermocouple based contact probe	- Easy application	- Intrusive - Thermocouple response time

Annex 3: Modeling of a free surface: Emphasis on VOF discretization techniques

Free surface flows require an accurate representation of the shape and the location of the free surface as well as its temporal evolution. For an arbitrary Eulerian mesh, a variety of numerical methods to calculate free surface deformation exists. These can be broadly categorized into Surface or Volume methods [19]. In *Surface* methods the interface is either explicitly tracked by marking it with special marker points or by attaching the interface to the mesh surface. On the other hand, in *Volume* methods, the fluids on either side of the interface are marked by particles (markers in fluid) of negligible mass or by an indicator function. The exact position of the interface is not known explicitly and special techniques are required in order to reconstruct a well-defined interface.

We focus on the VOF method, which is quite economical as only one value (i.e. the volume fraction of a given phase) must be stored in each mesh element. Yeoh and Tu [19] and Ubbink [148] can be referred for further VOF method related information. VOF discretization techniques can be broadly categorized into two groups: Donor–Acceptor formulation and line techniques. D-A formulation basic idea is to exploit the information about the volume fraction downstream (i.e. Acceptor cell) as well as upstream (i.e. Donor cell) of a cell face in order to establish a crude interface shape and then to employ this shape while computing the flux across that face. Line techniques on the other hand fit the interface using oblique lines or piecewise linear segments. A comparison of different line techniques is illustrated in Figure 102. The Piecewise Linear Interface Construction (PLIC) technique proposed by Youngs [149] is an example. A major drawback of this technique is the discontinuities that it gives when the interface is reconstructed using 'un-joined' segments.

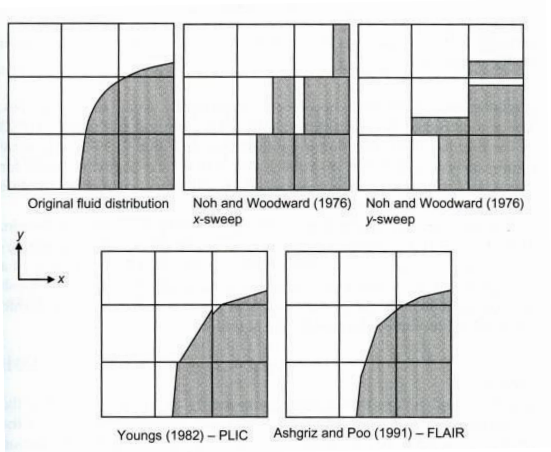

Figure 102: Comparison of different line techniques [148]

Concerning VOF method, Table 28 compares some interface advection schemes available in ANSYS Fluent.

Table 28: VOF advection schemes [73]

Scheme	Implicit	Explicit	Accuracy	Computational time
QUICK	YES	YES	Low	High
Modified HRIC	YES	YES	Medium	High
CICSAM	NO	YES	High	Medium
Compressive	YES	YES	High	Medium to High
GeoReconstruct	NO	YES	Very High	Low to Medium
BGM	YES	NO	Very High	Low to Medium

GeoReconstruct has been selected for the present study as this scheme provides the best compromise for calculation of a sharp interface while limiting computing resources. GeoReconstruct is based on the PLIC method and can be described in the following manner:

- Step1: calculation of a linear projection of the interface in each cell containing an interface, with the help of the volume fraction and its gradient.
- Step2: calculation of the advection of fluid through each face with the help of the calculated linear interface (step 1) as well as velocity distribution on the faces.
- Step3: calculation of the new volume fraction value in each cell using flux balancing calculated in step 2.

Annex 4: Interfacial area density approximation method

As previously presented in A3.2.1.2, the interfacial area density can be approximated by three different expressions [73] [74]. Since the precision of these three approximations is unknown, we have performed tests with known interface shapes. Interface shapes such as those of a cylinder, a hollow cylinder, a sphere and a torus for which the exact surface area value may be obtained analytically were successively considered. The interfacial area density calculated using the expressions in Table 8 was integrated over the complete shape volume to obtain the total surface area S. Table 29 presents a comparative analysis of the analytical area value with that calculated by the various expressions. For cylindrical shapes, A is the most precise expression, while for a simple spherical interface approximation B gives better results and for a torus approximation C is best suited. Thus, it can be concluded that the best approximation should be selected according to the case under study.

Table 29: Relative error associated to various interfacial area approximation methods

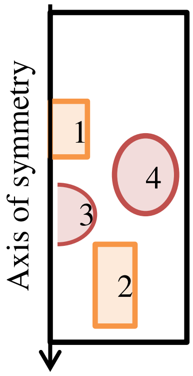

Shape	S_A $A_I = \lvert\nabla\alpha_l\rvert$	S_B $A_I = 2\alpha_l\lvert\nabla\alpha_l\rvert$	S_C $A_I = 6\alpha_l(1-\alpha_l)\lvert\nabla\alpha_l\rvert$
1) Cylinder	**-0,39%**	-2,62%	10,72%
2) Hollow cylinder	**-0,35%**	-3,37%	3,91%
3) Sphere	8,30%	**1,61%**	-10,92%
4) Torus	15,83%	10,23%	**0,93%**

* error % calculated with respect to S_{theory}

Similar tests were performed for the case of a dome shaped interface, representative of the deformation of the liquid metal free surface encountered in an induction furnace. This interface was fitted with a polynomial of degree six. The polynomial equation allowed us then to obtain by numerical integration a *theoretical* value of the surface area, which was then compared with the integral of the interfacial area density obtained using the various expressions, as presented in Table 30. A conclusion can be drawn in the favor of approximation C.

Table 30: Comparison of various expressions to calculate the area of a dome interface

	S_A	S_B	S_C
Dome shaped interface	25%	33%	**10%**

* error % calculated with respect to $S_{theory,fitted}$

Annex 5: Particle size distribution function for $MgAl_2O_4$

The characteristics of the non-metallic and undissolved inclusions (type, density, size and shape) considered in the present work originate from measurements by LiMCA and PoDFA techniques. A database was developed at C-TEC, describing several characteristics for each type of inclusion: density, minimum, mean and maximum diameters, diameter distribution, shape and a frequency index of observation in PoDFA samples. Thanks to these observations, it was possible to reconstruct for $MgAl_2O_4$ inclusions (spherical shape) a representative particle size distribution (Figure 103–black curve). This distribution was fitted using a log-normal distribution [91] (Figure 103– red curve), as expressed in Eq. 110.

$$f_{LN}\left(d_{p,i}\right) = \frac{1}{1.38 d_{p,i}} \exp\left(-\frac{\left(ln\left(d_{p,i}\right) - 3.74\right)^2}{0.605}\right) \qquad (110)$$

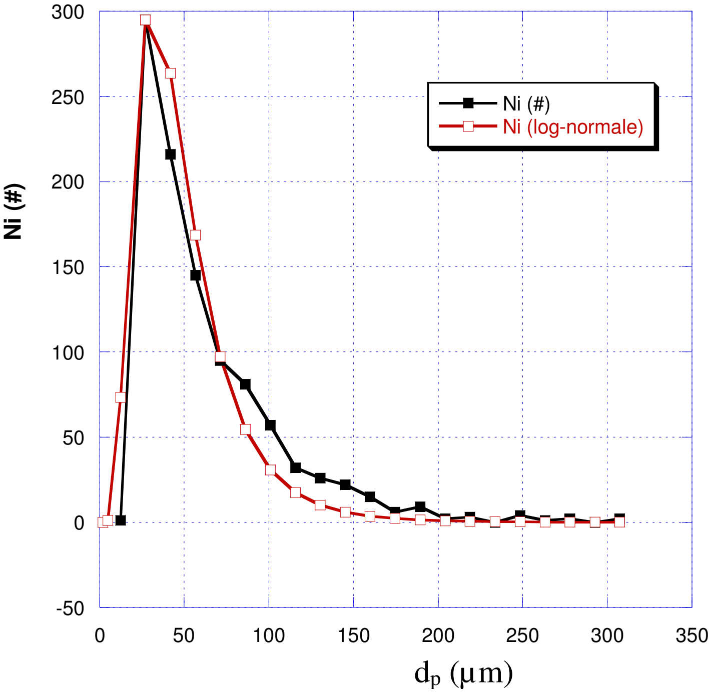

Figure 103: Particle size distribution - measured and fitted (using log-normal law)

This deduced log-normal law was adopted as the initial inclusion psd while calculating the inclusion behavior in the aluminum bath in chapter C2.

Annex 6: Total turbulent collision rate

Zaichik et al. [117] presented the turbulent collision rate between two particles ${V_{ij}}^t$ as a sum of V_{ij}^{in} and V_{ij}^{sp}. The former represents the inertial collision rate while the latter corresponds to the spatial collision rate.

$$V_{ij}^{t} = \left((V_{ij}^{in})^2 + (V_{ij}^{sp})^2\right)^{1/2} \tag{111}$$

$$V_{ij}^{in} = |1 - Avm| \left(\frac{fu_i + fu_j}{2} - fu_i fu_j\right)^{1/2} u' \tag{112}$$

$$V_{ij}^{sp} = \left(\frac{\left((1 - Avm)fu_i + Avm\right)\left((1 - Avm)fu_j + Avm\right)Sll_{ij}}{2}\right)^{1/2} \tag{113}$$

u', fu_i and Sll_{ij} respectively represent the velocity fluctuation of the fluid, the response coefficient and the longitudinal structure function. The response coefficient given by Eq. 114 is a function of $\Omega \equiv \tau_{p,i}/T_{Lp}$ and z $\equiv \tau_{Tay}/T_L$, which are in turn functions of the particle response time $\tau_{p,i}$, the eddy particle interaction time scale T_{Lp}, the Taylor differential timescale τ_{Tay} and the Lagrangian integral timescale T_L.

$$fu_i = \frac{2\Omega + z^2}{2\Omega + 2\Omega^2 + z^2} \tag{114}$$

In Eq. 115, within the viscous range ($d_{p,ij} \leq \eta_k$), the longitudinal structure function Sll_{ij} solely depends on the turbulence dissipation rate, the kinematic viscosity and the collision diameter. Over the remaining spatial range, the function may be written as a function of the velocity fluctuation, the dimensionless collision diameter $\bar{d} = d_{p,ij}/\eta_k$, the Taylor scale Reynolds number $Re_\lambda = (15u'^4/\varepsilon\nu)^{1/2}$ and a constant $C = 2$.

$$Sll_{ij} = \begin{cases} \dfrac{1}{15}\dfrac{\varepsilon}{\nu}{d_{p,ij}}^2; if\ d_{p,ij} \leq \eta_k \\ 2u'^2\left(1 - \exp\left(-\dfrac{\bar{d}}{(15C)^{3/4}}\right)\right)^{4/3}\left(\dfrac{15^3\,\bar{d}^4}{15^3\,\bar{d}^4 + (2Re_\lambda/C)^6}\right)^{1/6} ; else \end{cases} \tag{115}$$

In the above expressions, $Avm = (1 + C_{Avm})\rho_f/(\rho_p + C_{Avm}\rho_f)$ corresponds to the ratio between the densities of the fluid and the particle phases, where C_{Avm} is the added mass coefficient and is equal to 0.5 for spherical particles.

Annex 7: Oxide layer fragmentation observations in a lab scale IMF

The breaking-up of oxide layers was observed during some experiments at the industrial scale. Therefore, in order to reproduce and study this phenomenon at the lab scale, qualitative observations (camera images and videos) were made during the structured light campaign, where the filling levels, the electrical parameters and the alloy type were varied. In the case of Al-1050, only slight stretching of the oxide layer was observed without any breaking. This was also observed for Al-7050, where the stretching increased as a function of the generator power. An illustration of such a behavior for Experiment 14 is seen in Figure 104. The white lines all across the free surface are due to the oxide layer stretching, without any visual evidence of fragmentation. We also observe two zones where the liquid metal seems stuck to the refractory wall, which could be an unintended result of the melting process of solid blocks of metal alloy.

Figure 104: Camera image of oxide layer stretching
(Al-7050 at 50 % filling level and $P_{gen} = 15$ kW)

On the other hand, due to the presence of highly reactive magnesium, oxide layers for alloy Al-5182 behaved differently. Figure 105(a – c) presents the raw images for a varying generator power. A top layer of crumbled oxides was observed, while any, if at all present, oxide layer fragmentation was hidden underneath. The crumbled oxides may be attributed to the presence of a large quantity of magnesium oxides.

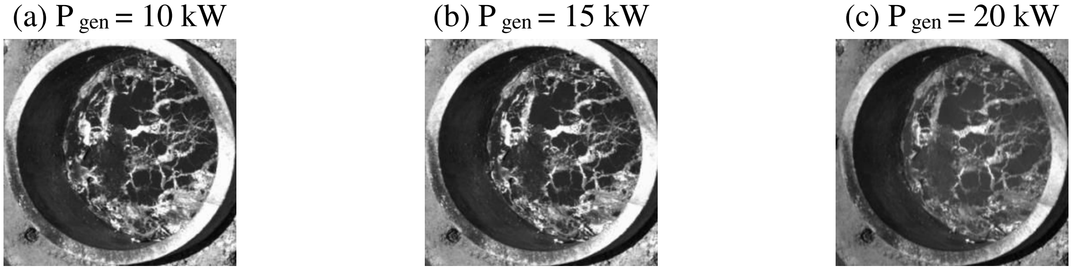

(a) $P_{gen} = 10$ kW (b) $P_{gen} = 15$ kW (c) $P_{gen} = 20$ kW

Figure 105: Raw images for different generator powers for Al-5182 (75 % filling)

Experiment 15 was performed, where the previously observed crumbled layer was carefully skimmed off and revealed the underlying oxide layer. Consequently, slight oxide layer stretch marks were observed, quite similar to previously noted Al-7050 layer. Additionally, we also used a high speed camera to locally study any breaking and re-oxidation between the stretched zones. However, apart from small free surface fluctuations, no other discernable observation could be made. The small crucible diameter (~10 cm) and the ensuing wall effect on the forces acting on the oxide layer could play a role in such a behavior of the oxide layer. Thus for the current configuration, we did not observe any oxide layer fragmentation. The experiments at the industrial scale, on the other hand, show evidence of some fragmentation of the oxide layer which could not be studied in the scope of this dissertation.

Annex 8: Free surface deformation measurements by laser telemetry in a lab scale IMF

The Time of Flight (ToF) technique, described in section A.2.2.1, was implemented using a laser telemetry device (Figure 106 (a)). A Bosch GLM250VF laser telemeter was used on a support system which allowed two degrees of freedom along two orthogonal horizontal axes (Figure 106 (b)) with a step of 10 mm.

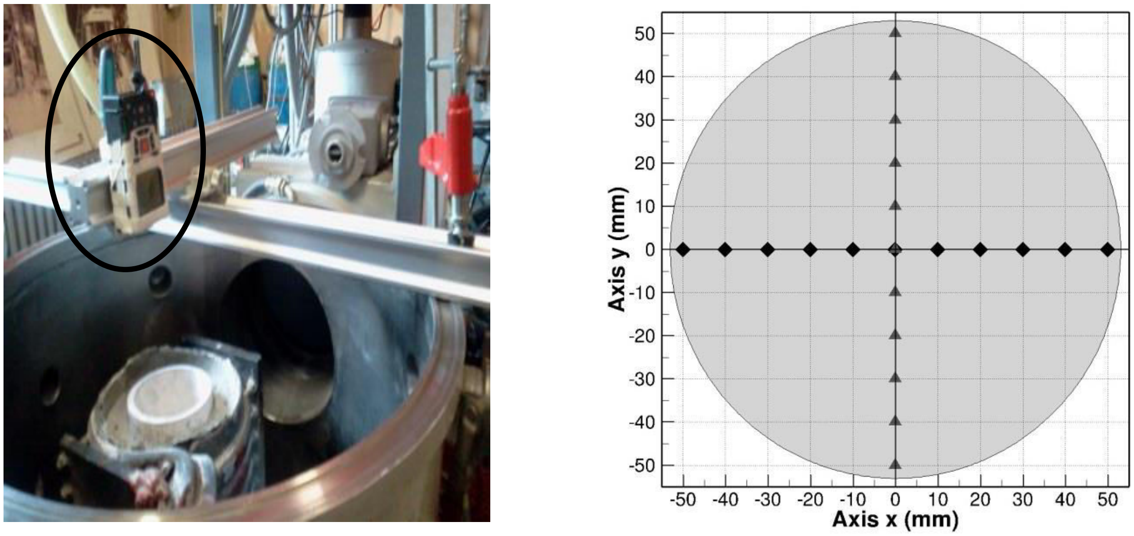

Figure 106: (a) Laser Telemeter setup over the inductor, (b) x and y locations of the telemetry measurements

To avoid overheating of the device, the generator power was cut off between each point of measurement, so that the method follows the sequence in Figure 107.

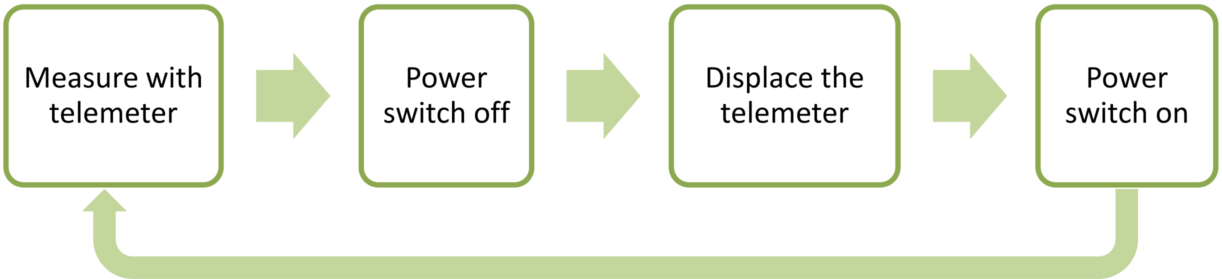

Figure 107: Laser telemeter measurement protocol

Distance between the dome surface and the telemeter was measured. The distance of the initial free surface (at P_{gen} = 0 kW) was measured and taken as the reference distance. These two distances approximated the relative deformation of the free surface as a function of the operating parameters.

Figure 108 shows the deformation along the two axes in 3D for Experiment 3 (75% liquid metal filling and 20 kW generator power). The deformation of the free surface along the y axis was ± 25mm, while that along the x axis was between -40 mm and +25 mm, with respect to the level (z=0 mm).

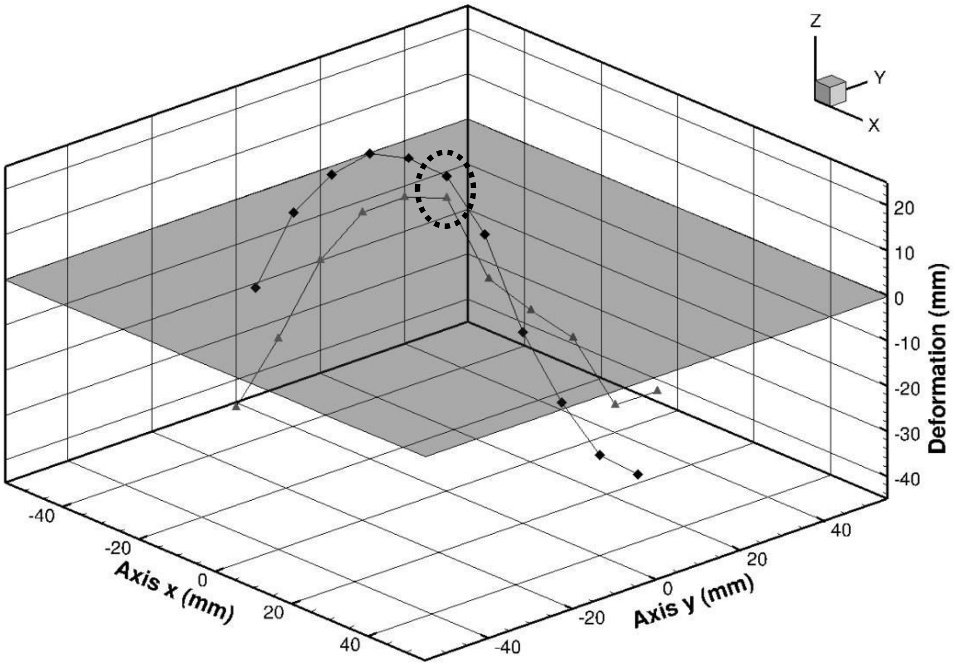

Figure 108: 3D representation of the free surface deformation measured by laser telemetry – Experiment 3

It can be observed that the only intersecting point at x = y = 0 (encircled in dotted black), did not have the same deformation. This is due to the experimental protocol where the generator power was switched off during every telemeter displacement. In some cases, this made the oxide layer stick to the crucible walls which disturbed the surface deformation and thus rendered the results non-reproducible. Therefore, the use of laser telemetry to measure the spatial as well as the temporal evolution of the free surface was deemed impractical.

Annex 9: Impact of the turbulence damping factor near the bath free surface

The need of turbulence damping at the interfacial region has been discussed in section A.3.2.1.1. The additional turbulence damping source term in the ω equation is written as:

$$S_{damp,t} = A_i \Delta n \beta \rho_i \left(\frac{\boldsymbol{B} 6 \mu_i}{\beta \rho_i \Delta n^2} \right)^2 \tag{116}$$

B is the turbulence damping factor. This adjustable factor was previously kept at its default value, equal to 10 as proposed in the ANSYS Fluent documentation. Since damping is active only in the interfacial region, it was hypothesized that any modification of the turbulence damping factor may impact the free surface deformation. Therefore, simulations while varying the damping factor were performed. Figure 109 presents the dome profile for B = 0 and B = 100.

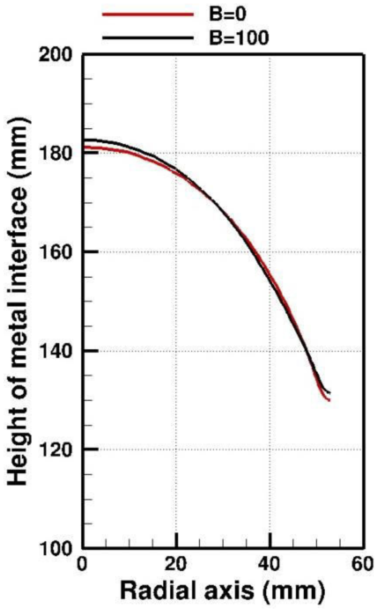

Figure 109: Comparison of dome profiles: B = 0 vs B = 100 – Experiment 9

It is noted that the variation in the turbulence damping factor does not have any significant impact on the dome profile.

Résumé en Français

Dans le secteur aéronautique, la performance des alliages d’aluminium connait une amélioration continue, grâce notamment à l’optimisation des procédés d’élaboration. Dans ce cadre, le travail de recherche vise à prédire le comportement des inclusions dans un bain d’aluminium brassé par induction afin d’améliorer la propreté inclusionnaire des alliages coulés. Un modèle numérique a été développé pour simuler le comportement magnétohydrodynamique du bain d’aluminium dans le creuset suivi par la modélisation du comportement d’une population d’inclusions non-métalliques. Le modèle 2D axisymétrique en régime transitoire s’appuie sur le code de CFD commercial ANSYS Fluent, bien que de nombreuses fonctions utilisateurs aient été introduites pour simuler les phénomènes spécifiques comme l’induction électromagnétique et la résolution des bilans de population. Le modèle MHD résout dans un unique maillage les phénomènes d’induction électromagnétiques, l’écoulement turbulent du bain d’Al, la déformation de la surface libre et les effets de la présence d’une couche de métal oxydée en surface du bain. Une méthode dite de vitesse de glissement (entre les particules et le fluide) a été choisie pour simuler à la fois le transport macroscopique des inclusions dans le bain d’Al et les interactions mésoscopique entre les inclusions (c.à.d. les mécanismes d’agrégation et de fragmentation). Des campagnes expérimentales à l’échelle d’un four de laboratoire et d’une installation industrielle accompagnent le travail numérique pour le valider. Les résultats de modélisation MHD exprimés sous la forme du profil de déformation du bain sont en accord raisonnable avec les mesures faites au laboratoire. Les résultats numériques démontrent également l'effet du frottement induit par la couche d'oxyde sur le profil du bain, ainsi que sur l'écoulement à proximité de la surface du dôme. Pour des conditions opératoires du four industriel en mode de maintien, l’évolution temporelle de la population au sein du bain est calculée. Il apparaît que la séparation magnétique est très intense, particulièrement dans la peau électromagnétique, et est ainsi responsable du transport et de la capture d’une grande fraction de la population d’inclusions à la paroi du four.

Mots clés : Inclusions, Ecoulement Multiphasique, Alliage Aluminium, Mécanique des Fluides Numérique, Métrologie

Abstract

With an objective of improving processing and development of aerospace aluminum alloys, the current dissertation presents experimental and numerical tools which help comprehend the behavior of a non-metallic inclusion population in an Al bath stirred by induction. The mechanisms occurring in the metallurgical reactor were separated into two interlinked issues – (i) Magnetohydrodynamics (MHD) of the induction furnace, and (ii) Inclusion population dynamics in the Al bath, which were modeled using the ANSYS Fluent software and in-house User Defined Functions. For a 2D axisymmetric geometry, numerical simulations were performed in a single framework and calculated: (i) the electromagnetic forces using the A-V formulation, (ii) the free surface deformation using the Volume Of Fluid method, (iii) the turbulent stirring of the bath using a RANS-based k-omega model and (iv) the friction force due to the oxide layer by imposing a pseudo-wall condition on the bath free surface. The steady state MHD results and the physical properties of the inclusion population were used as input data for the transient inclusion behavior modeling. A combination of the Drift Concentration Method and the Population Balance Method was developed to respectively model the mean transport of inclusions within the bath at the macroscopic scale and the inclusion interactions (turbulent aggregation and fragmentation) at the mesoscopic scale. The performance of the MHD numerical tool was evaluated by comparing the model results with experimental results at laboratory and industrial scales. The simulation results in the form of the average bath surface profile were found to be consistent with the laboratory measurements. The results also illustrated the impact of the friction due to the oxide layer on the bath surface deformation as well as on the flow near the dome interface. The inclusion behavior simulations were performed for the holding mode operation of an industrial IMF. The deduced removal frequency compared the relative importance of each phenomenon. It was found that the electromagnetic migration, especially in the electromagnetic skin, dominates the inclusion dynamics and is responsible for the capture of a large fraction of the inclusion population.

Keywords: Inclusions, Multiphase flow, Aluminum alloys, Computational Fluid Dynamics, Experimental analysis